Thèse de doctorat

Study of charmonium production using decays to hadronic final states with the LHCb experiment

Études de production des états de charmonium avec leurs désintégrations vers des hadrons dans l'expérience LHCb

Thèse de doctorat de l'Université Paris-Saclay
préparée à l'Université Paris-Sud
Laboratoire de l'accélérateur linéaire

Ecole doctorale n°576 Particules, Hadrons, Énergie, Noyau, Instrumentation, Imagerie, Cosmos et Simulation (PHENIICS)
Spécialité de doctorat : Physique des particules

Thèse présentée et soutenue à Orsay, le 05 Juillet 2019, par

ANDRII USACHOV

Composition du Jury :

Fabien Cavalier Directeur de recherche (LAL)	Président
Claudia Patrignani Professor (University of Bologna)	Rapportrice
Antonio Vairo Professor (Technical University of Munich)	Rapporteur
Vincenzo Vagnoni Professor (INFN, Bologna)	Examinateur
Tatsuya Nakada Professor (EPFL, Lausanne)	Examinateur
Achille Stocchi Professeur (LAL)	Examinateur
Sergey Barsuk Directeur de recherche (LAL)	Directeur de thèse

LAL 19-014

Contents

List of Figures

List of Tables

Chapter 1

Introduction

Studies of charmonium production provide stringent tests of Non-Relativistic QCD-based models. The so far theory tests come mostly from the measurements of experimentally clean 1^{--} charmonium states, the J/ψ and $\psi(2S)$, decaying to a pair of muons. In addition, χ_{c1} and χ_{c2} states are reconstructed via their radiative transitions to J/ψ, which however requires a reconstruction of low-energy photons. Reconstructing charmonium decays to hadrons allows to perform production studies of all known charmonium states. Using charmonia decays to $p\overline{p}$ and $\phi\phi$ final states I study production of $\eta_c(1S)$, $\eta_c(2S)$ and χ_{cJ} states with the LHCb experiment. For that I proposed a technique to select pure multi-ϕ final states free from kaon combinatorial background. This analysis report first measurement of χ_{c0} and $\eta_c(2S)$ production in b-hadron inclusive decays and the most precise χ_{c1} and χ_{c2} production in the mixture of all b-hadrons. In addition, the evidence of the decay $\eta_c(2S) \to \phi\phi$ is reported for the first time. Two different techniques have been employed to measure the $\eta_c(1S)$ production using the $\eta_c(1S) \to p\overline{p}$ decay. In addition, using this decay, the most precise single determination of the $\eta_c(1S)$ mass is also performed in the thesis. The first measurement of the $\eta_c(1S)$ prompt production in proton-proton collision at $\sqrt{s} = 13\,\text{TeV}$ is reported together with the most precise determination of the branching fraction $b \to \eta_c(1S)X$. Also, reported measurement of the $\eta_c(1S)$ mass is the most precise measurement from a single experiment to date.

In order to compare the obtained result to theory predictions, I proposed to use a simultaneous fit of the measured production for charmonium states with linked long-distance matrix elements using prompt charmonium production and production in b-hadron inclusive decays. This allows to strongly restrict the allowed phase-space of the matrix elements describing charmonium production. This also demonstrates a limit of theory application and calls for further model development.

In addition, a search for other charmonium(-like) states production in b-hadron inclusive decays is performed relative to the production of charmonium states with similar quantum numbers. I measure the branching fraction of the $\eta_c(1S) \to \phi\phi$ decay to resolve a tension in other existing measurements.

Finally, B_s^0 mesons are reconstructed via decays to two or three ϕ mesons. This allows to perform an independent measurement of $\mathcal{B}(B_s^0 \to \phi\phi)$ and the first evidence of the decay $B_s^0 \to \phi\phi\phi$. A resonance structure of the $B_s^0 \to \phi\phi\phi$ decay as well as ϕ meson polarization is studied with limited available decay sample.

This thesis is organised as follows. Chapter 2 introduces selected available phenomenological approaches to describe charmonium production and confronts their predictions to the production observables measured at different facilities. Chapter 3 summarises charmonium decays channels to hadrons, which can potentially be used to reconstruct charmonium at LHCb. Chapter 4 describes the LHCb detector and shows how hadronic final states can be reconstructed and triggered. Chapter 5 describes the analysis of $\eta_c(1S)$ production at $\sqrt{s}$ =13 TeV using decays to $p\overline{p}$. Chapter 5.6 addresses the analysis of χ_c and $\eta_c(2S)$ production measurement in b-hadron inclusive decays using decays to $\phi\phi$. Chapter 7 compares obtained experimental results with theory predictions. A simultaneous fit of S-wave charmonium states production is also reported. Chapter 8 documents measurements of charmonium resonance parameters using both $p\overline{p}$ and $\phi\phi$ decay channels. Chapter 9 describes a study of B_s^0 meson decays to ϕ mesons. Finally, Chapter 10 summarises the study and discusses future prospects of charmonium production measurements at LHCb. Other studies requiring reconstruction of charmonium states using their decays to hadrons are also addressed.

Chapter 2

Charmonium production

This chapter describes the state of art of charmonium production. The charmonium production is a branch of heavy flavour production studies, which is essential for understanding of the dynamics of strong interactions. From a theory point of view, the production of charmonium or bottomonium is a problem involving several energy scales and to be solved by QCD. The interplay between different scales makes this problem more complex and requires accurate calculations of the entire production process by using different approaches to describe effects happening at different scales.

The experimental studies are being performed since more than 40 years and include many measured observables. As will be shown in this chapter, the theory aims at simultaneous description of most of the measured experimental observables. Despite a significant progress from both theory and experimental sides, a comprehensive description of observables remains a challenge. It will be shown, that the LHCb measurements of the η_c[1] and χ_c production play an outstanding role in formulating the charmonium production puzzle. Besides, further measurements requested by theory can be performed at LHCb.

After the introducing quarkonium in Section 2.2, different theoretical approaches to describe quarkonium production are addressed in Section 2.3. The current status of charmonium production puzzle is given in Section 2.4 by confronting available measurements of charmonium production observables at many facilities to theory predictions.

[1]The $\eta_c(1S)$ meson is denoted as η_c throughout the thesis. In some places, to be more explicit the $\eta_c(1S)$ denotion is used for clarity.

2.1 Introduction

The Quantum Chromodynamics (QCD) is a sector of Standard Model (SM) aiming to describe strong interactions. The QCD originates from the first theories addressing a structure of hadrons such as Gell-Mann's quark model [2] and parton model [3, 4]. A development of the theory describing interactions of the hadron constituents was triggered by first experimental results probing an internal structure of a proton [5]. At the same time a color charge of strong interactions has been introduced [6] considering hadrons as colourless objects.

The discovery of the first charmonium state J/ψ in 1974 - so-called November revolution - happened only 10 years after the initial Gell-Mann's paper. The J/ψ meson was discovered by the experiments at BNL [7] and SLAC [8]. This was a great success of the Gell-Mann's quark model [2] and the first observation of c-quark. The existence of fourth quark was predicted [9] to explain a suppresion of flavour-changing neutral currents, and in particular the $K_L \to \mu^+\mu^-$ decay. The suppression has been explained only one year before the J/ψ discovery by Glashow, Iliopoulos and Maiani by so-called GIM mechanism [10]. Systematic studies of charmonium properties started shortly after its discovery.

The strong dynamics is modulated by a strong coupling constant α_s. The behaviour of α_s depending on the energy scale is such, that at high energies (short distances) the α_s is small, which causes the asymptotical freedom regime. It also means that at large energies, a strong dynamics can be described perturbatively using an expansion on α_s. Contrary to the electomagnetic coupling constant, the α_s becomes large at small energies and confinement regime takes place. The confinement explains the existence of the color field only inside hadron matter in mesons and baryons. However, the confinement has never been obtained analythically. At low energies, the expansion on α_s has not much sense and perturbative methods don't work anymore. The non-perturbative dynamics can be derived from the first principles using for example lattice calculations [11]. However, the predicting power of lattice calculations remains limited.

The quarkonium - charmonium and bottomonium - production is a complex process involving several well-separated energy scales. A number of phenomenological approaches aims at its description by introducing factorization, expansion on scales etc. The interplay between the scales and the treatment of the initial state plays a crucial role in the QCD phenomenology.

The first measurements at Tevatron [12] demonstrated that existing theoretical framework within Color Singlet (CS) model underestimates the measured J/ψ production cross-section by an order of magnitude, which was explained by a large Color Octet (CO)

contribution. Moreover, further measurements of the J/ψ polarisation in hadron-hadron collisions showed that J/ψ meson is produced almost unpolarized contrary to the CO theory prediction. This is known as the J/ψ polarization puzzle.

Existing theoretical frameworks give links between production observables of different quarkonim states. This work follows the first measurement of the η_c production at LHCb [13] in 2014, which has to be described by theory simultaneously with the J/ψ production and polarization. Contrary to expectations, Color Octet contributions largely overestimate the measured η_c production cross-section. This is an example how current phenomenological approaches are challenged by a limited number of measured observables. Finally, a perspective approach aims at simultaneous description of charmonium production in different collision processes.

A significant experimental progress can be achived by performing measurements of new charmonium production observables at LHC following an example of the η_c production measurement. The LHCb experiment is probably the only LHC experiment, which is capable to provide a set of new measurements using signatures of charmonium decays to hadrons. However, further investigations are still needed.

2.2 Quarkonium

The quarkonium is a bound state consisting of a heavy c (charmonium) or b (bottomonium) quark-antiquark pair. Quarkonium is as much important object for Quantum Chromodynamics (QCD) as positronium or hydrogen atom for Quantum Electrodynamics (QED). The quark Q is considered to be heavy if its mass m_Q is much larger than the QCD scale $\Lambda_{QCD} \approx 200$ MeV. Only c, b and t quarks satisfy this requirement. Note that here only a qualitative relation is discussed, while for strict description one needs to define a quark mass value and always estimate the corresponding uncertainty.

Quarkonium is a non-relativistic object such that the values of v^2 is about 0.3 (0.1) for charmonium (bottomonium) states, where v is the heavy quark velocity in the charmonium rest frame. Hence, the mass of ground state quarkonium is comparable with the $2m_Q$. Note, that only two flavours form quarkonium. The t quark is the heaviest particle in the Standard Model (SM), so in principle it could form a non-relativistic $t\bar{t}$ bound state (toppomonium) with $v^2 \sim 0.01$. However, the lifetime of the t quark is about $5 \times 10^{-25}\,s$, which is one order of magnitude smaller than the time scale of the strong interaction. It means, that the t quark decays before its hadronisation to bound state. The s quark is much lighter than c quark and hence the $s\overline{s}$ mesons are rather relativistic. Another issue is that the lightest known "pure" $s\overline{s}$ state, $\phi(1020)$, is not a bound state but a resonance since its mass is above the K^+K^- threshold differently from charmonium or bottomonium states below $D\overline{D}$ and $B\overline{B}$ mass threshold, respectively.

A first approach to describe quarkonium was done with potential model describing non-relativistic quark-antiquark interaction. A generic central potential can be written as

$$V(r) = -\frac{4}{3}\frac{\alpha_s}{r} + b\,r, \tag{2.1}$$

where α_s is the strong coupling constant, r is a radial distance between quark and antiquark and b is a parameter. The first term represents a Coulomb potential with a quark color factor 4/3. The asymptotics of the first term represents an asymptotic freedom of quark at small distance. The dependence of α_s on the scale has to be taken into account to describe the running constant as

$$\alpha_s(r) = \frac{2\pi}{9\,ln\frac{1}{r\Lambda_{QCD}}}. \tag{2.2}$$

An illustrative dependence of the α_s on r is shown on Fig. 2.1. The last expression is done in one-loop approximation, while for taking into account higher order corrections

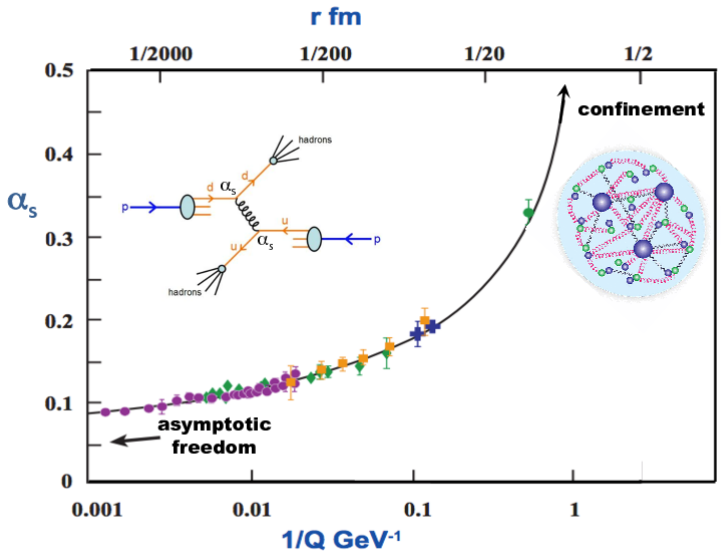

Figure 2.1: The dependence of α_s on distance r.

a specific renormalization scheme should be used (see for example Refs. [14, 15]). The second term in Eq. 2.1 represents a long-distance interaction and is related to confinement. The dependence of second term on r can be different; the only trend is that it should grow with inrease of r. The choice of linear dependence is coming from the description of interaction as string-like at long distances. The most popular non-relativistic potential of this shape is Cornell potential [16–19].

Similarly to QED, the potential can be improved in order to take into account relativistic spin interactions as discused in Ref. [20] as

$$V_1(r) = V_{LS}(\vec{L}\vec{S}) + V_T(r)[S(S+1) - 3\frac{(\vec{S}\cdot\vec{r})(\vec{S}\cdot\vec{r})}{r^2}] + V_{SS}(r)[S(S+1) - 3/2], \quad (2.3)$$

where V_{LS}, V_T and V_{SS} described spin-orbit, tensor and spin-spin interactions, respectively; S, L are spin and orbital momentum quantum numbers. The V_{SS} is responsible for mass splitting between singlet and triplet quarkonium states, for example between η_c and J/ψ. After V_{LS}, V_T and V_{SS} terms are defined, the solution of Shrödinger equation will produce a quarkonium spectrum. A general review of charmonium potential models is given in Ref. [20].

Another model is Buchmüller-Tye model [21] developed in 1980. Results of this model are often used as an estimate charmonium wave function at origin. Interestingly, that original paper [21] predicts triplet-singlet mass of ground state charmonium splitting

(J/ψ-η_c mass difference) to be about 100 MeV, which is not far from current world average value of 113.3 MeV.

In potential models the potential should reflect also non-perturbative effects and hence needs to be tuned in order to describe quarkonium spectrum.

It is important to emphasize that for lowest level S-wave quarkonia ($\Upsilon(1S)$, J/ψ, η_c) and B_c^+, the binding energy is relatively large such that $m_Q v^2 \gtrsim \Lambda_{QCD}$, which is not the case for excited quarkonium states (Fig. 2.2). This allows to apply perturbative theory for S-wave quarkonia since non-perturbative corrections are small. Moreover, it means that precision physics is possible for these states to extract important model parameters, such as masses of b or c quarks, strong coupling constant, hyperfine splittings, natural width, leptonic decay widths, etc. For excited quarkonium states the computations are more sophisticated since non-perturbative effects are large and an input from lattice calculations is needed. However, both spin-dependent and spin-independent potentials can been computed on lattice.

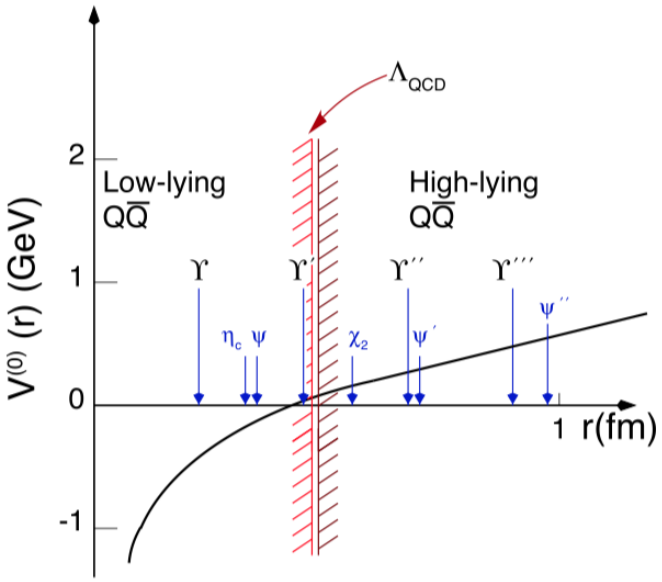

Figure 2.2: Static $Q\bar{Q}$ potential as a function of quarkonium radius r [1].

Several approaches have been used in order to obtain spin-dependent and spin-independent potentials from QCD without relying on perturbation theory. The spin-dependent and spin-independent $Q\bar{Q}$ potentials up to $O(1/m_Q^2)$ were obtained for example in Refs. [22–26] and then investigated using lattice [27]. It has been pointed out that some potentials are missed [28, 29]. Also, the infra-red divergences in the perturbative

computations of P-wave quarkonium decays were impossible to accommodate in the framework of potential models.

In general framework, well-distinguished scales of quarkonium physics such as m_Q, relative momentum of heavy quarks $m_Q v$ and binding energy $m_Q v^2$ are treated with a help of Nonrelativistic Effective Field Theories. Indeed, for quarkonium the following hierarchy of scales takes place $m_Q \gg m_Q v \gg m_Q v^2$. The EFTs take an advantage from scales separation by integrating out higher energy scales in order to describe observables at lower energy regions. Non-relativistic EFTs are originated from QCD by systematically integrating out the high energy scales and replacing QCD by suitable expansions. The EFT should be equivivalent to QCD if all orders of the scale expansion are considered. As will be shown later, the potential picture of quarkonium dynamics can be obtained as a particular case of Nonrelativistic EFTs.

The following EFTs have been developed for quarkonium physics:

- Non-Relativistic QCD (NRQCD) [30, 31], factorizing contibutions from the scale m_Q (see Section 2.3.3);
- potential NRQCD (pNRQCD) [32, 33], dedicated to describe quarkonium states close to threshold. The pNRQCD arises from QCD by integrating out all energy scales above mv^2 such as m and mv.

The pNRQCD provides a description, which is close to Shrödinger description. The Lagrangian of pNRQCD can be written as a sum of static potential lagrangian, corrections to potential and interactions with other low-energy degrees of freedom.

Specific EFTs have been also developed to describe charmonium-like states above $D\overline{D}$ threshold, where additional degrees of freedom (open heavy flavour, molecule, hybrid, etc.) can play an important role. Examples for $X(3872)$ state can be found in Refs. [34–36].

In this work I will focus on most of charmonium states below $D\overline{D}$ threshold. Namely, S-wave charmonium states η_c and J/ψ together with their radial excitations $\eta_c(2S)$ and $\psi(2S)$ and P-wave states χ_{c0}, χ_{c1}, χ_{c2} and to some extend h_c will be discussed. A scheme of charmonium family under $D\overline{D}$ threshold together with charmonium states quantum numbers and dominant transitions are shown on Fig. 2.3. The notation of charmonium states follows traditional form of atomic physics $^{2S+1}L_J$, where J is a total angular momentum. Currently, all charmonium states with a mass below the $D\bar{D}$ threshold have been observed and have their quantum numbers J^{PC} well established.

Generally, quarkonium provides many important observables for understanding nature of strong interactions. Both perturbative and non-perturbative effect are involved.

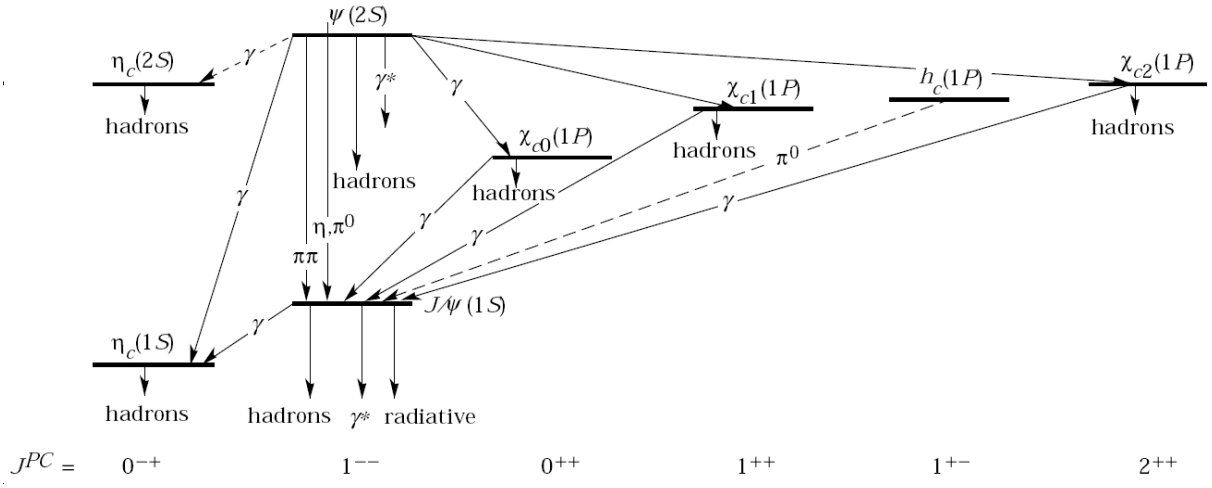

Figure 2.3: Quantum numbers and decays of charmonium states below $D\bar{D}$ threshold.

Quarkonium spectroscopy and decays provide important information for QCD due to natural annihilation diagrams allowing separation between initial and final states in the first approximation. In the following sections, charmonium production in different processes is addressed.

2.3 Theoretical formalism of quarkonium production

Generally, quarkonium can be produced in many processes, and each of them provides an important observable for various theoretical formalisms based on QCD. In this work, I focus on inclusive production of single quarkonium in hard processes: parton scattering and decays.

Among the complementary observables not mentioned in this work, one can highlight multiple quarkonium production in hard processes, jet-associated production, production in ion collisions, various exclusive production processes. The multiple quarkonium production in hard processes provides important complementary observables to the theoretical framework addressed in this section, which come however through the description of multiple parton scattering. Quarkonium production in medium (e.g. ion collisions) measures nuclear modification factors to study properties of cold nuclear matter or quark-gluon plasma (QGP) by comparing the quarkonium production in pp, pA and AA collisions, where A denotes an ion with the mass number A. The central exclusive quarkonium production in soft processes are essential for soft QCD and should be described by entirely different theoretical approaches. It has an advantage of most direct theory interpretation by for example Regge-based theory. The only color singlet state can be created in the central exclusive production process.

The inclusive production of quarkonium states implies at least three well-distinguished intrinsic momentum scales: the mass of the heavy quark, m_Q; the relative momentum of heavy quarks of order $m_Q v$ and the binding energy $m_Q v^2$. For quarkonium produced in the scattering process, the scattering scale p_{hard} also enters the description of quarkonium production. Below, I consider the case of charmonium, while similar considerations apply also for bottomonium. However, the bottomonium production description can differ from charmonium one. Since two of the mentioned scales involve relative quark velocity v, one naively expects that higher-order corrections on these scales are smaller for bottomonium. Therefore, the color octet mechanism described in this section is likely to be relevant to a lesser extend for bottomonium than for charmonium. Nevertheless, with more available data on different bottomonium states production, theory will utilize powerful comparisons of charmonium and bottomonium production under expansions in v.

Quarkonium can be inclusively produced in following hard processes:

- Transitions from higher mass quarkonium states (feed-down),
- b-hadron decays[2],

[2]relevant for charmonium only

- Bottomonium decays[2],
- e^+e^- collisions,
- ep collisions,
- Initial parton scattering in hadron-hadron collisions (hadroproduction),
- Z, W, Higgs or t-quark decays.

Experimentally, the measured production cross-section includes the feed-down from higher mass quarkonium states, which can be produced in the same production process. In the case of hadron-hadron collision, the total production process (sum of hadroproduction and the feed-down contributions) constitute prompt production. The feed-down subtracted production cross-section is often referred as direct production.

The feed-down contributes to the most of production cases and can be estimated using theoretical and experimental input. The amount of the feed-down contribution depends on the production cross-section of higher mass charmonium states and on the branching fractions of the feed-down transitions. The feed-down can be experimentally subtracted if the production of states, which are its dominant sources, is measured in the same kinematical regime and input branching fractions are known. The total feed-down contribution can be quite sizeable. For example, about 30% of promptly produced J/ψ at Tevatron or LHC are coming from χ_c and $\psi(2S)$ transitions to J/ψ. In this case, the feed-down contributions should be taken into account carefully because theoretical uncertainty on J/ψ hadroproduction cross-section is comparable. At the same time, the experimental observables are rather well measured. While measurement of χ_c and $\psi(2S)$ production cross-sections can be accessed experimentally and then used in the J/ψ production description, the experimental determination of the feed-down contribution to η_c production cross-section is more complicated. The dominant expected source of the feed-down to η_c state is the h_c charmonium state, which decays to $\eta_c\gamma$ with a branching fraction of about 50%. The production of the h_c state has been never measured at hadron machines. Hence, the feed-down from h_c state can be addressed only theoretically and using experimental upper limits if any. On the other hand, the heaviest charmonium states below the $D\overline{D}$ threshold are feed-down free, since the resonances above the threshold would rather decay strongly to $D\overline{D}$ with the branching fraction close to 100%. Consequently, all effects of the feed-down contributions to any J/ψ production observable can be studied by measuring the same observable for radially excited $\psi(2S)$ state, which is feed-down free.

The Z, W, Higgs or t-decays can provide an important test of quarkonium production but are extremely complicated to measure at available facilities. Both production cross-section and branching fraction of Z, W, Higgs or t-decays to quarkonium are very small. Hence, these cases of quarkonium production suffer from the lack of data. Also, not many experimental measurements are available for bottomonium decays to charmonium.

Apart from the production cross-section, another important observable is the quarkonium polarisation, which should be described simultaneously within the same theoretical framework.

The hard scale parameter is estimated differently for different production processes: in the case of quarkonium production in hadron-hadron collisions, the scale is usually defined as the order of charmonium transverse momentum, p_{T}, while for the e^+e^- collisions or production in decays the quarkonium momentum in the e^+e^- rest frame, p^*, is used.

Naively one might expect that the good separation between the scales would lead to splitting quarkonium production process into two independent stages of $Q\bar{Q}$ pair creation and its hadronisation to the quarkonium state. The latter is known as the factorisation assumption, where the amplitude of the entire production process can be written as the sum of products of the short-distance and long-distance matrix elements. The $Q\bar{Q}$ pair creation is a short-distance process happening at the p_{hard} scale and can be calculated perturbatively using an expansion in α_s. The hadronisation is a long-distance process, and its dynamics is characterised by the scales $m_Q v$, $m_Q v^2$ and Λ_{QCD}. The long-distance matrix elements (LDME) describing hadronisation cannot be calculated perturbatively and are expanded in terms of $m_Q v$ and $m_Q v^2$. The LDME values are obtained from phenomenology or lattice calculations. The independence of stages of the production leads to the universality assumption, that the values LDMEs are the same for production processes, whose scale p_{hard} is large enough.

2.3.1 Factorization and PDFs

The short distance process of quarkonium production is firstly described at the level of parton interactions. The quarkonium hadroproduction at LHC energies is happening predominantly via gluon-gluon fusion. Precise theoretical description also need to take into account other partonic processes (e.g. take into account quark-quark process) since their contribution is not negligible.

In order to obtain the hadroproduction cross-section, the partonic cross-sections should be convoluted with corresponding non-perturbative probability density functions (PDFs) of partons (e.g. gluons and quarks in the case of hadron-hadron collisions). The PDFs of

gluons and quarks of different flavours are extracted from global fits to many measured production observables.

The treatment of the partons of initial state can be different. Most of the theoretical calculation of quarkonium production is performed within collinear factorisation [37, 38]. In the collinear factorisation the transverse momentum of initial partons is neglected. Hence, the PDFs do not depend on parton transverse momentum. Within collinear factorisation, full Next-to-Leading-Order in α_s calculations of quarkonium production are available as will be shown in Section 2.4.

The k_{T}-factorisation [39–41] is another approach to perform factorisation to describe quarkonium production. The k_{T}-factorisation approach takes into account a dependence of partonic PDFs on their transverse momentum k_{T} and longitudinal momentum fraction x carried by parton. The gluon dynamics is described by Balitsky-Fadin-Kuraev-Lipatov (BFKL) evolution equation [42, 43] resumming logarithmic contributions by introducing reggeized gluons. The k_{T}-factorisation works in high energy regime, i.e. $\sqrt{s} \to \infty$ or small-x limit. In the collinear factorisation approach, the initial state parton can receive some transverse momentum at NLO by emitting additional parton. The same term appears in the k_{T}-factorisation at LO so that there is an interplay between k_{T}-factorisation and collinear factorisation. Physically, one can interpret that higher order terms appear due to taking into account initial state radiation. The latter leads to more accurate LO calculations with k_{T}-factorisation than LO predictions made with collinear factorisation. On the other hand, k_{T}-dependence is poorly constrained since it requires a special transverse momentum dependent PDFs (TMDs), while collinear factorization uses integrated PDFs. Another issue of k_{T}-factorisation is that only the LO calculations are available so far.

Similarly, TMD factorisation, firstly introduced in Ref. [44] and discussed in Refs. [45] works at lower energy limit and resumes many parton emissions from initial state. The complications of TMD factorisation is that some cancellations appear only after the integration over transverse momentum. The TMD factorisation works better at low-p_{T} range compared to collinear factorisation. The NLO computation within TMD factorization for quarkonium production is not available, however it is done for Higgs production [46].

Below, different theoretical models describing inclusive quarkonium production in hard processes are summarised. The key difference between models is the approach to the long-distance hadronisation description.

2.3.2 Color evaporation model

The colour evaporation model (CEM) is an easy and historically one of the first phenomenological models of quarkonium production [47–49].

The CEM assumes that produced $Q\bar{Q}$ pair hadronizes into quarkonium if the initial mass of $Q\bar{Q}$ is below the threshold of the two open-flavour mesons creation (e.g. $D\overline{D}$ threshold in the case of charmonium). Hence, in the CEM the total inclusive production cross-section of charmonium state H in $A + B$ collision is expressed as

$$\sigma_{A+B\to H+X} = F_H \int_{4m_Q^2}^{4M^2} dm^2_{Q\bar{Q}} \frac{d\sigma_{A+B\to H+X}}{dm^2_{Q\bar{Q}}}, \tag{2.4}$$

where $m_{Q\bar{Q}}$ is the mass of $Q\bar{Q}$ pair, the M is the mass of the lightest open flavour meson containing quark Q, the $d\sigma_{A+B\to H+X}/dm^2_{Q\bar{Q}}$ is the differential production cross-section and the F_H is the probability of hadronization of $Q\bar{Q}$ to a given quarkonium H.

The F_H is a non-perturbative constant, which does not depend on the momentum nor on the process. The F_H is the only parameter of the model and can be determined using a measurement of total H production cross-section. Once F_H is determined, the prediction of differential production cross-section in any process and kinematical conditions can be obtained in a straightforward way. The Eq. 2.4 implies internal sum over spin and colour states of $Q\bar{Q}$. The model assumes that the colour of $Q\bar{Q}$ system is neutralised by the surrounding field (colour evaporation). In other words, CEM assumes that the requirement of quarkonium colourlessness does not imply any constraint on colour states of $Q\bar{Q}$ and all of them contribute to overall production. Note, that the sum of F_H for different charmonium states is less than unity because the $Q\bar{Q}$ system can receive some energy from a surrounding medium during the hadronisation stage. Naively, taking into account the probability to produce a colourless object among 3×3 possible color combinations of $Q\bar{Q}$ one can expect that

$$\sigma_{A+B\to H+X} = \frac{1}{9} \int_{4m_Q^2}^{4M^2} dm^2_{Q\bar{Q}} \frac{d\sigma_{A+B\to c\bar{c}+X}}{dm^2_{Q\bar{Q}}}, \tag{2.5}$$

while the remaining part of the $c\bar{c}$ pair production cross-section should be accounted by the open flavour production. In the case of hadron-hadron collisions, the Eq. 2.4 should be written for parton-parton interactions, $i + j \to H + X$, and then convoluted with PDFs.

The CEM at LO predicts the p_{T}-differential production cross-section of charmonium production in hadron-hadron collisions to be proportional to a δ-function or, in other

words, charmonium is produced with $p_{\mathrm{T}} = 0$. The production processes of $i + j \to kQ\bar{Q}$ can produce charmonium with non-zero p_{T}, where k is another quark or gluon. Hence, in order to describe p_{T}-differential production cross-section, first complete NLO calculations for CEM have been performed for hadron-hadron collisions [50, 51].

The CEM has been extensively tested and compared with other theoretical models and measurements. For a corresponding review see Refs. [52, 53]. A straightforward prediction of CEM is that the production ratio of any pair of quarkonium states is the same for different production processes. The apparent violation of this prediction is observed in the comparison of the feed-down contribution from χ_c states to J/ψ prompt production to J/ψ production in b-hadron decays as will be discussed in next section. In addition, CEM predicted a qualitative description of the J/ψ, $\psi(2S)$ and χ_c p_{T}-differential production cross-sections obtained for example at CDF [52]. However, the quality of fits to data is poor. CEM predicts the production rate of χ_{cJ} states to be proportional to $2J + 1$, which is strongly violated as shown in Chapter 7.

The independence of production on the spin of the $Q\bar{Q}$ pair leads to the prediction of non-polarisation of quarkonium, which contradicts to the observed non-zero polarisation of J/ψ meson in many processes (see Section 2.4). The recently developed Improved Color Evaporation Model (ICEM) aims at describing both quarkonium production and polarisation more appropriately without increasing the number of parameters of the model [54]. Particularly, the ICEM distinguishes soft emitted gluons by the $Q\bar{Q}$ system from exchanged gluons. Therefore, the interaction of $Q\bar{Q}$ pair with surrounding strong field is described in more details.

The ICEM gives a reasonable basic description of the relative charmonium production contrary to naive CEM. In addition to that, ICEM predicts non-zero polarisation of J/ψ mesons [55]. Further improvement of ICEM is ongoing by exploiting k_{T}-factorisation for calculations.

One can conclude that CEM is an easy illustrative model, which depends on a single parameter for each charmonium state, with however limited predicting power. Significant improvements came from introducing ICEM.

2.3.3 Non-Relativistic QCD (NRQCD)

The non-relativistic QCD (NRQCD) [31] is so far the most successful theoretical framework predicting inclusive quarkonium production. Contrary to CEM, NRQCD recognises separate contributions from different spin and colour states of $Q\bar{Q}$. The latter is achieved by taking into account a description of the hadronisation via expansion in $m_Q v$ and $m_Q v^2$.

A generic expansion for quarkonium production in NRQCD can be written as

$$d\sigma_{A+B\to H+X} = \sum_n d\sigma_{A+B\to Q\bar{Q}[n]+X}\langle O^H(n)\rangle, \tag{2.6}$$

where n denotes the color and spin state of $Q\bar{Q}$ and the $\langle O^H(n)\rangle$ is the LDME describing the evolution of $Q\bar{Q}[n]$ to a quarkonium state H.

Historically NRQCD is an extension of Color Singlet (CS) Model (CSM) - the first model describing quarkonium production [56–59]. The CSM assumes that only colourless $Q\bar{Q}$ state contributes to the quarkonium production. CSM also requires $Q\bar{Q}$ to have the same spin state as the resulting H.

The most profound internal theoretical evidence of the incompleteness of the CS model comes from the presence of infrared divergences in the production cross sections and decay rates of P-wave quarkonium. The presence of infrared divergences implies a failure of the simple factorisation assumption, upon which the CS model is based.

The NRQCD approach provides a natural solution by introducing a Color Octet (CO) mechanism in addition to nominal CS. Within CO mechanism, the colour and spin states of $Q\bar{Q}$ and quarkonium can be different and are adjusted during the hadronisation stage. Heavy quark pairs that are produced at short distances in a CO state can evolve into physical charmonium via emitting soft gluons when the quark pair has already expanded to the charmonium size. According to the power counting rules described below, all CO matrix elements for the production (or decay) of S-wave quarkonia are suppressed by powers of the velocity compared to the CS contribution. Hence, the CS model is naturally included in NRQCD and represents the first term of expansion on v. However, CO processes can become significant, and even dominant, if the short-distance cross section for producing $Q\bar{Q}$ in a CO state is enhanced.

Contrary to CEM and CSM, NRQCD is a rigorous EFT, which aims at describing of quarkonium at scales smaller than m_Q. The Lagrangian NRQCD can be derived from the QCD one by using an expansion in $1/m_Q$. The NRQCD Lagrangian up to $O(1/m_Q^2)$ can be written as.

$$\mathcal{L}_{NRQCD} = \mathcal{L}_g + \mathcal{L}_l + \mathcal{L}_\psi + \mathcal{L}_\chi + \mathcal{L}_{\psi\chi}, \tag{2.7}$$

where the interaction term $\mathcal{L}_{\psi\chi}$ is expressed in terms of singlet and octet operators $O_1(^1S_0)$, $O_1(^3S_1)$, $O_8(^1S_0)$, $O_8(^3S_1)$ as

$$\mathcal{L}_{\psi\chi} = \frac{f_1(^1S_0)}{m_Q^2}O_1(^1S_0) + \frac{f_1(^3S_1)}{m_Q^2}O_1(^3S_1) + \frac{f_8(^1S_0)}{m_Q^2}O_8(^1S_0) + \frac{f_8(^3S_1)}{m_Q^2}O_8(^3S_1), \tag{2.8}$$

$$\begin{aligned} O_1(^1S_0) &= \psi^+\chi\chi^+\psi, \\ O_1(^3S_1) &= \psi^+\boldsymbol{\sigma}\chi\chi^+\boldsymbol{\sigma}\psi, \\ O_8(^1S_0) &= \psi^+T^a\chi\chi^+T^a\psi, \\ O_8(^3S_1) &= \psi^+T^a\boldsymbol{\sigma}\chi\chi^+T^a\boldsymbol{\sigma}\psi, \end{aligned} \tag{2.9}$$

where ψ is a spinor that annihilates the quark and χ is a spinor that creates the antiquark, T^a is a basis generator of the fundamental representation of the $SU(3)$ group. As was already mentioned, NRQCD introduces CO LDMEs. The color-octet contributions can not be incorporated using potential models.

The NRQCD factorization predicts a scale dependence of short-distance matrix elements. For example, the contributions corresponding to different S-wave LDMEs relevant for J/ψ production have the following asymptotic behaviour

$$d\sigma^{J/\psi}_{^3S_1^{[8]}}/dp_{hard} \sim 1/p_{hard}^4 \tag{2.10}$$

$$d\sigma^{J/\psi}_{^1S_0^{[8]}}/dp_{hard} \sim 1/p_{hard}^6 \tag{2.11}$$

$$d\sigma^{J/\psi}_{^3P_J^{[8]}}/dp_{hard} \sim 1/p_{hard}^6 \tag{2.12}$$

$$d\sigma^{J/\psi}_{^3S_1^{[1]}}/dp_{hard} \sim 1/p_{hard}^6. \tag{2.13}$$

That is why in a high momentum region, the production is sensitive to $O_8^{J/\psi}(^3S_1)$, while at lower momenta, two matrix elements $O_8^{J/\psi}(^1S_0)$ and $O_1^{J/\psi}(^3S_1)$ have similar asymptotic behavior. For illustration, typical diagrams for charmonium hadroproduction via both CO and CS mechanisms are given on Fig. 2.4 together with their asymptotical behaviour.

It has to be stated that NRQCD factorization hypothesis has not been rigorously proven for quarkonium production yet (contrary to quarkonium annihilation). Hence, the universality assumption for LDMEs has not been strictly proven neither. Its possible violation can be related to effects, which are neglected under a definition of LDME. The complication of NRQCD is that at least two remaining scales mv and mv^2 should be taken into account in a single expansion. Therefore, NRQCD does not have unique power counting rules.

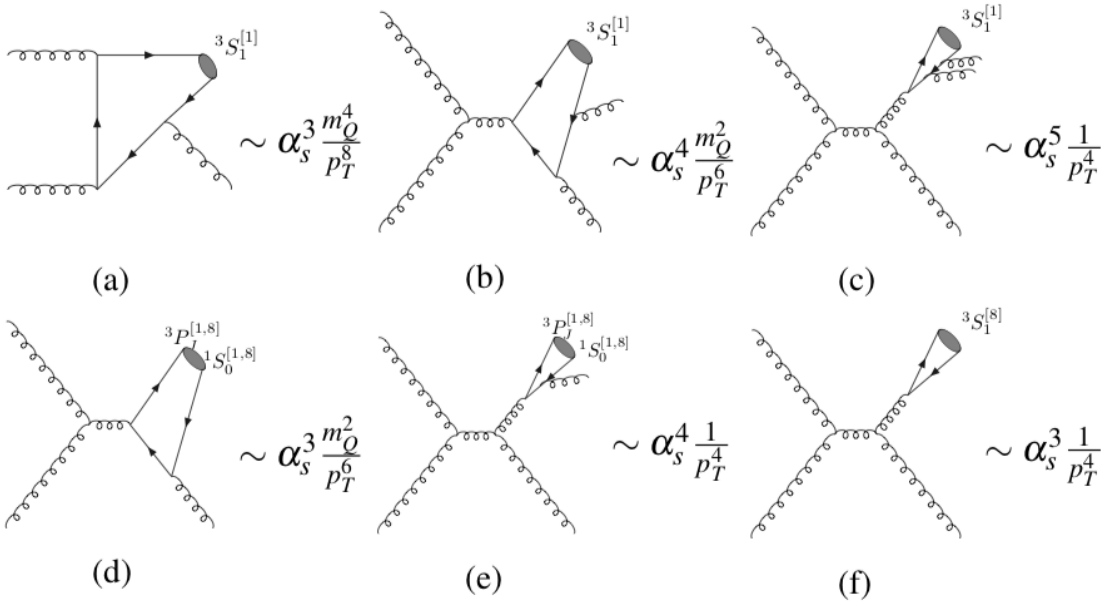

Figure 2.4: The CS (a-e) and CO (d-f) diagrams contributing to charmonium production at leading orders [60].

Since LDMEs cannot be calculated perturbatively and are usually taken as parameters extracted from the fits to data, the NRQCD has an infinite number of parameters. However, the importance of the various LDMEs of NRQCD can be assessed with power counting rules [61] using an expansion of v. They can be derived by considering the Fock state decomposition of a quarkonium state $|H\rangle$ in Coulomb gauge,

$$|H\rangle = \psi^H_{Q\bar{Q}}|Q\bar{Q}\rangle + \psi^H_{Q\bar{Q}g}|Q\bar{Q}g\rangle + ... \tag{2.14}$$

The dominant component $|Q\bar{Q}\rangle$ comprises a heavy quark pair in a colour-singlet state and with angular momentum quantum numbers $^{2S+1}L_J$ that are consistent with the quantum numbers of the physical quarkonium. The higher Fock states, such as $|Q\bar{Q}g\rangle$, contain dynamical gluons or light $q\overline{q}$ pairs. Thus heavy quark pair can be in either a CS or a CO state with spin $S = 0, 1$ and angular momentum $L = 0, 1, 2$, etc. All higher Fock states have probabilities suppressed by powers of v compared to that of $|Q\bar{Q}\rangle$. The $|Q\bar{Q}g\rangle$ states with the highest probability of $\mathcal{O}(v)$ are those that can be reached from the dominant $|Q\bar{Q}\rangle$ state through a chromoelectric interaction. Higher Fock states $|Q\bar{Q}g\rangle$ which can be reached from the dominant $|Q\bar{Q}\rangle$ state through the chromomagnetic interaction have probabilities of $\mathcal{O}(v^2)$. Both chromoelectric and chromomagnetic transitions change the colour state of the $Q\bar{Q}$ pair from CS to CO, and from CO to either CS or CO.

A difference between NRQCD and CEM in velocity suppression factors up to order of v^4 has been demonstated in Ref. [53] and is shown in Table 2.1.

	NRQCD											
	$^1S_0^1$	$^3S_1^1$	$^1S_0^8$	$^3S_1^8$	$^1P_1^1$	$^3P_0^1$	$^3P_1^1$	$^3P_2^1$	$^1P_1^8$	$^3P_0^8$	$^3P_1^8$	$^3P_2^8$
$\eta_{c,b}$	1		v^4	v^3					v^4			
J/ψ , Υ		1	v^3	v^4						v^4	v^4	v^4
	CEM											
H	1	1	1	1	v^2	v^2	v^2	v^2	v^2	v^2	v^2	v^2

Table 2.1: Velocity suppression factors for LDMEs in S-wave $Q\bar{Q}$ in the NRQCD and in the CEM. The $^{2S+1}L_J^1$ indicates the CS and the $^{2S+1}L_J^8$ indicated the CO states, respectively [53].

Experimental differential production cross-section can be fitted to the theory model to extract the information about relative contributions of CS and CO mechanisms. By taking into account dominant CS and CO contributions, NRQCD provides a basic description of available experimental information in a significant p_{T} range.

Moreover, the heavy quark spin symmetry (HQSS) provides relations between LDMEs of different charmonium states. Therefore, it also creates intrinsic links between the production observables of different quarkonium states. Namely, states with the same orbital angular momentum and radial quantum numbers are linked. Investigation of complementary charmonium states with different J quantum numbers is consequently a powerful tool to further constrain available theoretical descriptions.

One of the first candidates is the simultaneous study of the lowest charmonium states η_c and J/ψ since both are experimentally accessible and a link between the $\eta_c(1S)$ and J/ψ matrix elements can be established. Spin symmetry gives the following relation between the $\eta_c(1S)$ and the J/ψ color-singlet matrix elements:

$$O_1^{J/\psi}(^3S_1) \approx 3 \times O_1^{\eta_c}(^1S_0). \tag{2.15}$$

Relation between color-octet matrix elements are shown below.

$$O_8^{J/\psi}(^3S_1) \approx 3 \times O_8^{\eta_c}(^1S_0), \tag{2.16}$$

$$O_8^{J/\psi}(^1S_0) \approx O_8^{\eta_c}(^3S_1), \tag{2.17}$$

$$O_8^{J/\psi}(^3P_J) \approx \frac{2J+1}{3} \times O_8^{\eta_c}(^1P_1). \tag{2.18}$$

The links between LDMEs are not exact, and are satisfied up to $o(v^2)$ precision.

Note, that LDMEs of the CS mechanism are related to the quarkonium wave function and can be extracted either from the potential model (for example Ref. [21], from lattice calculations or from the measurements of branching fractions of quarkonium decays. The CS LDMEs are considered as well known with 10-20% precision.

In summary, development of NRQCD yielded a framework that reasonably describes hadroproduction of the measured quarkonium states in a wide range of transverse momentum (p_{T}) and rapidity. However, a comprehensive simultaneous description of the production and polarisation of the J/ψ state at Tevatron and LHC energies in an entire p_{T} range remains a challenge. Similarly, NRQCD describes the quarkonium production in other processes.

The NRQCD is often used with collinear factorization. The NLO calculations are necessary for NRQCD as will be seen below. The comparisons of NRQCD predictions to experimental measurements are shown in Section 2.4. Once main experimental results obtained in this thesis are presented, Chapter 7 will outline a systematic discussion of their description by NRQCD.

2.4 Theory vs experiment: state of art

In this section, I compare earlier measured observables of charmonium production with theoretical predictions. For the predictions, we will focus on the NRQCD as the most successful framework to date. A more complete review on quarkonium production can be found in Refs. [1, 62, 63]. The most up to date review including the last LHC results and the latest progress in quarkonium production phenomenology can be found in Ref. [64].

The charmonium production in hard processes provides several important observables, which allow selective comparison to theoretical predictions:

- total production cross-section,
- the shape of differential production cross-section in p_{T} and p^* and rapidity,
- polarisation of vector or tensor charmonium states.

The production cross-section is the first powerful observable to understand the production mechanism, since mesurements of the differential cross-section is naturally more complicated to perform. As will be shown below, often, the cross-section is measured to be much larger than the CSM prediction, which indicates a need for CO contribution or taking into account higher order calculations. Qualitatively, the CO mechanism includes possiblity of charmonium creation from a single gluon, which leads to transverse polarization of produced vector charmonium. The shape of p_{T}- or p^*-differential cross-sections provides an additional constraint on CS and different CO contributions, which have different asymptotical behaviour. The polarisation of charmonium is also a powerful observable to distinguish CS and CO contributions since the predictions of CS and CO lead to the opposite expected polarisations. Experimentally, the polarisation is conveniently accessed by measuring the angular distribution of charmonium decays, which is customarily parametrized using the polarization observables λ_θ, λ_ϕ, and $\lambda_{\theta\phi}$ as

$$W(\theta, \phi) \sim 1 + \lambda_\theta cos^2(\theta) + \lambda_\phi sin^2(\theta) cos(2\phi) + \lambda_{\theta\phi} sin(2\theta) cos(\phi). \tag{2.19}$$

Here, at the example of the $J/\psi \to \mu^+\mu^-$ probe, θ and ϕ are respectively the polar and azimuthal angles of muons momenta in the J/ψ rest frame. The values $\lambda_\theta = 0, +1, -1$ correspond to unpolarized, fully transversely polarized, and fully longitudinally polarized J/ψ mesons, respectively. This defines polarisation observables in helicity frame. Alternatively, the polarisation can be measured at different frames: Collins-Soppers [65], target frame [66], which is the case for polarisation analyses at HERA, as will be shown below.

Different production observables of different production processes can be used in simultaneous studies. Namely, the joint fits aim at using the same set of LDMEs to describe all observables in different production processes for linked charmonium states. Within the NRQCD description, the four independent LDMEs are used to describe the production of S-wave charmonium η_c and J/ψ. Only two LDMEs are used to describe P-wave charmonium (χ_{c0}, χ_{c1}, χ_{c2} and h_c). The relevant LDMEs together with HQSS relations are summarised in Table 2.2. Anologous relations apply for radially excited states ($\eta_c(2S)$ and $\psi(2S)$).

	HQSS relations	independent LDMEs
S-wave (η_c and J/ψ)	$\langle O_1^{\eta_c}(^1S_0)\rangle = \frac{1}{3}\langle O_1^{J/\psi}(^3S_1)\rangle$	$\langle O_1^{J/\psi}(^3S_1)\rangle$
	$\langle O_8^{\eta_c}(^1S_0)\rangle = \frac{1}{3}\langle O_8^{J/\psi}(^3S_1)\rangle$	$\langle O_8^{J/\psi}(^3S_1)\rangle$
	$\langle O_8^{\eta_c}(^3S_1)\rangle = \langle O_8^{J/\psi}(^1S_0)\rangle$	$\langle O_8^{J/\psi}(^1S_0)\rangle$
	$\langle O_8^{\eta_c}(^1P_1)\rangle = 3\langle O_8^{J/\psi}(^3P_0)\rangle$	$\langle O_8^{J/\psi}(^3P_0)\rangle$
P-wave (χ_{cJ} and h_c)	$\langle O_1^{\chi_{cJ}}(^3P_J)\rangle = (2J+1)\langle O_1^{\chi_{c0}}(^3P_0)\rangle$	$\langle O_1^{\chi_{c0}}(^3P_0)$
	$\langle O_8^{\chi_{cJ}}(^3S_1)\rangle = (2J+1)\langle O_8^{\chi_{c0}}(^3S_1)\rangle$	$\langle O_8^{\chi_{c0}}(^3S_1)\rangle$
	$\langle O_1^{h_c}(^1P_1\rangle = 3\langle O_1^{\chi_{c0}}(^3P_0)\rangle$	
	$\langle O_8^{h_c}(^1S_0)\rangle = 3\langle O_8^{\chi_{c0}}(^3S_1)\rangle$	

Table 2.2: The LDMEs relevant for joint description of charmonium states.

2.4.1 Production in b-hadron inclusive decays

The b-hadron decays provide a good opportunity to study charmonium since the branching fractions of inclusive b-hadron decays to charmonium are relatively large (order of 1% for S-wave charmonium) and large b-hadron samples have been accumulated. The decays of b hadrons are studied at e^+e^- (B- or Z- factories) or hadronic machines. Among the available approaches to exploit inclusive $b \to (c\bar{c})X$ transitions, the most precise studies can be done for decays integrating over all available b-hadrons since the resonstruction of exclusive decays has smaller efficiency. The inclusive branching fractions of b-hadron mixtures to charmonium have been measured at LEP [67–69]. The CLEO collaboration measured the branching fraction of the $B \to J/\psi X$ decay for the first time [70]. Later B-factories succeeded to measure the branching fractions of the light B-mesons (B^+, B^0 and sometimes B_s^0) mixture to charmonium using clean event samples. The resulting measurements by BaBar and CLEO2 have outstanding precision of about 1% [71, 72] and report, in addition, feed-down subtracted direct branching fraction.

However, in general, the available experimental results on inclusive charmonium production from b-hadron decays are limited and are shown in Table 2.3. According to the

	$B^-/\overline{B}^0$ mixture	$B^-/\overline{B}^0/\overline{B}_s^0$/$b$-baryon mixture
η_c (1S)	$< 0.9@90\%CL$	0.488 ± 0.097
J/ψ (1S)	1.094 ± 0.032	1.16 ± 0.10
χ_{c0} (1P)	–	–
χ_{c1} (1P)	0.355 ± 0.027	1.4 ± 0.4
h_c(1P)	–	–
χ_{c2} (1P)	0.100 ± 0.017	–
η_c (2S)	–	–
$\psi(2S)$	0.307 ± 0.021	0.286 ± 0.028

Table 2.3: Branching fractions (in %) of the inclusive b-hadron decays into charmonium states [73], excluding results reported in this work (Chapter 5.6). The mixture of light B^+ and $\overline{B}^0$ mesons is shown for the measurements of the e^+e^- experiments operating at centre-of-mass energy around $\Upsilon(4S)$resonance, while mixtures of B^-, $\overline{B}^0$, $\overline{B}_s^0$ and b-baryons are considered for measurements from experiments at LEP, Tevatron and LHC.

experimental conditions, these measurements involve different mixtures of b-hadron species. At the time, where the majority of b-physics results were coming from the experiments operating around $\Upsilon(4S)$ resonance energy, the b-samples comprised light B^- and $\overline{B}^0$ mesons. The results from the CLEO and Belle experiments operating around $\Upsilon(5S)$ resonance energy, can involve in addition $\overline{B}_s^0$ mesons. At LEP experiments, operating around Z resonance region, and the Tevatron and LHC, TeV scale machines, all b-hadron

species are produced, including weakly decaying B^-, $\overline{B}^0$, $\overline{B}^0_s$, B^-_c mesons and b-baryons.

The world average values for charmonium branching fractions in the inclusive decays of mixture of light B-mesons are dominated by CLEO [72,74], Belle [75,76] and BaBar [71] results. While the measurement of J/ψ, $\psi(2S)$ and χ_{c1} branching fractions are consistent across different experiments, yielding the average of better than 10% precision, the CLEO result [74] on the χ_{c2} branching fraction is significantly smaller with respect to those by Belle [75] and BaBar [71], and PDG gives a 3σ precise average value [77].

An upper limit on the inclusive η_c meson production in b-hadron (B^- and $\overline{B}^0$ mesons) decays was established by CLEO experiment, $\mathcal{B}(B^-, \overline{B}^0 \to \eta_c(1S)X) < 9 \times 10^{-3}$ at the 90% confidence level [78]. Recently, LHCb measurement reached a precision allowing first measurement of this decay (involving all b-species) of $\mathcal{B}(b \to \eta_c(1S)X) = (4.88 \pm 0.64 \pm 0.29 \pm 0.67) \times 10^{-3}$, where the third uncertainty is associated to the $b \to J/\psi X$ and $\eta_c(1S) \to p\overline{p}$ branching fractions [13]. The world average values for the branching fraction of the J/ψ and $\psi(2S)$ inclusive production in b-hadron decays, where all b-species are involved, are known at a 10% level, with the results dominated by the measurements at LEP [67–69]. The ratio of $\psi(2S)$ and J/ψ yields have been measured at the LHC, by the LHCb and CMS experiments, to a 5% level [79, 80]. The only PDG input for the χ_c family, is the χ_{c1} inclusive production in b-hadron decays, which is a 3.5 σ average between DELPHI and L3 measurements [67,68]. This reflects a difficulty to reconstruct low-energy photons in high multiplicity events, and in particular in a hadron machine environment. However, many measurements of charmonium production at LHC reviewed in the next section don't report the branching fractions and hence didn't enter the PDG list.

The branching fractions of $B \to \psi X$ measured at B-factories are significantly larger than the predictions of NRQCD at LO [81]. The full NLO analysis of the inclusive B-decays to charmonium has been performed for S-wave charmonium states [82,83]. Ref. [82] provides in addition a description of the P-wave charmonium states. These predictions will be used in Chapter 7. In both cases, authors extracted linear combinations of LDMEs. The obtained values of CO LDMEs are smaller than the ones obtained from the fit to Tevatron and LHC hadroproduction data.

The shape of the p^*-distribution of charmonium in b-decays is sensitive to the production mechanism including potential contributions from intermediate states. The p^*-distribution has been studied in Ref. [84].

The polarisation of J/ψ produced in B-decays has been studied in Refs. [85, 86] predicting the values of λ_θ parameter. The result is consistent with the measurement performed by CLEO collaboration [85]. Generally, NRQCD is able to describe observables

of S-wave charmonium produced in b-decays.

Ref. [87] provides a prediction of the χ_c states production in B-decays. Note that χ_{c0} and χ_{c2} states cannot be produced at LO in CSM [88, 89], while the CO LDME contribution is proportional to $2J + 1$. As will be shown later, the description of the χ_c states production in b-hadron decays is challenging, which was expected by the authors of Ref. [82]. Charmonium production in b decays has been extensively studied during the era of the first generation of B-factories in 90s. Each campaign of new precision measurements of charmonium production observables may potentially indicate a demand to revisit their theoretical description. Particularly the relative χ_c production rate in b-hadron decays is not accomodated by available predictions. A detailed comparison of the measurements of S- and P-wave charmonium production in b-decays, performed in this thesis, is given in Chapter 7.

2.4.2 Hadroproduction

J/ψ and $\psi(2S)$ prompt production and polarisation

Study of prompt charmonium production and especially measurement of J/ψ total and differential production cross-section is an essential part of the physics program at Tevatron and LHC. The first measurement of prompt J/ψ production has been performed by CDF experiment at $\sqrt{s}$ =1.8 TeV [12, 90]. The comparison with CS model shown that the measured cross-section is an order of magnitude larger than the prediction made at LO, which triggered the development of the CO concept followed by the introduction of the NRQCD approach. All these theory considerations equally apply for the $\psi(2S)$ state.

At the LHC, the differential cross-section measurements have been performed by the LHCb, ATLAS and CMS experiments at $\sqrt{s}$ =2.76, 7, 8 and 13 TeV yielding well-consistent results, complementary to each other [80, 91–104]. The results of prompt J/ψ production cross-section in bins of transverse momentum for LHC experiments [80, 95, 105] are shown on Fig. 2.5. Measurements from these experiments cover different regions in p_{T} and partially overlap, which allows a partial direct comparison.

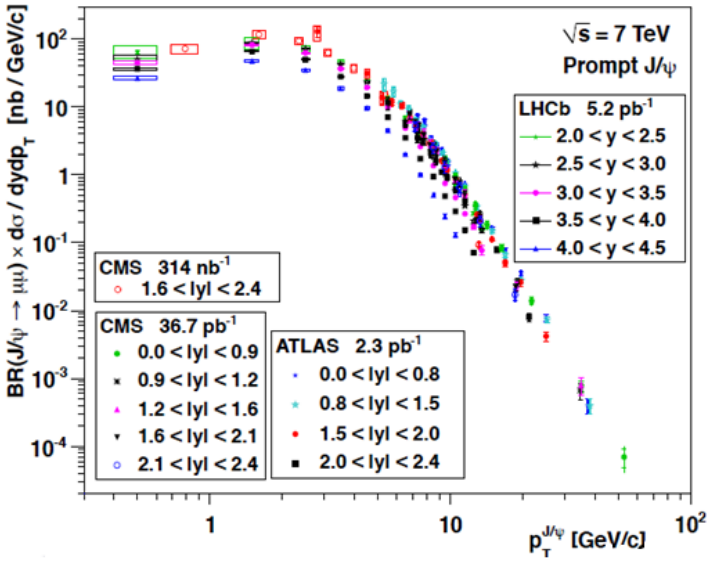

Figure 2.5: The p_{T}-differential cross-section of prompt J/ψ production at the LHC experiments [80, 95, 105] at $\sqrt{s}$=7 TeV.

The comparison of measured p_{T}-differential production cross-sections with different theoretical models is is shown taking as an example the LHCb measurement of J/ψ prompt production at $\sqrt{s}$ =7 TeV [92] on Fig. 2.6. The measurement is compared to direct NRQCD predictions at LO [106] and NLO [107]; CS model prediction at NLO

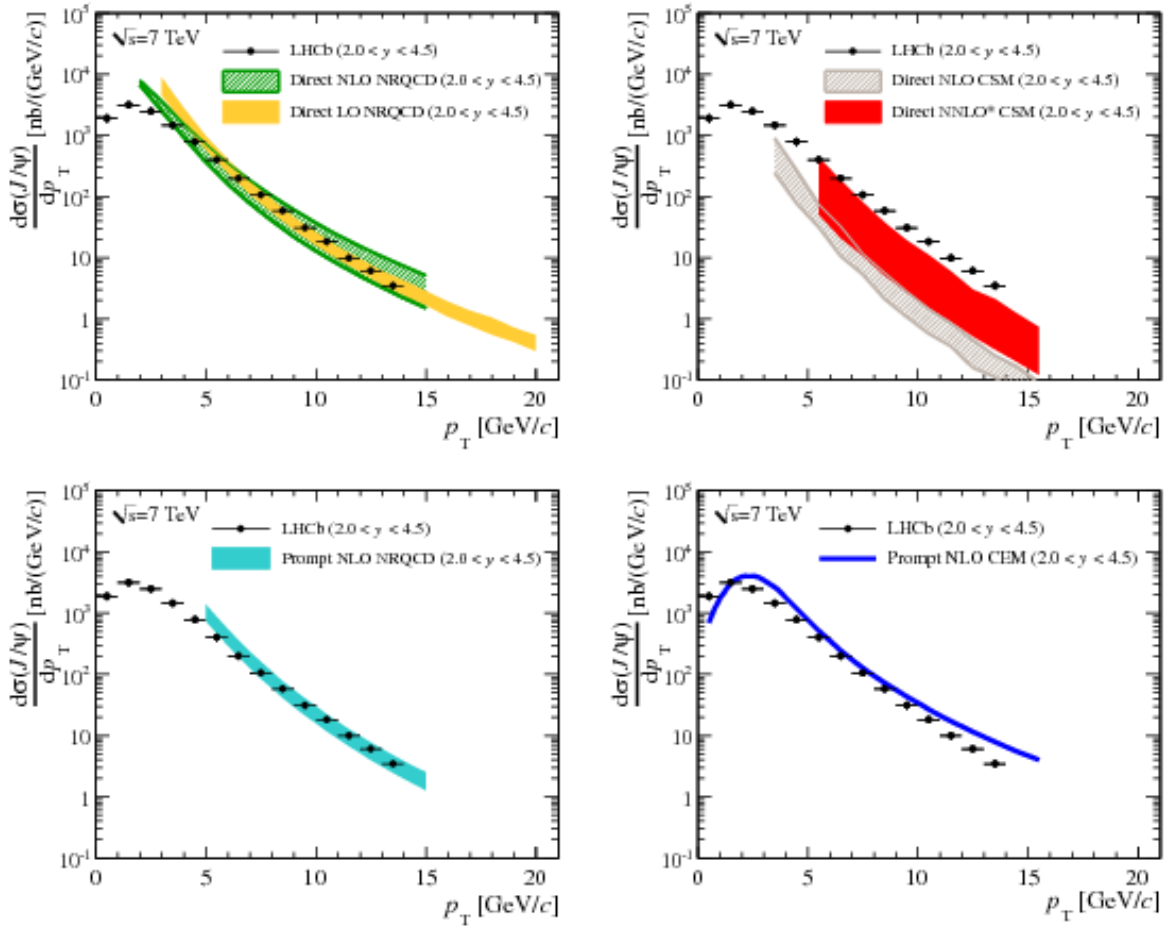

Figure 2.6: The p_{T}-differential cross-section of prompt J/ψ production at LHCb at $\sqrt{s}$ =7 TeV compared to theory: direct NLO and LO NRQCD (top left), NLO and NNLO CS model (top right), prompt NLO NRQCD (bottom left), CEM (bottom right) [92].

and NNLO* [108], where NNLO* denotes NLO calculations with taking into account additional NNLO contributions; NRQCD prediction at LO taking also into account feed-down contributions [109]; CEM prediction [110]. The comparison shows that CSM cannot describe J/ψ production at NLO and NNLO* underestimating production cross-section. The CEM model provides a description of the experimentally available p_{T}-range only at a qualitative level.

NRQCD provides the best description at NLO. One can note that NRQCD is applicable above $p_{\mathrm{T}} > 6$ GeV. Possible interpretations of a poor description at low-p_{T} region by NRQCD at NLO are that the production process is not hard enough to satisfy the factorisation assumption (collinear factorisation was used) or that the convergence of the v expansion is not perfect because charmonium is still too light. The latter statement

should be tested since NRQCD does not directly predict the p_{T}-region of its applicability.

Recently, a k_{T}-factorisation prediction, which used NRQCD, showed a good description of J/ψ and $\psi(2S)$ p_{T}-differential prompt production measurements at LHCb as discussed in Ref. [111, 112]. Due to a different factorization approach, a good description is achieved for entire experimentally measured p_{T}-range.

The first measurement of J/ψ prompt polarisation has been performed at Tevatron by CDF collaboration [104, 113] and then updated with a larger data sample. This represents so-called the CDF polarisation puzzle since the measurement performed using CDF Run I data is not compatible with the CDF Run II measurement. The reason of this incompatibility is, however, not well understood. As an illustation, a comparison of CDF measurements to the NRQCD prediction [114] is given on Fig. 2.7. The CDF Run II measurement is consistent to the results at LHC described below.

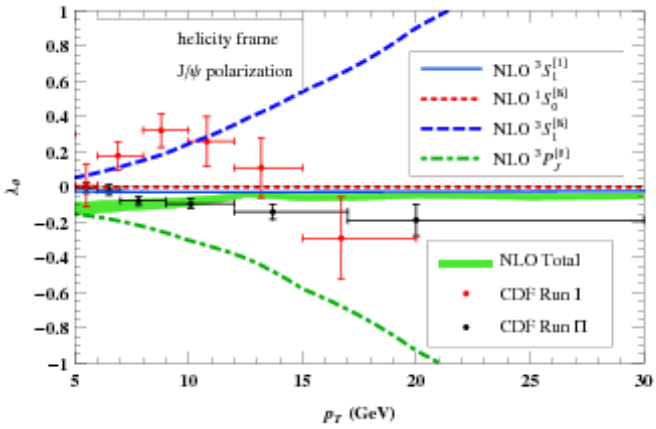

Figure 2.7: The λ_θ polarisation parameter measured by CDF and compared to NRQCD prediction [114].

Polarization of J/ψ was investigated by the LHCb [115], ALICE [103] and CMS [102] experiments. All results show small polarization and are consistent with each other (Fig. 2.8(a)). Comparison of polarisation measurement at LHCb [115] to theory predictions by the models developed to describe charmonia production [114, 116, 117] is shown on Fig. 2.8.

The NRQCD factorization framework predicts a strong polarization for CS mechanism. In addition, fits to the J/ψ production cross-section shown that the CO is the dominant process for J/ψ hadroproduction at large p_{T}, having less sharp p_{T} spectrum than the CS contribution. In the CO, a $Q\bar{Q}$ pair can be produced from a single gluon and hence a transverse polarisation of prompt J/ψ mesons is expected at large p_{T}.

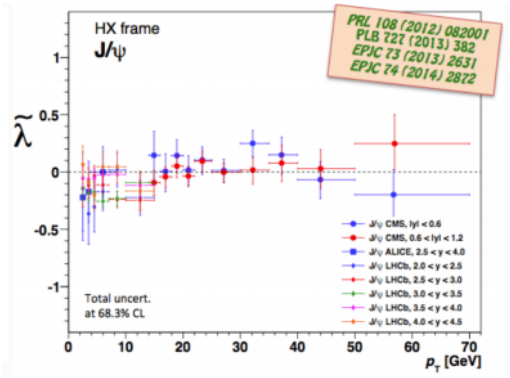

(a) J/ψ polarisation measurements at LHC [102, 103, 115].

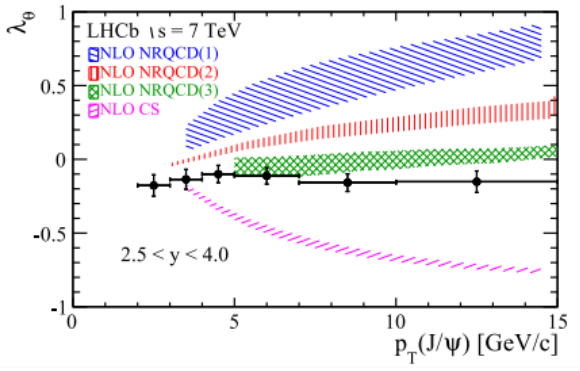

(b) LHCb measurement compare to theory [115].

Figure 2.8: J/ψ polarisation (λ_θ) measurements at LHC as a function of p_{T}.

The tension between the NRQCD and the polarisation measurements can be reduced (as shown e.g. in Ref. [117]) by taking into account that a large fraction (about 30%) of prompt J/ψ mesons is coming from the feed-down of χ_c and $\psi(2S)$ states. Its polarization is substantially different from the polarisation of the directly produced J/ψ mesons.

The puzzle of the J/ψ polarisation and the impact of the feed-down contributions receive more information from the studies of $\psi(2S)$ polarization since no feed-down sources are expected in this case. At the same time, the production rate of $\psi(2S)$ is much smaller than the one of J/ψ, and hence the measurement precision is reduced. The polarisation of the $\psi(2S)$ has been measured by CDF experiment [104] and the comparisons with theoretical predictions are not conclusive due to large experimantal uncertainties. After that, the $\psi(2S)$ polarisation has been measured at LHC by CMS [102] and LHCb [118]. In Ref. [119] authors report a good description of $\psi(2S)$ polarization measured at CDF, CMS and LHC. The comparison of measurements with theoretical description is given on Fig. 2.9. Despite reasonable description, a more precise measurement of $\psi(2S)$ polarization (especially at large p_{T}) is needed due large experimental uncertainties of existing results.

A polarization of J/ψ was known to be problematic for description by k_{T}-factorizarion approach due to large predicted polarization contrary to measurements. Refs. [111, 112] provide a reasonable description of mentioned J/ψ and $\psi(2S)$ polarization measurements by using k_{T}-factorization approarch together with NRQCD. A good description of J/ψ polarization is achieved due to the cancellation of contributions from ${}^3P_1^{[8]}$ and ${}^3P_2^{[8]}$ CO terms in the process ${}^3S_1^{[8]} \to {}^3P_J^{[8]} \to J/\psi$.

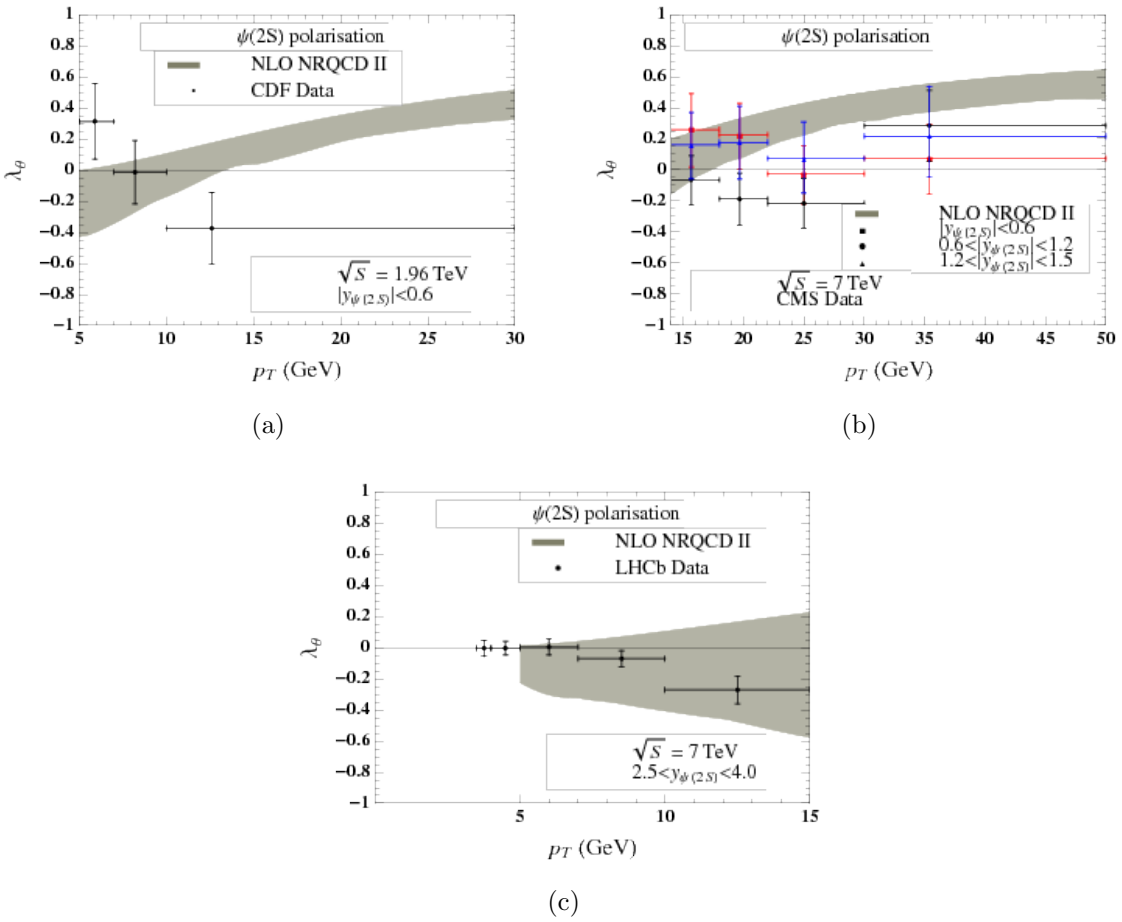

Figure 2.9: Theory description [119] of measured $\psi(2S)$ polarization (λ_θ) at CDF (a), CMS (b) and LHCb (c).

η_c and $\eta_c(2S)$ prompt production

The η_c state is much less studied due to complications of its reconstruction at LHC. At charm factories a sample of η_c mesons is reduced due to small branching fraction of $\psi(2S)$ and J/ψ decays to η_c. A large data sample and selective trigger is needed in order to observe a signal from prompt η_c mesons. The only measurement of prompt and b-decays production cross-section has been performed so far.

The LHCb collaboration measured for the first time a cross-section of the η_c meson prompt production in proton-proton collisions at $\sqrt{s} = 7$ and 8 TeV [13]. Due to challenging background conditions and limited trigger bandwidth, some bins of the measurement of p_{T}-differential production cross-section have uncertainties larger than the uncertainties in NRQCD predictions. The experimental uncertainties are dominated by statistical ones. A more precise measurement of the η_c production with large data set at higher

$\sqrt{s}$ with increased production cross-section is required to validate the observed effect and study its energy dependence. A larger data sample allows to improve a technique of the measurement by explicit modelling its decay-time distribution. For J/ψ production studies [94], a measurement of the ratio of production cross-sections at different $\sqrt{s}$ has largely reduced theory and experimental uncertainties. Contrary to that, a similar ratio for η_c production cross-section would be less precise than a single measurement, since experimental uncertanties are strongly dominated by statistical ones. In principle, a large enough data sample would allow to extend presently studied p_{T}-range.

The measurement has been compared to four NRQCD predictions [114, 116, 117, 120]. The predictions are obtained by projecting the J/ψ production cross-section using HQSS relations. More details are discussed in Chapter 7. The comparison shows that the CS contribution already saturates the observed cross-section and CO contribution projected from the J/ψ production studies would largely overshoot the measured p_{T}-differential production cross-section.

The tension between the theory and experimental result is clear for all available predictions. The LHCb measurement demonstrated a lack of comprehensive theoretical models, which are able to simultaneously describe a production cross-section of the J/ψ and η_c states and a polarisation of the J/ψ meson. The links between the LDMEs corresponding

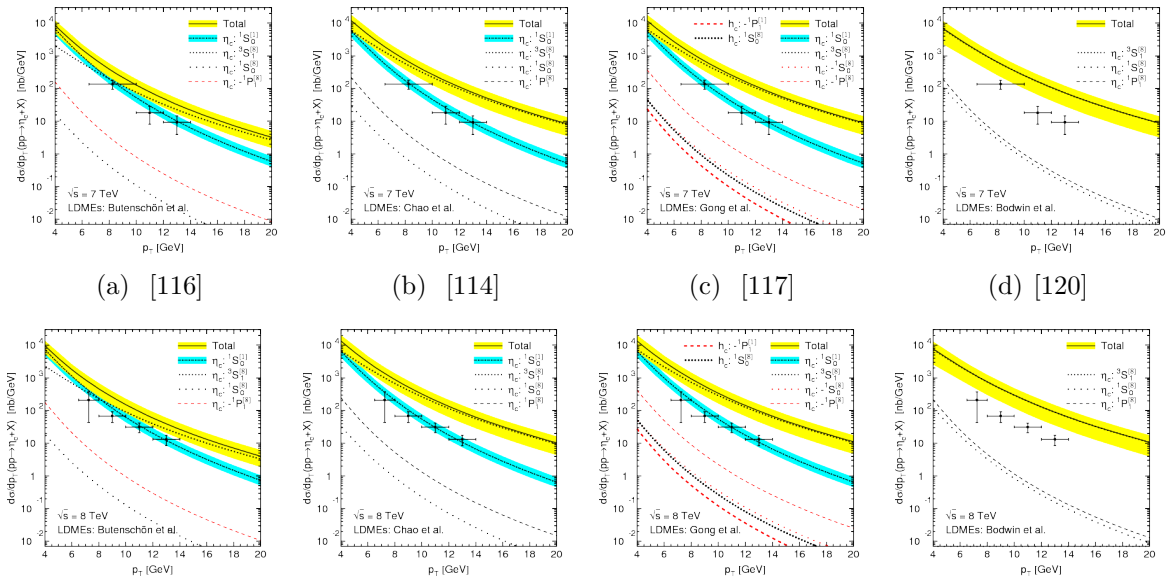

(a) [116] (b) [114] (c) [117] (d) [120]

(e) [116] (f) [114] (g) [117] (h) [120]

Figure 2.10: Comparison of predictions from Refs. [114, 116, 117, 120] to the η_c prompt production measurements at $\sqrt{s}$ =7 (a-d) and 8 (e-h) TeV by LHCb. The yellow (blue) band represents the CO (CS)contribution. Figure is taken from Ref. [121].

to the J/ψ and η_c production within a heavy-quark spin symmetry assumption as discussed in Section 2.3 allow to make a prediction of η_c prompt production using LDMEs determined from the fit to J/ψ production measurement.

The LHCb measurement triggered new efforts to describe S-wave charmonium production. A revisiting of the theoretical framework followed [112, 122–127]. Recent progress by theorists [128] yielded a good description of η_c production in a limited p_{T}-range by taking into account both CS and CO contributions (Fig. 2.11). Currently, this is the only available successful description of the η_c production by NRQCD; and values od LDMEs were constrained by the η_c prompt production measurement. A good description of the data points is achieved by two CO contributions cancelling each other, which creates a hierarchy problem. This calls for further development of theory models describing S-wave charmonium production. Note, that a blue band on Fig. 2.11 doesn't represent a theory uncertainty but represents an uncertainty of 100% due to reasons described below. Authors didn't use the η_c prompt production measurement in the simulataneous fit. Instead of that, they neglected the dominant CS contribution in the η_c production to obtain a very conservative constraint (upper limit) on relevant CO LDMEs. The obtained CO LDMEs were projected to the prompt J/ψ polarisation measurements by LHCb [115] and ALICE [103]. Figure 2.12 compares the NRQCD prediction with and without a constraint obtained using η_c prompt production measurement.

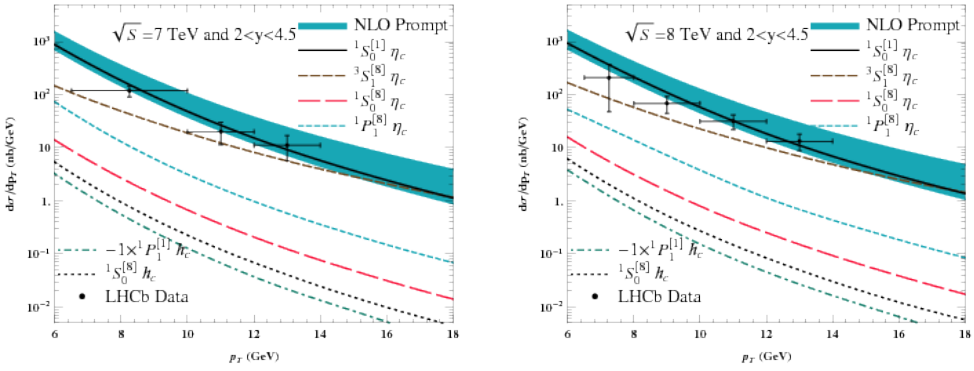

(a) (b)

Figure 2.11: The η_c production measurement compared to the prediction from Ref. [128].

Recently, authors of Ref. [129] provided a description of the η_c prompt production with k_{T}-factorization incorporating NRQCD. This work provides a simultaneous fit of J/ψ [130] and η_c [131] prompt production measurements at LHC contrary to the NRQCD prediction made within collinear factorisation addressed above. In addition, no kinematical

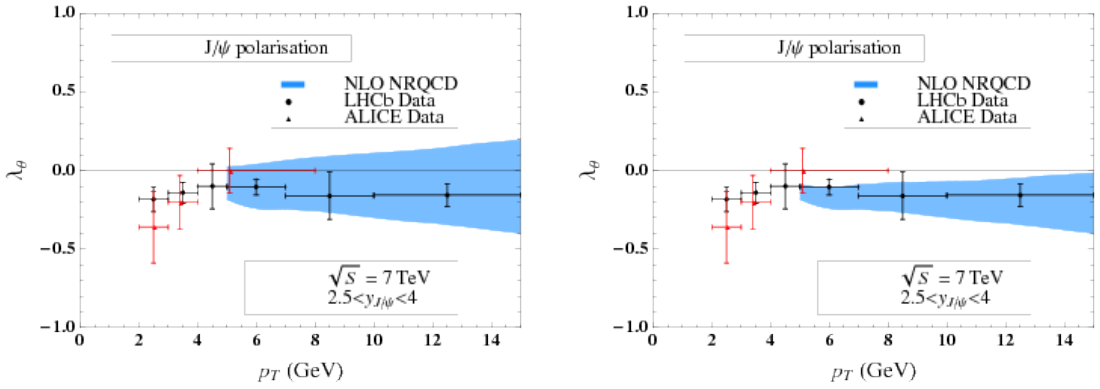

(a) (b)

Figure 2.12: The NRQCD prediction of J/ψ polarisation compared to the LHCb [115] and ALICE [103] measurements without (a) and with (b) the contraint from the η_c production measurement as discussed in the text. Figures are taken from Refs. [119, 128].

requirements on the p_{T} or rapidity range were used. The fit takes into account feed-down contributions from χ_c and $\psi(2S)$ to J/ψ and from h_c to η_c. The results of simultaneous fit on Fig. 2.13 for J/ψ prompt production are compared to CMS measurement [130] and for η_c prompt production compared to LHCb measurement. The contributions from different CS and CO states and feed-down sources are shown on Fig. 2.14 to J/ψ prompt production and for η_c prompt production. This result showed a good simultaneous description of both J/ψ and η_c prompt production measurements at LHC in a considered p_{T} range. Note, that on the plots a contrinution from ${}^1S_0^{[8]}$ to the η_c production is not present due to cancellations in CO processes similar to those mentioned for J/ψ polarisation description within k_{T}-factorization. Within this fit a theoretical description is strongly constrained. This is reflected by small theoretical uncertaintites displayed, which include uncertaintites due to scale and LDME values only.

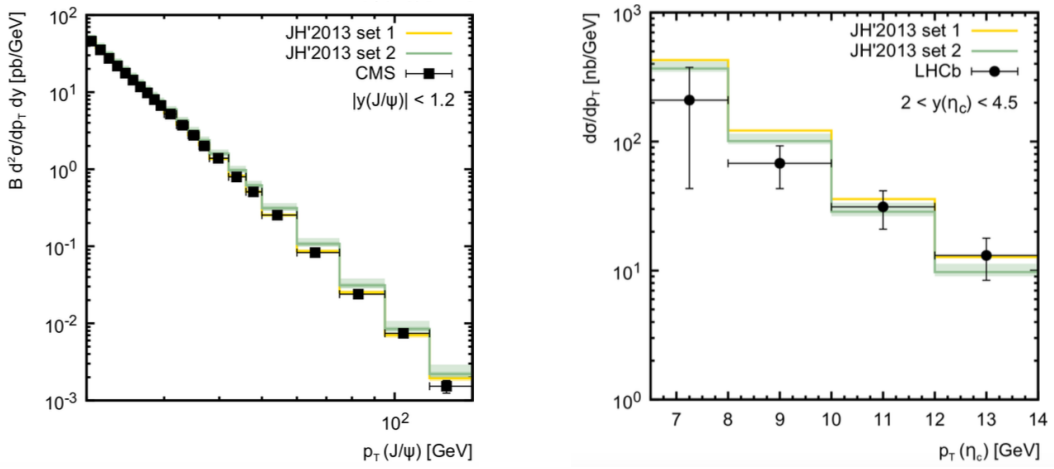

(a) (b)

Figure 2.13: A simultaneous fit of the J/ψ (a) and the η_c (b) prompt production measured at CMS [130] and LHCb [131] compared to the k_{T}-factorization prediction incorporating NRQCD [129].

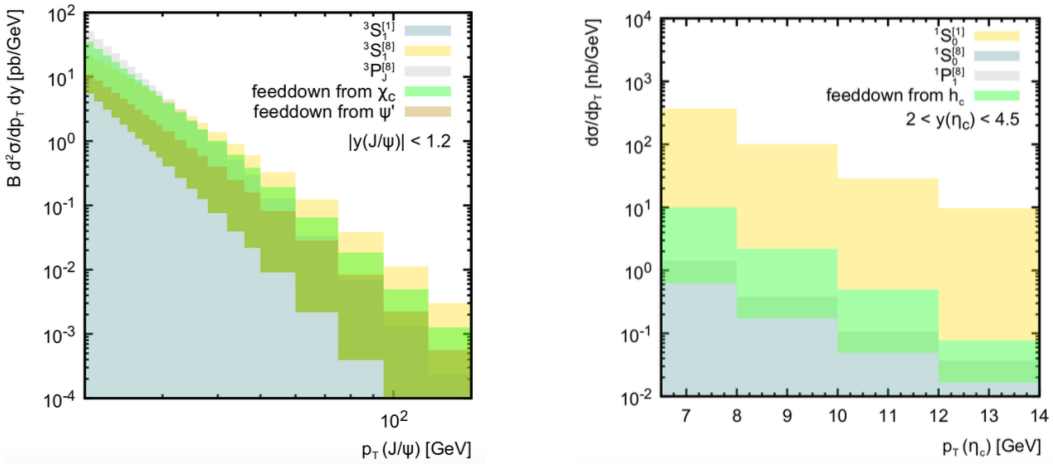

(a) (b)

Figure 2.14: Contributions to J/ψ (a) and η_c (b) prompt production within k_{T}-factorization prediction incorporating NRQCD [129].

No difference in the relation between $2S$ states and $1S$ states production is expected. Since similar links between LDMEs apply also between $\psi(2S)$ and $\eta_c(2S)$, Lansberg and Shao suggested to measure prompt $\eta_c(2S)$ at LHCb using $\eta_c(2S) \to p\overline{p}$ decay. The measurement of the $\eta_c(2S)$ prompt production would be a further stringent test of the NRQCD model developed for the η_c and J/ψ production. The advantage of $\eta_c(2S)$ and $\psi(2S)$ states is that both are expected to be feed-down free. The reconstruction of the $\eta_c(2S)$ state is however more complicated than that of η_c. Not many $\eta_c(2S)$ decays have been observed, and only a few measurements of branching fractions are available. The discussion on applicable decay channels to reconstruct $\eta_c(2S)$ at $\sqrt{s}$ =13 TeV at LHCb is given in Chapter 3.

A predictions for the $\eta_c(2S)$ production can be done in a similar way as for η_c and is available in Ref. [132] together with projections to the LHCb fiducial region. The NRQCD prediction for the p_{T}-differential prompt production cross-section at $\sqrt{s}$ =13 TeV of $\eta_c(2S)$ at LO and NLO is shown on Fig. 2.15.

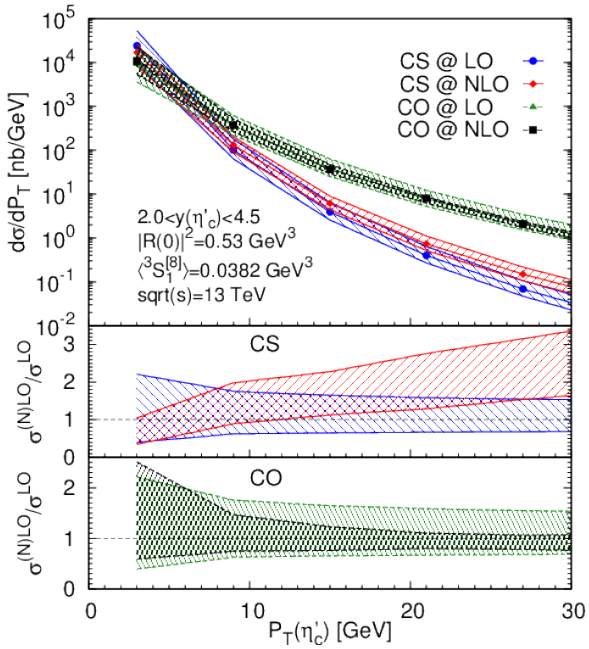

Figure 2.15: The NRQCD prediction of the p_{T}-differential $\eta_c(2S)$ production cross-section for the LHCb fiducial region at $\sqrt{s}$ =13 TeV [132].

The predictions for the η_c production using LDMEs from three theoretical groups [117, 119, 133] are shown on Fig. 2.16. The prediction from Ref. [117] has the largest uncertainty due to allowed negative values of LDMEs contrary to two other predictions. The prediction from Ref. [133] has the smallest uncertainty. A measurement of the $\eta_c(2S)$ prompt production is an important test of mentioned predictions.

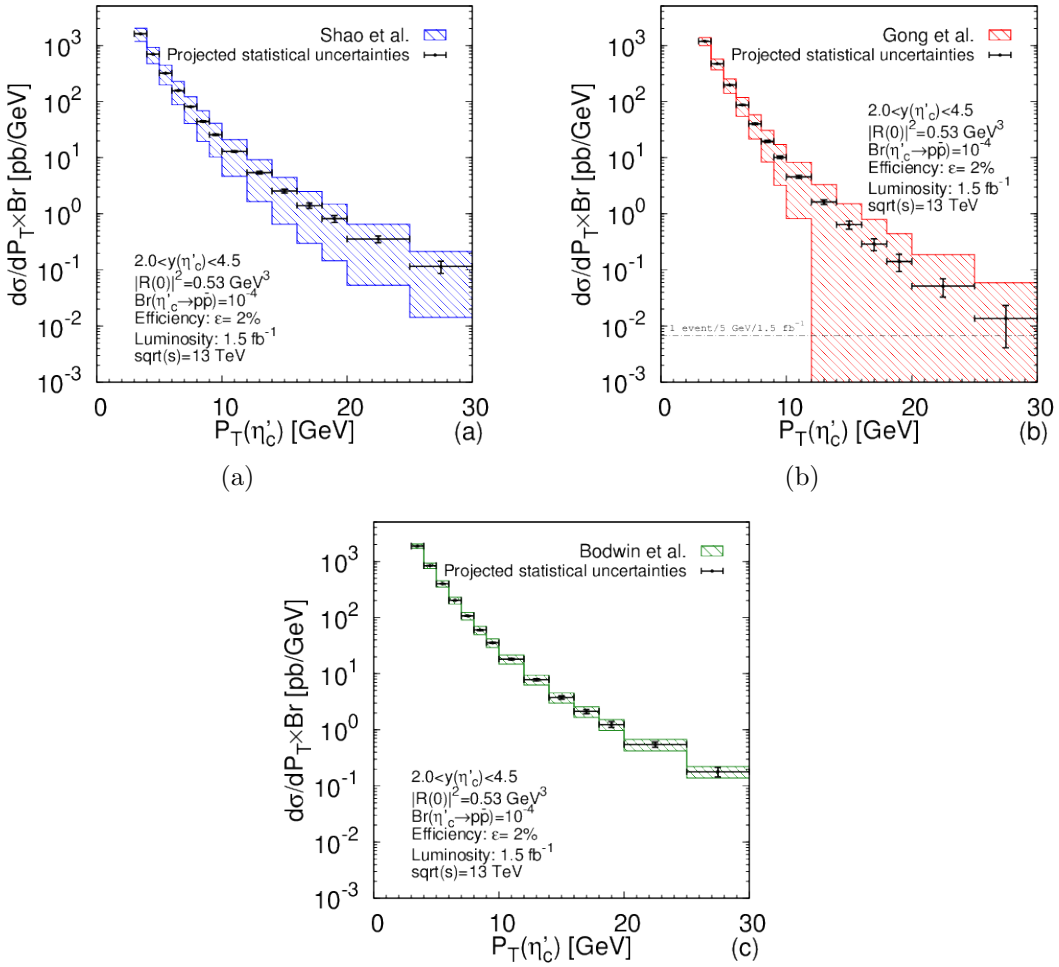

Figure 2.16: The NRQCD predictions of the p_{T}-differential $\eta_c(2S)$ production cross-section for the LHCb fiducial region at $\sqrt{s}$ =13 TeV from Refs. [119] (a) [117] (b) [133] (c). Figure is taken from Ref [132].

χ_c prompt production

The prompt production of χ_c mesons is conventionally studied using $\chi_{c1,2} \to J/\psi \to \mu^+\mu^-\gamma$ decays. In addition, a reconstruction of J/ψ decay to pair of muons, requires a reconstruction of a photon with an energy of a few handred MeV. The χ_{c1} (χ_{c2}) states have relatively large branching fractions of radiative transition to J/ψ of about 30%(20%). The χ_{c0} is more complicated to reconstruct due to a smaller branching fraction (1.4%) and lower photon energy. The photon energy is reconstructed using calorimeter or tracking detectors for photon conversions to a e^+e^- pair takes place. Calorimeter resolution for low-energy photons is often compromised, as in the case of LHCb calorimeter optimized to resolve photons from radiative b-decays. Since masses χ_{c1} and χ_{c2} states are separated by 40 MeV, limited detector resolution can lead to overlapping peaks and hence χ_{c1} and χ_{c2} signals will be complicated to separate. Below, the available results on the χ_{c1} and χ_{c2} prompt production are discussed, while there is no measurement of χ_{c0} $p_{\rm T}$-differential production cross-section.

The prompt production of χ_{c1} and χ_{c2} states has been measured by CDF [90] at $\sqrt{s}$ =1.8 TeV; ATLAS [134], CMS [135] and LHCb [136] at $\sqrt{s}$ =7 TeV. In the same paper, the LHCb collaboration also reported a value of integral χ_{c0} relative production with a significane of about 4 σ.

The NRQCD prediction at NLO [137] well describes data point measured by ATLAS. It can also be compared to $k_{\rm T}$-factorisation prediction [138], showing that $k_{\rm T}$-factorisation overshoot data points. Later calculations have been updated with incorporating NRQCD [139], which showed a good description of measurements. Another powerful observable is the relative χ_{c2}-to-χ_{c1} production ratio, which has to be also addressed. The comparison of the LHCb measurement of the ratio to the NLO NRQCD prediction [137] is shown on Fig. 2.17. The NRQCD at NLO describes well the ratio for $p_{\rm T} > 6$ GeV only.

Note, that all measurements of χ_c prompt production is done under the assumption that χ_c states are produced unpolarized. In addition, the NRQCD fit two production observables with two LDMEs. Additional observables would over-constrain the P-wave charmonium production description. Unfortunately, the χ_{c0} and h_c hadroproduction and χ_{cJ} and h_c prompt polarisation have not been measured so far. A measurement of χ_c production down to small $p_{\rm T}$ can be done by exploiting recently discovered $J/\psi \to \chi_c\mu^+\mu^-$ decays to study the low-$p_{\rm T}$ region, where the NRQCD doesn't provide reliable description of data points.

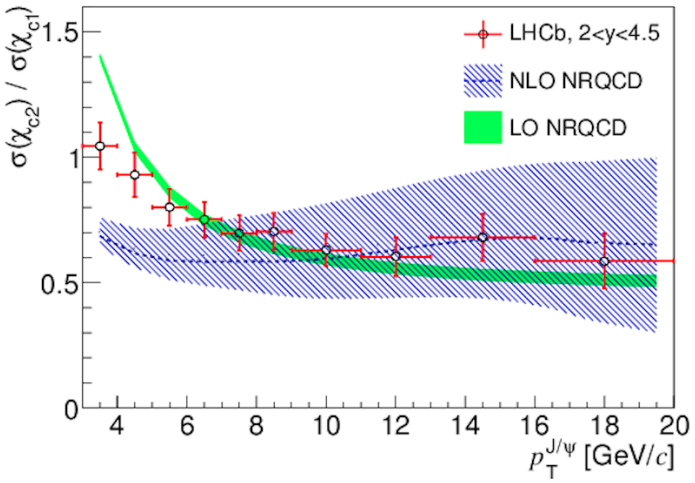

Figure 2.17: The χ_{c2}-to-χ_{c1} prompt production ratio measured at LHCb [136] compared to the NRQCD prediction at NLO [137] and LO [140]. Figure is taken from Ref. [136].

2.4.3 Photoproduction in *ep* collisions

The photoproduction of charmonium can also be studied using *ep* collisions. The production process at *ep* collisions is characterised by a dynamical variable z (elasticity) that is defined as a fraction of the virtual photon momentum carried by the final state charmonium. Depending on the value of z, the production can happen at different regimes. The direct photoproduction regime takes place for small photon virtuality q^2 and $z \gtrsim 0.3$. Another important observable is an invariant mass of γp system, $W_{\gamma p}$ or W, which reflects the energy of incoming photon. Hence the differential production cross-section in W is also measured. In this case, the electron scattering angle is small, and the photon can be treated as quasi-real. Naively, one can expect that the description of the photoproduction is easier than the hadroproduction. Indeed, the diagrams representing photo- and hadro-production are similar. One needs to replace a gluon in the initial state by a photon in hadroproduction diagram to obtain a diagram for photoproduction. For example, diagrams relevant for J/ψ within CS mechanism are shown for hadroproduction on Fig. 2.18 and for photoproduction on Fig. 2.19.

However, in addition to direct photoproduction, the photon can interact with c quark via hadronic component (e.g. resolved process at $z \lesssim 0.3$). The resolved process is more complicated to describe theoretically. In addition to that, the exclusive and diffractive production cross-section is comparable for the photoproduction. Hence, all the processes mentioned above should be considered to achieve a comprehensive theory description.

From the experimental side, due to small values of total cross-section, large collected

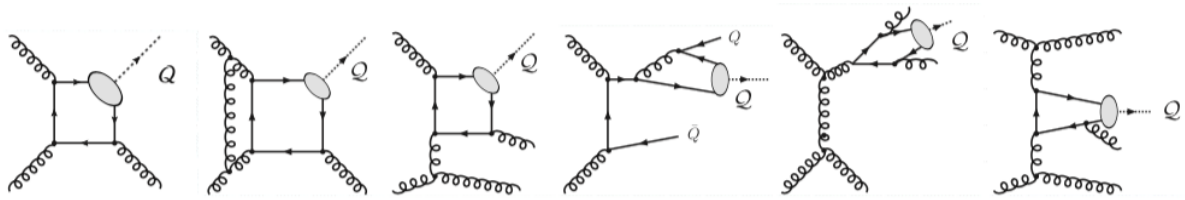

Figure 2.18: Diagrams representing J/ψ hadroproduction within CS mechanism. Figure is taken from Ref. [64].

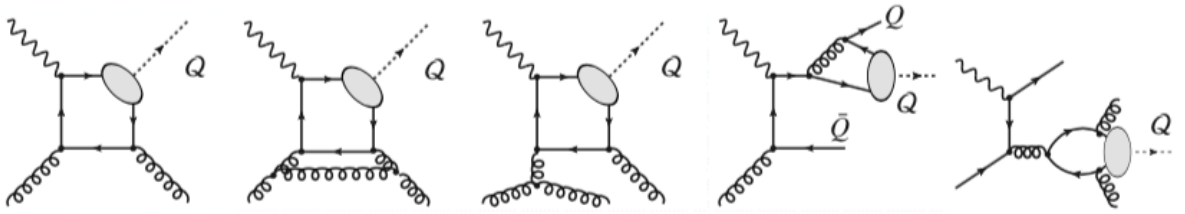

Figure 2.19: Diagrams representing J/ψ photoproduction within CS mechanism. Figure is taken from Ref. [64].

luminosities are needed to study charmonium photoproduction. The J/ψ and $\psi(2S)$ inelastic production cross-sections in ep collisions have been measured at HERA by ZEUS and H1 collaborations [141–144]. Later, z and p_{T}-differential cross-sections have been reported [145]

The first NLO calculation of the charmonium photoproduction has been performed in Refs. [146,147] and shows a reasonable description of the measured cross-sections. Later, it has been shown that the values of factorisation and renormalisation scales used in Ref. [146] are probably too low and after correcting the scale, the NLO prediction underestimates the H1 and ZEUS [148–153] results. The J/ψ photoproduction at HERA has also been studied using k_{T}-factorisation approach at LO [154–156] with CSM. The CSM can explain measured p_{T} and z distributions within large uncertainties arising from parton PDFs. The first complete NLO analysis with the CO contribution considered is reported in Ref. [148]. The obtained predictions are compatible with the H1 measurement of both p_{T}- and $z-$differential cross-section. This result has been used in the simultaneous fit of the J/ψ hadroproduction and photoproduction [116]. The NLO NRQCD fit is performed to prompt production cross-section measurements at RHIC [157], Tevatron [12,158] and LHC [105,159–161], and photoproduction at HERA [141–143]. The χ^2/ndf of the fit is $\chi^2/\mathrm{ndf} = 857/194 = 4.42$. For most of cases, theoretical uncertaintites are larger that experimental ones. The fit resonably describes hadroproduction measurements with a slight tension with CMS measurement at large p_{T}. The worst description takes place for z-differential photoproduction cross-section measurements due to complications mentioned

above. The obtained values of LDMEs will be compared to the result of simultaneous fit to hadroproduction and production in b-hadron decays in Chapter 7. The results in Ref. [116] are also compared to J/ψ production measurements in $\gamma\gamma$ collisions addressed in the next section.

The polarisation of the J/ψ has also been measured at HERA. The H1 collaboration measured both λ and ν parameters in helicity and Collins-Soppers frames and required $0.3 < z < 0.9$ to suppress diffractive contributions [142]. The ZEUS collaboration performed a measurement in target spin-quantisation frame. The measurements show small longitudinal polarisation decreasing with p_{T}. The description of the polarisation is reasonable for both CSM [142, 144, 149, 150] and with considering entire NRQCD at NLO [162]. Taking into account uncertainties, it is not clear whether the CO contribution is needed to describe the observed polarisation.

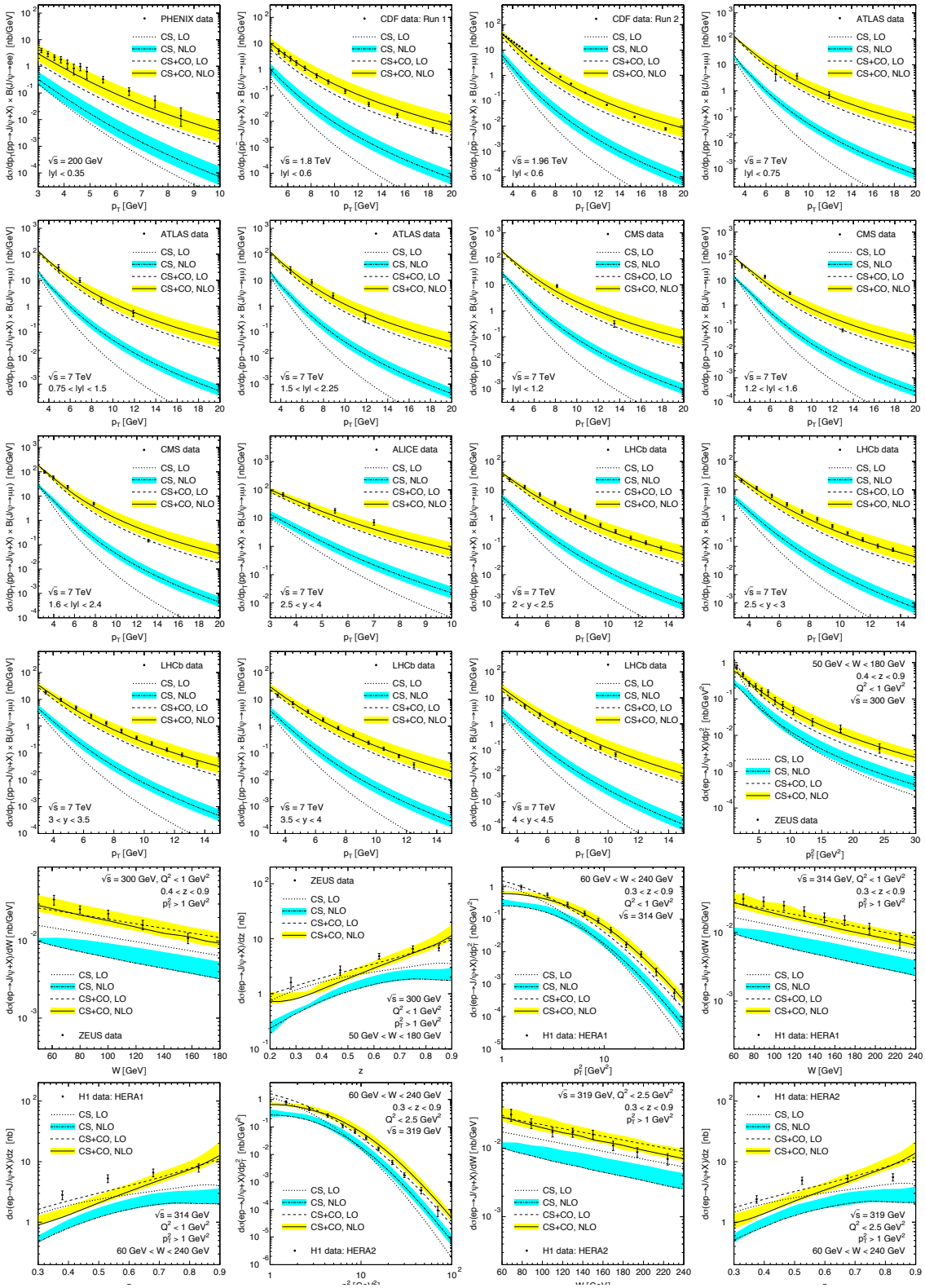

Figure 2.20: The NRQCD NLO fit to hadroproduction at RHIC, Tevatron and LHC and protoproduction measurements at HERA [116].

2.4.4 Inclusive production in $\gamma\gamma$ collisions

Another important observable of charmonium production comes from $\gamma\gamma$ collisions. Similarly to the photoproduction case, in addition to direct production, the resolved photons can contribute to the production mechanism. Moreover, one can distinguish the processes with a single resolved photon ($i\gamma \to (c\bar{c})i$) and with two resolved photons (double-resolved) $ij \to (c\bar{c})k$, where i, j and k denote either the light quark or a gluon. A single resolved process is similar to a photoproduction, while the double-resolved process is similar to the hadroproduction.

The integral inclusive production of J/ψ in $\gamma\gamma$ collisions has been measured at LEP by DELPHI experiment [163]. The limited data sample size did not allow to perform precise measurement of differential production cross-section. The measurement has been compared to the CSM predictions at LO [164–168] showing that theory underestimates the measured cross-section. The first complete NLO prediction was found to be similar to the LO one [116]. In Ref. [169], the contribution from $\gamma\gamma \to J/\psi\, c\bar{c}X$ has been addressed at NLO level, and it has been shown that this process might dominate the CS production.

All above suggests that the CO contribution can be dominant, but the existing prediction [116] is several times smaller than the experimental result. This, however, is not conclusive given large uncertainties from both theory and experimental sides. This calls for a new precise measurement of the J/ψ production in $\gamma\gamma$ collisions.

2.4.5 Inclusive production in e^+e^- collisions

The prompt inclusive production cross-section of the J/ψ meson in e^+e^- collisions, $e^+e^- \to J/\psi X$, has been measured most precisely by BaBar [170] and Belle [171] experiments. However, results from other e^+e^- experiments are also available. To describe this process, theory predictions should also take into accoung contributions from specific $e^+e^- \to J/\psi\, c\bar{c}$, $e^+e^- \to J/\psi\, gg$ and $e^+e^- \to J/\psi\, q\bar{q}{+}gg$ processes, where q denotes u, d or s quark [172–177]. The LO calculations using CSM predict the cross-section, which is 3-5 times smaller than the measured values. In addition, the measurement of the $e^+e^- \to J/\psi\, c\bar{c}$ cross-section by Belle [178] is 5 times larger than the LO NRQCD prediction with both CS and CO [173–177, 179] mechanisms considered.

Later, the Belle collaboration measured the cross-section of $e^+e^- \to J/\psi X$, $e^+e^- \to J/\psi\, c\bar{c}$ and $e^+e^- \to J/\psi X_{non-c\bar{c}}$ [180]. The value of the $e^+e^- \to J/\psi X$ cross-section was found to be almost twice smaller than the first measurement. Nevertheless, the updated measurement of the $e^+e^- \to J/\psi X$ cross-section is still larger than theory predictions.

Authors of Ref. [181] shown that NLO calculations lead to significant enhancement

by about factor 2 in the production cross-section compared to the LO result when using the same set of input parameters. Further investigations have been done by taking into account the QED contributions from the $e^+e^- \to 2\gamma^* \to J/\psi\, c\bar{c}X$ and $e^+e^- \to \chi_c c\bar{c}X$ processes [181] and the feed-down contribution from the $\psi(2S)$ state, which produces a contribution of about 35% to the $e^+e^- \to J/\psi\, c\bar{c}X$ cross-section. After taking into account all contributions mentioned above, the discrepancy between theory and measurements is largely reduced. Similarly, corrections to the $e^+e^- \to J/\psi\, gg$ process at NLO have been calculated [182, 183]. Finally the result became consistent with the latest Belle measurement of the $e^+e^- \to J/\psi\, X_{non-c\bar{c}}$ cross-section as shown below.

$$\begin{aligned} \sigma^{Belle}(e^+e^- \to J/\psi\, X_{non-c\bar{c}}) &= 0.43 \pm 0.09 \pm 0.09\,\text{pb}, \\ \sigma^{NLO}(e^+e^- \to J/\psi\, gg) &= 0.29 - 0.41\,\text{pb}. \end{aligned} \tag{2.20}$$

In addition, the measured p^* distributions of the $e^+e^- \to J/\psi\, c\bar{c}$ and $e^+e^- \to J/\psi\, X_{non-c\bar{c}}$ processes [180] are reasonably compatible with the NLO prediction of $e^+e^- \to J/\psi\, gg$ [182, 183].

Later, it has been shown that the relativistic corrections produce an enhancement in the $\sigma(e^+e^- \to J/\psi\, gg)$ cross-section [184, 185]. If one takes into account these corrections together with the NLO computation, the CS contribution will saturate the measured $e^+e^- \to J/\psi\, X_{non-c\bar{c}}$ cross-section. It has been understood that a poor description of the measurements originated from the values of LDMEs, which were extracted from the fit to J/ψ hadroproduction at Tevatron [186] at LO.

To conclude, the studies of J/ψ production in e^+e^- collisions also challenge NRQCD. It took more than ten years to achieve a reasonable description of the production observables. The important consequence of the studies is that the LO calculations cannot describe J/ψ production observables and at least the NLO level is needed.

In the next chapter, I will discuss the charmonium decays to hadronic final states, which can be used to study charmonium production in the LHCb experiment.

Chapter 3

Charmonium decay channels

This chapter summarises charmonium decay channels, which are used or can potentially be used to reconstruct different charmonium states and measure their production and properties. The listed decay channels are promising for studies at the LHCb experiment. Therefore they are most useful for further discussion. Not many charmonium decays to hadrons have been reconstructed in the hadron machine environment. Therefore, it is often difficult to predict the corresponding physics reach before proceeding to the actual data analysis. In should be stated, that in order to study promptly produced charmonium with a specific hadronic decay channel, a dedicated online trigger line should be developed.

The decays including neutral particles in the final state are used at B-factories but are more challenging at LHCb, have not been used in the studies performed within the thesis and hence are omitted.

The charmonium decays receive much attention from theory since measurements of their branching fractions often challenge theoretical predictions. This topic is also explicitly excluded from the discussion.

The most precise charmonium studies employ decays into clean dimuon final state, which is possible for $J^{PC} = 1^{--}$ charmonia. In addition to the 1^{--} states, the χ_c family can be accessed via radiative transitions to J/ψ, $\chi_c \to J/\psi(\to \mu^+\mu^-)\gamma$. However, low-energy photon reconstruction is required. Other states from the charmonium family cannot be explored using decays to a pair of muons. Therefore other final states should be investigated [187].

In this chapter possible decay channels to study the η_c, χ_{c0}, h_c and $\eta_c(2S)$ mesons, which can't be accessed using their decays to $\mu^+\mu^-$ or $(J/\psi \to \mu^+ \mu\text{m})\gamma$ are discussed. The known branching fractions [188] of promising decays discussed below are summarised in Table 3.1. Many of these branching fractions can be measured more precisely at Belle, Belle II, BES III, or future high-luminosity tau-charm experiments.

The charmonia decays to $p\overline{p}$ have been proposed to measure charmonium production at LHC [187]. The first measurement of the η_c production at the LHCb experiment has been performed using the $\eta_c \to p\overline{p}$ decay [131]. This demonstrated that the $p\overline{p}$ final state is powerful to reconstruct the η_c meson, even though the measurement is performed only for transverse momentum larger than 6.5 GeV due to available trigger bandwidth. This decay is also used to study exotic candidates decaying to $(\eta_c \to p\overline{p})\pi^-$ [189]. The branching fraction of the $\eta_c \to p\overline{p}$ channel is known to about 10% precision [188]. The studies of η_c would benefit from more precise measurement of $\mathcal{B}(\eta_c \to p\overline{p})$ or $\mathcal{B}(\eta_c \to p\overline{p})/\mathcal{B}(J/\psi \to p\overline{p})$. Branching fractions of $\chi_{cJ} \to p\overline{p}$ and $\psi(2S) \to p\overline{p}$ decays have been measured to about 3-5% precision. Recently, LHCb observed the $\eta_c(2S) \to p\overline{p}$ decay channel using a data sample of exclusive $B^+ \to p\overline{p}K^+$ decays [190]. Together with the measurement of $\mathcal{B}(B^+ \to \eta_c(2S)K^+)$ by Belle [191], the branching fraction of the $\eta_c(2S) \to p\overline{p}$ is indirectly determined to be about 0.7×10^{-4}. Therefore, the decay $\eta_c(2S) \to p\overline{p}$ is promising for the $\eta_c(2S)$ hadroproduction studies at LHC.

Another promising final state to study prompt production of charmonium is $\phi\phi$. The 1^- charmonium states are forbidden to decay to $\phi\phi$. The LHCb measured the $\chi_{c0,1,2}$ and $\eta_c(2S)$ production in inclusive b-hadron decays using the $\phi\phi$ final state with the first evidence of the $\eta_c(2S) \to \phi\phi$ decay [192]. In Section 9.1.3, a tension between the PDG fit value of $\mathcal{B}(\eta_c \to \phi\phi)$ and the PDG average value [188] by about two times was pointed out and the ratio of branching fractions $\mathcal{B}(\eta_c \to \phi\phi)/\mathcal{B}(\eta_c \to p\overline{p})$ was measured. Further measurements are needed to establish a robust value of the $\mathcal{B}(\eta_c \to \phi\phi)$. Following the evidence of $\eta_c(2S) \to \phi\phi$, this channel is also promising to study a hadroproduction of the $\eta_c(2S)$. Similarly, the ϕK^+K^- and the $\phi\pi^+\pi^-$ final states can potentially be used including final states with intermediate resoncances such as ϕf, where f decays to $\pi^+\pi^-$ or K^+K^-.

The branching fractions of charmonium decays to long-lived baryons such as $\Lambda\bar{\Lambda}$ and $\Xi^+\Xi^-$ are measured for most charmonium states. Reconstruction of these decay channels is challenging for LHCb due to a flight distance of these baryons, so that they escape the Vertex Locator (VELO), which causes a reduced reconstruction and trigger efficiency.

Decays involving short-lived baryons are reconstructed by LHCb with better efficiency. The decays $\chi_{c0,2} \to \Lambda(1520)\bar{\Lambda}(1520)$ have been observed by the BES III collaboration [193] while the $J/\psi \to \Lambda(1520)\bar{\Lambda}(1520)$ decay is not observed so far. This channel becomes another candidate to measure hadroproduction of charmonium states [194].

The least studied charmonium state below the $D\overline{D}$ threshold is the h_c meson with only a few of h_c decays observed so far. The h_c meson is expected to decay to $p\overline{p}$, however, the upper limit on $\mathcal{B}(h_c \to p\overline{p})$ reported by the BES III collaboration [195] is more than an one order of magnitude smaller than the theoretical prediction [187]. Alternatively, the h_c can be reconstructed using its radiative transition $h_c \to \eta_c\gamma$ with the branching fraction about 50%, which requires a reconstruction of the photon in addition to the η_c state. Recently, LHCb observed new clean decays $\chi_{c1,2} \to J/\psi\,\mu^+\mu^-$, and measured precisely the χ_{c2} mass and natural width [196]. Following this observation, the $h_c \to \eta_c\mu^+\mu^-$ decay can also be searched. Recently, BES III has observed the $h_c \to p\overline{p}\pi^+\pi^-$ decay and measured its branching fraction to be $(2.89 \pm 0.32 \pm 0.55) \times 10^{-3}$ [197], which makes it promising for studies at LHCb.

The reconstruction of various charmonium states is important for systematic studies of charmonium production and properties. Many measurements in b-physics (searches of hadron exotics, b-anomalies, etc.) study decays with clean signatures from J/ψ decays to leptons in the final state. Many studies would benefit from the analogous measurements exploiting other charmonium states in the final state. As a conclusion, a number of hadronic final states are promising to simultaneously reconstruct charmonium states. Incorporating charmonium states other than 1^{--} implies a systematic measurements of hadronic branching fractions of their decays. Some charmonium states are poorly studied and not many decays have been observed so far, which makes expectations of their signal significances more complicated.

In this thesis, I study charmonia using their decays to hadrons with the LHCb detector. In the next chapter I will describe the LHCb experiment, and more specifically the detector features essential to reconstruct charmonia via hadronic decays.

[1]Indirect determination

	$\mathcal{B} \times 10^3$								
	$p\bar{p}$	$\phi\phi$	ϕK^+K^-	$\phi\pi^+\pi^-$	$\Lambda\bar{\Lambda}$	$\Xi^+\Xi^-$	$\Lambda(1520)\bar{\Lambda}(1520)$	$\eta_c\gamma$	$p\bar{p}\pi^+\pi^-$
η_c	1.52 ± 0.16	1.79 ± 0.20	2.9 ± 1.4	unknown	1.09 ± 0.24	9.0 ± 2.6	-	-	5.3 ± 1.8
J/ψ	2.12 ± 0.03	forbidden	0.83 ± 0.12	0.87 ± 0.09	1.89 ± 0.08	0.97 ± 0.08	unknown	17 ± 4	6.0 ± 0.5
χ_{c0}	0.22 ± 0.01	0.80 ± 0.07	0.97 ± 0.25	unknown	0.33 ± 0.02	0.48 ± 0.07	0.31 ± 0.12	forbidden	2.1 ± 0.7
h_c	< 0.15	forbidden	unknown	unknown	unknown	unknown	unknown	510 ± 60	unknown
χ_{c1}	0.076 ± 0.003	0.42 ± 0.05	0.41 ± 0.15	unknown	0.11 ± 0.01	0.08 ± 0.02	< 0.09	forbidden	0.50 ± 0.19
χ_{c2}	0.073 ± 0.003	1.06 ± 0.09	1.42 ± 0.29	unknown	0.18 ± 0.02	0.14 ± 0.03	0.46 ± 0.15	forbidden	1.32 ± 0.34
$\eta_c(2S)$	0.07^1	unknown	unknown	unknown	unknown	unknown	unknown	forbidden	unknown
$\psi(2S)$	0.29 ± 0.01	forbidden	0.07 ± 0.02	0.12 ± 0.03	0.38 ± 0.01	0.29 ± 0.01	unknown	3.4 ± 0.5	0.60 ± 0.04

Table 3.1: The branching fractions $\times 10^3$ of charmonium decays to hadrons and radiative decays to $\eta_c\gamma$.

Chapter 4

LHCb detector

The analyses of charmonium production using decays to hadrons, described in Chapters 5 and 5.6 have been performed using data collected by the LHCb experiment. The LHCb experiment is well suited and is the most performant among the experiments at hadron machines to reconstruct hadronic decays of charmonium states. Even though such studies have not been considered as a part of the core program of the experiment, a flexible trigger of the LHCb experiment provides an opportunity to measure η_c, χ_{cJ} and $\eta_c(2S)$ production observables using $p\overline{p}$ and $\phi\phi$ final state signatures.

After introducing the Large Hadron Collider (LHC) in the CERN accelerator complex in Section 4.1, the LHCb detector is described in Section 4.2 with the accent on the detector features most relevant for charmonium reconstruction via decays to hadrons. The vertex and track reconstruction at LHCb are discussed in Section 4.3. The particle identification within LHCb experiment is described in Section 4.4. Finally, the LHCb trigger together with dedicated selections for prompt charmonium reconstruction via decays to hadrons is addressed in Section 4.5.

4.1 Large Hadron Collider

The Large Hadron Collider (LHC) [198] is a synchrotron with a circumference of 27 km located near Geneva Swiss-French border located about 100 m underground at CERN exploiting proton-proton, proton-lead and lead-lead collisions. During the core proton-proton collisions program of the LHC Run I and II in 2011-2018 years, the counter-propagating proton beams were accelerated to an energy of 7, 8 and 13 TeV.

Before the injection into the LHC proton beams pass several steps of acceleration. The protons obtained from hydrogen atoms are firstly accelerated by the linear accelerator LINAC2 up to an energy of 50 MeV, then the BOOSTER accelerates protons to an energy of 1.4 GeV. After that, protons are injected into the Proton Synchrotron (PS) and accelerated to an energy of 26 GeV, which followed by the injection into the Super Proton Synchrotron (SPS), yielding the proton beams with an energy of 450 GeV.

The beams from SPS are then injected into LHC and accelerated to the final energy using 16 Radio-Frequency (RF) cavities located along the LHC ring. The conduction of the beams along the ring is performed by 12300 superconducting dipole magnets providing a magnetic field of 8.3 T. The coils of magnets are cooled by a liquid helium cryogenic system to a temperature of 1.9 K. The focusing of the beams is ensured using about 400 quadrupole magnets.

For the nominal proton-proton program, LHC provides proton beams of 1.3×10^{11} protons per bunch with a collision rate of $40MHz$ and an instanteneous luminosity up to $10^{34}cm^{-2}s^{-1}$. The four main LHC experiments are placed around four collision points. The scheme of the CERN accelerating complex is shown on Fig. 4.1.

The LHC experiments are:

- ATLAS (A Toroidal LHC ApparatuS) [200],
- CMS (Compact Muon Solenoid) [201],
- ALICE (A Large Ion Collider Experiment) [202],
- LHCb (Large Hadron Collider beauty) (see Section 4.2),
- LHCf (Large Hadron Collider forward) [203],
- TOTEM (TOTal Elastic and diffractive cross-section Measurement) [204],
- MoEDAL (Monopole and Exotics Detector At the LHC) [205].

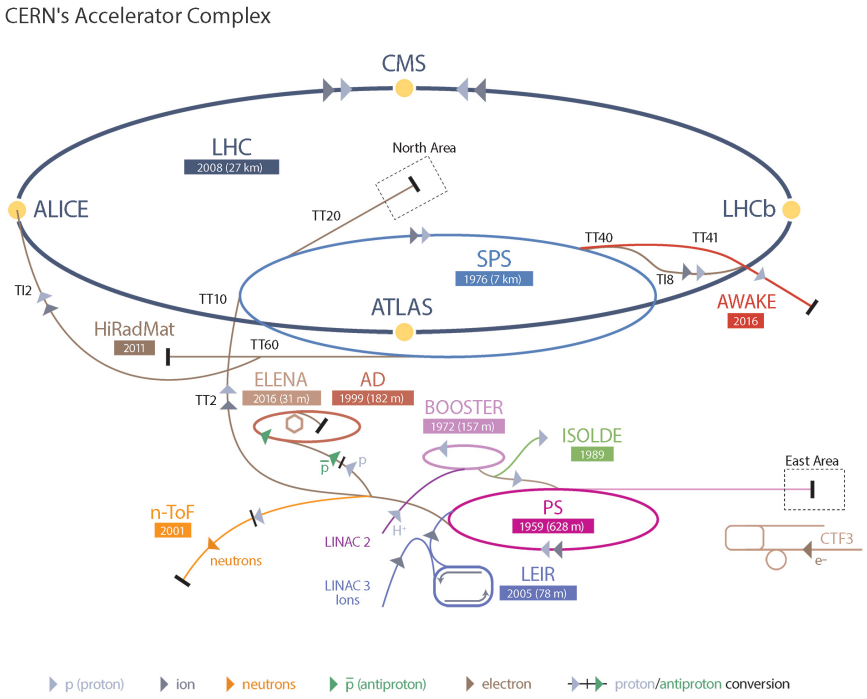

Figure 4.1: The LHC and CERN accelerating complex [199].

The ATLAS and CMS are so-called 4π experiments performing direct studies of Standard Model (SM) particles and searches for New Physics (NP). Their core physics programs overlap and aim at studying the Higgs boson and t quark properties and decays and direct searches for new supersymmetric (SUSY) particles, additional Higgs bosons, etc. Another important part of the ATLAS and CMS programs is dedicated for heavy flavour physics in b and c quark sectors.

The ALICE is an experiment designed to exploit in lead-lead, proton-lead and lead-proton collisions. The main goal of the ALICE experiment is to look for signatures of the deconfined state of hadronic matter Quark Gluon Plasma (QGP). The studies are performed by measuring, for example, the heavy flavour production suppression and comparing it for different kinds of collisions. Besides, the studies of other in-matter production effects, such as cold nuclear matter effect, are performed.

The TOTEM experiment is designed for measuring elastic, diffractive and dissociative proton scattering cross-sections. Their measurements are essential for soft Quantum Chromodynamics (QCD). The LHCf experiment is designed for measurements aiming to simulate the cosmic rays in the laboratory conditions. The MoEDAL is performing searches for Dirac magnetic monopole.

4.2 LHCb experiment

The LHCb experiment [206, 207] is designed for studies of heavy flavour - b and c quark - sectors in the forward region. The core physics program of the LHCb experiment is dedicated to precision measurements or searches of:

- CP-violation in b and c quark mixing and decays including measurement of the unitarity triangle parameters,
- Search for indirect contributions of NP to (rare) processes, including contributions to B-meson decays involving a lepton pair in the final state and tests of lepton universality,
- b- and c-hadrons spectroscopy (B_s^0, B_c^+ mesons, b and c-baryons, quarkonium etc.) and searches for hadron exotics (tetraquarks, pentaquarks, etc.),
- QCD effects in b-decays to open charm particles or charmonium,
- Heavy flavour production and soft QCD processes,
- Electroweak physics,
- Heavy ion physics.

The LHCb experiment is a forward single-arm spectrometer covering the pseudorapidity range of $2 < \eta < 5$. The angular acceptance of the LHCb is 10-300 mrad on x-axis and 10-250 mrad on y-axis. Typically, LHCb is capable to detect particles in the p_{T} range of $0.25 \text{ GeV} < p_{\mathrm{T}} < 20 \text{ GeV}$.

In hadron-hadron collisions, a $b\bar{b}$ (or similarly $c\bar{c}$) quark pair production is dominated by $gg \to b\bar{b}$, $q\bar{q} \to b\bar{b}$, $gg \to b\bar{b}g$ and $q\bar{q} \to b\bar{b}g$ processes, where g denotes a gluon and q denotes a light quark. At the LHC energies, the processes mentioned above lead to the $b\bar{b}$ production predominantly in the forward region. The $b\bar{b}$ production cross-section as a function of the b and $\bar{b}$ quarks pseudorapidity is shown on Fig. 4.2 and is compared with LHCb, ATLAS and CMS acceptances. By covering only about of 4% of the full solid angle, the LHCb detector receives fraction of total $b\bar{b}$ production cross-section comparable with the one of a 4π experiment, such as ATLAS or CMS. This feature together with precise vertex reconstruction, powerful particle identification and selective trigger (see Sections 4.3, 4.4 and 4.5) makes LHCb exclusive or at least more profitable to study most of heavy flavour physics observables compared to other LHC experiments. In addition, LHCb covers the p_{T} and rapidity ranges complementary to those of ATLAS and CMS.

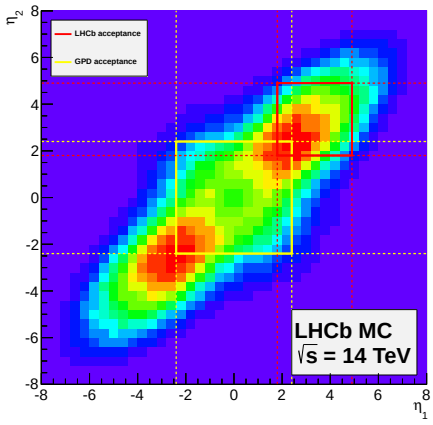

Figure 4.2: The $b\bar{b}$ production as a function of quarks pseudorapidity. The red rectangle shows the LHCb acceptance. The yellow rectangle shows the ATLAS and CMS acceptance [213].

In total, about 5×10^{11} $b\bar{b}$ pairs and about 3×10^{12} $c\bar{c}$ pairs are created within LHCb acceptance per fb^{-1} of integrated luminosity at $\sqrt{s}$ =14 TeV.

In the heavy flavour physics program, LHCb is competing with the so-called B-factories (b-sector) and charm factories (c-sector). The B-factories, such as Belle [208] and BaBar [209], are the asymmetric e^+e^- experiments operating at the centre-of-mass energy of $\Upsilon(4S)$ resonance mass, which decays strongly to the B^+B^- or $B^0\overline{B}^0$ with a branching fraction close to 100%. The advantage of B-factories is that the underlying experimental environment is clean and most of the events contain a pair of light B-mesons. Due to its detector design choice, the LHCb experiment has reduced reconstruction performance of neutral particles contrary to B-factories. Hence, the reconstruction of B-meson decay modes involving neutral particles in the final state is much better accessed by B-factories. At the same time, the production cross-section of $\Upsilon(4S)$ resonance in e^+e^- collisions is three orders of magnitude smaller compared to the $b\bar{b}$ production cross-section in hadron-hadron collisions at TeV energies. Also, LHCb is capable to study b-hadrons other than lightest B-mesons, i.e. B_s^0, Λ_b^0, B_c^+, etc. Charm factories (for example BES [210]) operate at e^+e^- collision energies in the charmonium mass region to produce J/ψ, $\psi(2S)$ charmonium states. The charm factories provide many of the most precise measurements of charmonium decays. The most precise measurements of resonance parameters of many charmonium states are performed at $\bar{p}p$-collision experiments (E760 and E835 [211]) and also e^+e^- experiments such as KEDR [212].

During the data taking, LHCb reduces the nominal LHC instantaneous luminosity (luminosity levelling) by two orders of magnitude. This leads to both reduced total yield

of the $b\bar{b}$ production and smaller detector occupance. The latter is crucial for the online trigger, which has limited bandwidth. Also, the luminosity reduction improves the track and vertex reconstruction performance and timing characteristics. Another benefit from the luminosity levelling is that the detector components ageing is reduced. The luminosity levelling is made in the way that the instantaneous luminosity is constant during the LHC fill and is adjusted by adding an offset between the beams at the collision point. The typical target value of the number of interactions per beam crossing (pile-up) at LHCb is $\mu = 1.5$. Since the LHC instantaneous luminosity during the fill is decreasing, the offset is adjusted by using information from online luminosity monitoring. More information about the luminosity levelling with offset beam is given in Ref. [214].

During the LHC Run I and Run II, LHCb recorded integrated luminosity of:

- 0.04 fb^{-1} at $\sqrt{s}$ =7 TeV in 2010,
- 1.11 fb^{-1} at $\sqrt{s}$ =7 TeV in 2011,
- 2.08 fb^{-1} at $\sqrt{s}$ =8 TeV in 2012,
- 0.33 fb^{-1} at $\sqrt{s}$ =13 TeV in 2015,
- 1.67 fb^{-1} at $\sqrt{s}$ =13 TeV in 2016,
- 1.71 fb^{-1} at $\sqrt{s}$ =13 TeV in 2017,
- 2.19 fb^{-1} at $\sqrt{s}$ =13 TeV in 2018

in proton-proton collisions (Fig. 4.3).

The sketch of the LHCb detector is shown on Fig. 4.4. The detector comprises a high-precision tracking system consisting of a silicon-strip vertex detector surrounding the pp interaction region [215], a large-area silicon-strip detector located upstream of a dipole magnet, and three stations of silicon-strip detectors and straw drift tubes [216] placed downstream of the magnet. Different types of charged hadrons are distinguished using information from two ring-imaging Cherenkov detectors [217]. Photons, electrons and hadrons are identified by a calorimeter system consisting of scintillating-pad and preshower detectors, an electromagnetic calorimeter and a hadronic calorimeter. Muons are identified by a system composed of alternating layers of iron and multiwire proportional chambers [218].

To reduce the LHC bunch-crossing frequency of 40 MHz to storable event rates LHCb employs a two-level trigger system, including a hardware (L0) trigger and a software

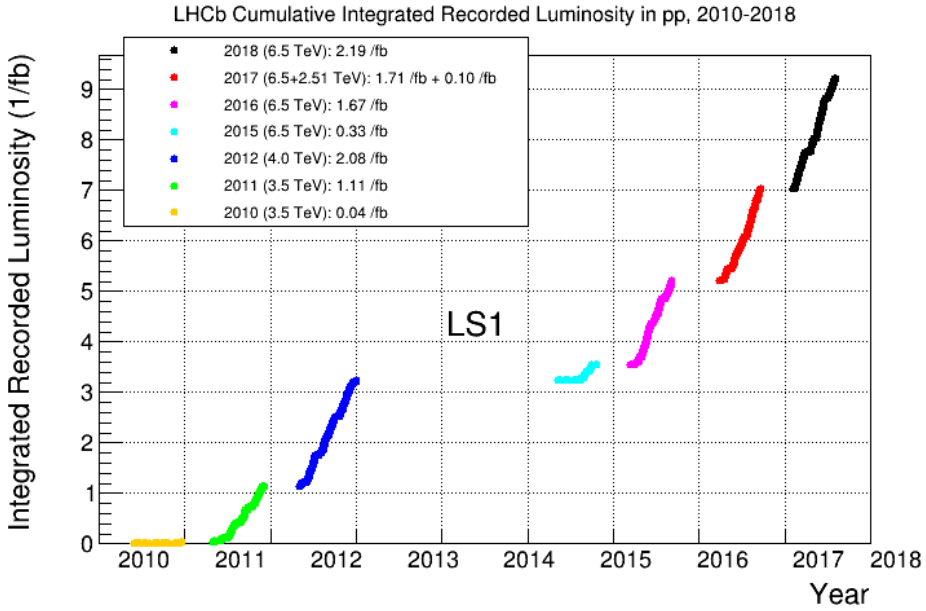

Figure 4.3: Integrated luminosity collected by LHCb during LHC Runs I and II.

(HLT) trigger implemented in a processor farm. A general idea of the most of online (L0 and HLT1) trigger requirements is to select particles, which have large p_{T} and/or are well displaced from any collision vertex since weakly decaying b and c-hadrons fly a significant distance before the decay. The L0 reduces the rate to about 1 MHz, and the L0 triggered events are passed to the online stage of the software trigger (HLT1), which partially reconstructs events, confirming (or not) the L0 decision. The second level of software trigger (HLT2) processes fully reconstructed events and stores relevant information about selected decay candidates.

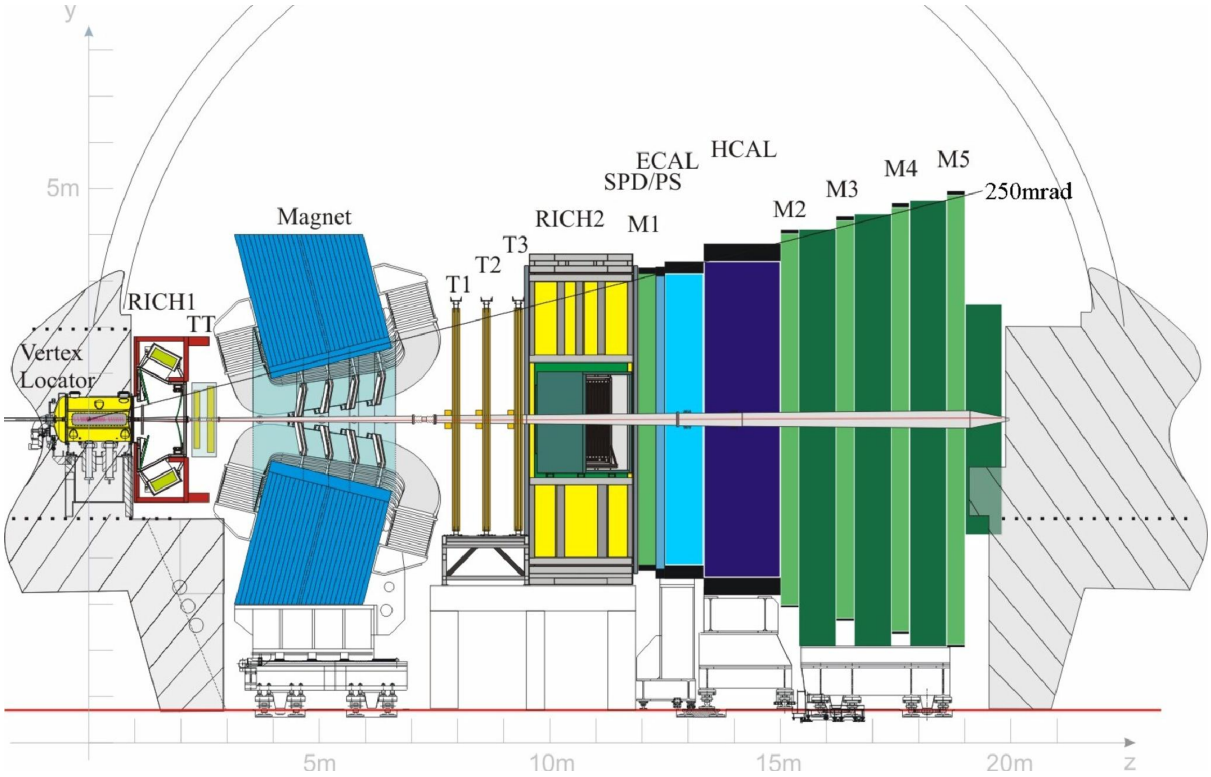

Figure 4.4: The LHCb detector [206].

4.3 Vertex and track reconstruction

4.3.1 Vertex reconstruction

The goal of the vertex reconstruction is to recognise vertices, distinguish primary (PV) from b (or c)-decays ones and measure the flight distance of the decaying b-hadron and assign tracks to vertices.

The vertex reconstruction in LHCb is performed thanks to the Vertex Locator (VELO) [219]. VELO is a silicon strip detector, which measures trajectories of charged particles close to the interaction point. The sketch of VELO is shown on Fig. 4.5. VELO consists of 42 semicircular silicon modules along the beam forming two halves of the detector, which can approach or move away from each other. Each module consists of r and Φ sensors measuring track hit polar coordinates r and ϕ, respectively. This configuration allows making faster track reconstruction than the geometry of the rectangular strips. The strips of r-sensor are concentric rings with a variable pitch that increases linearly from 38 µm at the inner edge to 102 µm at the outer edge. The strips of ϕ-sensor strips are divided into two regions at $r = 17.25\,\text{mm}$ in order to reduce the occupancy and to avoid large strip pitches at the outer edge of the sensors. The strips have a pitch of 38 µm in the inner region (increasing to 78 µm at the outer edge), while the strips in the outer region have a pitch of 39 µm (increasing to 97 µm at the outer edge). The sketch of both sensors is shown on Fig. 4.6.

The inner radius (i.e. distance to beam axis) of VELO module is about 8 mm. At this distance, severe radiation can cause destruction of the modules. A mechanical moving system is designed to open or close VELO modules when needed. During the phase of stable beams of data taking the VELO modules are closed, while during other phases when beams are circulating in the LHC unsqueezed, VELO is kept in the safe opened state. The monitoring system ensures that VELO can be closed by using the online information about the number of reconstructed vertices. The time needed for VELO to close from a completely opened state is about 3 minutes via iterative procedure of refining vertex position.

The inner faces of the vessels (RF-foils) separate the VELO vacuum from the LHC vacuum. The RF-foils are designed to minimise the material traversed by particles before crossing VELO sensors. Furthermore, the geometry of the RF-foils is such that it makes the two halves of the VELO overlap when it is moved to the closed position.

VELO dominates the measurements of the PV position and the track's impact parameter (IP) with respect to PV, which is crucial for trigger and further event selections. The IP is measured with a resolution of $(15 + 29/p_{\mathrm{T}})$ µm, where p_{T} is the component of

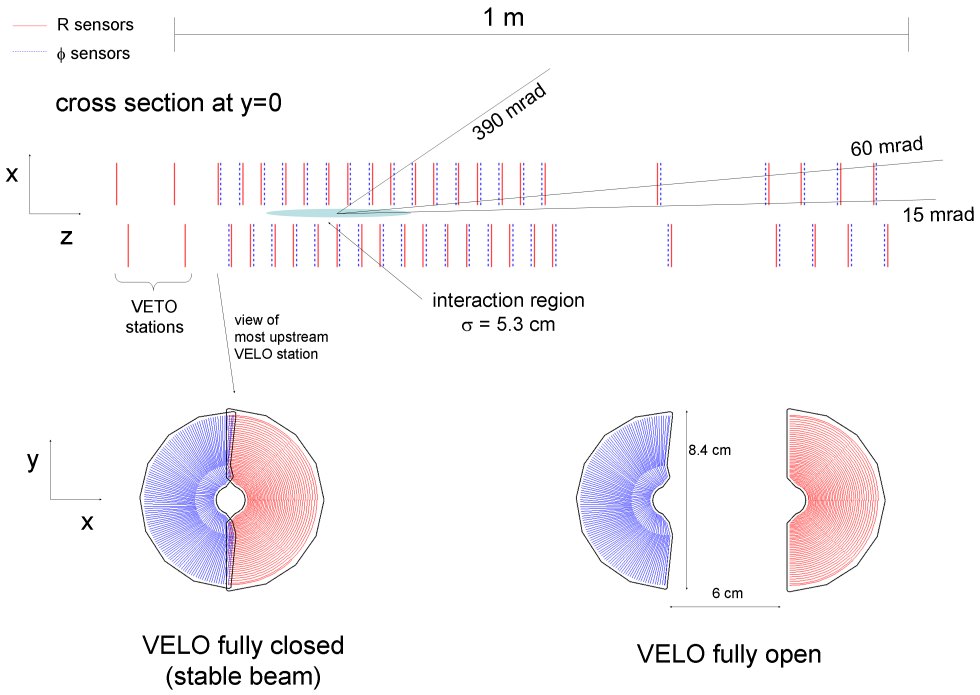

Figure 4.5: Sketch of the VELO detector [220].

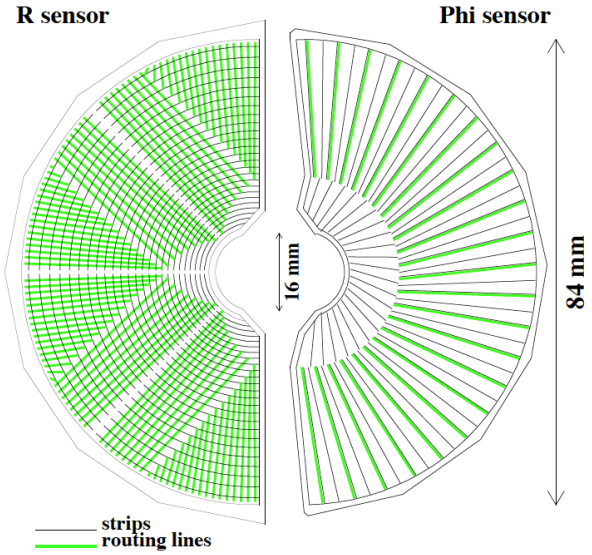

Figure 4.6: The r (left) and ϕ (right) sensors of the VELO detector [220].

the momentum transverse to the beam, in GeV. The IP resolution determination driven by VELO is the best among all LHC experiments. The PV position and resolution along and across the beam as a function of the vertex multiplicity and the IP resolution are shown on Fig. 4.7.

Since VELO opens and closes many times, its alignment is important during operations to match online and offline reconstruction. During the Run I, the alignment and calibration have been performed offline. The online reconstruction in Run I was more simple compared to that of Run II. Therefore, the data passing trigger was reprocessed every year to take into account and correct possible effects of alignment and calibration. During LHCb Run II the alignment and calibration were performed online. The data recorded at the beginning of the LHC fill was used to update alignment and calibration constants if needed. The alignment of all detectors (VELO, trackers, RICH mirros) takes in total about 20-30 minutes, while the VELO alignment takes only few minutes.

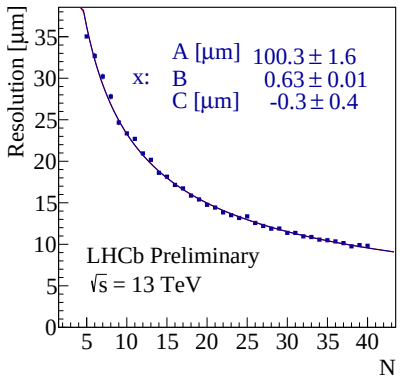

(a) The PV x-coordinate resolution.

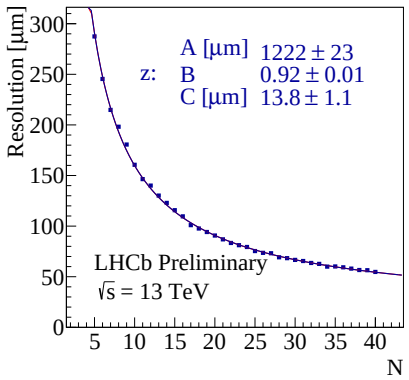

(b) The PV z-coordinate resolution.

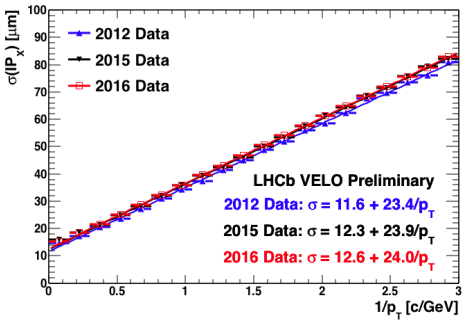

(c) The IP resolution.

Figure 4.7: The resolution of PV position and IP provided by VELO [220].

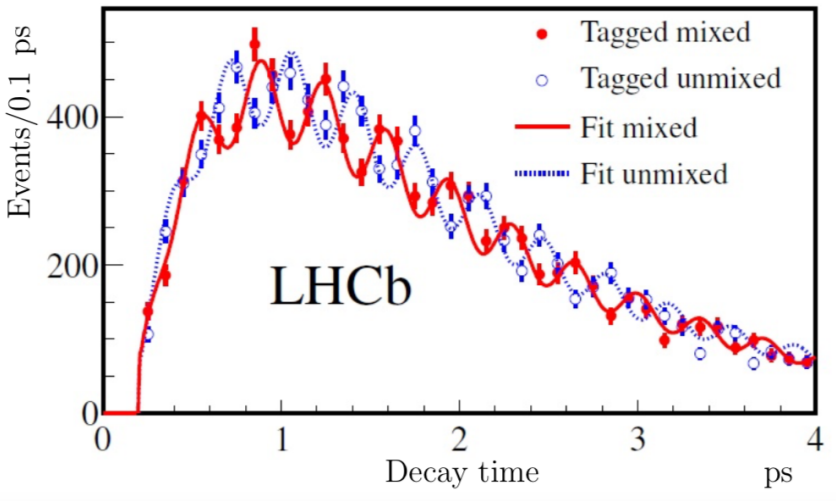

Figure 4.8: Decay time distribution for B_s^0 candidates tagged as mixed (different flavour at decay and production; red, continuous line) or unmixed (same flavour at decay and production; blue, dotted line). The data and the fit projections are plotted in a signal window around the reconstructed B_s^0 mass [221].

Vertex reconstruction precision using the LHCb tracking system is illustrated by resolving rapid B_s^0-$\bar{B}_s^0$ oscillations [221]. Fig. 4.8 shows decay time distribution for B_s^0 candidates, reconstructed via $B_s^0 \to D_s^+\pi^+$, with the D_s^+ decaying via $D_s^+ \to K^+K^-\pi^-$, $D_s^+ \to K^{*0}K^-$, $D_s^+ \to K^-\pi^+\pi^-$ and $D_s^+ \to \pi^-\pi^+\pi^-$, tagged as mixed or unmixed.

4.3.2 Track reconstruction

The LHCb tracking system is designed for the reconstruction of the tracks of stable charged particles and measurement of their charge and momenta. The momenta of particles are determined by measuring the curvature of tracks bent in the magnetic field of the LHCb dipole magnet.

The LHCb experiment uses a warm dipole magnet [222] with a total weight of about 1,600 tons. The magnetic field is created by two identical trapezoidal coils located symmetrically in the magnets yoke. The magnet provides an integrated magnetic field of about 4 T along the y-axis mainly. The non-uniformities of the field amount to about 1% and are important for track reconstruction. Therefore, the map of the magnetic field is used for track reconstruction. The opposite magnet polarities "Up" and "Down" are alternated during the data taking in order to reduce systematic uncertainties related to detector asymmetries, which could lead to potential asymmetries in reconstruction of particles with opposite charge. Approximately the same amount of integrated luminosity is collected with two different polarities.

The tracking system of the LHCb experiment comprises four tracker stations: Tracker Turicensis (TT) placed upstream the LHCb magnet and three stations T1, T2 and T3 placed downstream the magnet. Two different technologies are used in the inner (Inner Tracker) and outer (Outer Tracker) regions of the T1-T3 stations in order to withstand the different particle flux. The TT and IT together costitute the LHCb Silicon Tracker (ST), since the same technology is used for both detector systems.

The different kinds of tracks at LHCb are categorised as:

- Long tracks consisting of hits in VELO, TT and T1-3 detectors. The reconstruction of long tracks has the best performance. This kind of tracks are used in data analyses described in Chapters 5 and 5.6.
- Upstream tracks, which are reconstructed from hits in VELO and TT. These tracks belong to particles with low momentum such that they escape the T1-3 acceptance due to the magnetic field.
- Downstream tracks consisting of hits in TT and T1-3 but not in VELO. These tracks can belong to long-lived particles such as K_S^0, Λ, Ξ_b, etc., whose lifetime is enough to leave the VELO detector.
- T track composed from hits in T1-3 stations only. These tracks can belong to secondary particles created due to the interaction of the primary particle with a material of detector.
- VELO tracks consisting of hits in VELO detector only.

The different categories of tracks in LHCb are illustrated on Fig. 4.9.

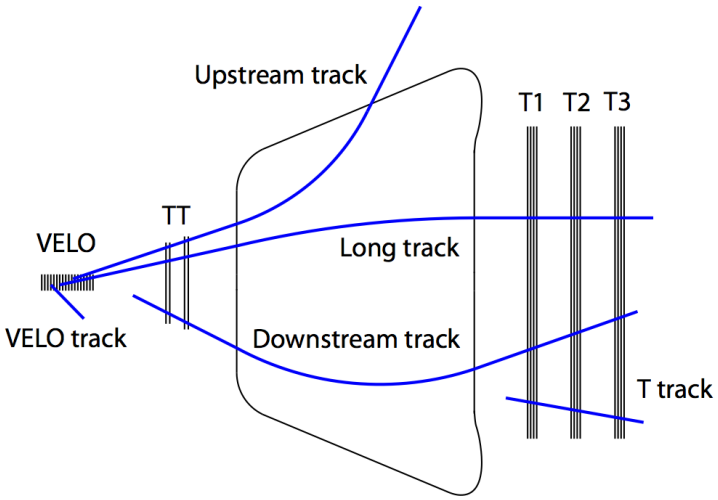

Figure 4.9: Track categories at LHCb.

Tracker Turicensis (TT)

The TT is located upstream of the magnet and improves the precision of VELO tracks. Another important goal of TT is to reconstruct vertices formed by downstream tracks, e.g. corresponding to decays of long-lived strange hadrons.

The TT is a silicon microstrip detector with a pitch between sensors of 183 μm. The TT consists of four rectangular detector layers places in so-called $x-u-v-x$ configuration. The x-layers are located vertically, while the $u(v)$ stereo layers are rotated by $-5°(+5°)$ relative to the vertical position. Such arrangement improves a spatial resolution of the detector. The TT comprises two substations $x-u$ (TTa) and $v-x$ (TTb) separated by a distance of 27 cm along z-axis. The total active area of TT is 8 m^2. The sketch of TT is shown on Fig. 4.10. The TT is designed to cover the entire acceptance of the magnet. Each layer is made of 9.44 cm × 9.64 cm rectangular sensors 0.5 mm thick with 512 strips in total. The sensors are organised into half-modules containing 7 sensors each, which are then grouped into read-out sectors. The central sectors are smaller due to higher detector occupancy. The important feature of TT is that the front-end electronics and the cooling system are located outside of the LHCb acceptance. The TT provides a spatial resolution of 50 μm.

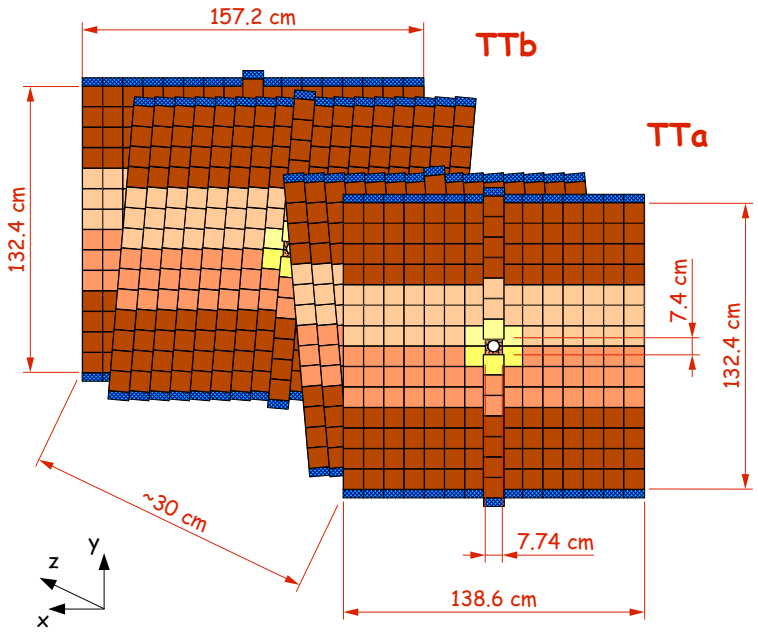

Figure 4.10: Sketch of Tracker Turicensis [223].

Inner Tracker (IT) and Outer Trackers (OT)

The tracking stations T1-3 measure the tracks deflected by the magnet and hence are important for the determination of the particles' momenta. Three stations of IT are arranged similarly to TT. The IT covers about 2% of total acceptance area of the tracking station, which corresponds to about 20% of particle flux. The IT comprises four detector boxes consisting of four layers similarly to TT as shown on Fig. 4.11.

The IT modules consist of two or three sensors, which are shifted along the beam direction with respect to OT detector modules from the same tracking station. The IT provides a spatial resolution of about 50 µm depending on the detector occupancy. The IT is described in more details in Ref. [224].

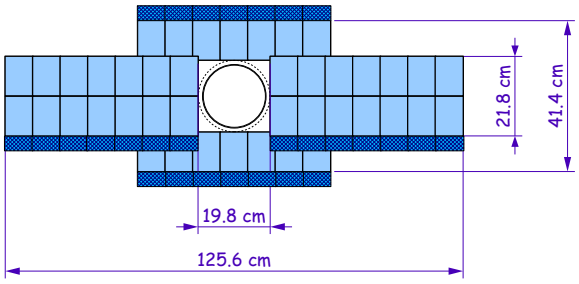

Figure 4.11: Sketch of Inner Tracker station [223].

The OT detector is a gaseous detector based on straw tubes and covering the total area of 597 cm × 485 cm. The straw tubes have a length of 2.4 m and the inner diameter of 4.9 mm filled with a mixture of Ar and CO_2 gases with a small fraction of O_2. Such gas mixture provides a drift time of 50 ns and a tolerable ageing. The vertical positioning of straw tubes avoids the sagging of the anode, which is located at the centre of the straw tube. The tubes are fixed to carbon-fibre panels forming gas-tight boxes enclosing detector modules.

The OT layer is composed of 14 long and eight short modules, containing two staggered layers of straw tubes each. The OT layers are located vertically with the same $x-v-u-x$ configuration as for TT and IT and form the OT station. The schematical view of OT and its module is shown on Fig. 4.12.

The OT measures the time of arrival of the signal with respect to the LHCb clock, which provides a measurement of the drift length and improves position resolution to about 200 µm. The performance of the OT is given in Ref. [225].

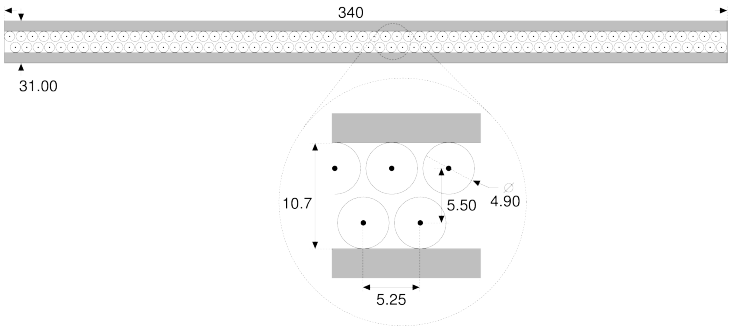

(a) Module cross section.

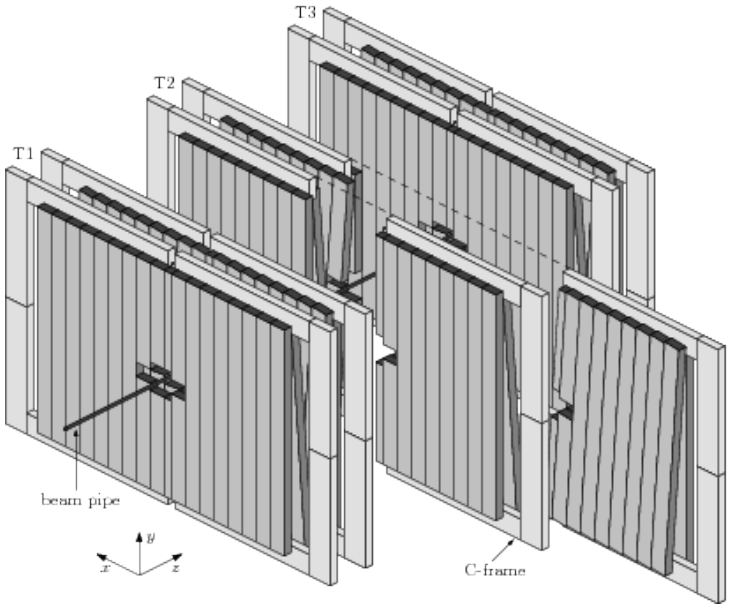

(b) Arrangement of OT drift tube modules in layers and stations

Figure 4.12: Outer Tracker detector [225].

4.4 Particle identification

The particle identification (PID) is a complex task of distinguishing among different kind of limited number of (quasi) stable particles measuring their energy or momentum and studying their interaction with detector material.

The Electromagnetic Calorimeter (ECAL) performs PID of electrons, photons and π^0 in the decay $\pi^0 \to \gamma\gamma$. Also, ECAL measures photon energy and corrects the energy of electron by identifying emitted bremsstrahlung photons. At trigger level, charged hadrons are identified by fast Hadronic calorimeter (HCAL), while precise hadron ID of charged pions, kaons, protons and deuterons is performed by two Ring Imaging Cherenkov (RICH) detectors. The Muon detector is designed for identifying muons.

4.4.1 Calorimeters

Calorimeter system comprises SPD, PS, ECAL and HCAL and is organised in a preudo-projective geometry. In all detectors, the light from scintillating tiles is transmitted to photon detectors by optical fibres. The four detectors play a key role in the LHCb trigger. In addition, they provide particle ID and energy measurement for neutral particles.

SPD and PS

Apart from the ECAL and HCAL, the calorimeter system of LHCb [226] comprises the Pre-Shower detector (PS) and Scintillating Pad Detector (SPD). The main goal of the PS is to initiate the shower in front of the ECAL by the electromagnetic particles. The task of SPD is to distinguosh charged particles from uncharged ones. The PS distinguishes electrons from photons. An illustration of the principle of PID with the LHCb calorimeters is shown on Fig. 4.13.

Both SPD and PS are planar scintillating pad detectors separated by a distance of 56 mm. A 15 mm thick layer of lead is inserted between the two detectors. The amount of lead corresponds to 2.5 electromagnetic interaction length (X_0) and a small fraction of hadron interaction length (0.1 λ_I). Within this configuration, hadrons cross SPD and PS without losing sizeable fractions of their energies, while electrons and photons create electromagnetic showers in PS. Contrary to photons, electrons leave signal in the SPD detector. It is also important to say that the number of hits in the SPD detector is used as a proxy for event multiplicity. The total detection area of SPD and PS is 6.2 m $\times$ 6.6 m. Similarly to other detectors, the granularity of PS and SPD decreases from inner to the outer region. The size of the cell is about 40 mm $\times$ 40 mm in inner section,

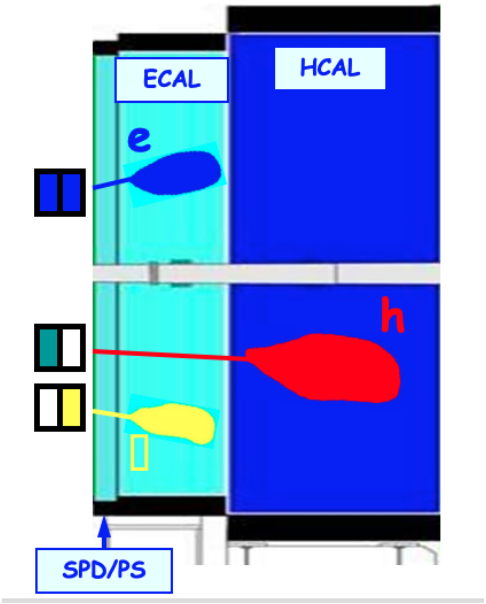

Figure 4.13: Principle of PID with the LHCb calorimeter system comprising PS, SPD, ECAL and HCAL. Hadronic (red) and electromagnetic (yellow and blue) showers are illustrated.

60 mm × 60 mm in the middle section and 120 mm × 120 mm in the outer section. The light in scintillator planes is conducted by wavelength shifting fibres connected to Multi-Anode PhotoMultiplier Tubes (MaPMTs).

Electromagnetic Calorimeter (ECAL) and Hadronic Calorimeter (HCAL)

ECAL measures the energy of electromagnetic particles by absorbing their showers. The ECAL is a "shashlyk"-type calorimeter made from the alternate detector and absorbed layers. The detector layers are made of polystyrene scintillator planes 4 mm thick. For an absorber, lead layers with a thickness of 2 mm are used. The total depth of ECAL (42 cm) corresponds to about $25\,X_0$ to ensure that electron and photon showeers are entirely absorbed. On the other hand, the depth of ECAL corresponds to about $1.1\,\lambda_I$, which means that ECAL is effectively a pre-shower detector for HCAL. The total detection area of ECAL is 7.8 m × 6.3 m. The granularity of ECAL is also split into three different regions with effectively the same cell sizes as for SPD and PS.

The ECAL provides a relative energy resolution of

$$\frac{\sigma_E}{E} = \frac{10\%}{\sqrt{E}} + 1\%, \tag{4.1}$$

where the energy E is expressed in GeV.

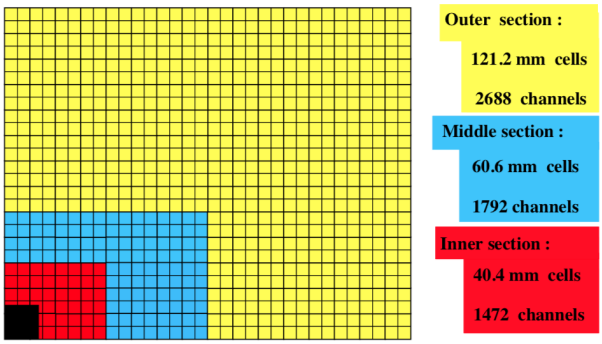

(a) SPD, PS and ECAL.

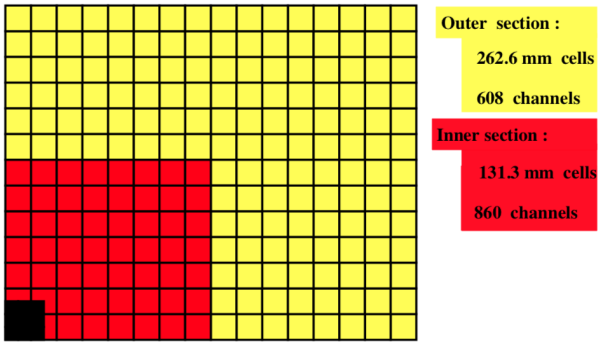

(b) HCAL.

Figure 4.14: Segmentation of LHCb calorimeters [226].

The HCAL is a sampling detector made of scintillating (3 mm thick) and iron absorber (16 mm thick) tiles, which are glued to master plates. Contrary to ECAL geometry, the tiles are oriented along the beam axis. The depth of HCAL is defined by 1.65 m of absorber, which corresponds to about $5.6\,\lambda_I$. The total detection area of HCAL is $8.4\,\text{m} \times 6.8\,\text{m}$. The size of the HCAL cell is 121 mm × 121 mm in the inner region and 263 mm × 263 mm in the outer region. The segmentation of LHCb calorimeters is summarised on Fig. 4.14.

The worse energy resolution of HCAL compared to the one of ECAL is caused by fluctuations of hadron showers and is shown below.

$$\frac{\sigma_E}{E} = \frac{69\%}{\sqrt{E}} + 9\%, \tag{4.2}$$

where the energy E is expressed in GeV. The HCAL is not used for offline measurement of charged hadron energy since it can be measured more precisely using the information from both tracking system and RICH detectors. On the other hand, HCAL can be used for measurement of neutron energy. However, HCAL provides very fast information about

the presence of sizeable transverse energy deposit, which corresponds to the hadron with large p_{T}. This information is used in the first hardware level of the trigger.

4.4.2 RICH detectors

Charged hadron identification plays a crucial role in the reconstruction of charmonium using its hadronic decays. It is thanks to charge hadron ID, that LHCb experiment can reconstruct decays, which are not accessible by ATLAS and CMS experiments.

In LHCb, charged pions, kaons and protons are distinguished with two Ring Imaging CHerenkov detectors (RICH). When a charged particle tranverses a dielectric medium with speed β that is larger than a speed of light in this medium ($1/n$, where n is a refractive index of the medium), a cone of the Cherenkov light is emitted. The angle of the light emission is a function of the particle velocity:

$$cos(\theta_C) = \frac{1}{n\beta}. \tag{4.3}$$

The choice of the radiator is crucial for detector performance. The radiator defines a hadron momentum range, where RICH detector possesses a separating power. The most illustrative separation between hadrons is achieved near the threshold of Cherenkov light emition. As an example, the dependence of the Cherenkov angle on track momentum is shown on Fig. 4.15 for C_4F_{10} radiator.

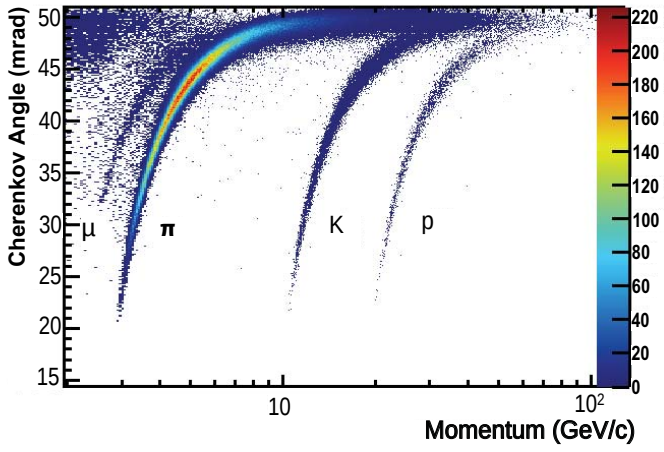

Figure 4.15: Cherekov angle in C_4F_{10} gas as a function of particle momentum for different kinds of charged hadrons [227].

The RICH detector makes use of this radiation by projecting the cone of Cherenkov light onto planar photodetectors by use of a spherical mirrors. The radius of the obtained ring is a function of the particle velocity. Having a measurement of the track momentum from the tracking detector and the measured radius of the associated ring in the RICH detector, one can calculate the mass of the particle. The only charged particles produced that can reach the RICH detectors are e^-, μ^-, π^-, K^-, p and d (and nuclei), thus one categorises the rings according to all possible PID hypothesis. LHCb uses two RICH detectors (RICH1 and RICH2) to distinguish three kinds of charged hadrons: pions, kaons and protons in a wide range of momentum.

The RICH1 is located upstream the magnet before the TT and aims at providing the PID of particles with lower momentum from 1 to 60 GeV, which also includes particles leaving upstream tracks. For that, the silica aerogel and C_4F_{10} gas were used as radiators. For the LHCb Run II, the aerogel was removed from the RICH1 detector, which increased the effective lower limit of momentum for PID provided by RICH1. The amount of material of RICH1 corresponds to only about $0.08\,X_0$.

The RICH2 is located downstream of the magnet and covers higher momentum range from 15 to 100 GeV. In RICH2, the CF_4 gas with a small fraction of CO_2 is used as a radiator. The amount of material of RICH2 corresponds to only about $0.015\,X_0$.

For both RICH1 and RICH2, the spherical mirrors are used to focus the light onto the flat mirror, which then projects the light onto the plane of Hybrid Photodetectors (HPDs). The use of flat mirror allows to reduce the geometrical size of detectors and to locate the photodetector outside the LHCb acceptance. The optical systems are split into two halves: top-bottom for RICH1 and left-right for RICH2. The optical system is shown on Fig. 4.16 at the example of RICH1.

The HPD is a hybrid of PMT and silicon pixel detectors. Firstly, photons produce photoelectrons from the photocathode, then the electrons are accelerated by the electric field of 16 kV in the vacuum tube and then are focused onto silicon pixel array providing a signal multiplication in one step. The pixel size of HPD is 2.5 mm $\times$ 2.5 mm.

For PID a global likelihood variable using information from all PID detectors is used. This variable is a product of the likelihoods from individual detectors. For the case of RICH detectors, the reconstructed rings are compared with the ring expected from the measured track momentum with different charged hadron hypotheses. The combination of constructed likelihoods together with the information from calorimeters and muon detector yields a global likelihood value. The $PIDp$ variable represents the likelihood of proton hypothesis, PIK - kaon hypothesis, etc. Another technique used in the LHCb is based on the multivariate classification by the neural network, which yields alternative

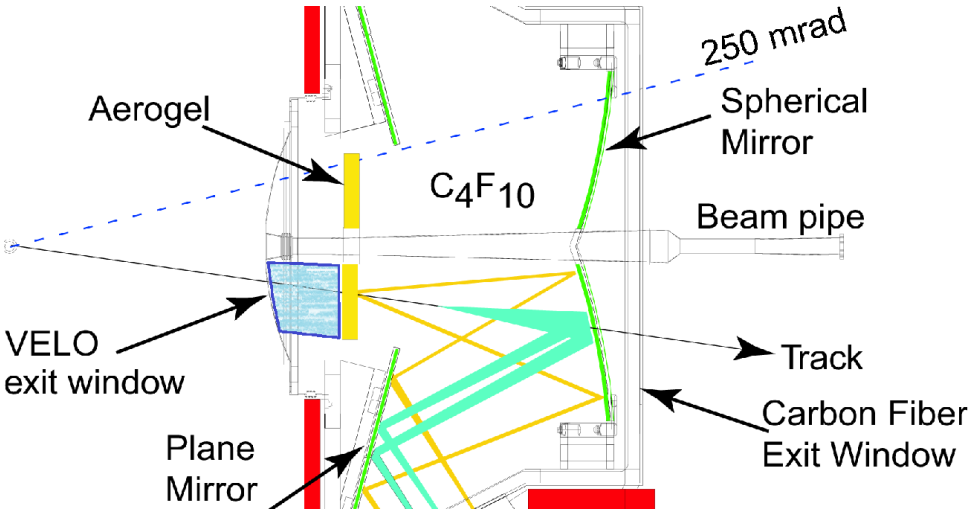

Figure 4.16: Sketch of RICH1 detector [228].

`ProbNN` variable. The latter approach shows a better separation power due to taking into account possible correlations between signals in all detector systems. A performance of charged hadron ID is illustrated on Fig. 4.17. Typically, RICH detectors provide good proton ID for large proton momenta (above 30 GeV), while kaon PID is performant at lower momentum range up to 60 GeV.

To improve the accuracy of PID simulation, the LHCb uses calibration samples of well-known decays. The requirement on the decays used for PID calibration is that they can be selected using only kinematical requirements. For example, decays $\Lambda \to p\pi^-$, $\Lambda_c \to pK^+\pi^-$, $K^0_S \to \pi^+\pi^-$ and $D^{*+} \to (D^0 \to K^-\pi^+)\pi^+$ are used to extract calibration samples for protons, kaons and pions. The *PIDCalib* package makes use of these calibration samples and provides efficiency tables of the PID requirement as a function of kinematical and multiplicity variables. Often, these tables are used in data analyses to estimate total PID efficiency and correct simulation samples.

A performance of charged hadron ID can also be illustrated with the following example. The performance of charged hadron ID is illustrated in Fig. 4.18, which compares the invariant mass spectra of $B^0 \to \pi^+\pi^-$ with and without information from the RICH detectors. If the RICH information is not used, the observed peak is a sum of different b-hadron decay modes to two charged hadrons (left plot), and only RICH PID is providing relatively clean and narrow $B^0 \to \pi^+\pi^-$ sample (right plot).

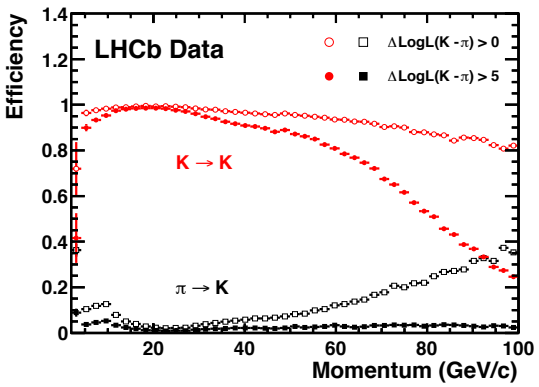

(a) Kaon PID efficieny (red) and $\pi \rightarrow K$ misidentification (black).

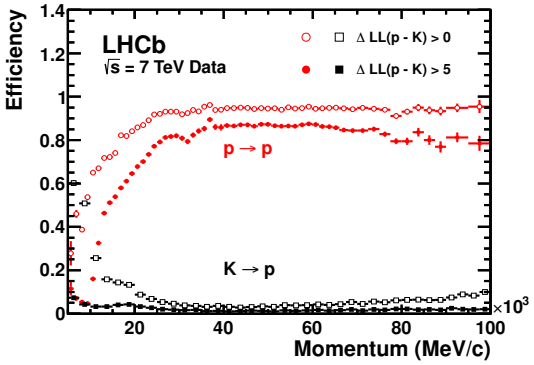

(b) Proton PID efficieny (red) and $K \rightarrow p$ misidentification (black).

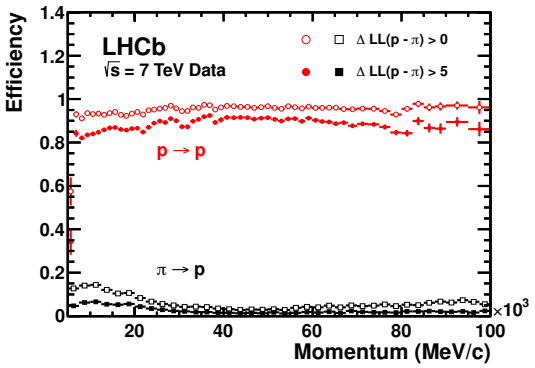

(c) Proton PID efficieny (red) and $\pi \rightarrow p$ misidentification (black).

Figure 4.17: Performance of charged hadron ID [228].

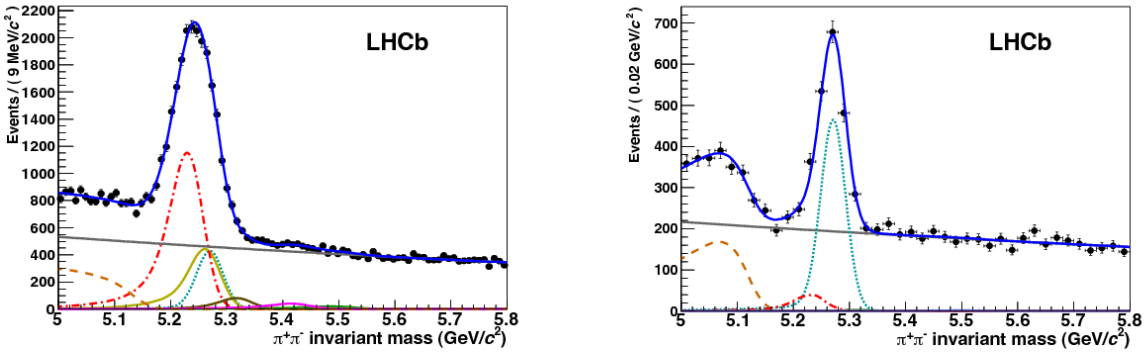

(a) The $\pi^+\pi^-$ invariant mass spectrum without RICH information.

(b) The $\pi^+\pi^-$ invariant mass spectrum with RICH information.

Figure 4.18: Comparison of the $B^0 \to \pi^+\pi^-$ candidates invariant mass distribution with (right) and without (left) information from RICH detectors [227]. The contributions from different b-hadron decay modes ($B^0 \to K^+\pi^-$ red dashed-dotted line, three body B^0 decays orange dashed-dashed, $B_s^0 \to K^+K^-$ yellow line, $B_s^0 \to K^+\pi^-$ brown line, $\Lambda_b^0 \to pK^-$ purple line, $\Lambda_b^0 \to p\pi^-$ green line), are eliminated by requiring a positive identification of pions, kaons and protons and only the signal and two background contributions remain visible in the plot on the right. The grey solid line is the combinatorial background.

4.4.3 Muon detector

The muon detector is designed to provide muon particle identification. For studies of charmonium states via their decays to hadrons, the information from the muon detector is not used. However, a robust muon identification is crucial for analyses involving, for example, $J/\psi \to \mu^+\mu^-$ or $\psi(2S) \to \mu^+\mu^-$ decays.

The muon detector consists of five stations M1-5. The first station M1 is located between the RICH2 detector and the calorimeters to improve track matching between tracking and muon detectors, while the stations M2-5 are located downstream the HCAL. The size of stations is increasing with increasing the distance from the interaction point. The sketch of the muon detector is shown on Fig. 4.19. The stations are divided into

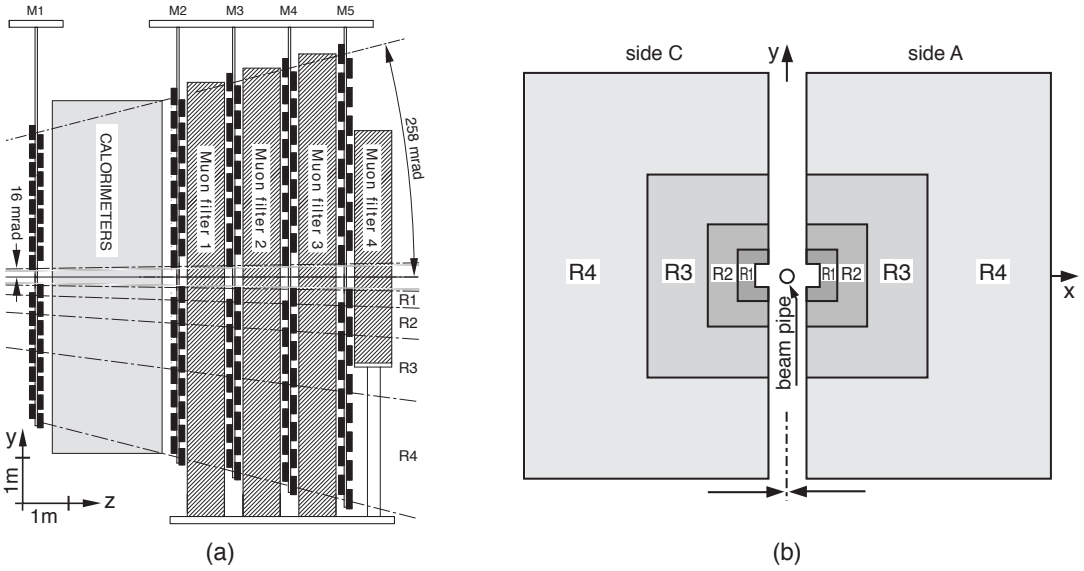

Figure 4.19: The LHCb muon detector [229].

four regions R1-4. The linear scale of the next region is twice bigger than the scale of the previous one. The R2-4 regions are made of Multi-Wire Proportional Chambers (MWPC), the central R1 region is made of Gas Electron Multipliers (GEM) due to large particle fluxes in the central region and higher radiation resistance of GEM detectors. The chambers are composed of logical pads of different dimensions, depending on the distance from the beam axis and the from interaction point. The sizes of chambers in the inner regions vary between 6.3 mm × 31.3 mm in M2 station and 31 mm × 39 mm in the last station, in order to maintain the occupancy similar in each region. The MWPCs uses a mixture of Ar, CO_2 and CF_4 gases.

Between the M2-5 stations, iron absorber of thickness of 80 cm thick are placed, which

depth corresponds to $15\lambda_I$. The acceptance of the muon detector is similar to that of the trackers. The muons stations are also used in the online (HLT1) and offline (HLT2) trigger for fast muon identification. Note, that only muon identification is used in the online trigger. The LHCb muon system is described in more details in Ref. [229].

4.5 Trigger and data processing

A flexible trigger system of LHCb consists of low-level L0, HLT1 software and off-line HLT2 levels [230]. The 40 MHz rate of LHC bunch crossings corresponds to roughly 10 MHz of interactions visible by LHCb. The hardware trigger L0 reduces this rate to about 1 MHz. Then the online software trigger selects events with a rate of above 100 kHz. Finally, the output rate of the offline HLT2 trigger decisions is about 10 kHz, which is a storable event rate.

The trigger schemes used during the LHCb Run I and II are shown on Fig. 4.20.

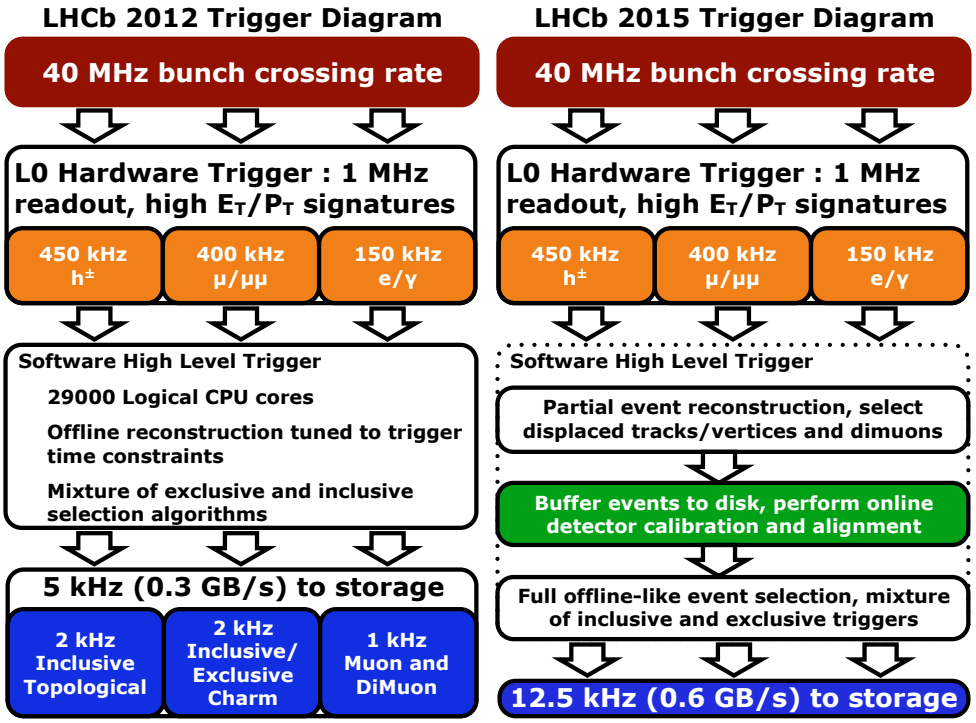

Figure 4.20: The scheme of the LHCb trigger for (left) Run I and (right) Run II.

The lowest level L0 trigger uses a fast information from calorimeter, muon and VELO detectors. Thanks to L0 trigger, the event rate is reduced to a level appropriate for a fast analysis of the information from other detector systems. The HLT1 trigger performs a

partial event reconstruction including simplified tracks and vertex reconstruction further reducing the rate. The HLT2 trigger performs a full event reconstruction including a complex particle identification needed to perform a selection of certain exclusive and inclusive b or c decays. The events or candidates passing HLT2 trigger are then stored to the disk. The bandwidth of the software trigger is limited by the available computing resources. The trigger requirements are adjusted in order to split the available bandwidth between different physics cases in an optimal way.

The following positive trigger decisions are defined:

- Trigger On Signal (TOS) - the final reconstructed candidate is the one satisfying trigger requirement;
- Trigger Independent from Signal (TIS) - another candidate in the event triggered the decision;
- Trigger Decision (DEC) - a logical sum of TIS and TOS.

4.5.1 Hardware L0 trigger

The L0 trigger is synchronized with the LHC bunch crossing. Depending on the state of the Front-End electronics, the L0 can either pass or throttle the event satisfying the trigger requirement. The L0 trigger comprises three different types of trigger decisions.

The `L0_Muon` and `L0_DiMuon` are based on the information from muon detector to select events containing muons with sufficient transverse momentum. The trigger based on the information from calorimeters are `L0_Hadron`, `L0_Electron` or `L0_Photon`. The `L0_PileUp` is used for luminosity measurement.

The Muon trigger uses L0 processors connected to each quadrant of the muon detector. Processors perform a search among the tracks with $p_{\mathrm{T}} > 500$ MeV and identify two tracks with largest p_{T} in the corresponding quadrant. The `L0_Muon` sets a threshold on the minimum transverse momentum of the track with a typical value of about 1.5 GeV, while the `L0_DiMuon` sets a threshold on the minimal product of two muon tracks p_{T} with a typical value of about $(1.3\ \mathrm{GeV})^2$. The trigger also sets a threshold on the maximal number of hits in the SPD detector to reject events producing an excessively high level of combinatorial background. The transverse momentum is measured using Muon detector only, which provides a p_{T} resolution of about 20%. All M1-5 stations are required to have track hits. The presence of M1 station, located upstream the calorimeters, is essential for the p_{T} measurement at the L0 trigger level. This trigger is especially important for studies involving reconstruction of resonances decaying into a pair of muon (e.g. J/ψ,

$\psi(2S)$, $\Upsilon(1S)$, $\Upsilon(2S)$). Notably, this trigger is used for J/ψ and $\psi(2S)$ production and polarisation measurements.

The `L0_PileUp` trigger uses the information from two r-sensors of the VELO detector. This trigger identifies events with single and multiple interactions.

The Calorimeter trigger is based on the transverse energy, E_T, deposit calculation in the ECAL or HCAL. The transverse energy is computed from clusters of 2×2 cells located in the same zone. Each of the calorimeters front-end board selects the highest E_T among 32 clusters. The `L0_Photon` requires a presence of E_T deposit in ECAL above the threshold of about 2.5 GeV with a matching signal from PS and no signal from the corresponding cells of SPD. The `L0_Electron` requirement is similar, but contrary to `L0_Photon`, at least one SPD cell hit should be present in a region corresponding to PS cells hits. The `L0_Hadron` requires a presence of E_T deposit in HCAL and the matching cluster of ECAL higher than the threshold of about 3.5 GeV.

The `L0_Hadron` trigger is used in the analyses described in Chapters 5 and 5.6. The efficiency of `L0_Hadron` trigger for several hadronic B- and D-meson decay modes is shown on Fig. 4.21. As expected, the efficiency is increasing with the transverse momentum.

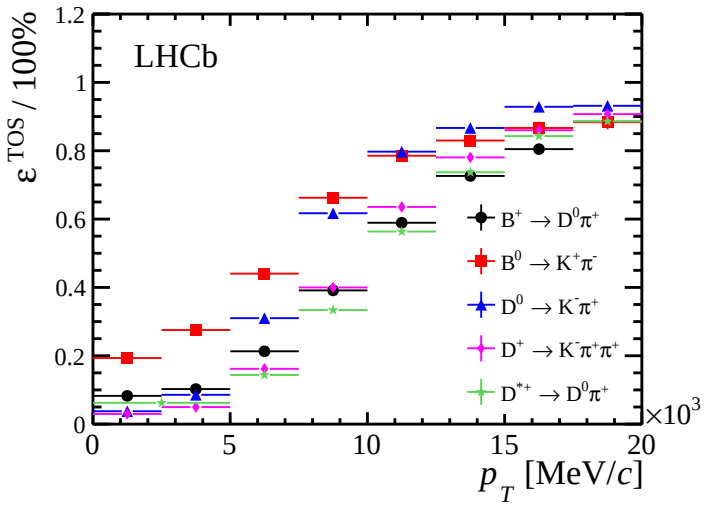

Figure 4.21: The TOS efficiency of `L0_Hadron` trigger for $B^+ \to D^0\pi^+$, $B^0 \to K^+\pi^-$, $D^0 \to K^+\pi^-$, $D^+ \to K^-\pi^+\pi^+$ and $D^{*+} \to D^0\pi^+$ decays.

4.5.2 Software trigger and stripping

HLT1

The event passing the decision of any of the L0 triggers, it is transferred to the Event Filter Farm, which is used to execute the HLT1 applications. At the level of HLT1, the track and vertex reconstruction is performed without a full event reconstruction. The idea of HLT1 is to find tracks with high p and p_{T} and to search for vertices with a reasonable fit quality. In addition, the tracks with large IP significance are selected to identify b- and c-decay candidates. Besides, the track and vertex reconstruction, a fast muon PID is performed at the HLT1 level. This is done by extrapolating VELO tracks to muon stations and comparing the signal from muon detector. The information from TT is used for better determination of track p_{T}. The track reconstruction is optimised in order to achieve a fast execution.

Charged hadron ID using RICH detectors requires a reconstruction of the rings associated with tracks. The timing of the rings reconstruction is similar to that needed for tracking. However, fast algorithms of rings reconstruction are available. Unfortunately, the PID using RICH information is not performed at the HLT1 trigger level. The studies of any prompt decays to hadrons would benefit from the PID at the HLT1 level with a dramatic decrease of the HLT1 bandwidth. Due to limited timing of the HLT1, the PID would require the RICH calibration constants to be available online, which is not the case for the existing implementation of the HLT1 trigger.

A similar situation takes place for the reconstruction of the downstream tracks. The studies of long-lived particles and long-lived baryons such as Λ and Ξ would benefit from the downstream track reconstruction with increased total efficiency.

There are two HLT1 trigger lines dedicated to prompt charmonium studies using decays to hadrons. The `Hlt1DiProtonDecision` aims at selecting prompt and non-prompt $p\overline{p}$ pairs. This trigger line selects hadron tracks with large p_{T}, which form a good quality vertex. The p_{T} of the proton-antiproton system is required to be larger that 6.5 GeV. More details about the `Hlt1DiProton` requirements are given in Chapter 5. Initially, this trigger line was created to study prompt $\eta_c(1S)$ mesons. For the data taking in 2018, I suggested the line splitting into two lines `Hlt1DiProtonLow` covering $p\overline{p}$ invariant mass range of 2.8-3.3 GeV and `Hlt1DiProtonHigh` covering $p\overline{p}$ invariant mass range of 2.8-3.3 GeV. Besides, the requirement on the minimum transverse momentum of the proton-antiproton system was reduced to 5.5 GeV. This change was implemented in order to search for prompt $\eta_c(2S)$ mesons with a possible prompt production measurement predicted by theorists. The total rate of `Hlt1DiProton` lines in 2018 was about 10 kHz.

Another trigger line prepared for 2018 data taking is devoted to prompt charmonium decays to $\phi\phi$ (`Hlt1Ccbar2PhiPhi`). This line selects four hadrons with a large p_{T}. Pairs of hadrons with a kaon mass hypothesis are restricted to have a good vertex with an invariant mass compatible with that of $\phi(1020)$ meson. The $\phi\phi$ system is also required to form a good quality common vertex. The effective requirement on the $\phi\phi$ system p_{T} is about $p_{\mathrm{T}} > 5$ GeV. Following the observation of the $\eta_c(2S) \to \phi\phi$ described in Chapter 5.6, this line is also designed for studies of prompt charmonium decays to $\phi\phi$. The η_c, $\eta_c(2S)$ and χ_{c0} states are targeted. The total rate of `Hlt1Ccbar2PhiPhi` lines in 2018 was about 1 kHz.

The `Hlt1TrackAllL0` trigger line is meant to be "universal" for most analyses of b-hadron decays. The outcome of this trigger line is registered for all L0 trigger decisions. The selection requires to have a track with IP larger than 0.1 mm and transverse momentum larger than 1.6 GeV. In the LHCb Run II this line was split into two: `Hlt1OneTrackMVA` and `Hlt1TwoTrackMVA`, where a multivariate classifier was used in order to distinguish events with one and two displaced tracks, respectively.

HLT2

The offline trigger HLT2 performs a more complete event reconstruction. Events passing the HLT1 decision are stored in the buffer for further execution of the HLT2 algorithms execution. Information from all detector systems available at the HLT2 level.

At this stage specialised trigger selections for a number of inclusive and exclusive final states are applied. They are meant to include all types of events of interest for LHCb. Events passing the HLT2 decision are then stored.

The HLT2 uses more accurate track and vertex reconstruction compared to the one of HLT1 also using information from online alignment and detector calibration. The selections applied at the HLT2 level are more complex and are targetting specifical cases. The deferred trigger, developed for RunII, allows HLT an overcommitment of 20-30%. Using a 1 PB storage at the farm, the deferred trigger then runs between the LHC fills. Using a deferred trigger made it possible to lower track reconstruction thresholds. The HLT2 in the configuration applied in Run I writes about 5 kHz to the storage, including about 2 kHz of inclusive b-hadron candidates, about 2 kHz of inclusive charm candidates and about 1 kHz decay signatures with muons.

Trigger lines selecting prompt $p\overline{p}$ and $\phi\phi$ decays of charmonia are applied similarly as for HLT1. In addition to kinematic restrictions, the PID using RICH information for protons and kaons is required to reject specific decays producing a hadronic background. The

trigger line selecting prompt $p\bar{p}$ pairs will be used in the analysis described in Chapter 5.

A complex universal HLT2 trigger lines select multibody decays of b-hadrons. These lines use the topology of event and are named `Hlt2Topo(2,3,4)BodyBBDT`. The selection relies on the presence of high-p_{T} displaced track, which contributed to a good quality vertex significantly displaced from PV. The remaining tracks of the vertex are required to have a large p_{T} sum. Then a sample of simulated b-hadron inclusive decays was used to traine the multivariate classification based on a Bonsai Boosted Decision Tree [231]. The most powerful variable used in the classification is the corrected mass defined as $M_{corr} = \sqrt{M^2 + p_{\mathrm{T}miss}^2} + p_{\mathrm{T}miss}$, where M is an invariant corresponding to a vertex and $p_{\mathrm{T}miss}^2$ is an observed missing momentum due to mismatching between the direction of reconstructed momentum of decaying particle and the direction defined by PV and decay vertex. In the thesis, this HLT2 trigger line is used for a precision $\eta_c(1S)$ mass determination discussed in Chapter 8 and also in the analysis described in Chapter 5.6.

Data processing and stripping

The total amount of raw data recorded by LHCb corresponds to approximately 1 Tb/s, which is impossible to store with available computing resources and techniques. Therefore, raw events passing trigger requirements are stored in terms of reconstructed charged and neutral tracks, PID information in Data Summary Tape (DST) files. The obtained DST files are stored and reduced into reduced DST (rDST) files by eliminating unnecessary information from the event. The data stored in rDST format allows to measure momentum of tracks, positions of PV and decay vertices, etc. The rDST files are then reprocessed using a set of preselection criteria (Stripping lines), which further reduces the amount of data. In order to take into account correlations between different stripping lines, during the stripping, the data is grouped into several streams according to the event topology, final states, PID, etc. The stripped data is then saved and replicated at special GRID storages available for LHCb users. In LHCb Run II, a part of the data passing HLT2 decision is stored directly without offline stripping procedure to the disk into so-called Turbo streams.

Chapter 5

Study of $\eta_C(1S)$ production using its decay to $p\overline{p}$ at $\sqrt{s}$ =13 TeV

The pioneering LHCb measurement of the η_c at $\sqrt{s}$ =7 and 8 TeV has been performed using the $p\overline{p}$ channel. Due to the challenging background level and limited trigger bandwidth, the precision of the measurement and available fiducial region were limited. Despite that, the obtained η_c production measurement is a perfect example of how even imprecise measurement can challenge the theory. Besides the physical result, it demonstrated the accessibility of the promptly and non-promptly produced η_c mesons by the LHCb experiment. To date, the $p\overline{p}$ decay channel is the most popular for studies requiring the η_c reconstruction at LHCb. This chapter documents the measurement of the η_c production cross-section in pp collisions at $\sqrt{s}$ =13 TeV using the $\eta_c \to p\overline{p}$ decay. The analysis validates the η_c production measurement at $\sqrt{s}$ =7 and 8 TeV and yields the first η_c prompt production measurement at $\sqrt{s}$ =13 TeV. The obtained result is more precise than the one obtained at $\sqrt{s}$ =7 and 8 TeV. At this point, the measurements of the η_c production using its decay to $p\overline{p}$ at LHCb remain the only available η_c production measurements at hadron colliders.

After the analysis setup introduced in Section 5.1, the data and simulation samples are discussed in Section 5.2. Selection criteria and signal efficiencies are addressed in Section 5.3. The two analysis techniques are described in Sections 5.4 and 5.5. The results are discussed in Section 5.6.

5.1 Analysis setup

For a measurement of the η_c prompt production, a pseudo-proper lifetime is calculated and modeled similarly to the analysis described in Ref. [94] in order to distinguish between prompt production and b-decays production (t_z-*fit technique*). The production of the η_c in b-hadron decays is performed using *separation technique* used in Ref. [13]. The ratio of the η_c and J/ψ production cross-sections is measured in bins of $p_{\rm T}$ and then the η_c production is derived using measured J/ψ production at LHCb [94]. The ratio of the η_c and J/ψ production can be expressed as

$$\begin{aligned} \frac{\sigma^{prompt}_{\eta_c}}{\sigma^{prompt}_{J/\psi}} &= \frac{N^{prompt}_{\eta_c}}{N^{prompt}_{J/\psi}} \times \frac{\epsilon_{J/\psi}}{\epsilon_{\eta_c}} \times \frac{\mathcal{B}_{J/\psi\to p\overline{p}}}{\mathcal{B}_{\eta_c\to p\overline{p}}}, \\ \frac{\sigma^{b}_{\eta_c}}{\sigma^{b}_{J/\psi}} = \frac{\mathcal{B}_{b\to\eta_c(1S)X}}{\mathcal{B}_{b\to J/\psi X}} &= \frac{N^{b}_{\eta_c}}{N^{b}_{J/\psi}} \times \frac{\epsilon_{J/\psi}}{\epsilon_{\eta_c}} \times \frac{\mathcal{B}_{J/\psi\to p\overline{p}}}{\mathcal{B}_{\eta_c\to p\overline{p}}}, \end{aligned} \tag{5.1}$$

where $\sigma^{prompt}_{\eta_c(J/\psi)}$ is the prompt production cross-section of η_c (J/ψ), $\sigma^{b}_{\eta_c(J/\psi)}$ is the production cross-section of η_c (J/ψ) in inclusive b-decays, $\mathcal{B}_{b\to\eta_c(J/\psi)X}$ is the inclusive branching fraction of the b-quark decay to η_c (J/ψ), $N^{prompt}_{\eta_c(J/\psi)}$ is the yield of prompt η_c (J/ψ) candidates, $N^{b}_{\eta_c(J/\psi)}$ is the yield of η_c (J/ψ) from inclusive b-decays, $\frac{\epsilon_{J/\psi}}{\epsilon_{\eta_c}}$ is the ratio of total efficiencies to reconstruct, trigger and select $J/\psi\to p\overline{p}$ and $\eta_c\to p\overline{p}$ decays, $\mathcal{B}_{J/\psi\to p\overline{p}}$ and $\mathcal{B}_{\eta_c\to p\overline{p}}$ are the branching fractions of the $J/\psi\to p\overline{p}$ and $\eta_c\to p\overline{p}$ decays from Ref. [188], respectively.

Using the measurement of J/ψ prompt differential production cross-section and the J/ψ production in inclusive b-decays performed using the $J/\psi\to\mu\mu$ decay from Refs. [94, 188], the η_c production can be extracted as

$$\begin{aligned} \sigma^{prompt}_{\eta_c} &= \sigma^{prompt}_{J/\psi} \times \frac{N^{prompt}_{\eta_c}}{N^{prompt}_{J/\psi}} \times \frac{\epsilon_{J/\psi}}{\epsilon_{\eta_c}} \times \frac{\mathcal{B}_{J/\psi\to p\overline{p}}}{\mathcal{B}_{\eta_c\to p\overline{p}}}, \\ \sigma^{b}_{\eta_c} &= \sigma^{b-decays}_{J/\psi} \times \frac{N^{b}_{\eta_c}}{N^{b}_{J/\psi}} \times \frac{\epsilon_{J/\psi}}{\epsilon_{\eta_c}} \times \frac{\mathcal{B}_{J/\psi\to p\overline{p}}}{\mathcal{B}_{\eta_c\to p\overline{p}}}, \\ \mathcal{B}_{b\to\eta_c(1S)X} &= \mathcal{B}_{b\to J/\psi X} \times \frac{N^{b}_{\eta_c}}{N^{b}_{J/\psi}} \times \frac{\epsilon_{J/\psi}}{\epsilon_{\eta_c}} \times \frac{\mathcal{B}_{J/\psi\to p\overline{p}}}{\mathcal{B}_{\eta_c\to p\overline{p}}}. \end{aligned} \tag{5.2}$$

Both prompt production and production in b-decays are measured using two different techniques: t_z-*fit technique* and *separation technique*. The ratio of the signal event yield for the η_c prompt production measurement is quoted using t_z-*fit technique* technique, while the *separation technique* is used for a cross-check. The η_c production in inclusive b-hadron decays is quoted by *separation technique* and t_z-*fit technique* is used for a cross-check.

5.2 Data sample, trigger and simulation

This analysis uses the pp collision data recorded by the LHCb experiment at $\sqrt{s} = 13$ TeV with an integrated luminosity $\int \mathcal{L}dt \approx 2.0\,\text{fb}^{-1}$ accumulated in 2015 and 2016. All detector subsystems were stable and fully operational during the data taking period corresponding to the present analysis. For data processing, the reconstruction version Reco15a (Reco16), and stripping version Stripping24 (Stripping28) were used for 2015 (2016) data.

The basic level L0 Hadron (`L0HadronDecision_TOS`) trigger is applied. The candidates are required to be selected (`TOS`) by dedicated trigger lines of HLT1 and HLT2, `Hlt1DiProtonDecision_TOS`, `Hlt2DiProtonDecision_TOS` (`Hlt2CcDiHadronDiProtonDecision_TOS`) are used for the analysis of charmonium production for both 2015 (2016) data.

For the η_c mass measurement, a low-background data sample with larger statistics selecting $b \to \eta_c$X is used. In the data sample, the basic level `L0 Hadron decision` (L0HadronDecision_TOS) trigger is applied. The trigger lines `TOS` of HLT1, `Hlt1(Two)TrackMVADecision_TOS`, and HLT2, `Hlt2Topo(2,3,4)BodyDecision_TOS` are used.

The Monte Carlo (MC) samples used to study the η_c and the J/ψ mass resolution, as well as the background contribution from the $J/\psi \to p\bar{p}\pi^0$ channel are summarised in the Table 5.1. In the simulation, pp collisions are generated using Pythia [232, 233] with a specific LHCb configuration [234]. Decays of hadronic particles are described by EvtGen [235], in which final-state radiation is generated using Photos [236]. The interaction of the generated particles with the detector, and its response, are implemented using the Geant4 toolkit [237, 238] as described in Ref. [239]. For all simulation samples

Sample	Sample size
prompt η_c	2015: 0.62 M
	2016: 2.40 M
η_c from-b	2015: 0.26 M
	2016: 1.01 M
prompt J/ψ	2015: 0.67 M
	2016: 2.41 M
J/ψ from-b	2015: 0.19 M
	2016: 0.60 M
$J/\psi \to p\bar{p}\pi^0$	2015: 0.80 M
	2016: 3.01 M

Table 5.1: Simulated samples.

a phase-space decay model is used, the daughter proton and antiproton are required to flight into detector's acceptance and to have transverse momentum of $p_{\mathrm{T}}(p) > 0.9\,\mathrm{GeV}$ to speed-up MC production. For MC samples of prompt J/ψ, J/ψ from b-decays and $J/\psi \to p\overline{p}\pi^0$, the J/ψ meson was generated without polarisation. The prompt η_c mesons are generated as J/ψ with modified mass and width according to known values from Ref. [188]. The latter is done in order to optimize MC samples generations since generation of promptly produced η_c mesons is much slower compared to that of J/ψ. For all MC samples reconstructed signal candidates and their daughter particles are required to match the generated ones.

5.3 Event selection

Due to large number of random $p\overline{p}$ combinations originated from PV, the background conditions and the limited trigger bandwidth complicate the analysis. In order to achieve a tolerable trigger rate, strongly selective requirements, including proton identification, are applied already at the trigger level.

The η_c and J/ψ candidates are reconstructed from a pair of oppositely charged tracks identified as protons by the LHCb detector. Both proton track candidates are required to have a good quality of track reconstruction, $\chi^2/\mathrm{ndf} < 2.5$ and probability that track consists of random hit combinations (ghost probability) less than 0.2. In order to suppress combinatorial background and reduce the trigger bandwidth, the proton tracks are required to have transverse momenta larger than 1.9 GeV and momenta larger than 12.5 GeV. The distance of closest approach between two tracks is required to be less than 0.1 mm. The transverse momentum of the proton-antiproton system is required to be higher than 6.5 GeV, and charmonium candidate vertex quality $\chi^2/\mathrm{ndf} < 4$. Trigger specifically rejects high multiplicity events, causing excessively high combinatorial background, by requiring the SPD multiplicity to be less than 300.

A sample enriched in true protons have to be selected already at the trigger level. For that, the information from RICH detectors is used at the trigger level to separate protons from pions and kaons. The proton identification requirements $\Delta \log \mathcal{L}^{p-K} > 10$ and $\Delta \log \mathcal{L}^{p-\pi} > 20$ are used at the level of the HLT2.

Further selection performed by a dedicated stripping line (`StrippingCcbar2PpbarLineDecision`) applies almost the same requirements as in the trigger selection. The only exception is a more tight PID requirement of $\Delta \log \mathcal{L}^{p-K} > 15$. Trigger settings of dedicated `Hlt1DiProton` line were tightened before

	Variable	HLT1	HLT2	Stripping	Offline selection
Trigger		L0Hadron	Hlt1DiProton	–	L0Hadron_TOS Hlt1DiProton_TOS Hlt2DiProton_TOS
Protons	p_{T}, GeV	> 1.9	> 1.9	> 1.95	> 2.0
	p, GeV	> 12.5		> 10.0	> 12.5
	p_{T}/p	> 0.0366			> 0.0366
	Track χ^2/NDF	< 2.5	< 3.0	< 4.0	< 2.5
	Ghost probability	< 0.2			< 0.2
	$\Delta \log \mathcal{L}^{p-\pi}$	–	> 20	> 20	> 20
	$\Delta \log \mathcal{L}^{p-K}$	–	> 10	> 15	> 15
$p\overline{p}$	p_{T}, GeV	> 6.5	> 6.5	> 6.0	> 6.5
	Vertex χ^2/ndf	< 4	< 9		< 4.0
	Vertex DOCA, mm	< 0.1			< 0.1
	Mass, GeV/c	$2.8 - 3.3$	$2.8 - 4.0$	$2.8 - 4.0$	$2.85 - 3.25$
	SPD multiplicity	< 300	< 300	< 300	< 300

Table 5.2: Trigger, stripping and offline selection criteria.

2016 data taking. When combining 2015 and 2016 data samples, more tight cuts, matching trigger requirements from 2016 settings, are used in the offline selection. Additional cuts are applied to cut off tails of distributions created by mismatching between HLT1 and HLT2 requirements to avoid unnecessary edge effects.

The set of selection criteria used in the trigger, stripping and offline selection are almost identical, as illustrated in Table 5.2.

Since the masses of η_c and J/ψ states are close to each other and kinematic distributions in $J/\psi \to p\overline{p}$ and $\eta_c \to p\overline{p}$ decays are similar, one expects similar reconstruction, trigger and stripping efficiencies. The efficiency ratio of $J/\psi \to p\overline{p}$ and $\eta_c \to p\overline{p}$ is determined using simulation samples to be

$$\frac{\epsilon_{J/\psi}}{\epsilon_{\eta_c}} = 1.00 \pm 0.02, \tag{5.3}$$

where the uncertainty is due to MC sample sizes. Note that, uncertainty on efficiency ratio gives a negligible contribution to a total systematic uncertainty (see Sections 5.4.3 and 5.5.2). Effect of the J/ψ meson polarisation is taken into account in the evaluation of systematic uncertainty. The efficiency ratio is also extracted in bins of p_{T} with no significant deviation from unity observed. No significant difference is found between efficiencies of prompt charmonia production and charmonia production in inclusive b-decays. The efficiency ratio for prompt and for inclusive b-decays production in bins of p_{T}

is shown on Fig.5.1.

The PID efficiency ratio for η_c and J/ψ has been cross-checked by applying tighter PID cuts on MC. For this cross-check the selection requrements $[PIDp > 25\,\&\,(PIDp - PIDK) > 15]$, $[PIDp > 20\,\&\,(PIDp - PIDK) > 20]$ and $[PIDp > 25\,\&\,(PIDp - PIDK) > 20]$ are used. Comparison of efficiency ratios for different PID selection requirements is shown in Table 5.3. No significant effect is observed, and the result is considered to be stable against PID requirement variations.

PID requirement		$\epsilon_{J/\psi}/\epsilon_{\eta_c}$
(nominal)	$PIDp > 20\,\&\,(PIDp - PIDK) > 15$	1.00 ± 0.02
	$PIDp > 25\,\&\,(PIDp - PIDK) > 15$	0.99 ± 0.02
	$PIDp > 20\,\&\,(PIDp - PIDK) > 20$	1.00 ± 0.02
	$PIDp > 25\,\&\,(PIDp - PIDK) > 20$	0.99 ± 0.02

Table 5.3: The J/ψ and η_c efficiency ratio from MC for different PID requirements.

Another cross-check of PID efficiency is done by estimating PID efficiency ratio using the PID calibration samples within *PIDCalib* package. The PID efficiency map is extracted using calibration samples of $\Lambda \to p\pi^-$ for LHCb Run II data and then applied to the η_c and J/ψ MC samples. The extracted PID efficiency ratio is compared to PID efficiency ratio extracted from MC samples as

$$\epsilon^{PID,PIDCalib}_{J/\psi}/\epsilon^{PID,PIDCalib}_{\eta_c} = 0.98 \pm 0.04,$$
$$\epsilon^{PID,MC}_{J/\psi}/\epsilon^{PID,MC}_{\eta_c} = 0.99 \pm 0.04$$

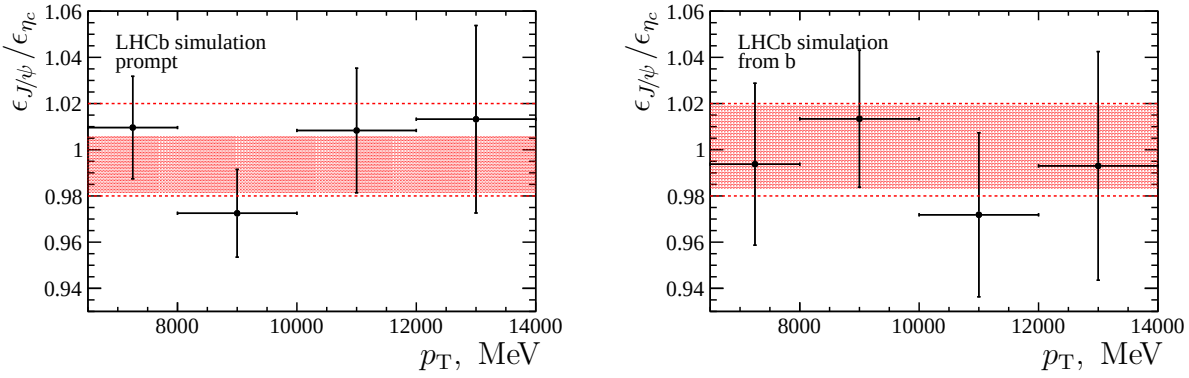

(a) The efficiency ratio for prompt production.

(b) The efficiency ratio for production in b-decays.

Figure 5.1: The J/ψ to η_c total efficiency ratio in bins of p_T. Red boxes show the total efficiency ratio. Red dashed lines illustrate the efficiency ratio uncertainty considered in the analysis.

No significant difference of J/ψ and η_c efficiency ratio from unity is observed for both performed cross-checks.

Below, two different techniques are employed to measure the η_c production cross-section.

5.4 t_z-fit technique

In order to distinguish between promptly produced charmonium candidates and charmonium candidates from b-hadron decays, the yields of J/ψ and η_c are extracted in bins of pseudo-proper lifetime t_z. The t_z value is defined as

$$t_z = \frac{(z_d - z_p)M_{p\overline{p}}}{p_z}, \tag{5.4}$$

where z_p and z_d are the z-coordinates of PV and charmonium candidate decay vertices, respectively, $M_{p\overline{p}}$ is the reconstructed charmonium mass and p_z is the longitudinal component of its momentum.

The yields of J/ψ and η_c candidates are determined from simultaneous extended binned maximum-likelihood fit to the $M(p\overline{p})$ distribution. Fit of the invariant mass is performed simultaneously in 28 bins of $[p_{\mathrm{T}};\, t_z]$. The bin edges of charmonium p_{T} are [6.5, 8.0, 10.0, 12.0, 14.0] expressed in GeV and the t_z bin edges are [-10.0, -0.125, -0.025, 0., 0.2, 2., 4., 10.] expressed in ps. In the simultaneous fit, the masses of J/ψ and η_c mesons and the resolution parameter, described below, are common free fit parameters throughout all 28 bins.

The extracted yields in bins $[p_{\mathrm{T}};\, t_z]$ together with their statistical uncertainties are fitted to t_z in 4 bins of p_{T} to distinguish promptly produced charmonia and charmonia produced in inclusive b-decays. For that the simultaneous integral χ^2 fit was used, which finds the bin centre-of-mass according to the shape of the fit function. The latter is important for sharp functions as it is the case for the fit to t_z. From the fit to t_z distribution, the ratios of prompt η_c and prompt J/ψ yields $\frac{N^{prompt}_{\eta_c}}{N^{prompt}_{J/\psi}}$, and η_c yields from b-decays and J/ψ yields from b-decays $\frac{N^{b}_{\eta_c}}{N^{b}_{J/\psi}}$, are extracted together with their uncertainties in four bins of charmonium p_{T}.

To measure total η_c production cross-section the same procedure is implemented with p_{T} integrated over the range $6.5\,\mathrm{GeV} < p_{\mathrm{T}} < 14.0\,\mathrm{GeV}$.

5.4.1 Fit to the invariant mass

The signal shape is defined by the detector resolution and the natural width in the case of the η_c resonance. The detector resolution effect on invariant mass distribution is described by a double Gaussian function. Parameters of double Gaussian are extracted from simultaneous unbinned maximum-likelihood fit of four MC samples (prompt η_c, prompt J/ψ, η_c from b-decays and J/ψ from b-decays) to $M_{p\overline{p}} - M^{Gen}_{p\overline{p}}$, where $M_{p\overline{p}}$ is the

reconstructed mass and $M_{p\bar{p}}^{Gen}$ is the generated mass. The resolution ratio for the η_c and J/ψ peaks is fixed to the value from simulation. Corresponding systematic uncertainties are estimated in section 5.4.3.

The $M_{p\bar{p}} - M_{p\bar{p}}^{Gen}$ distribution for all MC samples together with the fit curve are shown on the Fig. 5.2. In the fit to MC samples the same resolution models for prompt η_c (J/ψ) and η_c (J/ψ) from b-decays are used. The ratio of J/ψ and η_c resolutions is introduced as a ratio of η_c and J/ψ narrow gaussian widths $\sigma_n(\eta_c)/\sigma_n(J/\psi)$. The mean values of η_c and J/ψ double Gaussians are different independent fit parameters. The ratio of double Gaussian width σ_n/σ_w and the fraction of narrow gaussian component f_n are common fit parameters for all four MC samples. Simultaneous fit shows good description of $M_{p\bar{p}} - M_{p\bar{p}}^{Gen}$ for all samples.

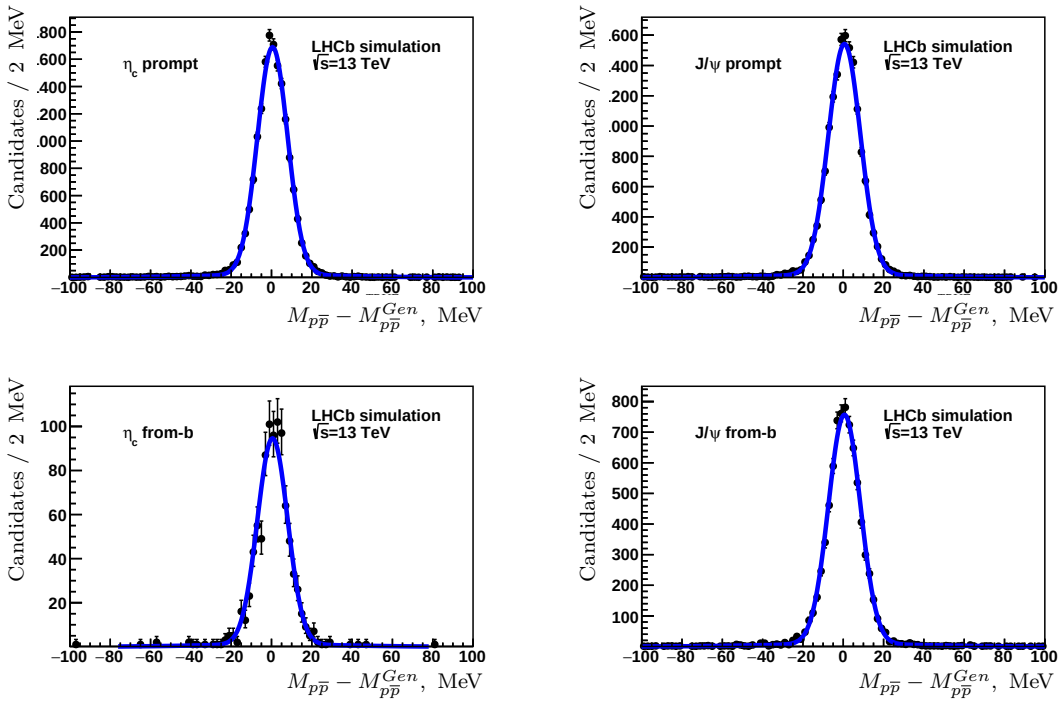

Figure 5.2: Distribution of the $M_{p\bar{p}} - M_{p\bar{p}}^{Gen}$ value in the MC samples: prompt η_c (top left), prompt J/ψ (top right), η_c from b-decays (bottom left) and J/ψ from b-decays (bottom right). The solid blue lines represent a simultaneous fit by a double Gaussian function to all four MC samples.

The fit yields the ratio of J/ψ and η_c resolutions to be $\sigma_{\eta_c}/\sigma_{J/\psi} = 0.94 \pm 0.07$, the ratio of the two Gaussian widths to be $\sigma_n/\sigma_w = 0.21 \pm 0.01$ and the fraction of the narrow Gaussian component f_n to be about 95%. Note, that only the ratio of the η_c and J/ψ resolutions is taken from MC when fitting data, while the absolute values are constrained

by the narrow and significant J/ψ peak when fit to data is performed.

In order to study a dependence of the invariant mass resolution model as a function of charmonium transverse momentum, the same fit is performed in bins of p_{T} using simulation samples. The corresponding dependences of $\sigma_{\eta_c}/\sigma_{J/\psi}$, f_n, σ_n/σ_w are shown on Fig. 5.3. No significant p_{T}-dependence is observed for $\sigma_{\eta_c}/\sigma_{J/\psi}$, f_n and σ_n/σ_w, hence no p_{T}-dependence is assumed in the nominal fit to data. The linear slope of p_{T}-dependence of σ_n is extracted from simulation and is then used in the fit to data for differential production cross-section measurement. The value of the slope is extracted to be $a_{\sigma_n^{MC}} = (3.1 \pm 2.9) \times 10^{-2}$. The slope is cross-checked using $b \to \eta_c(1S)X$ data sample; the fit to data yields the slope value of $a_{\sigma_n^{data}} = (9.4 \pm 5.6) \times 10^{-2}$ and is consistent with simulation.

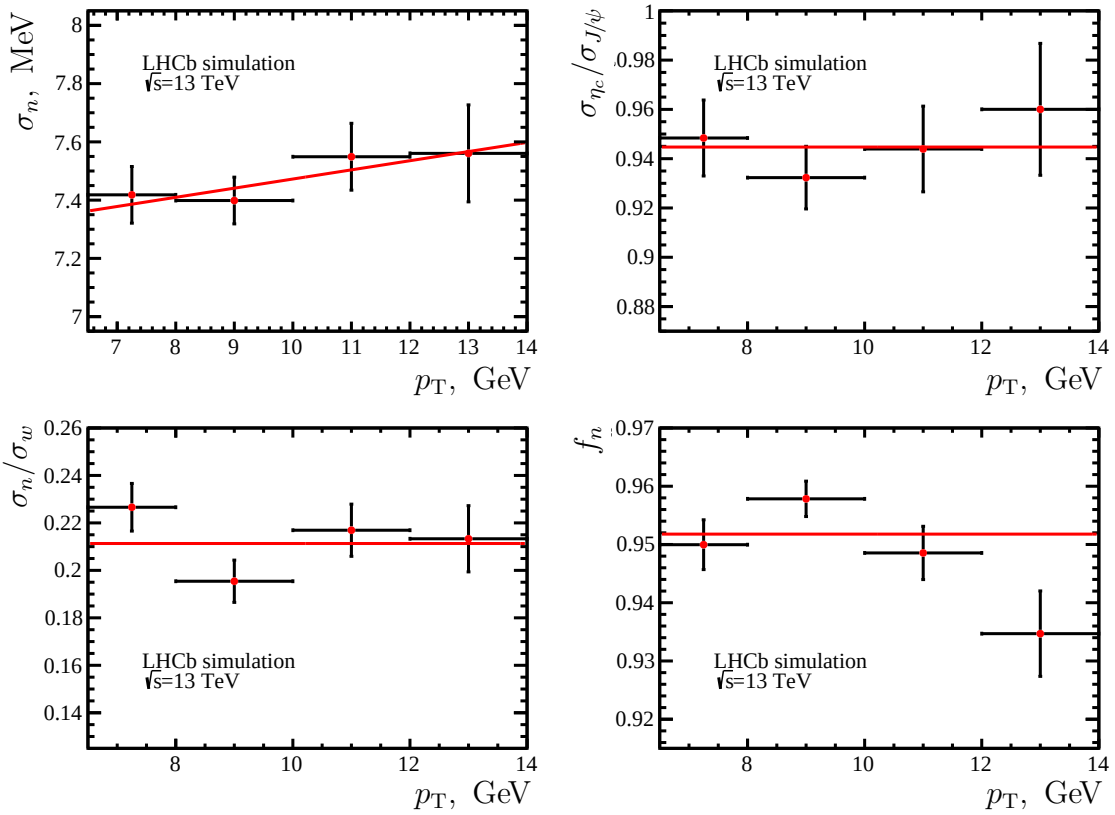

Figure 5.3: The p_{T} dependences of double Gaussian parameters of invariant mass resolution obtained from simultaneous fit to all four MC samples. Red lines represent p_{T}-dependences used in the fit to data.

A dependence of reconstructed charmonium mass as a function of t_z is considered. Figure 5.4 shows the curve of simultaneous invariant mass fit to data in seven t_z bins for a p_{T}-integrated data sample. In the fit model on Fig. 5.4, peak positions are assumed to be the same in all t_z bins. Pull distributions show clear shifts of peak positions in several

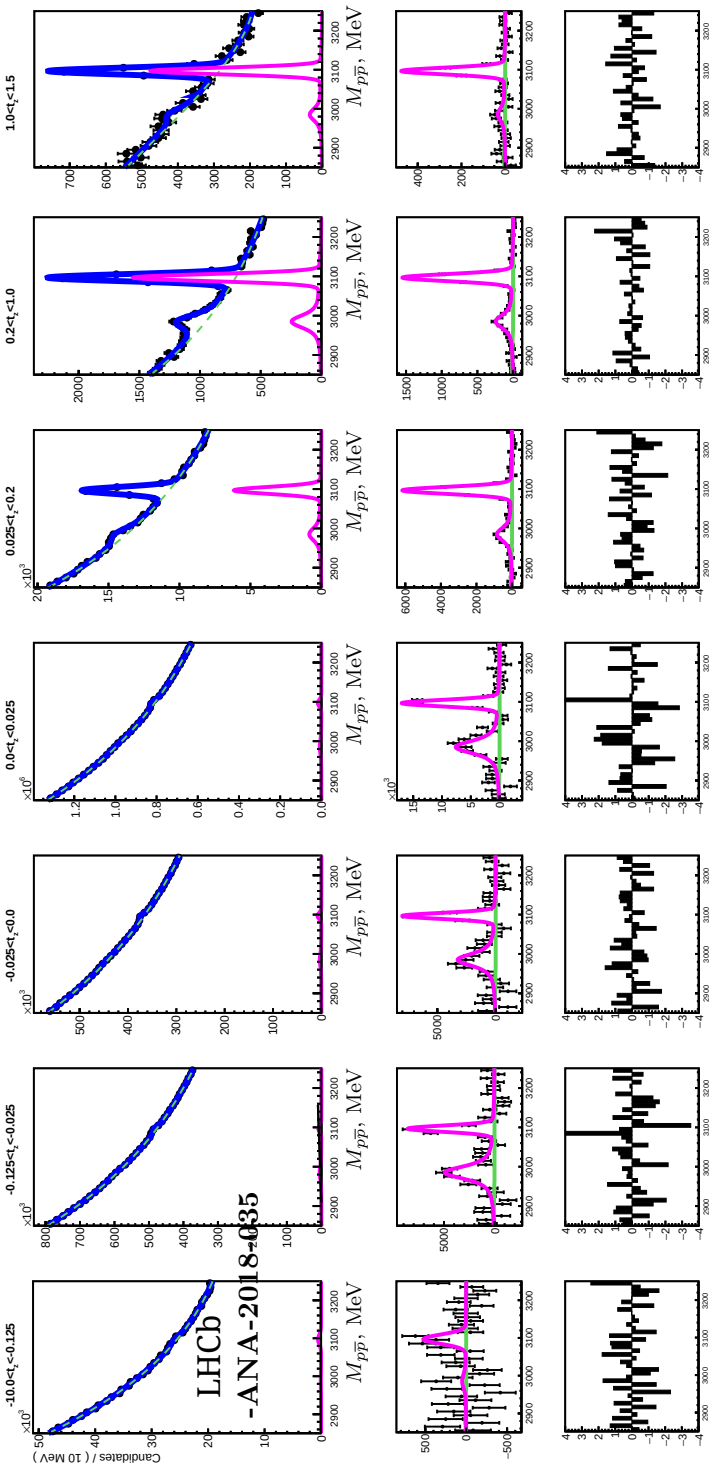

Figure 5.4: The $M_{p\bar{p}}$ distribution for seven bins of t_z in the p_{T}-integrated sample ($6.5\,\mathrm{GeV} < p_{\mathrm{T}} < 14.0\,\mathrm{GeV}$). The solid blue lines represent the total fit result **assuming the same peak positions in t_z bins**. Magenta and green lines show the signal and background components, respectively. The corresponding residual and pull distributions are shown on second and third line plots.

bins of t_z. The most notable shifts are observed in the second and fourth t_z bins.

Reconstructed charmonium mass as a function of t_z is studied using simulation samples. Simultaneous unbinned maximum-likelihood fit to $M_{p\bar{p}} - M_{p\bar{p}}^{Gen}$ in bins of t_z is performed using J/ψ and η_c MC samples. The fit model assumes the shifts of η_c and J/ψ peak positions to be the same, while the resolution is described by the double Gaussian function as described above. Deviations with respect to the peak position in the last t_z bin (Δm_{t_z}) are shown on Figure 5.5(a) in bins of t_z. The deviations vary by up to 4 MeV, which can cause a substantial bias when extracting signal yields in bins of t_z. Hence the corrections on peak positions in bins of t_z are applied, while the difference of the J/ψ and η_c masses is kept constant throughout t_z bins.

Similar effect is observed for the invariant mass resolution. Using MC samples, the correction factors, α_{t_z}, of mass resolution parameter σ_{η_c} in t_z bins are extracted from the fits. The α_{t_z} is the ratio of the resolution in a given t_z bin to that in the last t_z bin. The obtained values of α_{t_z} in bins of t_z are shown on Figure 5.5(b). This effect is taken into account by introducing α_{t_z} parameters in the fit model.

Alternatively, as a cross-check, mass shifts and mass resolution correction factors are extracted from data by performing invariant mass fits in bins of t_z for a total p_{T}-integrated data sample (Figs. 5.5(a) and 5.5(b)). Corresponding systematic uncertainty is estimated in Section 5.4.3.

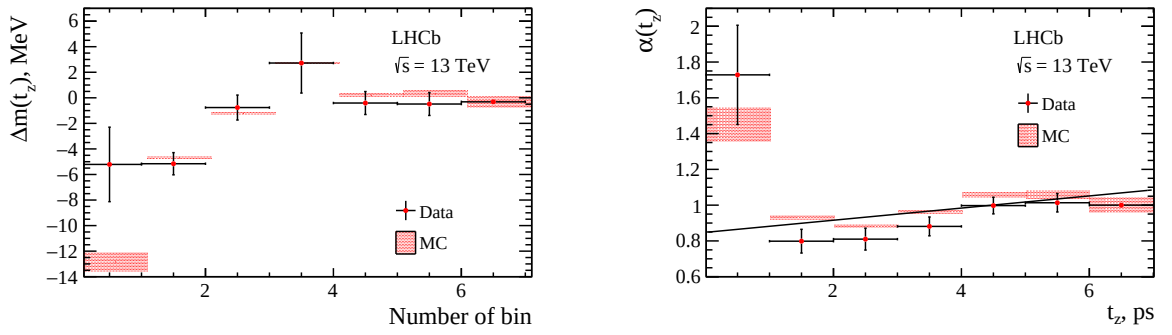

(a) Deviations of reconstructed mass, Δm_{t_z}.

(b) Correction factors of mass resolution, α_{t_z}.

Figure 5.5: Mass deviations (a) and correction factors of mass resolution (b) as a function of t_z bin mumber from simultaneous fit to the η_c and J/ψ invariant masses in the MC samples in bins of t_z (red boxes) and from fit to total p_{T}-integrated data sample (black points with error bars).

Peak position shifts extracted from data with and without implementing momentum scale calibration are compared on Fig. 5.6. The shifts from data are extracted from simultaneous fit in 7 bins of t_z. No significant effect of momentum scale calibration is

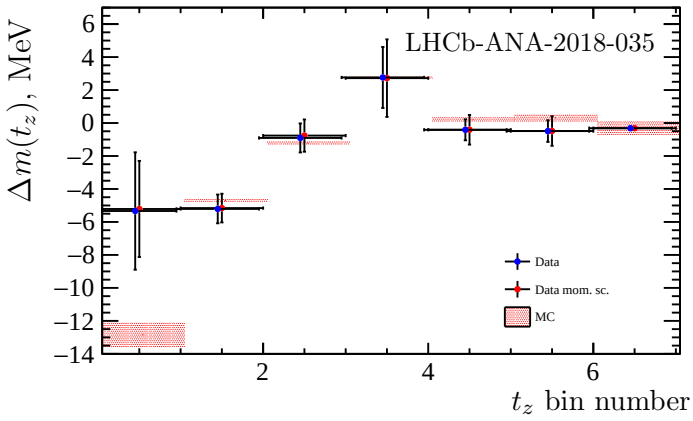

Figure 5.6: Peak position shifts from p_{T}-integrated data sample with applying momentum scale calibration (blue points), without applying momentum scale calibration (red points) and from MC (red boxes) as function of t_z bin number.

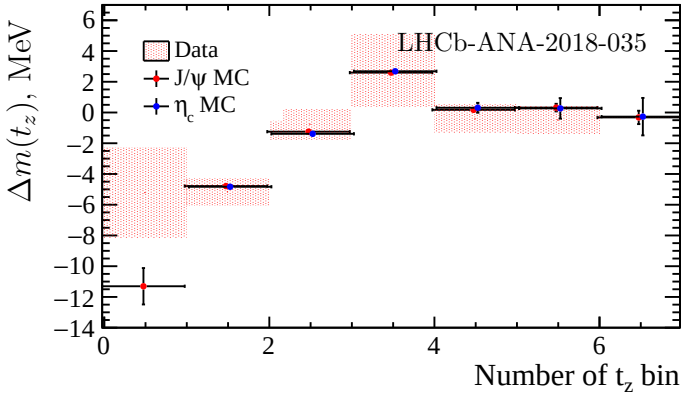

Figure 5.7: Peaks positions shifts for η_c (blue points) and J/ψ (red points) separately from p_{T}-integrated MC sample.

observed.

The comparison of peak position shifts for η_c and J/ψ obtained from simulation is shown on Fig. 5.7. No significant difference between η_c and J/ψ shifts is observed.

The comparison of peak position shifts obtained with simulation in bins of p_{T} is shown on Fig. 5.8. No significant p_{T}-dependence of shifts is observed.

The effect of η_c natural width Γ_{η_c} exceeds that of the detector resolution σ_n in signal shape model. The η_c peak is thus described using a convolution of double Gaussian (DG) and relativistic Breit-Wigner (RBW) functions in the fit to data, while J/ψ peak is described by a double Gaussian function.

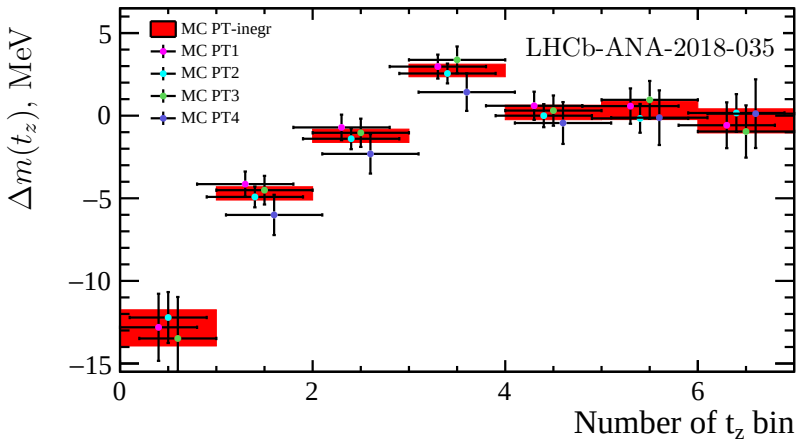

Figure 5.8: Peak position shifts in p_{T}-bins (points) from binned and from p_{T}-integrated MC samples (red boxes).

Complete signal shape model used in the fit to data is summarised by Eq. 5.5.

$$\begin{aligned} S_{\eta_c}(M_{p\bar{p}}) &\propto RBW(M_{p\bar{p}}, m_{\eta_c} + \Delta m_{t_z}, \Gamma_{\eta_c}, J_{\eta_c} = 0) \otimes DG(\sigma_n \times \alpha_{t_z}, \sigma_n/\sigma_w, f_n) \\ S_{J/\psi}(M_{p\bar{p}}) &\propto \delta(M_{p\bar{p}} - m_{J/\psi} - \Delta m_{t_z}) \otimes DG(\sigma_n \times \frac{\sigma_{J/\psi}}{\sigma_{\eta_c}} \times \alpha_{t_z}, \sigma_n/\sigma_w, f_n), \end{aligned} \tag{5.5}$$

where $J_{\eta_c} = 0$ is the spin of η_c; σ_n, $\sigma_{J/\psi}/\sigma_{\eta_c}$, σ_n/σ_w and f_n are resolution parameters as discussed above; Δm_{t_z} and α_{t_z} are the peak position and resolution corrections in bins of t_z. The summary of signal shape parametrisation in the fit is given in Table 5.4.

Parameter	Comment
σ_n/σ_w	Fixed from MC
f_n	Fixed from MC
$\sigma_{\eta_c}/\sigma_{J/\psi}$	Fixed from MC
σ_n	Common free parameter, linear slope of p_{T}-dependence extracted from MC for differential production measurement
$m_{J/\psi} - m_{\eta_c}$	Common free parameter for all fits in bins of t_z and p_{T}
$m_{J/\psi}$	Common free parameter for all fits in bins of t_z and p_{T}
Γ_{η_c}	Fixed to world average value [188] (31.8 MeV)
Δm_{t_z}	Fixed from MC in each t_z bin
α_{t_z}	Fixed from MC in each t_z bin

Table 5.4: Summary of signal parametrisation in the simultaneous invariant mass fit.

The combinatorial background composed of random combinations of charged hadrons passing proton identification hypothesis is parametrised using an exponential function multiplied by a second order polynomial function.

Besides the pure combinatorial background, proton-antiproton pairs from higher mass charmonium states decays to three or more particles can produce wide structures in the $p\bar{p}$ invariant mass spectrum. The only notable partially reconstructed background is that from the $J/\psi \to p\bar{p}\pi^0$ decays with the contribution in the range below $M_{J/\psi} - M_{\pi^0} = 3096.9 - 135.0 = 2961.9$ MeV, which can potentially affects the η_c region description. This process is specifically included in the fit model. Its contribution to the $p\bar{p}$ invariant mass spectrum around the threshold region is parametrised by a square-root shape as in Ref. [13]:

$$f_{J/\psi\to p\bar{p}\pi^0}(M) \propto \begin{cases} \sqrt{M_{J/\psi} - M_{\pi^0} - M_{p\bar{p}}} & \text{if } M_{p\bar{p}} \leq M_{J/\psi} - M_{\pi^0} \ , \\ 0 & \text{if } M_{p\bar{p}} > M_{J/\psi} - M_{\pi^0}. \end{cases} \tag{5.6}$$

This shape contains no free parameters. Applicability of the shape from equation (5.6) is verified using the MC sample, as shown in Fig. 5.9. The suggested model shows a good agreement with MC yielding a good fit quality, $\chi^2/\text{ndf} < 1$. Using branching fractions

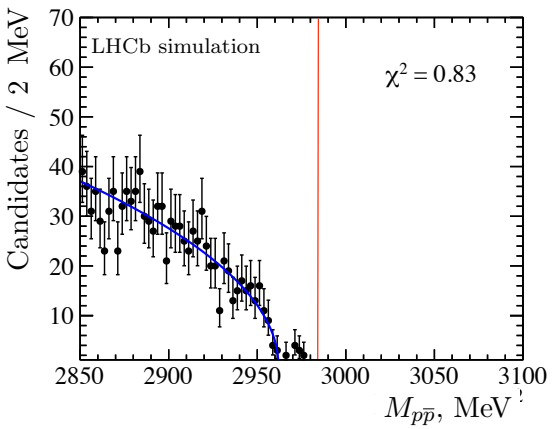

Figure 5.9: The $M_{p\bar{p}}$ distribution from the simulated $J/\psi \to p\bar{p}\pi^0$ sample. The solid blue line represents the fit by the square root function from Eq. 5.6. The η_c mass value is indicated by red solid line.

and the efficiencies in considered invariant mass range for $J/\psi \to p\bar{p}$ and $J/\psi \to p\bar{p}\pi^0$ channels, the contribution from $J/\psi \to p\bar{p}\pi^0$ is normalised as

$$n_{J/\psi\to p\bar{p}\pi^0} = n_{J/\psi\to p\bar{p}} \times \frac{\epsilon_{J/\psi\to p\bar{p}\pi^0}}{\epsilon_{J/\psi\to p\bar{p}}} \times \frac{\mathcal{B}_{J/\psi\to p\bar{p}\pi^0}}{\mathcal{B}_{J/\psi\to p\bar{p}}} \ . \tag{5.7}$$

Using the ratio of branching fractions $\mathcal{B}_{J/\psi\to p\overline{p}\pi^0}/\mathcal{B}_{J/\psi\to p\overline{p}} = 0.56 \pm 0.04$ from Ref. [188], and the ratio of efficiencies $\epsilon_{J/\psi\to p\overline{p}\pi^0}/\epsilon_{J/\psi\to p\overline{p}} = 0.062 \pm 0.002$ from simulation. The efficiency ratio is small due to mass fit region limit. One can conclude that the $J/\psi \to p\overline{p}\pi^0$ channel produces a non-peaking contribution to the $p\overline{p}$ invariant mass spectrum that amounts to about 3% of the $J/\psi \to p\overline{p}$ signal. In the fit to the invariant mass spectra, the amount of contribution from $J/\psi \to p\overline{p}\pi^0$ is bound to the observed yields of $J/\psi \to p\overline{p}$.

Fit to data

Projections of simultaneous fit for the entire p_T-range $6.5\,\mathrm{GeV} < p_\mathrm{T} < 14.0\,\mathrm{GeV}$ are shown on Fig. 5.10. The residual and pull distributions are displayed below the corresponding projections. In general, fit yields a good description of $M_{p\overline{p}}$ distributions in all t_z bins.

Projections of simultaneous fit in the p_T bins are shown on Figs. 5.11, 5.12, 5.13 and 5.14. The residual and pull distributions are displayed below the corresponding projections. Also in the projections the fit reproduces well the observed $M_{p\overline{p}}$ distributions.

The value of detector resolution parameter from the simultaneous fit is $\sigma_{\eta_c} = 7.78 \pm 0.12\,\mathrm{MeV}$ is reasonably comparable to the value from simulation $\sigma^{MC}_{\eta_c} = 7.50 \pm 0.05\,\mathrm{MeV}$. Simultaneous fit yields the following values of J/ψ mass $M_{J/\psi} = (3096.6 \pm 0.1)\,\mathrm{MeV}$ and J/ψ and η_c mass difference $\Delta M_{J/\psi\,,\,\eta_c} = (111.2 \pm 1.1)\,\mathrm{MeV}$, where the uncertainties are statistical only. These values agree with the world average values $M^{PDG}_{J/\psi} = (3096.900 \pm 0.006)\,\mathrm{MeV}$ and $\Delta M^{PDG}_{J/\psi\,,\,\eta_c} = (113.5 \pm 0.5)\,\mathrm{MeV}$ [188] once systematic uncertainty is considered (the systematic uncertainty on $M_{J/\psi}$ is about 0.6 MeV). Detailed consideration of the η_c mass and measurements is discussed in Chapter 8.

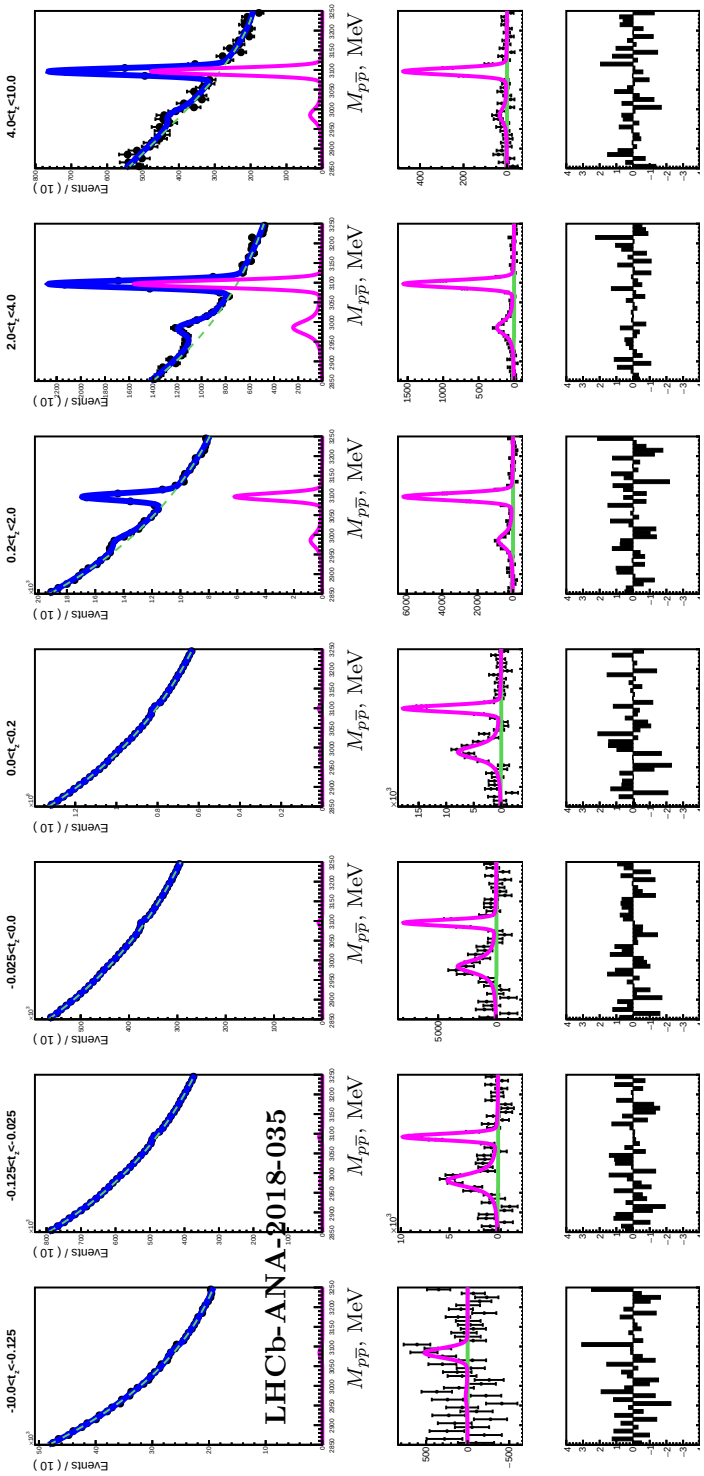

Figure 5.10: The $M_{p\overline{p}}$ distribution for seven bins of t_z for p_{T}-integrated sample $6.5\,\mathrm{GeV} < p_{\mathrm{T}} < 14.0\,\mathrm{GeV}$. The solid blue lines represent the total fit result. Magenta and green lines show the signal and background components, respectively. The corresponding residual and pull distributions are shown below.

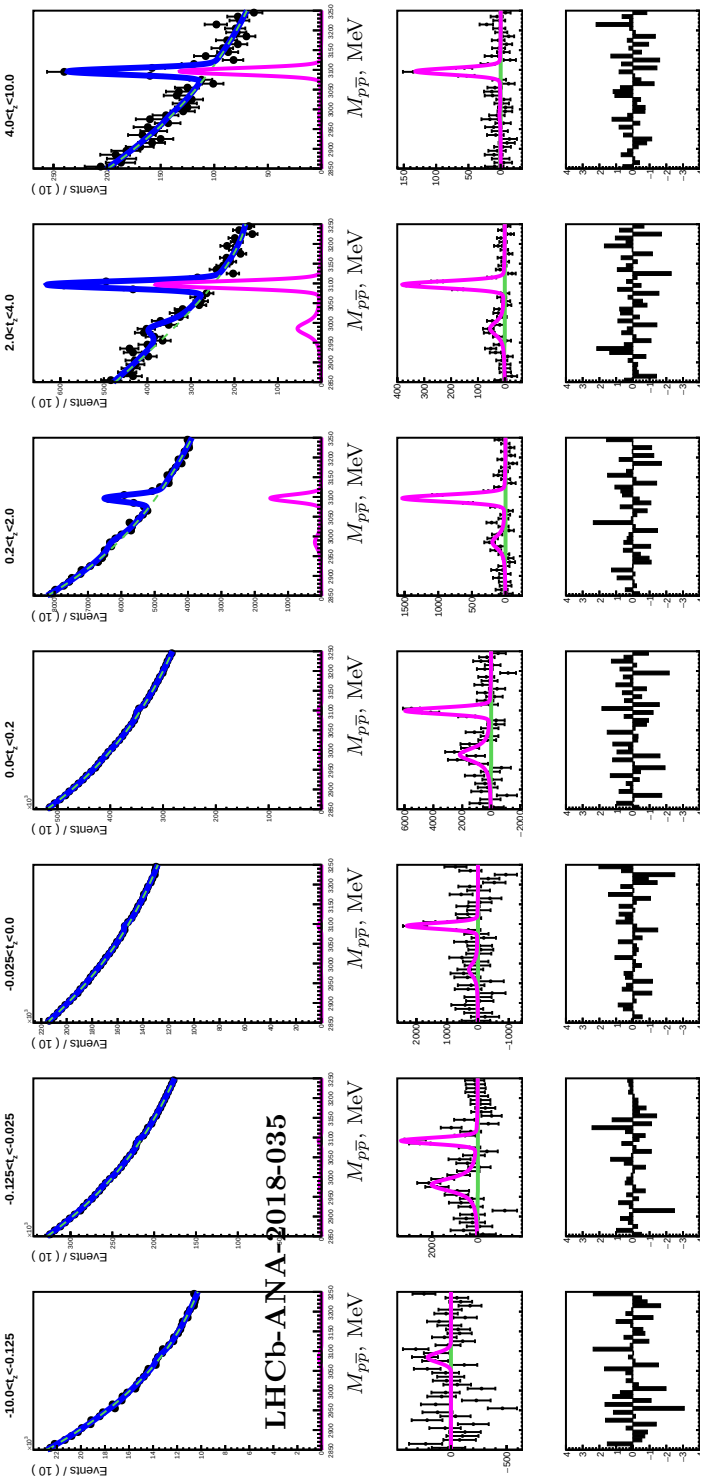

Figure 5.11: The $M_{p\bar{p}}$ distribution for seven bins of t_z for $6.5\,\text{GeV} < p_\text{T} < 8.0\,\text{GeV}$. The solid blue lines represent the total fit result. Magenta and green lines show the signal and background components, respectively. The corresponding residual and pull distributions are shown below.

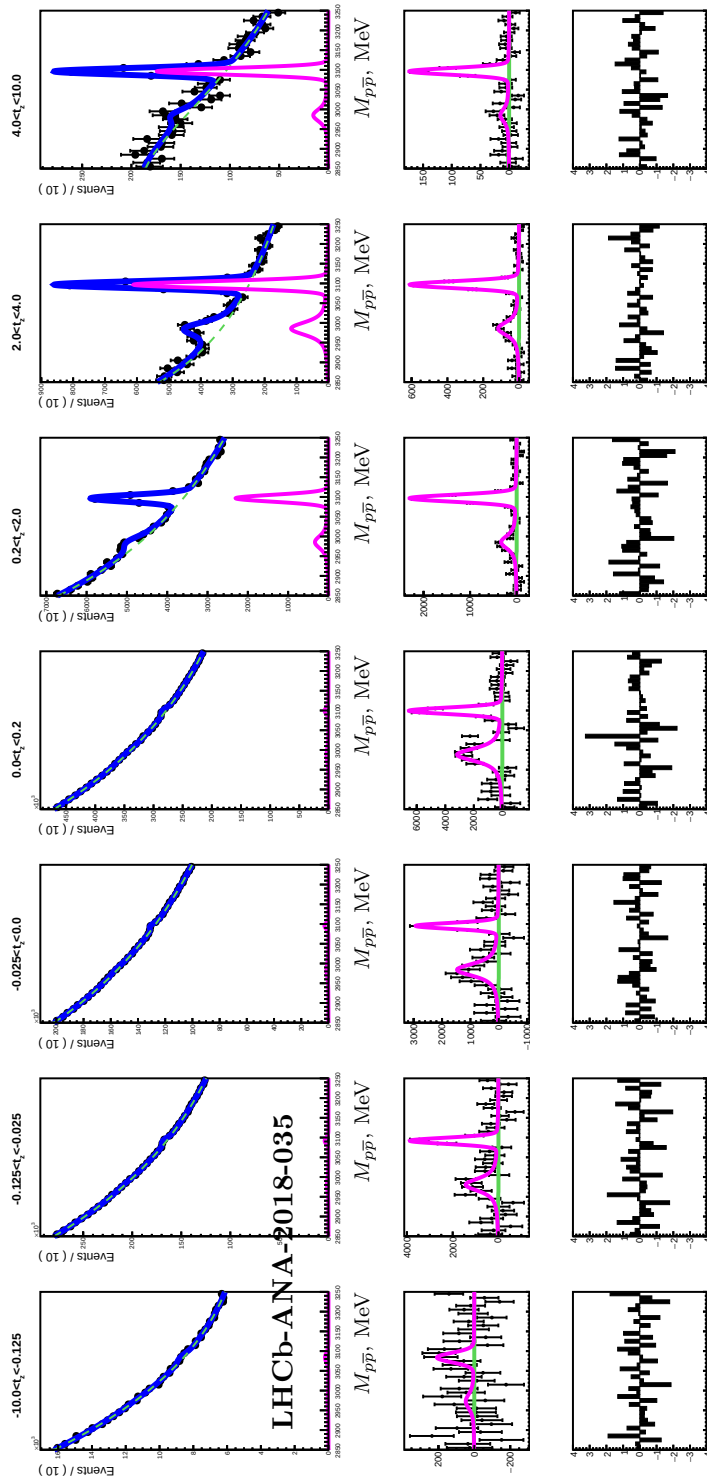

Figure 5.12: The $M_{p\bar{p}}$ distribution for seven bins of t_z for $8.0\,\text{GeV} < p_\text{T} < 10.0\,\text{GeV}$. The solid blue lines represent the total fit result. Magenta and green lines show the signal and background components, respectively. The corresponding residual and pull distributions are shown below.

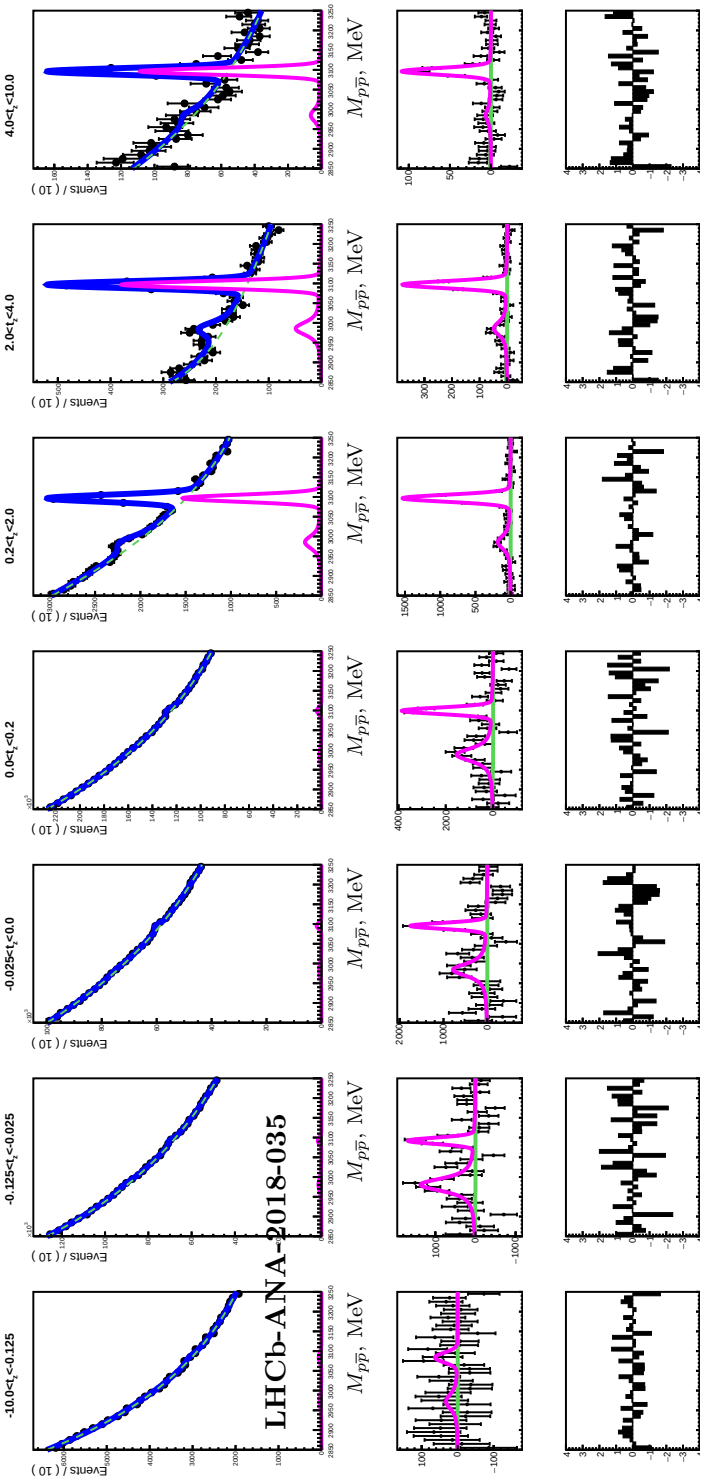

Figure 5.13: The $M_{p\bar{p}}$ distribution for seven bins of t_z for ($10.0\,\text{GeV} < p_\text{T} < 12.0\,\text{GeV}$. The solid blue lines represent the total fit result. Magenta and green lines show the signal and background components, respectively. The corresponding residual and pull distributions are shown below.

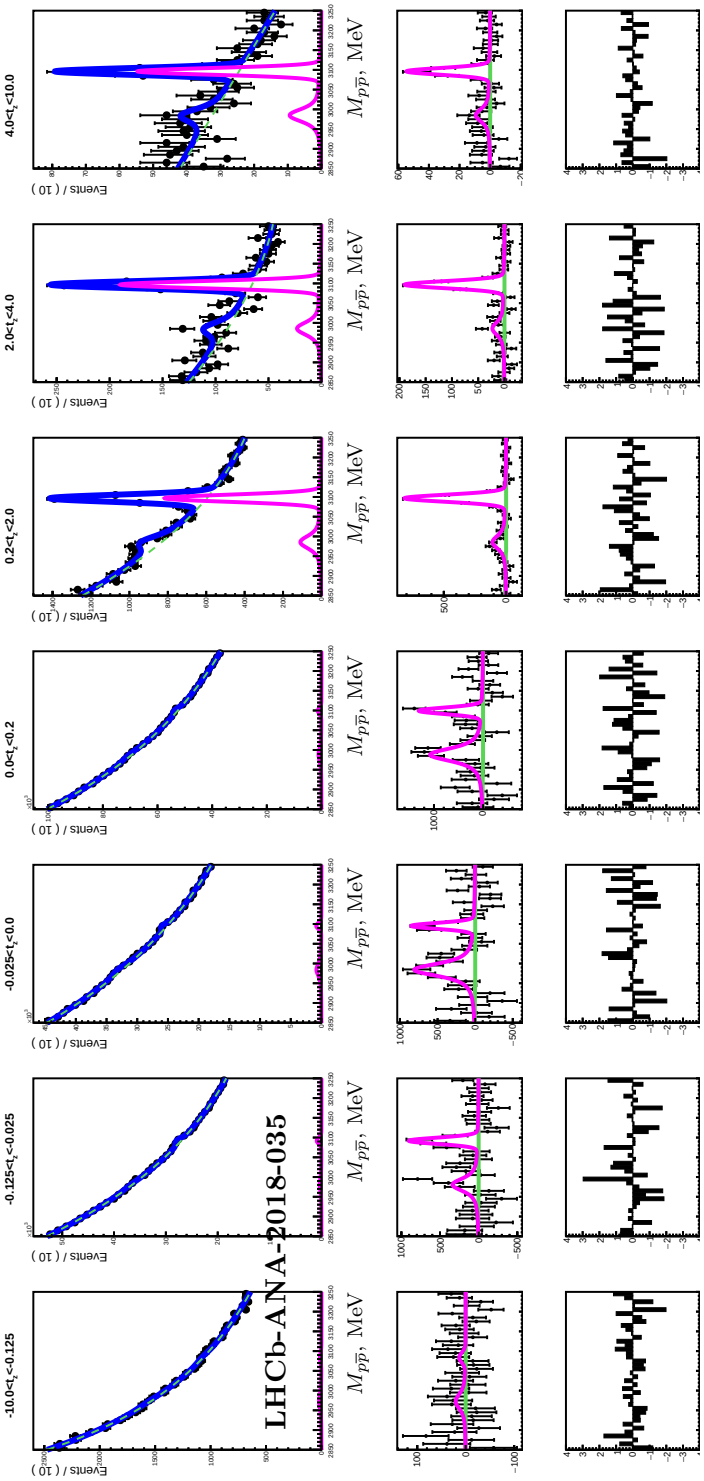

Figure 5.14: The $M_{p\bar{p}}$ distribution for seven bins of t_z for $12.0\,\text{GeV} < p_\text{T} < 14.0\,\text{GeV}$. The solid blue lines represent the total fit result. Magenta and green lines show the signal and background components, respectively. The corresponding residual and pull distributions are shown below.

5.4.2 Fit to the t_z distribution

The t_z resolution is studied using simulation samples similarly to the invariant mass resolution. Events with wrongly assigned primary vertex were excluded from the t_z resolution study, therefore obtained resolution model is not distorted by these events.

The t_z resolution is described by a double Gaussian function. The resolution model for η_c and J/ψ signals is assumed to be the same, which is confirmed by the fit described below. Parameters of double Gaussian are extracted from simultaneous unbinned maximum-likelihood fit of four MC samples (prompt η_c, prompt J/ψ, η_c from b-decays and J/ψ from b-decays) to $t_z - t_z^{Gen}$, where t_z is the reconstructed pseudo-proper lifetime and t_z^{Gen} is the pseudo-proper lifetime at generator level (Fig 5.15). The ratio of the two Gaussian widths is determined to be $S_w/S_n = 3.10 \pm 0.09$ and the fraction of the narrow Gaussian component β to be about 95%.

In order to study dependence of t_z resolution model on charmonium transverse momentum, the same fit is performed in bins of $p_{\mathrm{T}}(p\bar{p})$. The dependences of t_z bias μ,

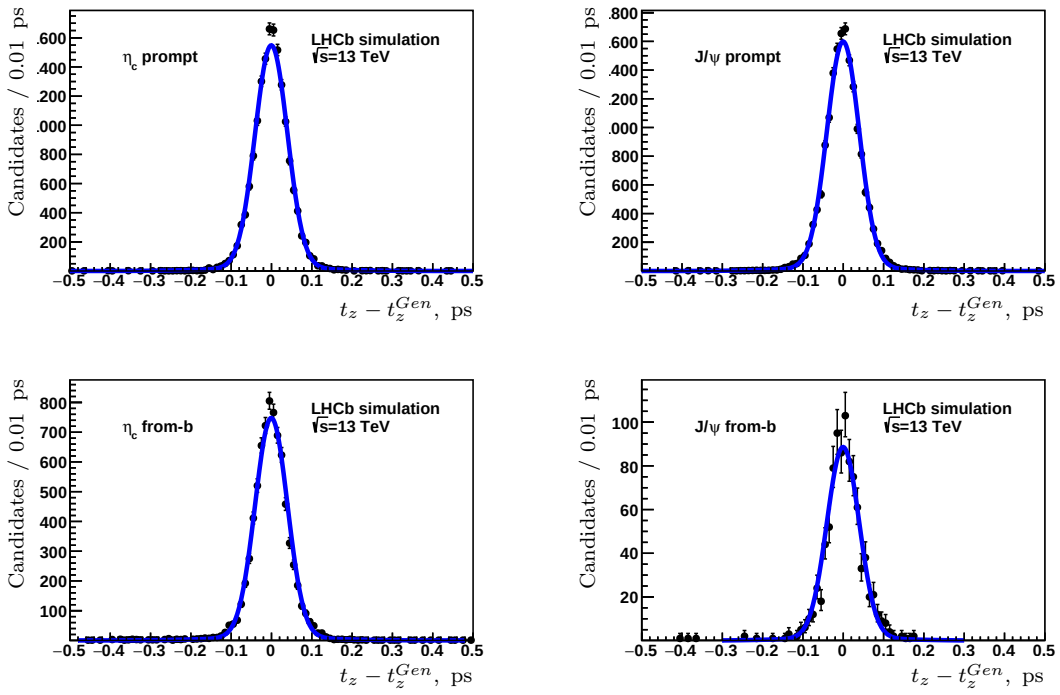

Figure 5.15: Distribution of the $t_z - t_z^{Gen}$ in the MC samples: prompt η_c (top left), prompt J/ψ (top right), η_c from b-decays (bottom left) and J/ψ from b-decays (bottom right). The solid blue lines represent the result of the simultaneous fit by a double Gaussian function to all four MC samples.

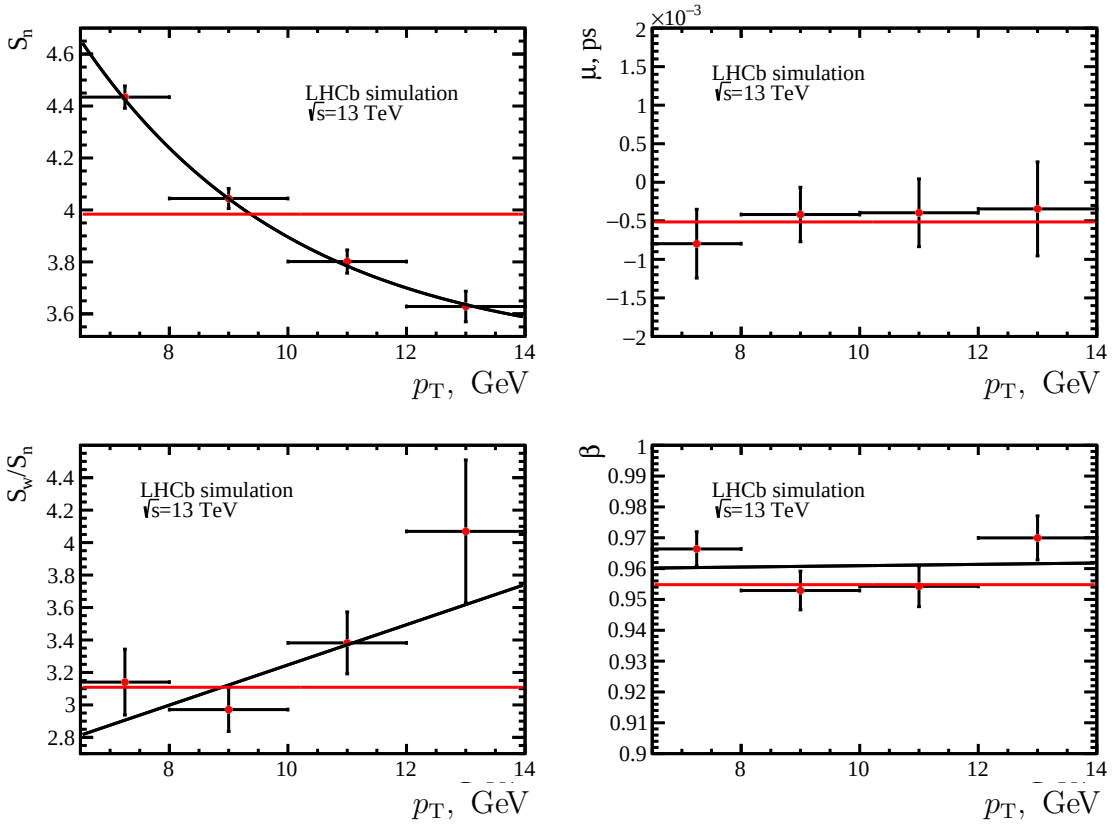

Figure 5.16: The p_T-dependences of double Gaussian parameters S_{η_c} (top left), μ (to right), S_w/S_n (bottom left) and β (bottom right) of the t_z resolution model, as obtained from the simultaneous fit to all four MC samples. Red solid horizontal lines represent values from the fit to the p_T-integrated MC samples. The black line shows the result of the fit for the S_n dependence on t_z (top left).

S_w/S_n, β on p_T are shown on Fig. 5.16. No significant p_T-dependence is observed for β, S_w/S_n and μ, hence no p_T-dependence of these parameters is assumed in the nominal fit to data. A notable p_T-dependence of S_n is observed and is described by the sum of an exponential function and a constant. The obtained dependence is used in the t_z-fit to data. The values of double Gaussian parameters from the fit to the p_T-integrated ($6.5\,\text{GeV} < p_T < 14.0\,\text{GeV}$) MC samples are shown by red solid horizontal lines.

Signal model includes two components: prompt charmonia, which is parametrised as a δ-function convoluted with a resolution function; and charmonia produced in inclusive b-decays, which is parametrised by a decay function convoluted with a resolution function.

The p_T-dependence of the exponential slope τ_b of the decay function for charmonia produced in inclusive b-decays is studied using MC samples of η_c from and J/ψ mesons originating from b-decays. Simultaneous extended maximum-likelihood fit is performed to

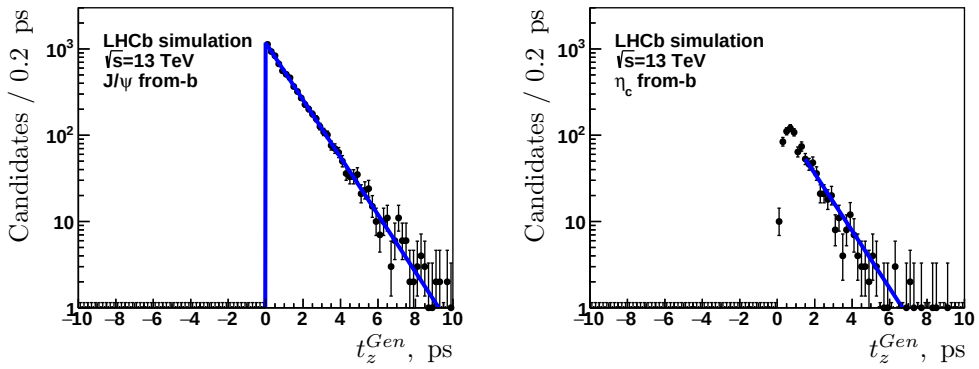

Figure 5.17: Distribution of the t_z^{Gen} in the MC samples comprising J/ψ from b-decays (left) and η_c from b-decays (right). The solid blue lines represent the result of the simultaneous fit by a decay function to both MC samples.

the t_z^{Gen} distributions. Since the η_c mesons from b-decays are restricted to be produced in the decays of long-lived (with lifetime more than 1 ps) b-hadrons at the generator level, the fit range for the η_c sample starts at 1.5 ps. The example of the fit to t_z^{Gen} for $p_{\rm T}$-integrated MC samples is shown on Fig.5.17. The values of τ_b extracted from the fits to MC in bins of $p_{\rm T}$ are shown on Fig.5.18. The $p_{\rm T}$-dependence of τ_b is approximated by a linear function; the shape of this dependence is used in the following fit to data.

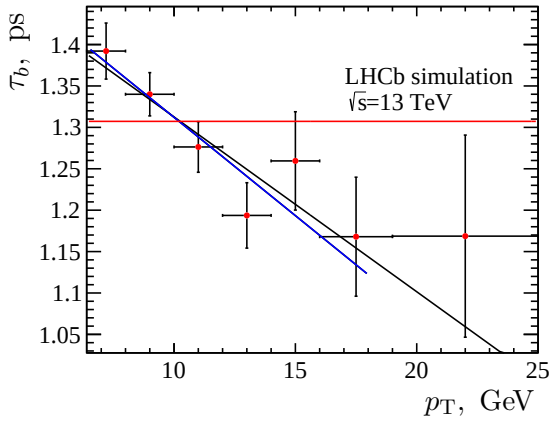

Figure 5.18: The $p_{\rm T}$ dependence of of τ_b from simultaneous fit to both η_c from b-decays and J/ψ from b-decays MC samples in four $p_{\rm T}$ bins. The black and blue lines represent the results of the fit by a linear function in different fit ranges. The red horizontal line shows the value of τ_b from the fit to $p_{\rm T}$-integrated MC samples.

Events with wrongly assigned PV are taken into account in the fit to data. The shape of the t_z-distribution for such events is extracted from data using the next-event method as explained by Eq. 5.8:

$$t_z^{next} = \frac{(z_{p\bar{p}} - z_{PV}^{next}) \times M_{p\bar{p}}}{p_z}, \tag{5.8}$$

where $z_{p\bar{p}}$ is the coordinate of b-decay vertex and z_{PV}^{next} is the primary vertex from the next event with the smallest impact parameter with respect to the b-decay vertex of the considered event. The shape is extracted using kernel estimated function in each bin of transverse momentum separately. The example of this shape as obtained for the entire p_{T}-range is shown on Fig. 5.19. In the fit model to data it is assumed that the shapes and the fractions of the events with wrongly assigned primary vertex are the same for the η_c and J/ψ signals.

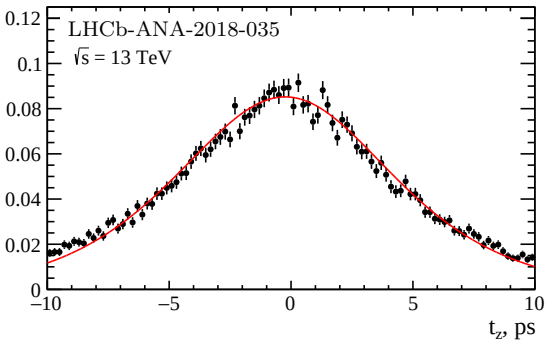

Figure 5.19: The t_z-distribution for the entire p_{T}-range from the next-event method. The red line represents the fit using non-parametric kernel estimated function.

Complete description of the t_z-fit model is thus given by Eq. 5.9

$$\begin{aligned} F^{\eta_c}(t_z) &= \left(N_p^{\eta_c}\delta(t_z) + \frac{N_b^{\eta_c}}{\tau_b}e^{-t_z/\tau_b}\right) \otimes DG(\mu, S_n, S_n/S_w, \beta) + N_m^{\eta_c} f_m(t_z), \\ F^{J/\psi}(t_z) &= \left(N_p^{J/\psi}\delta(t_z) + \frac{N_b^{J/\psi}}{\tau_b}e^{-t_z/\tau_b}\right) \otimes DG(\mu, S_n, S_n/S_w, \beta) + N_m^{J/\psi} f_m(t_z), \end{aligned} \tag{5.9}$$

where $N_p^{\eta_c(J/\psi)}$ is the yield of prompt η_c (J/ψ), $N_b^{\eta_c(J/\psi)}$ is the yield of the η_c (J/ψ) from b-decays, $N_m^{\eta_c(J/\psi)}$ is the yield of η_c (J/ψ) from events with wrongly assigned primary vertex, $f_m(t_z)$ denotes the shape of events with wrongly assigned primary vertex. The fractions of J/ψ and η_c candidates from events with wrongly assigned PV are assumed to be equal as

$$\frac{N_m^{J/\psi}}{N_b^{J/\psi} + N_p^{J/\psi}} \equiv \frac{N_m^{\eta_c}}{N_b^{\eta_c} + N_p^{\eta_c}}. \tag{5.10}$$

The summary of the t_z fit parametrisation is given in Table 5.5.

Parameter	Comment
μ	Common free parameter
S_n/S_w	Fixed from MC
β	Fixed from MC
S_n	Common free parameter, shape of p_{T}-dependence extracted from MC for differential production measurement
τ_b	Common free parameter of average value $\langle\tau_b\rangle$, shape of p_{T}-dependence extracted from MC for differential production measurement
$N_b^{J/\psi}, N_p^{J/\psi}$	Free fit parameters
$N_b^{\eta_c}/N_b^{J/\psi}, N_p^{\eta_c}/N_p^{J/\psi}$	Free fit parameters
$N_m^{J/\psi}/(N_b^{J/\psi}+N_p^{J/\psi})$ $N_m^{\eta_c}/(N_b^{\eta_c}+N_p^{\eta_c})$	Free fit parameters, required to be the same for J/ψ and η_c

Table 5.5: Summary on t_z-fit parametrisation used in the fit to data.

Results of the simultaneous fit to t_z for entire p_{T}-range are shown on Fig. 5.20. Results of simultaneous fit to t_z in each bin of p_{T} are shown on Fig. 5.21. Note that pull distributions take into account the integral option of the fit and the centre-of-mass of each bin is evaluated according to the shape of the fit function. Since the fit function is very sharp, the centre-of-masses of bins significantly differs from bins centers.

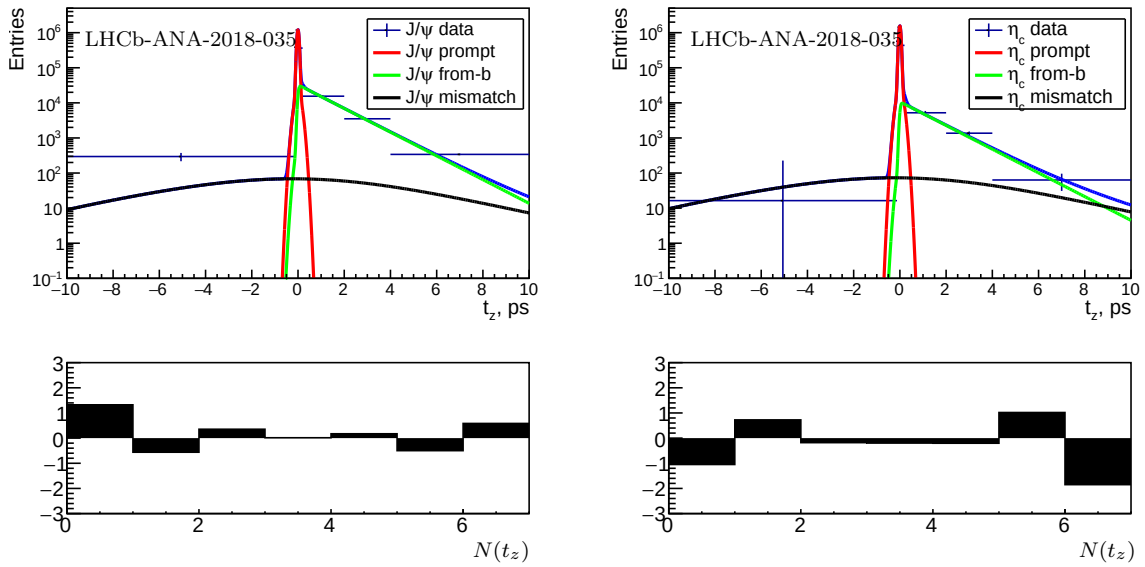

Figure 5.20: The t_z distribution for J/ψ (left) and η_c (right) for entire p_{T}-range $6.5\,\mathrm{GeV} < p_{\mathrm{T}} < 14.0\,\mathrm{GeV}$ and the result of simultaneous integral χ^2 fit. Red lines show prompt components, green lines show η_c and J/ψ from inclusive b-decays, black lines show contributions from the events with wrongly associated PV. The corresponding pull distributions are shown below, where the $N(t_z)$ on the pull distributions denotes the t_z bin number.

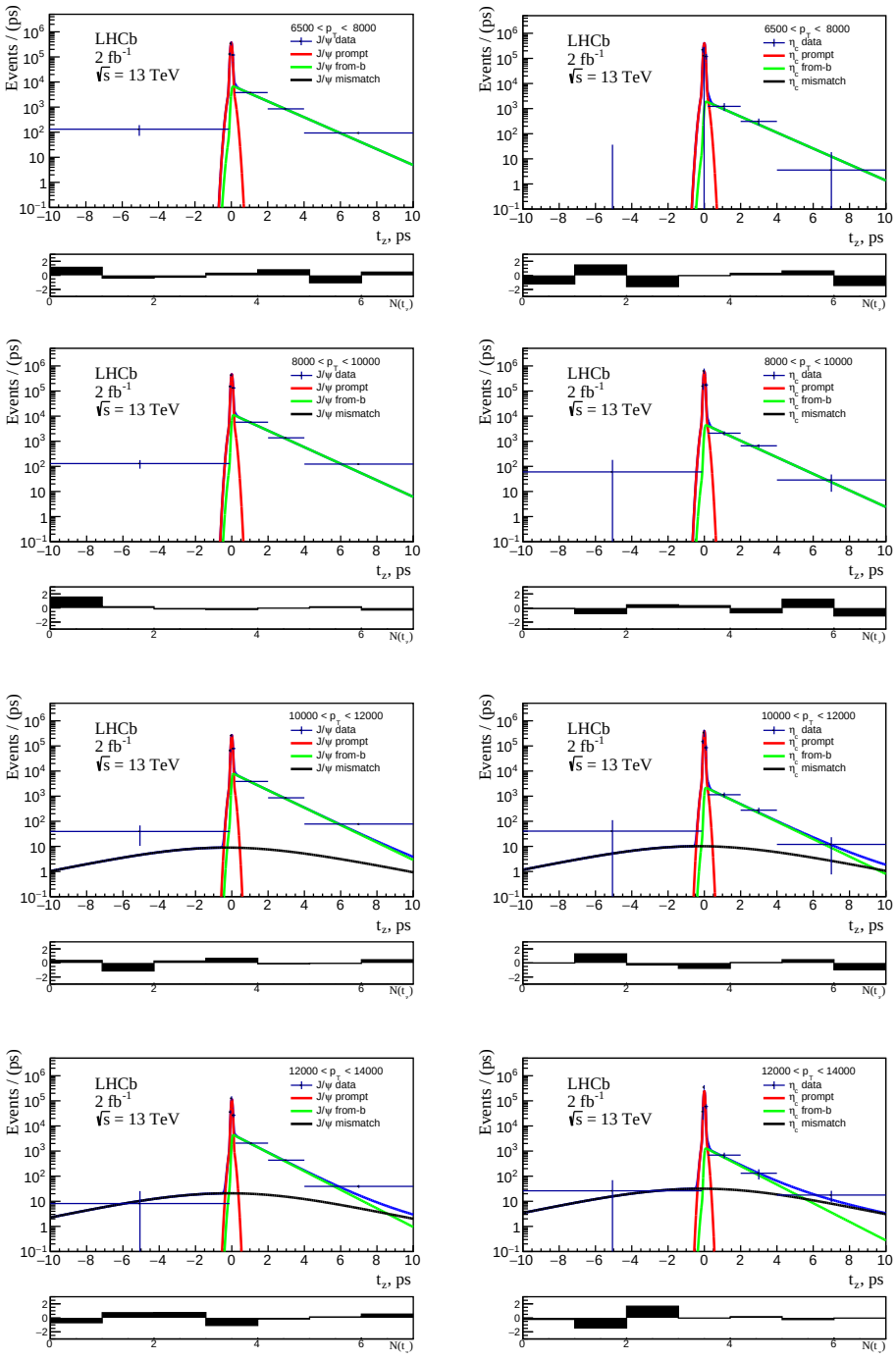

Figure 5.21: The t_z distribution for J/ψ (left) and η_c (right) for all p_{T}-bins and the result of simultaneous integral χ^2 fit. Red lines show prompt components; green lines show η_c and J/ψ from inclusive b-decays; black lines show contributions from the events with wrongly associated PV. The corresponding pull distributions are shown below, where the $N(t_z)$ on the pull distributions denotes the t_z bin number

Simultaneous fit yields the following values for the parameters, which are common across the p_{T}-bins:

$$\begin{aligned} \mu &= (-1.3 \pm 1.8) \times 10^{-3}\,\mathrm{ps}, \\ S_n &= (4.28 \pm 0.28) \times 10^{-2}\,\mathrm{ps}, \\ \langle \tau_b \rangle &= 1.28 \pm 0.02\,\mathrm{ps}. \end{aligned} \tag{5.11}$$

The value of μ is in good agreement with the value obtained from MC, $\mu^{MC} = (-0.5 \pm 0.2) \times 10^{-3}\,\mathrm{ps}$, as well as the value of $\langle \tau_b \rangle$, $\langle \tau_b^{MC} \rangle = 1.31 \pm 0.01\,\mathrm{ps}$. The value of S_n is also in a good agreement with simulation.

Values of τ_b parameter are expected to be the same for η_c and J/ψ. This is in agreement with the fact that simultaneous fit with common τ_b parameter for η_c and J/ψ well describes t_z^{Gen} distributions in the MC samples.

In general, B^0, B_s^0 and Λ_b lifetimes are close to 1.5 ps within 2% accuracy, which is better than the statistical precision of the τ_b parameter from the fit to the t_z distribution in data. However the B^+ meson has significantly different lifetime of 1.64 ps. A systematic shift can then impact the results only if the B^+ fraction contributing to the observed inclusive b-decays to η_c is significantly different from that to J/ψ. These considerations allow to perform the following very conservative reasoning. The upper limit of q possible impact corresponds to the difference between the τ_b for η_c and J/ψ of a value 5%, which is estimated from the lifetimes of different b-species and the corresponding fragmentation fractions.

Also, a fit to data with two different τ_b free parameters for η_c and for J/ψ is consistent with the same τ_b values for η_c and J/ψ, and also consistent to the fit assuming a 5% difference in τ_b values within a large uncertainty of the τ_b value for η_c:

$$\begin{aligned} \tau_b^{J/\psi} &= 1.28 \pm 0.03\,\mathrm{ps}, \\ \tau_b^{\eta_c} &= 1.19 \pm 0.12\,\mathrm{ps}. \end{aligned} \tag{5.12}$$

A cross-check fit to t_z was performed using the η_c and J/ψ τ_b values different by 5%. The results on the yield ratios in p_{T} bins are shown in Tab. 5.6 for prompt production and in Tab. 5.7 for production in b-decays. They are consistent with the baseline fit well within statistical uncertainties, where the baseline fit assumes equal τ_b values for η_c and J/ψ as described above.

The yields of prompt charmonia and charmonia from b-decays in p_{T}-bins from baseline simultaneous fit result and yields from fit to p_{T}-integrated data sample are summarised in Table 5.8.

p_{T}-range	Baseline fit	Fit with 5% difference between $\tau_b^{\eta_c}$ and $\tau_b^{J/\psi}$
$6.5\,\mathrm{GeV} < p_{\mathrm{T}} < 8.0\,\mathrm{GeV}$	1.08 ± 0.21	1.08 ± 0.21
$8.0\,\mathrm{GeV} < p_{\mathrm{T}} < 10.0\,\mathrm{GeV}$	1.29 ± 0.18	1.29 ± 0.18
$10.0\,\mathrm{GeV} < p_{\mathrm{T}} < 12.0\,\mathrm{GeV}$	1.46 ± 0.23	1.47 ± 0.23
$12.0\,\mathrm{GeV} < p_{\mathrm{T}} < 14.0\,\mathrm{GeV}$	2.13 ± 0.40	2.12 ± 0.40

Table 5.6: Yield ratio $N_{\eta_c}^{prompt}/N_{J/\psi}^{prompt}$ of prompt charmonia in bins of p_{T} for baseline fit and for the fit assuming 5% difference between $\tau_b^{\eta_c}$ and $\tau_b^{J/\psi}$.

p_{T}-range	Baseline fit	Fit with 5% difference between $\tau_b^{\eta_c}$ and $\tau_b^{J/\psi}$
$6.5\,\mathrm{GeV} < p_{\mathrm{T}} < 8.0\,\mathrm{GeV}$	0.281 ± 0.071	0.263 ± 0.068
$8.0\,\mathrm{GeV} < p_{\mathrm{T}} < 10.0\,\mathrm{GeV}$	0.396 ± 0.047	0.383 ± 0.046
$10.0\,\mathrm{GeV} < p_{\mathrm{T}} < 12.0\,\mathrm{GeV}$	0.277 ± 0.052	0.270 ± 0.051
$12.0\,\mathrm{GeV} < p_{\mathrm{T}} < 14.0\,\mathrm{GeV}$	0.293 ± 0.073	0.289 ± 0.073

Table 5.7: Yield ratio $N_{\eta_c}^{b-decays}/N_{J/\psi}^{b-decays}$ of charmonia from b-decays in bins of p_{T} for baseline fit and for the fit assuming 5% difference between $\tau_b^{\eta_c}$ and $\tau_b^{J/\psi}$.

p_{T}-range	$N_{J/\psi}^{prompt}$	$N_{J/\psi}^{b-decays}$	$\frac{N_{\eta_c}^{prompt}}{N_{J/\psi}^{prompt}}$	$\frac{N_{\eta_c}^{b-decays}}{N_{J/\psi}^{b-decays}}$
$6.5\,\mathrm{GeV} < p_{\mathrm{T}} < 8.0\,\mathrm{GeV}$	22650 ± 1658	5050 ± 182	1.082 ± 0.212	0.281 ± 0.071
$8.0\,\mathrm{GeV} < p_{\mathrm{T}} < 10.0\,\mathrm{GeV}$	25675 ± 1494	7943 ± 197	1.291 ± 0.177	0.396 ± 0.047
$10.0\,\mathrm{GeV} < p_{\mathrm{T}} < 12.0\,\mathrm{GeV}$	13817 ± 995	5296 ± 152	1.463 ± 0.229	0.277 ± 0.052
$12.0\,\mathrm{GeV} < p_{\mathrm{T}} < 14.0\,\mathrm{GeV}$	5712 ± 644	2789 ± 101	2.124 ± 0.401	0.293 ± 0.074
$6.5\,\mathrm{GeV} < p_{\mathrm{T}} < 14.0\,\mathrm{GeV}$	68298 ± 2545	21282 ± 357	1.316 ± 0.113	0.331 ± 0.030

Table 5.8: Yields of prompt charmonia and charmonia from b-decays in p_{T}-bins from baseline simultaneous fit to t_z and for p_{T}-integrated sample.

5.4.3 Systematic uncertainties

The systematic uncertainties due to following reasons are considered.

- Signal description in simultaneous fit to invariant mass:
  - Knowledge of the η_c natural width, Γ_{η_c};
  - Invariant mass resolution mismodeling;
  - p_{T}-dependence of η_c and J/ψ resolution ratio, $\sigma_{\eta_c}/\sigma_{J/\psi}$ (relevant for differential cross-section measurement);
  - Resolution correction factors α_{t_z} in bins of t_z;
- Background description in simultaneous fit to invariant mass:
  - Combinatorial background description;
  - Description of the feed-down from the $J/\psi \to p\bar{p}\pi^0$ decay;
- Signal description in simultaneous fit to t_z:
  - Bias μ;
  - The t_z-resolution mismodeling;
  - Mismodeling of p_{T}-dependence for t_z resolution; (relevant for differential cross-section measurement);
  - Mismodeling of p_{T}-dependence of τ_b distribution (relevant for differential cross-section measurement);
- The η_c and J/ψ efficiency ratio;
- Non-zero J/ψ polarisation;
- Uncertainties on $\mathcal{B}_{J/\psi\to p\bar{p}}$ and $\mathcal{B}_{\eta_c\to p\bar{p}}$;
- Uncertainties on J/ψ production (for absolute η_c production cross-section determination).

Systematic uncertainties on η_c production corresponding to signal and background description in fits to the invariant mass and t_z are estimated using alternative fit parameterisations. Each uncertainty is estimated as a difference between the nominal fit result and the alternative fit result. Bin-to-bin variations of uncorrelated systematic uncertainties remain small compared to statistical uncertainty. Since there are no physics reasons for these variations, they are interpreted as fluctuations and therefore bin contents are smoothed in order to reduce the effect of fluctuations.

Uncertainties related to signal and background shape description in the fit to invariant mass

The uncertainty corresponding to the knowledge of the η_c natural width is estimated by comparing the results of the simultaneous fit to invariant mass for the p_{T}-integrated data sample, when Γ_{η_c} is set to the world average value of 31.8 MeV [188] and when Γ_{η_c} is set to the value of 34.0 MeV from the analysis of $B^+ \to p\bar{p}K^+$ [240]. This uncertainty is correlated between p_{T}-bins. Therefore the relative systematic uncertainty obtained from p_{T}-integrated data sample is taken as an estimate of a relative systematic uncertainty in each bin.

The uncertainty corresponding a mismodeling of the invariant mass resolution is estimated by alternatively describing the detector resolution using a symmetric double-sided Crystal Ball function. The tail parameters and the ratio of η_c and J/ψ resolution parameters are extracted from the fit to MC samples and fixed in bins of p_{T}. The p_{T} dependence of the resolution parameter for the η_c signal is extracted from MC similarly to that is done for nominal fit parametrisation. This uncertainty is correlated between p_{T}-bins. Therefore the relative systematic uncertainty obtained from p_{T}-integrated data sample is taken as an estimate of a relative systematic uncertainty in each bin.

The uncertainty related to the p_{T}-dependence of the η_c and J/ψ resolution ratio is estimated by introducing a linear dependence of $\sigma_{\eta_c}/\sigma_{J/\psi}$ as a function of p_{T}. The slope of the linear function is extracted from MC. This systematic effect is relevant for differential cross-section measurement. This uncertainty is parametrised as a constant in all bins as shown on Fig. 5.22.

The uncertainty corresponding to the resolution correction factors α_{t_z} is estimated by parametrising t_z-dependence of α_{t_z} by a linear function. Parameters of the linear function are extracted from the fit to MC. This uncertainty is parametrised to be linearly dependent on the bin as shown on Fig. 5.23.

The uncertainty corresponding to combinatorial background description is estimated via an alternative combinatorial background parametrisation with a third-order polynomial function. This uncertainty is parametrised to be linearly dependent on the bin as shown on Fig. 5.24.

The uncertainty corresponding to the description of the feed-down from the $J/\psi \to p\bar{p}\pi^0$ decay is estimated by shifting the value of the efficiency ratio $\epsilon_{J/\psi\to p\bar{p}\pi^0}/\epsilon_{J/\psi\to p\bar{p}} = 0.062 \pm 0.002$ by its standard deviation and by shifting the value of the branching fraction ratio $\mathcal{B}_{J/\psi\to p\bar{p}}/\mathcal{B}_{J/\psi\to p\bar{p}\pi^0}$ according to the uncertainty from Ref. [188]. This uncertainty is parametrised to be linearly dependent on the bin as shown on Fig. 5.25.

Uncertainties related to signal description in the fit to t_z

The uncertainty corresponding to the t_z resolution mismodeling is estimated by introducing a linear p_{T}-dependence of S_w/S_n and β parameters extracted from simulation. This uncertainty is parametrised to be linearly dependent on the bin as shown on Fig. 5.26.

The uncertainty corresponding to the bias μ is estimated by alternatively setting $\mu \equiv 0$ in the fit to t_z. This uncertainty is parametrised as a constant in all bins as shown on Fig. 5.27.

The uncertainty corresponding to mismodeling of the p_{T}-dependence of t_z resolution is estimated by alternatively parametrising its shape as a sum of two exponential functions. Parameters of this shape are extracted from the fit to simulation. This uncertainty is relevant for the differential cross-section measurement. This uncertainty is parametrised to be linearly dependent on the bin as shown on Fig. 5.28.

The uncertainty corresponding to mismodeling of the p_{T}-dependence of τ_b is estimated by parametrising its shape using a linear function extracted from the fit to simulation in the extended fit range. This uncertainty is relevant for the differential cross-section measurement. This uncertainty is parametrised to be linearly dependent on the bin as shown on Fig. 5.29.

The uncertainty corresponding to the η_c and J/ψ efficiency ratio is estimated via changing the η_c and J/ψ efficiency ratio by the uncertainty corresponding to the MC sample sizes.

Possible non-zero polarisation of prompt J/ψ mesons affects their reconstruction efficiency. The J/ψ polarisation has not been measured yet by LHCb at the $\sqrt{s}$ =13 TeV centre-of-mass energy. The LHCb experiment studied J/ψ polarisation at $\sqrt{s}$ =7 TeV [100]. Small non-zero longitudinal polarisation was measured with no significant polarisation dependence on transverse momentum or rapidity observed. Small polarisation was also observed by ALICE experiment in the forward kinematical regime at $\sqrt{s}$ =7 TeV [103]. The CMS experiment measured the J/ψ polarisation to be small for $|y| < 1.2$ at $\sqrt{s}$ =7 TeV [102]. The uncertainty of the present measurement is estimated by reweighting prompt J/ψ simulation sample using the following weights:

$$\frac{3}{4\pi \times (3 - \lambda_\theta)} \times (1 - \lambda_\theta \cos^2 \theta) \ , \tag{5.13}$$

where θ is the angle between the proton direction in the J/ψ rest frame and the J/ψ boost axis and λ_θ is the polarisation parameter. To estimate the systematic uncertainty the MC sample is reweighted using a typical value of $\lambda_\theta = \pm 0.1$, as suggested by J/ψ production

cross-section measurement at the $\sqrt{s}$ =13 TeV [94]. This uncertainty is correlated between p_{T}-bins.

Systematic uncertainties on relative η_c production measurement in the entire $6.5\,\mathrm{GeV} < p_{\mathrm{T}} < 14.0\,\mathrm{GeV}$ range are shown in Table 5.9. Detailed tables of systematic uncertainties for each bin of p_{T} are given in Tables 5.10, 5.11, 5.12 and 5.13.

The dominant source of uncorrelated systematic uncertainty for prompt η_c production is related to combinatorial background description. The dominant sources of uncorrelated systematic uncertainties on η_c production in b-decays are related to combinatorial background description and the p_{T}-dependence of the η_c and J/ψ resolution ratio. The dominant source of correlated systematic uncertainties on both prompt η_c production and η_c production in b-decays is related to knowledge of η_c natural width and the invariant mass resolution model.

Uncertainties on the branching fractions of the $J/\psi \to p\overline{p}$ and $\eta_c \to p\overline{p}$ decay modes are taken into account to estimate corresponding uncertainties in the production cross-section measurements. They are combined in a separate systematic uncertainty, correlated between the bins of transverse momentum. The uncertainty consists of two separate uncertainties on $\mathcal{B}_{J/\psi\to p\overline{p}} = (2.120 \pm 0.029) \times 10^{-3}$ and $\mathcal{B}_{\eta_c\to p\overline{p}} = (1.50 \pm 0.16) \times 10^{-3}$ [188] and amounts to about 10%.

When extracting the absolute η_c production cross-section values, the uncertainties on the measured J/ψ production cross-section [94] are also taken into account.

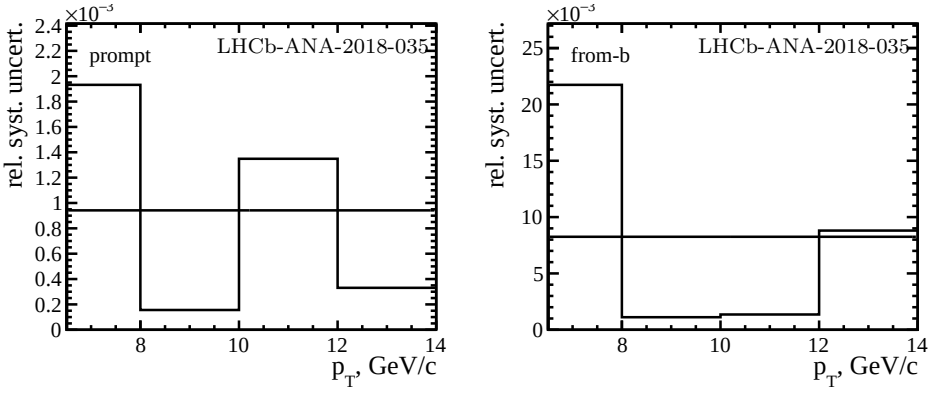

Figure 5.22: Relative systematic uncertainty due to the p_{T}-dependence of η_c and J/ψ resolution ratio in bins of p_{T}. The solid black line shows a smoothing curve.

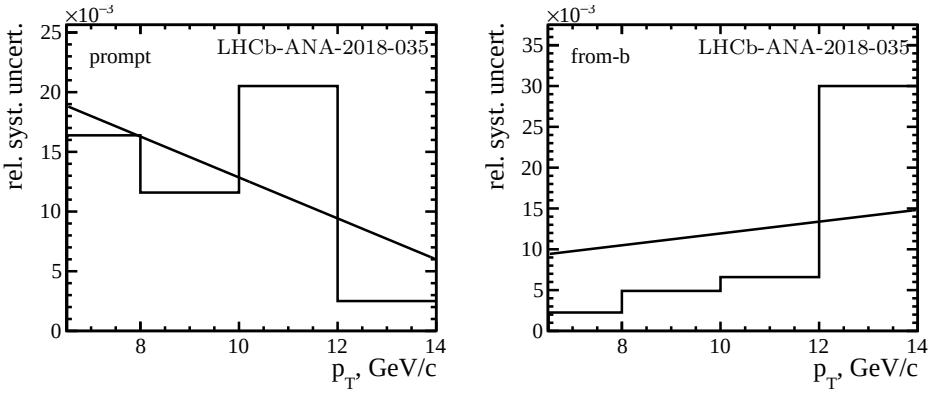

Figure 5.23: Relative systematic uncertainty due to resolution correction factors α_{t_z} in bins of p_{T}. The solid black line shows a smoothing curve.

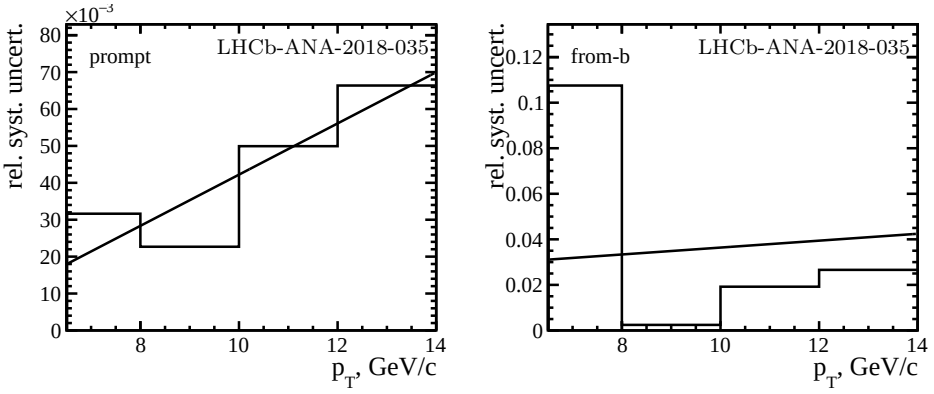

Figure 5.24: Relative systematic uncertainty due to combinatorial background description in bins of p_{T}. The solid black line shows a smoothing curve.

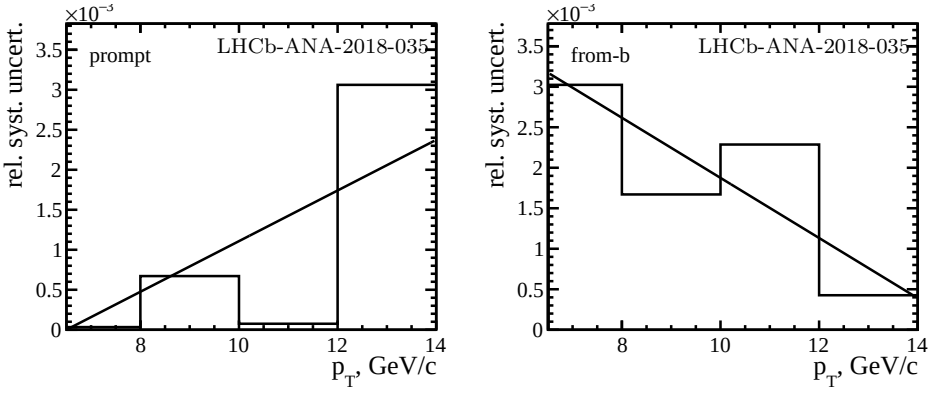

Figure 5.25: Relative systematic uncertainty due to description of the feed-down from the $J/\psi \to p\bar{p}\pi^0$ decay in bins of p_{T}. The solid black line shows a smoothing curve.

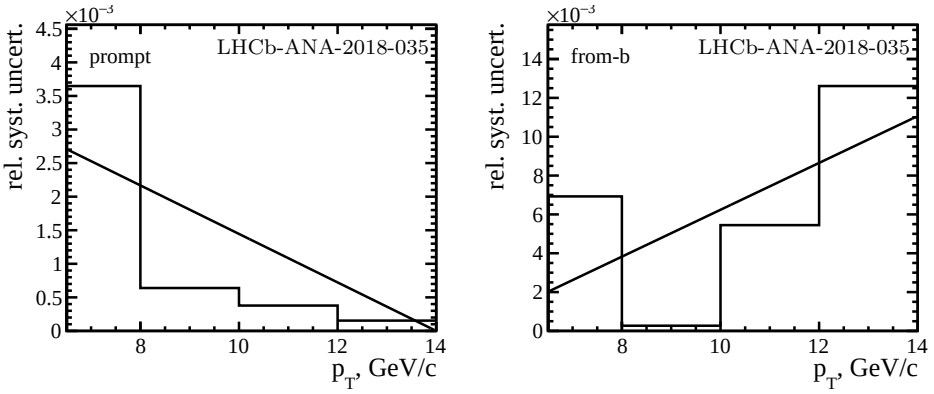

Figure 5.26: Relative systematic uncertainty due to t_z-resolution mismodeling in bins of p_{T}. The solid black line shows a smoothing curve.

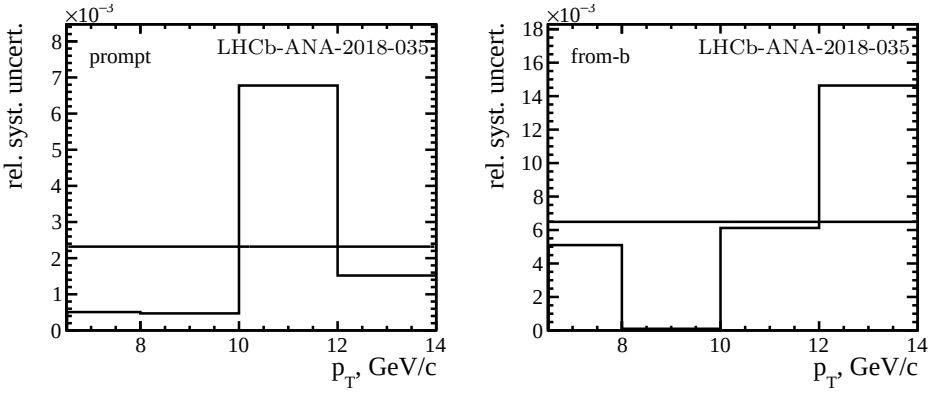

Figure 5.27: Relative systematic uncertainty due to bias μ in bins of p_{T}. The solid black line shows a smoothing curve.

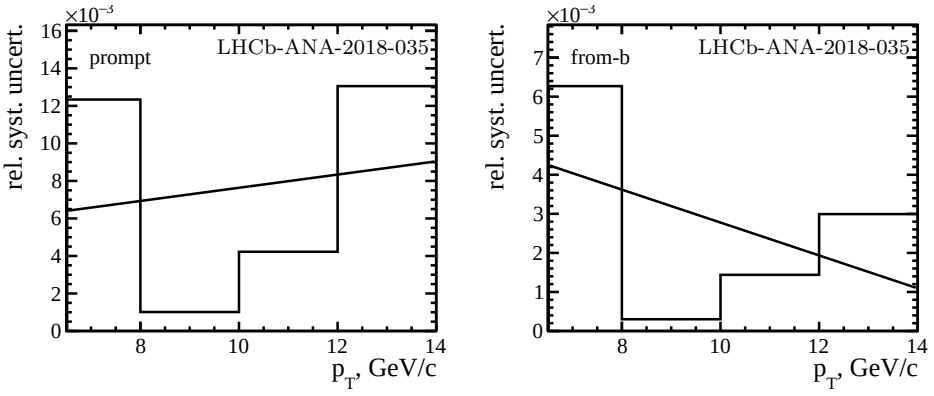

Figure 5.28: Relative systematic uncertainty due to mismodeling of p_{T}-dependence of t_z resolution in bins of p_{T}. The solid black line shows a smoothing curve.

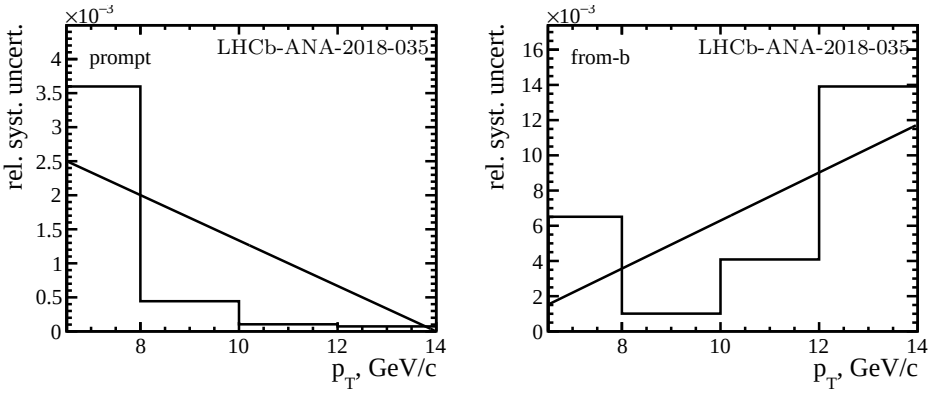

Figure 5.29: Relative systematic uncertainty due to mismodeling of p_{T}-dependence of τ_b distribution in bins of p_{T}. The solid black line shows a smoothing curve.

	$N_{\eta_c}^{prompt}/N_{J/\psi}^{prompt}$	$N_{\eta_c}^{b-decays}/N_{J/\psi}^{b-decays}$
Mean value	1.316	0.331
Stat. uncertainty	8.6	9.2
α_{t_z} corrections	1.7	0.3
Mass resolution model	3.0	3.8
Comb. bkg. description	3.4	1.7
Variation of $\Gamma(\eta_c)$	5.2	5.1
Contribution from $J/\psi \to p\bar{p}\pi^0$	< 0.1	0.7
Bias μ	0.7	0.2
t_z-resolution model	< 0.1	< 0.1
J/ψ polarisation	1.8	–
Total systematic	7.4	6.6

Table 5.9: Mean values and relative uncertainties (in %) in the η_c and J/ψ yield ratios for p_{T}-integrated $6.5\,\mathrm{GeV} < p_{\mathrm{T}} < 14.0\,\mathrm{GeV}$ data sample.

	$N_{\eta_c}^{prompt}/N_{J/\psi}^{prompt}$	$N_{\eta_c}^{b-decays}/N_{J/\psi}^{b-decays}$
Mean value	1.082	0.281
Stat. uncertainty	19.6	25.4
α_{t_z} corrections	1.8	1.0
p_{T}-dependence of $\sigma_{\eta_c}/\sigma_{J/\psi}$	0.1	0.8
Comb. bkg. description	2.3	3.2
Contribution from $J/\psi \to p\overline{p}\pi^0$	< 0.1	0.3
p_{T}-dependence of t_z resolution	0.7	0.4
p_{T}-dependence of τ_B	0.2	0.3
Bias μ	0.3	0.2
t_z-resolution model	0.2	0.3
Total systematic uncorrelated	3.0	3.6
J/ψ polarisation	2.1	–
Mass resolution model	3.0	3.8
Variation of Γ_{η_c}	5.2	5.1
Total systematic correlated	6.4	6.4
Total systematic	7.0	7.3

Table 5.10: Mean values and relative uncertainties (in %) in the η_c and J/ψ yield ratios for $6.5\,\mathrm{GeV} < p_{\mathrm{T}} < 8.0\,\mathrm{GeV}$.

	$N_{\eta_c}^{prompt}/N_{J/\psi}^{prompt}$	$N_{\eta_c}^{b-decays}/N_{J/\psi}^{b-decays}$
Mean value	1.291	0.396
Stat. uncertainty	13.7	12.0
α_{t_z} corrections	1.5	1.1
p_{T}-dependence of $\sigma_{\eta_c}/\sigma_{J/\psi}$	0.1	0.8
Comb. bkg. description	3.5	3.5
Contribution from $J/\psi \to p\overline{p}\pi^0$	0.1	0.2
p_{T}-dependence of t_z resolution	0.7	0.3
p_{T}-dependence of τ_B	0.2	0.5
Bias μ	0.3	0.2
t_z-resolution model	0.2	0.5
Total systematic uncorrelated	3.9	3.9
J/ψ polarisation	1.8	–
Mass resolution model	3.0	3.8
Variation of Γ_{η_c}	5.2	5.1
Total systematic correlated	6.3	6.4
Total systematic	7.4	7.5

Table 5.11: Mean values and relative uncertainties (in %) in the η_c and J/ψ yield ratios for $8.0\,\mathrm{GeV} < p_{\mathrm{T}} < 10.0\,\mathrm{GeV}$.

	$N_{\eta_c}^{prompt}/N_{J/\psi}^{prompt}$	$N_{\eta_c}^{b-decays}/N_{J/\psi}^{b-decays}$
Mean value	1.463	0.277
Stat. uncertainty	15.6	18.9
α_{t_z} corrections	1.1	1.3
p_{T}-dependence of $\sigma_{\eta_c}/\sigma_{J/\psi}$	0.1	0.8
Comb. bkg. description	4.9	3.8
Contribution from $J/\psi \to p\overline{p}\pi^0$	0.1	0.2
p_{T}-dependence of t_z resolution	0.8	0.2
p_{T}-dependence of τ_B	0.1	0.8
Bias μ	0.3	0.2
t_z-resolution model	0.1	0.7
Total systematic uncorrelated	5.1	4.3
J/ψ polarisation	1.6	–
Mass resolution model	3.0	3.8
Variation of Γ_{η_c}	5.2	5.1
Total systematic correlated	6.2	6.4
Total systematic	8.1	7.7

Table 5.12: Mean values and relative uncertainties (in %) in the η_c and J/ψ yield ratios for $10.0\,\mathrm{GeV} < p_{\mathrm{T}} < 12.0\,\mathrm{GeV}$.

	$N_{\eta_c}^{prompt}/N_{J/\psi}^{prompt}$	$N_{\eta_c}^{b-decays}/N_{J/\psi}^{b-decays}$
Mean value	2.125	0.293
Stat. uncertainty	18.9	25.2
α_{t_z} corrections	0.8	1.4
p_{T}-dependence of $\sigma_{\eta_c}/\sigma_{J/\psi}$	0.1	0.8
Comb. bkg. description	6.3	4.1
Contribution from $J/\psi \to p\overline{p}\pi^0$	0.2	0.1
p_{T}-dependence of t_z resolution	0.9	0.2
p_{T}-dependence of τ_B	< 0.1	1.0
Bias μ	0.3	0.2
t_z-resolution model	< 0.1	1.0
Total systematic uncorrelated	6.4	4.7
J/ψ polarisation	1.6	–
Mass resolution model	3.0	3.8
Variation of Γ_{η_c}	5.2	5.1
Total systematic correlated	6.2	6.4
Total systematic	8.9	7.9

Table 5.13: Mean values and relative uncertainties (in %) in the η_c and J/ψ yield ratios for $12.0\,\mathrm{GeV} < p_{\mathrm{T}} < 14.0\,\mathrm{GeV}$.

5.5 Separation technique

In the analysis of η_c production with LHCb Run I data, the data sample was split into prompt sample and b-decays sample. The charmonia signal in each sample is dominated by the corresponding production process. A separation between promptly produced charmonia decaying at PV and charmonia produced in b-decays with large typically t_z values is performed using t_z requirement. To select charmonia from b-decays, an additional requirement on impact parameter significance $\chi^2_{\rm IP}$[1] of both proton and antiproton candidates is applied. The efficiencies and cross-feed between the two samples are obtained from simulation to extract prompt and non-prompt production. Below, the same analysis technique is applied for data collected at $\sqrt{s}$ =13 TeV.

Signal selection criteria are the same as discussed in Section 5.3. The separation between samples is achieved by applying the requirement $t_z < 80\,\text{fs}$ to select the prompt sample and the requirements $t_z > 80\,\text{fs}$ and $\chi^2_{\rm IP} > 16$ to select the bquark-decays sample.

The number of observed η_c candidates in the prompt and bquark-decays sample can be written in the following way

$$\begin{cases} n^p_{\eta_c} &= \epsilon^{P\to P}\boldsymbol{N^P_{\eta_c}} + \epsilon^{b\to P}\boldsymbol{N^b_{\eta_c}} \\ n^b_{\eta_c} &= \epsilon^{b\to b}\boldsymbol{N^b_{\eta_c}} + \epsilon^{P\to b}\boldsymbol{N^P_{\eta_c}}, \end{cases} \tag{5.14}$$

where $n^p_{\eta_c}$ and $n^b_{\eta_c}$ are η_c yields in the prompt sample and in b-decays sample from simultaneous fit of the invariant mass of the two samples, respectively; $N^P_{\eta_c}$ is the number of promptly produced η_c; $N^b_{\eta_c}$ is the number of η_c produced in b-decays; $\epsilon^{P\to P}$ is the separating requirement efficiency for selecting promptly produced η_c using selection criteria of prompt sample; $\epsilon^{P\to b}$ is separating requirement efficiency efficiency for selecting promptly produced η_c using selection of b-decays sample; and the efficiencies $\epsilon^{b\to b}$ and $\epsilon^{b\to P}$ for η_c produced in b-hadron decays are defined in similar way. Similar definitions for J/ψ equally apply.

Solving equations (5.14), the number of promptly produced η_c meson is

$$N^P_{\eta_c} = \frac{\epsilon^{b\to b} n^p_{\eta_c} - \epsilon^{b\to P} n^b_{\eta_c}}{\epsilon^{P\to P}\epsilon^{b\to b} - \epsilon^{P\to b}\epsilon^{b\to P}}, \tag{5.15}$$

[1]The $\chi^2_{\rm IP}$ is defined as the χ^2 difference of the PV reconstructed with and without considered track.

and the number of η_c produced in b-hadron decays is

$$N^b_{\eta_c} = \frac{\epsilon^{P\to P} n^b_{\eta_c} - \epsilon^{P\to b} n^p_{\eta_c}}{\epsilon^{P\to P}\epsilon^{b\to b} - \epsilon^{P\to b}\epsilon^{b\to P}}. \tag{5.16}$$

Hence, the relative η_c and J/ψ production can be expressed in the following way.

$$\begin{aligned} \frac{\sigma^{prompt}_{\eta_c}}{\sigma^{prompt}_{J/\psi}} &= \frac{\epsilon^{b\to b} n^p_{\eta_c} - \epsilon^{b\to P} n^b_{\eta_c}}{\epsilon^{b\to b} n^p_{J/\psi} - \epsilon^{b\to P} n^b_{J/\psi}} \times \frac{\epsilon_{J/\psi}}{\epsilon_{\eta_c}} \times \frac{\mathcal{B}_{J/\psi\to p\overline{p}}}{\mathcal{B}_{\eta_c\to p\overline{p}}} \\ \frac{\sigma^{b-decays}_{\eta_c}}{\sigma^{b-decays}_{J/\psi}} = \frac{\mathcal{B}_{b\to\eta_c(1S)X}}{\mathcal{B}_{b\to J/\psi X}} &= \frac{\epsilon^{P\to P} n^b_{\eta_c} - \epsilon^{P\to b} n^p_{\eta_c}}{\epsilon^{P\to P} n^b_{J/\psi} - \epsilon^{P\to b} n^p_{J/\psi}} \times \frac{\epsilon_{J/\psi}}{\epsilon_{\eta_c}} \times \frac{\mathcal{B}_{J/\psi\to p\overline{p}}}{\mathcal{B}_{\eta_c\to p\overline{p}}}, \end{aligned} \tag{5.17}$$

where ϵ_{η_c} and $\epsilon_{J/\psi}$ are the total reconstruction and selection efficiencies before applying separating requirement for η_c and J/ψ respectively.

5.5.1 Separating requirements efficiencies

Efficiencies of the separating requirements are extracted from MC samples to evaluate the cross-feed between the samples. Values of the efficiencies are listed in Table 5.14. No significant difference between the η_c and J/ψ separating requirement efficiencies is observed.

$\epsilon^{P\to P}$	0.964 ± 0.011
$\epsilon^{b\to b}$	0.692 ± 0.013
$\epsilon^{P\to b}$	0.0007 ± 0.0002
$\epsilon^{b\to P}$	0.064 ± 0.003

Table 5.14: Cross-feed efficiencies between prompt and b-decays samples for *separation technique*.

A good agreement between data and MC in t_z distribution is observed for all parameters describing t_z-resolution model and τ_b, which leads to good agreement of t_z requirement efficiency between data and MC. To extract the efficiency of $t_z < 80\,\text{fs}$ ($> 80\,\text{fs}$) requirement from data one can integrate the curve of the fit to t_z obtained in Section 5.4.2. The comparison of this requirement efficiency estimated from data and from MC is shown in Table 5.15. The values are well consistent within the uncertainty due to MC sample sizes.

The requirement on proton χ^2_{IP} is also used in the analysis with *separation technique*. Here, its efficiency enters the definition of $\varepsilon^{P\to b}$ and $\varepsilon^{b\to b}$. The χ^2_{IP} variable is proved to be well described by MC. The cross-feed described by $\varepsilon^{P\to b}$ is small and the contamination of

	from t_z-*fit technique*	MC
$\varepsilon^{J/\psi,prompt}(t_z < 80\,\text{fs})$	$0.955 \pm 0.003_{(stat.uncorrelated)}$	0.964 ± 0.011
$\varepsilon^{J/\psi,b-decays}(t_z > 80\,\text{fs})$	$0.938 \pm 0.002_{(stat.uncorrelated)}$	0.936 ± 0.016

Table 5.15: Comparison of the $t_z < 80\,\text{fs}$ ($> 80\,\text{fs}$) requirement efficiency as estimated in data and MC for prompt charmonia and charmonia from b-decays.

b-decays sample by prompt η_c is about 1.5% (about 0.4% for J/ψ), which is estimated using known η_c prompt yield from t_z-*fit technique*. The effect of this cross-feed is also checked by setting $\varepsilon^{P\to b} \equiv 0$, which does not lead to a significant change in $N_{\eta_c}^{prompt}/N_{J/\psi}^{prompt}$ and $N_{\eta_c}^{b-decays}/N_{J/\psi}^{b-decays}$ within 1% level.

Since the contamination of b-decays sample by prompt candidates is small, one can evaluate the value of $\varepsilon^{b\to b}$ from data by comparing a signal yield in b-decays sample and the total number of signal candidates from b-decays obtained from t_z-*fit technique*. The comparison between data and MC values is shown in Table 5.16.

	from t_z-*fit technique* and *separation technique*	MC
$\varepsilon^{b\to b}$	$0.699 \pm 0.076_{(stat)}$	0.692 ± 0.013

Table 5.16: Comparison of the $\varepsilon^{b\to b}$ requirement efficiency from data and MC.

From all above one can conclude that all possible systematic effects due to the cross-feed efficiencies are well within the actual estimate of the cross-feed uncertainty.

5.5.2 Fit to the invariant mass

The same signal and background parameterisations as in Section 5.4.1 are used to describe the invariant mass distribution. No impact of separating requirement on the resolution model is observed using MC samples; hence, the resolution model is kept identical to that used in Section 5.4.3. The only difference is that the main resolution parameters σ_n in p_{T}-bins are free fit parameters. No significant peak position shifts are observed between prompt and b-decays samples. Therefore peak positions are required to be identical for prompt and b-decays samples. The mass of J/ψ meson and the J/ψ and η_c mass difference are free fit parameters in the fit to the invariant mass for p_{T}-integrated sample. Obtained values and statistical uncertainties of the J/ψ mass and the J/ψ and the η_c mass difference are then used in the gaussian constraints imposed for the fits in bins of p_{T}. The applicability of constraints on masses of J/ψ and η_c are cross-checked by performing individual fits to prompt and b-decays samples in p_{T}-bins.

A summary of signal shape parametrisation in simultaneous fit to both prompt and b-decay samples is shown in Table 5.17.

Parameter	
σ_n/σ_w	Fixed from MC
f_n	Fixed from MC
$\sigma_{\eta_c}/\sigma_{J/\psi}$	Fixed from MC
σ_{η_c}	Individual parameter for each p_{T}-bin
$m_{J/\psi} - m_{\eta_c}$	Common free parameter for both samples, gaussian constraint for fits in bins of p_{T}
$m_{J/\psi}$	Common free parameter for both samples, gaussian constraint for fits in bins of p_{T}
Γ_{η_c}	Fixed to the world average from Ref. [188] (31.8 MeV)

Table 5.17: Summary of signal parametrisation in the simultaneous invariant mass fit.

Projections of the simultaneous fit for the entire p_{T}-range $6.5\,\mathrm{GeV} < p_{\mathrm{T}} < 14.0\,\mathrm{GeV}$ are shown on Fig. 5.30. The residual and pull distributions are displayed below the corresponding projections. In general, fit yields a good description of both $M_{p\bar{p}}$ distributions. Simultaneous fit yields the following values of the J/ψ mass $M_{J/\psi} = (111.2 \pm 1.1)\,\mathrm{MeV}$ and the J/ψ and η_c mass difference $\Delta M_{J/\psi\,,\eta_c} = (3096.6 \pm 0.1)\,\mathrm{MeV}$. These values agree with the world average values $M^{PDG}_{J/\psi} = (3096.900 \pm 0.006)\,\mathrm{MeV}$ and $\Delta M^{PDG}_{J/\psi\,,\eta_c} = (113.5 \pm 0.5)\,\mathrm{MeV}$ [188].

Projections of the simultaneous fits to prompt and b-decays samples in p_{T} bins are shown on Figs. 5.31, 5.32, 5.33 and 5.34. In general, fit yields a good description of all $M_{p\bar{p}}$ distributions.

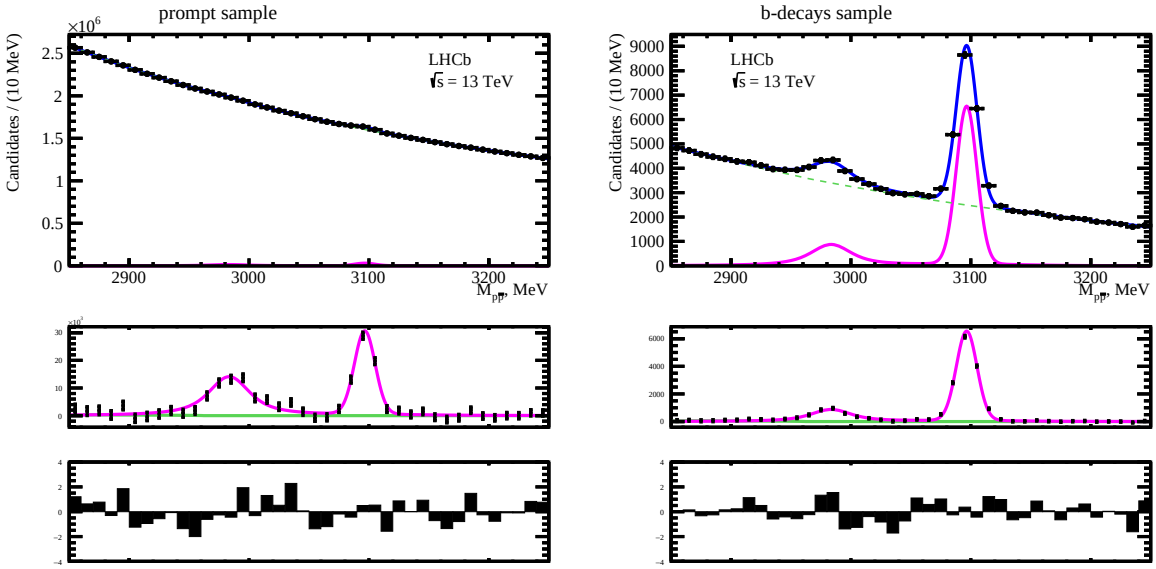

Figure 5.30: The $M_{p\bar{p}}$ distribution for prompt (left) and b-decays (right) p_{T}-integrated samples $6.5\,\mathrm{GeV} < p_{\mathrm{T}} < 14.0\,\mathrm{GeV}$. The solid blue lines represent the total fit result. Magenta and green lines show the signal and background components, respectively. The corresponding residual and pull distributions are shown below.

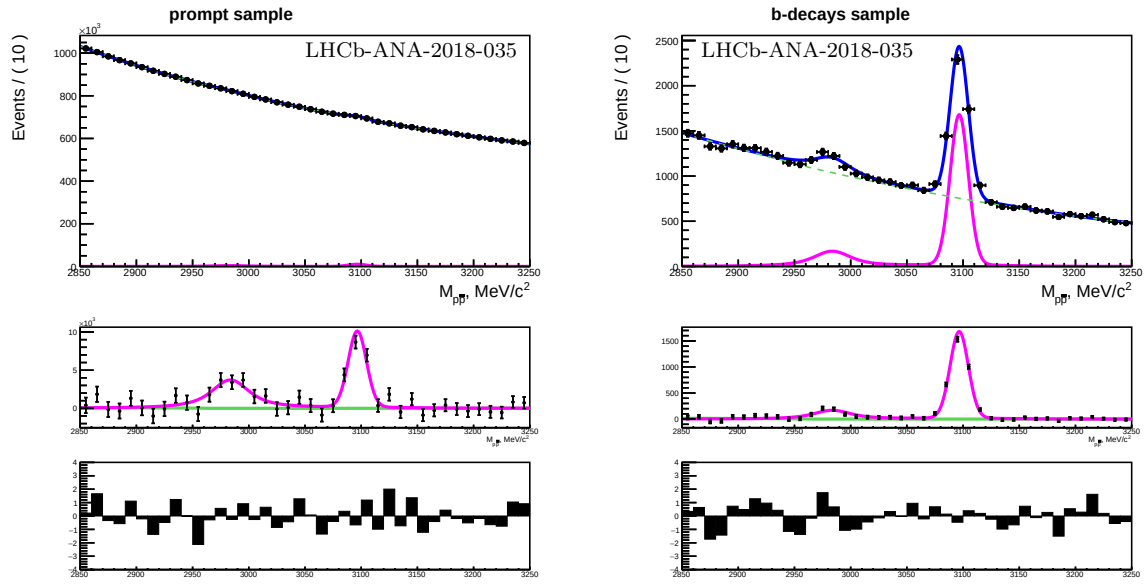

Figure 5.31: The $M_{p\bar{p}}$ distribution for prompt (left) and b-decays (right) for 6.5 GeV $< p_{\mathrm{T}} <$ 8.0 GeV. The solid blue lines represent the fit result. Magenta and green lines show the signal and background components, respectively. The corresponding residual and pull distributions are shown below.

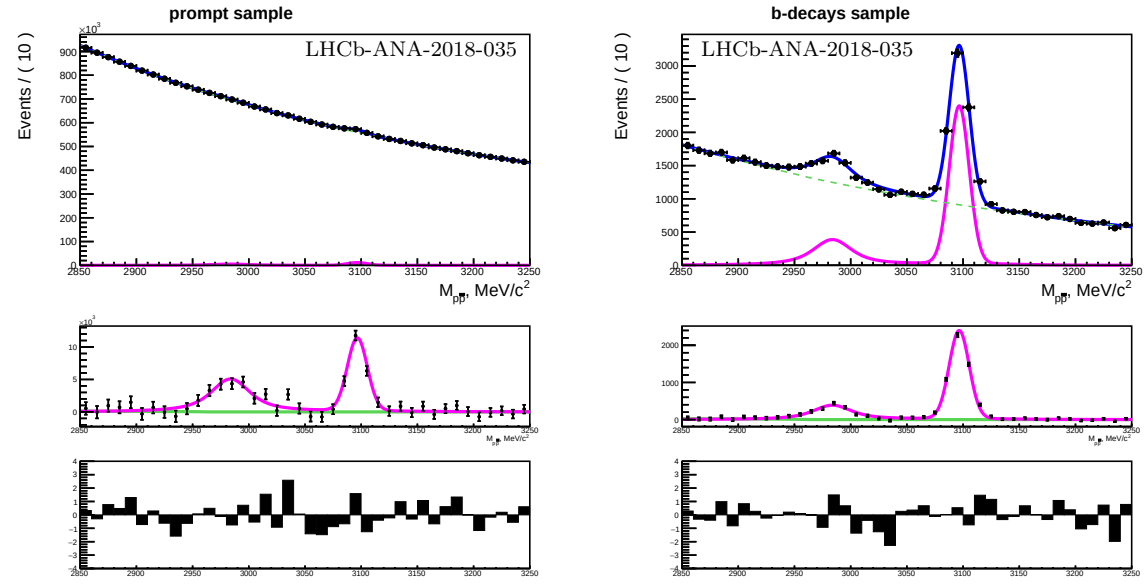

Figure 5.32: The $M_{p\bar{p}}$ distribution for prompt (left) and b-decays (right) for 8.0 GeV $< p_{\mathrm{T}} <$ 10.0 GeV. The solid blue lines represent the fit result. Magenta and green lines show the signal and background components, respectively. The corresponding residual and pull distributions are shown below.

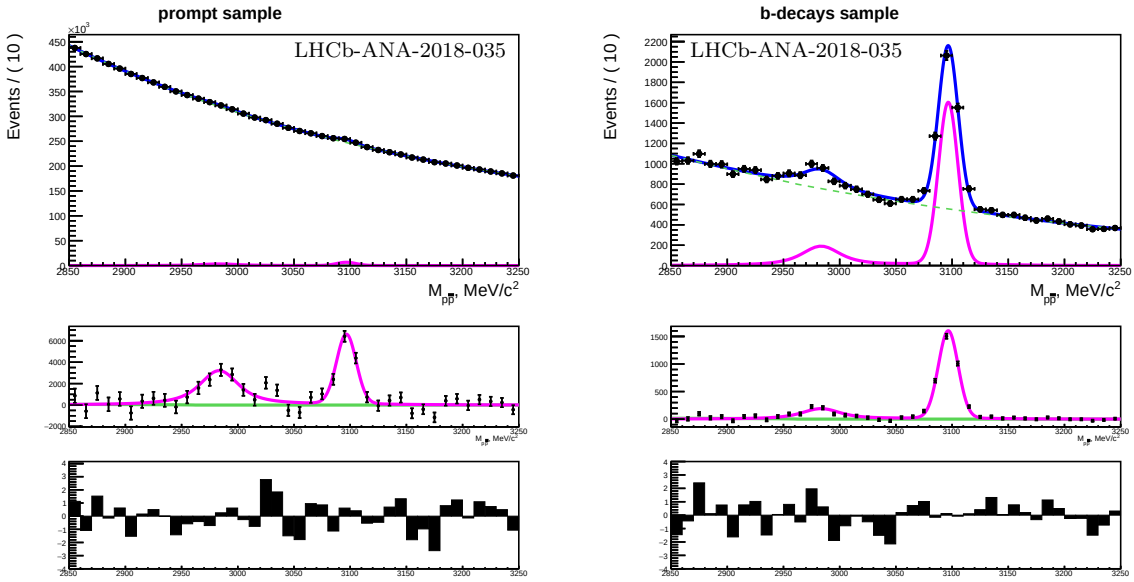

Figure 5.33: The $M_{p\bar{p}}$ distribution for prompt (left) and b-decays (right) for ($10.0\,\text{GeV} < p_{\text{T}} < 12.0\,\text{GeV}$. The solid blue lines represent the fit result. Magenta and green lines show the signal and background components, respectively. The corresponding residual and pull distributions are shown below.

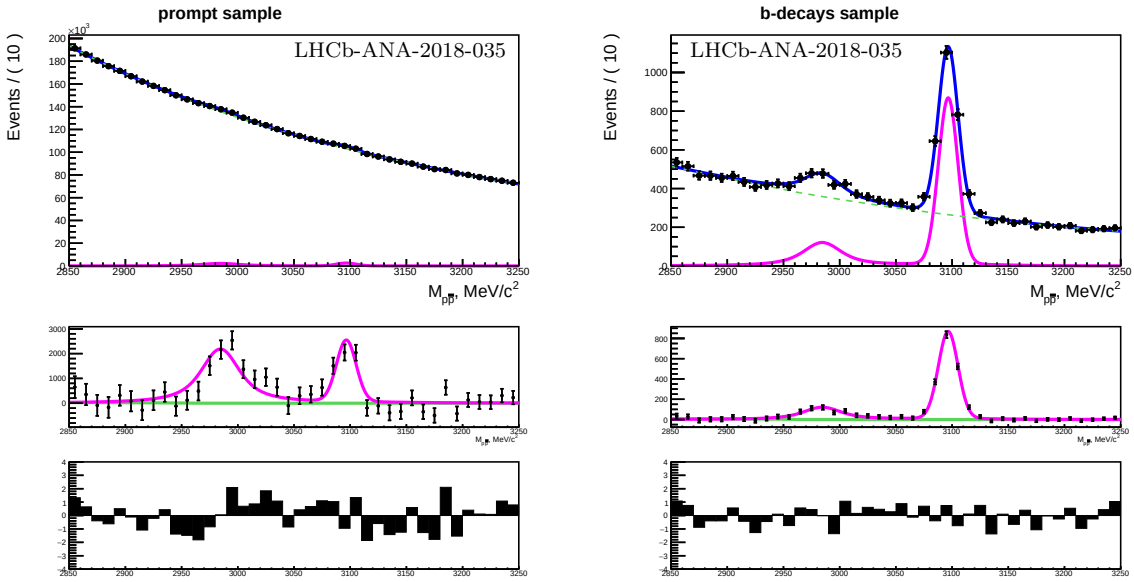

Figure 5.34: The $M_{p\bar{p}}$ distribution for prompt (left) and b-decays (right) for $12.0\,\text{GeV} < p_{\text{T}} < 14.0\,\text{GeV}$. The solid blue lines represent the fit result. Magenta and green lines show the signal and background components, respectively. The corresponding residual and pull distributions are shown below.

5.5.3 Systematic uncertainties

The following list of systematic uncertainties is identical for both *t_z-fit technique* and *separation technique*:

- Signal description in simultaneous fit to invariant mass distributions:
  - Knowledge of the η_c natural width, Γ_{η_c};
  - Invariant mass resolution mismodeling;
  - p_{T}-dependence of the η_c and J/ψ resolution ratio, $\sigma_{\eta_c}/\sigma_{J/\psi}$ (relevant for differential cross-section measurement);
- Background description in simultaneous fit to invariant mass distributions:
  - Combinatorial background description;
  - Description of the feed-down from the $J/\psi \to p\bar{p}\pi^0$ decay;
- The η_c and J/ψ efficiency ratio;
- Non-zero J/ψ polarisation;
- Uncertainties on $\mathcal{B}_{J/\psi\to p\bar{p}}$ and $\mathcal{B}_{\eta_c\to p\bar{p}}$;
- Uncertainties on J/ψ production for absolute η_c production cross-section measurement.

The estimation of each of these uncertainties is performed in the same way as in η_c production analysis using *t_z-fit technique* discussed in Section 5.4.3. The uncertainties related to the η_c and J/ψ efficiency ratio, combinatorial background description and the description of the feed-down from the $J/\psi \to p\bar{p}\pi^0$ decay are parametrised as shown on Figs. 5.35, 5.36 and 5.37 respectively.

The only additional systematic uncertainty is related to evaluation of the cross-feed. This uncertainty is estimated by modifying the efficiency values of the separating requirement by their uncertainties. Efficiencies of separation requirements are in good agreement between data and MC and possible discrepancies are well below the uncertainty due to MC sample sizes.

The dominant source of uncorrelated systematic uncertainty for prompt η_c production is related to combinatorial background description. The dominant sources of uncorrelated systematic uncertainties on η_c production in b-decays are related to combinatorial background description and the p_{T}-dependence of the η_c and J/ψ resolution ratio. The

dominant source of correlated systematic uncertainties on both prompt η_c production and η_c production in b-decays is related to the knowledge of the η_c natural width and the invariant mass resolution model.

Systematic uncertainties on relative η_c production measurement in the entire $6.5\,\text{GeV} < p_\text{T} < 14.0\,\text{GeV}$ range are shown in Table 5.18. Detailed tables of systematic uncertainties for each bin of p_T are given in Tables 5.19, 5.20, 5.21 and 5.22.

Uncertainties on the branching fractions of the $J/\psi \to p\overline{p}$ and $\eta_c \to p\overline{p}$ decay modes are combined in a separate systematic uncertainty as in Section 5.4.3.

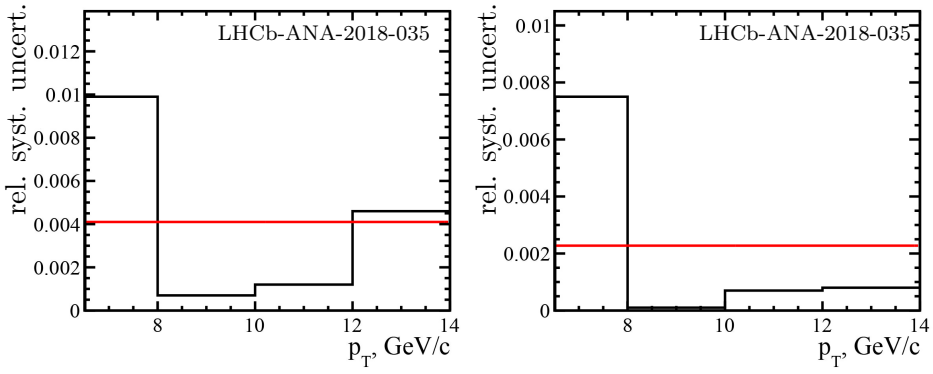

Figure 5.35: The relative systematic uncertainty due to the p_{T}-dependence of η_c and J/ψ resolution ratio in bins of p_{T}. The solid red line shows a smoothing curve.

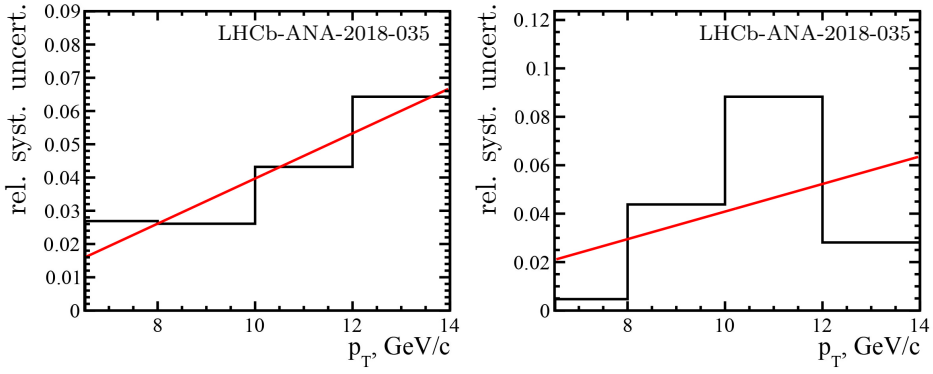

Figure 5.36: The relative systematic uncertainty due to combinatorial background description in bins of p_{T}. The solid red line shows a smoothing curve.

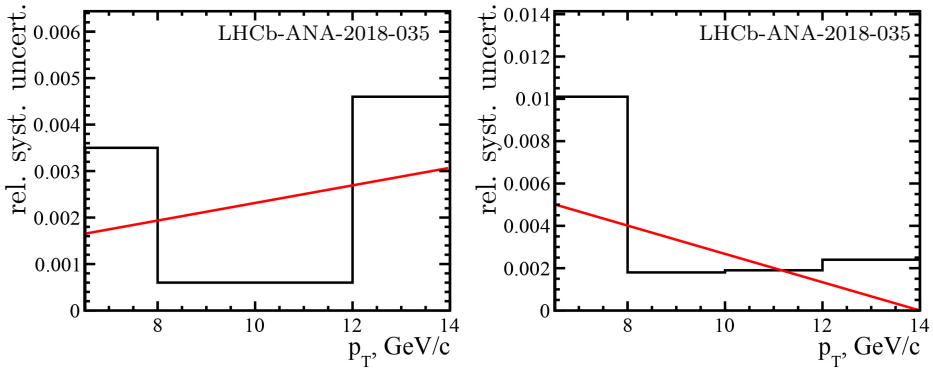

Figure 5.37: The relative systematic uncertainty due to description of the feed-down from the $J/\psi \to p\bar{p}\pi^0$ decay in bins of p_{T}. The solid red line shows a smoothing curve.

	$N^p_{\eta_c}/N^p_{J/\psi}$	$N^b_{\eta_c}/N^b_{J/\psi}$
Mean value	1.183	0.333
Stat. uncertainty	8.8	5.8
p_{T}-dependence of $\sigma_{\eta_c}/\sigma_{J/\psi}$	0.2	0.1
Comb. bkg. description	2.0	2.3
Contribution from $J/\psi \to p\overline{p}\pi^0$	< 0.1	0.2
Cross-feed	0.9	0.8
Mass resolution model	2.7	3.1
Variation of Γ_{η_c}	4.8	3.6
J/ψ polarisation	1.8	–
Total systematic	6.2	5.4

Table 5.18: Mean values and relative uncertainties (in %) in the η_c and J/ψ yields for p_{T}-integrated data sample $6.5\,\mathrm{GeV} < p_{\mathrm{T}} < 14.0\,\mathrm{GeV}$

	$N^p_{\eta_c}/N^p_{J/\psi}$	$N^b_{\eta_c}/N^b_{J/\psi}$
Mean value	0.984	0.263
Stat. uncertainty	22.7	15.4
p_{T}-dependence of $\sigma_{\eta_c}/\sigma_{J/\psi}$	0.4	0.2
Comb. bkg. description	2.1	2.5
Contribution from $J/\psi \to p\overline{p}\pi^0$	0.2	0.7
Cross-feed	1.9	1.4
Total systematic uncorrelated	2.9	3.0
Mass resolution model	2.7	3.1
Variation of Γ_{η_c}	4.8	3.6
J/ψ polarisation	2.1	–
Total systematic correlated	5.8	4.8
Total systematic	6.5	5.6

Table 5.19: Mean values and relative uncertainties (in %) in the η_c and J/ψ yields for the first p_{T} bin $6.5\,\mathrm{GeV} < p_{\mathrm{T}} < 8.0\,\mathrm{GeV}$

	$N^p_{\eta_c}/N^p_{J/\psi}$	$N^b_{\eta_c}/N^b_{J/\psi}$
Mean value	1.118	0.395
Stat. uncertainty	16.1	8.2
p_{T}-dependence of $\sigma_{\eta_c}/\sigma_{J/\psi}$	0.4	0.2
Comb. bkg. description	3.3	3.5
Contribution from $J/\psi \to p\overline{p}\pi^0$	0.2	0.5
Cross-feed	1.1	1.3
Total systematic uncorrelated	3.5	3.8
Mass resolution model	2.7	3.1
Variation of Γ_{η_c}	4.8	3.6
J/ψ polarisation	1.8	–
Total systematic correlated	5.7	4.8
Total systematic	6.7	6.1

Table 5.20: Mean values and relative uncertainties (in %) in the η_c and J/ψ yields for the first p_{T} bin $8.0\,\mathrm{GeV} < p_{\mathrm{T}} < 10.0\,\mathrm{GeV}$

	$N^p_{\eta_c}/N^p_{J/\psi}$	$N^b_{\eta_c}/N^b_{J/\psi}$
Mean value	1.241	0.290
Stat. uncertainty	16.9	12.8
p_{T}-dependence of $\sigma_{\eta_c}/\sigma_{J/\psi}$	0.4	0.2
Comb. bkg. description	4.6	4.7
Contribution from $J/\psi \to p\overline{p}\pi^0$	0.3	0.3
Cross-feed	1.2	1.7
Total systematic uncorrelated	4.8	5.0
Mass resolution model	2.7	3.1
Variation of Γ_{η_c}	4.8	3.6
J/ψ polarisation	1.6	–
Total systematic correlated	5.7	4.8
Total systematic	7.5	6.9

Table 5.21: Mean values and relative uncertainties (in %) in the η_c and J/ψ yields for the first p_{T} bin $10.0\,\mathrm{GeV} < p_{\mathrm{T}} < 12.0\,\mathrm{GeV}$

	$N^p_{\eta_c}/N^p_{J/\psi}$	$N^b_{\eta_c}/N^b_{J/\psi}$
Mean value	2.238	0.348
Stat. uncertainty	18.3	13.4
p_{T}-dependence of $\sigma_{\eta_c}/\sigma_{J/\psi}$	0.4	0.2
Comb. bkg. description	6.0	5.8
Contribution from $J/\psi \to p\overline{p}\pi^0$	0.3	0.1
Cross-feed	1.4	1.0
Total systematic uncorrelated	6.2	5.9
Mass resolution model	2.7	3.1
Variation of Γ_{η_c}	4.8	3.6
J/ψ polarisation	1.6	–
Total systematic correlated	5.7	4.8
Total systematic	8.4	7.6

Table 5.22: Mean values and relative uncertainties (in %) in the η_c and J/ψ yields for the first p_{T} bin $12.0\,\mathrm{GeV} < p_{\mathrm{T}} < 14.0\,\mathrm{GeV}$

5.6 Summary and discussion

The p_{T}-differential production of the η_c meson for both prompt charmonium production and production in inclusive b-hadron decays is obtained below.

The ratios of η_c and J/ψ differential production cross-sections obtained with the t_z-*fit technique* are shown on Fig. 5.38(a) for prompt η_c and on Fig. 5.38(b) for η_c produced in inclusive b-decays. The relative η_c prompt production is similar to those measured at $\sqrt{s}$ =7 and 8 TeV [13]. The linear slope of p_{T}-dependece of relative η_c to J/ψ prompt production is obtained to be 0.23 ± 0.11 GeV^{-1} and is not significantly different from zero. The relative η_c production in inclusive b-decays is consistent with those measured at $\sqrt{s}$ =7 and 8 TeV [13].

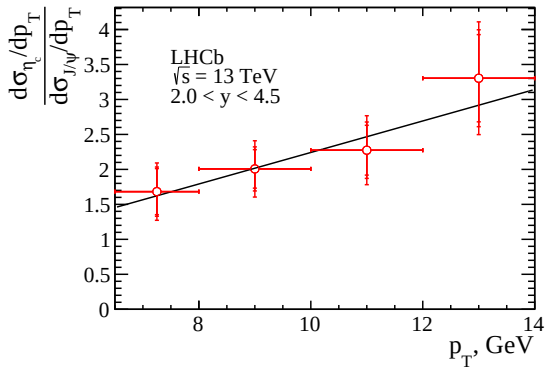

(a) Prompt-production. The result of the fit by a linear function is overlaid.

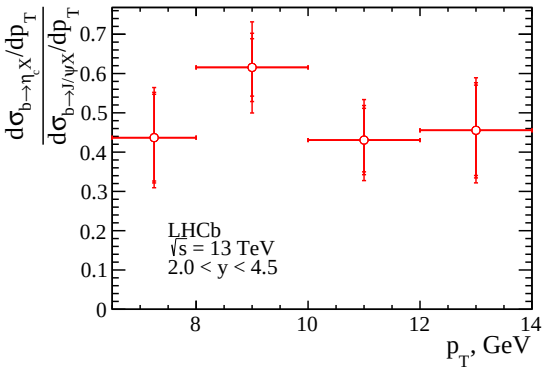

(b) Production in inclusive b-decays.

Figure 5.38: The ratios of η_c and J/ψ differential production cross-sections. The uncertainties shown are statistical, systematic, and the uncertainty due to the $J/\psi \to p\overline{p}$ and $J/\psi \to p\overline{p}$ branching fractions.

The comparison of the measurements using the *separation technique* and the t_z*-fit technique* is shown on Fig. 5.39. Both measurements give consistent results in all p_{T}-bins for both prompt production and production in b-decays. The two measurements are strongly correlated. For the prompt production the measurement using t_z*-fit technique* is more robust and is chosen as a final result. For the measurement of the production in b-decays the *separation technique* gives a more precise result which is retained. The obtained values of the relative differential cross-sections using both analysis techniques listed in Tables 10.1 and 5.24.

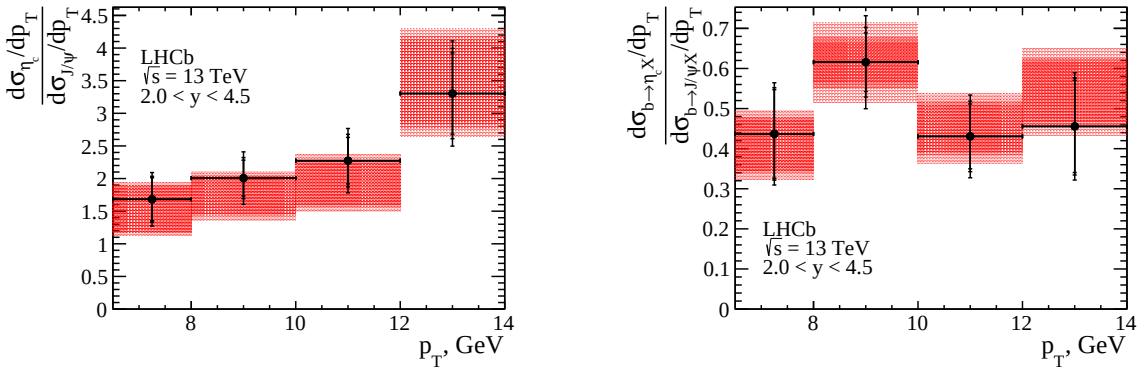

(a) Prompt production cross section.

(b) Production in inclusive b-decays.

Figure 5.39: The ratios of η_c and J/ψ differential production cross-sections (points) compared to result obtained with *separation technique* (red boxes). The uncertainties shown are statistical, systematic, and the uncertainty due to the $J/\psi \to p\overline{p}$ and $\eta_c \to p\overline{p}$ branching fractions.

p_{T}, GeV	$d\sigma_{\eta_c}^{prompt}/d\sigma_{J/\psi}^{prompt}$	
	t_z-fit technique	*separation technique*
6.5 - 8.0	1.68 ± 0.33 ± 0.06 ± 0.11 ± 0.21	1.53 ± 0.35 ± 0.05 ± 0.09 ± 0.19
8.0 - 10.0	2.01 ± 0.28 ± 0.09 ± 0.13 ± 0.25	1.74 ± 0.28 ± 0.07 ± 0.10 ± 0.22
10.0 - 12.0	2.27 ± 0.36 ± 0.13 ± 0.14 ± 0.28	1.93 ± 0.33 ± 0.10 ± 0.11 ± 0.24
12.0 - 14.0	3.30 ± 0.62 ± 0.22 ± 0.21 ± 0.41	3.48 ± 0.64 ± 0.23 ± 0.20 ± 0.43

Table 5.23: The p_{T}-differential ratios of η_c and J/ψ differential prompt production cross-sections.

p_{T}, GeV	$d\sigma_{\eta_c}^{b-decays}/d\sigma_{J/\psi}^{b-decays}$	
	t_z-fit technique	*separation technique*
6.5 - 8.0	0.44 ± 0.11 ± 0.02 ± 0.03 ± 0.05	0.41 ± 0.06 ± 0.01 ± 0.02 ± 0.05
8.0 - 10.0	0.62 ± 0.07 ± 0.03 ± 0.04 ± 0.08	0.61 ± 0.05 ± 0.03 ± 0.03 ± 0.08
10.0 - 12.0	0.43 ± 0.08 ± 0.02 ± 0.03 ± 0.05	0.45 ± 0.06 ± 0.02 ± 0.02 ± 0.06
12.0 - 14.0	0.46 ± 0.12 ± 0.02 ± 0.03 ± 0.06	0.54 ± 0.07 ± 0.03 ± 0.02 ± 0.07

Table 5.24: The p_{T}-differential ratios of η_c and J/ψ differential production cross-sections in inclusive b-decays.

The absolute η_c differential production cross-sections are shown on Fig. 5.40 for both prompt η_c and η_c produced in inclusive b-decays. The obtained values of the absolute differential cross-sections using both analysis techniques are listed in Tables 5.25 and 10.4. This is the first $p_{\rm T}$-differential cross-section measurement of the η_c prompt production at $\sqrt{s}$ =13 TeV. For illustative reasons, the exponential slopes of $p_{\rm T}$-dependences of η_c and J/ψ prompt production are obtained to be $e_{\eta_c} = 0.44\pm0.06\,{\rm GeV}^{-1}$ and $e_{J/\psi} = 0.57\pm0.01\,{\rm GeV}^{-1}$, respectively. Contrary to NRQCD expectations, the LHCb result indicates a steeper dependence of differential cross-section for J/ψ compared to that of η_c. It is important to confirm and possibly measure more accurately the difference in the $p_{\rm T}$-slope by extending the measurement to larger $p_{\rm T}$ values. A value of the $p_{\rm T}$-slope larger than prediction from Ref. [241]could be an indication of a possible color octet contribution.

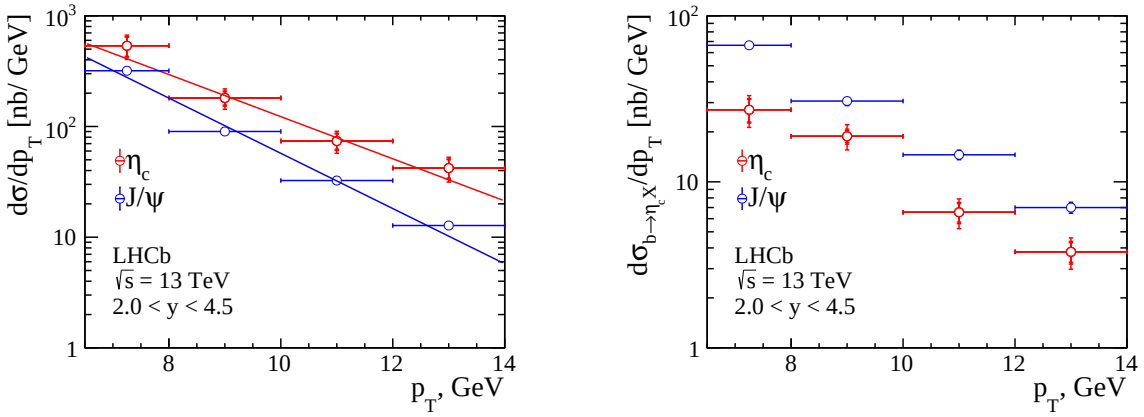

(a) Prompt-production cross section from t_z-*fit technique*. The results of the fits by exponential functions are overlaid.

(b) Production in inclusive b-decays from *separation technique*.

Figure 5.40: The η_c (red) and J/ψ (blue) $p_{\rm T}$-differential production cross section in inclusive b-decays from *separation technique*. The shown uncertainties for η_c production are statistical, systematic, and the uncertainty due to the $J/\psi \to p\overline{p}$ and $\eta_c \to p\overline{p}$ branching fractions and J/ψ production cross-section.

$p_{\rm T}$, GeV	$d\sigma^{prompt}_{\eta_c}/dp_{\rm T}$, nb/ GeV	
	t_z-fit technique	*separation technique*
6.5 - 8.0	536.09 ± 105.04 ± 19.61 ± 34.19 ± 70.67	487.53±110.49±17.01±28.24±64.27
8.0 - 10.0	180.92 ± 24.81 ± 7.90 ± 11.35 ± 24.97	156.68±25.23± 6.32± 8.97±21.62
10.0 - 12.0	73.92 ± 11.57 ± 4.07 ± 4.60 ± 10.32	62.70±10.61± 3.29± 3.54± 8.75
12.0 - 14.0	42.12 ± 7.95 ± 2.83 ± 2.62 ± 6.01	44.36± 8.13± 2.88± 2.52± 6.33

Table 5.25: The $p_{\rm T}$-differential η_c prompt production.

$p_{\rm T}$, GeV	$d\sigma^{b-decays}_{\eta_c}/dp_{\rm T}$, nb/ GeV	
	t_z-fit technique	*separation technique*
6.5 - 8.0	29.02 ± 7.33 ± 1.19 ± 1.86 ± 3.99	27.16± 4.23± 0.99± 1.34± 3.74
8.0 - 10.0	18.87 ± 2.24 ± 0.81 ± 1.19 ± 2.62	18.82± 1.52± 0.81± 0.91± 2.61
10.0 - 12.0	6.27 ± 1.18 ± 0.30 ± 0.41 ± 0.88	6.56± 0.84± 0.34± 0.32± 0.93
12.0 - 14.0	3.19 ± 0.81 ± 0.17 ± 0.21 ± 0.47	3.79± 0.51± 0.23± 0.18± 0.55

Table 5.26: The $p_{\rm T}$-differential η_c production cross-section in inclusive b-decays.

The relative prompt production rates of the η_c and J/ψ states in the LHCb fiducial region is measured to be

$$\left(\sigma_{\eta_c}/\sigma_{J/\psi}\right)^{6.5\,\text{GeV}<p_{\rm T}<14.0\,\text{GeV},2.0<y<4.5}_{13\,\text{TeV}} = 1.88 \pm 0.16_{stat} \pm 0.14_{syst} \pm 0.21_{norm}.$$

using *t_z-fit technique*. The η_c prompt production cross section in the LHCb fiducial region is then derived to be

$$\left(\sigma_{\eta_c}\right)^{6.5\,\text{GeV}<p_{\rm T}<14.0\,\text{GeV},2.0<y<4.5}_{13\,\text{TeV}} = (1.41 \pm 0.12_{stat} \pm 0.10_{syst} \pm 0.16_{norm})\ \mu\text{b}.$$

For comparison, according to Ref. [94], the J/ψ production at the same kinematic regime was measured to be:

$$\left(\sigma_{J/\psi}\right)^{6.5\,\text{GeV}<p_{\rm T}<14.0\,\text{GeV},2.0<y<4.5}_{13\,\text{TeV}} = (0.749 \pm 0.005 \pm 0.028 \pm 0.037)\ \mu\text{b}.$$

This is the first measurement of the η_c production at $\sqrt{s}$ =13 TeV. The obtained result supports the first conclusions from Ref. [13] on more prolific η_c production compared to J/ψ. The obtained η_c prompt production cross-section is in a good agreement with color singlet model prediction of $1.56^{+0.83\ +0.38}_{-0.49\ -0.17}$ μb, where the first and second uncertainties are due to scale and PDF (CT14NLO), respectively [241]. This leaves a limited room for a potential color octet contribution. This confirms the conclusion [120, 121, 128, 242] from η_c production studies at $\sqrt{s}$ =7 TeV and $\sqrt{s}$ =8 TeV [13].

The η_c inclusive branching fraction from b-hadron decays is measured to be:

$$\mathcal{B}_{b\to\eta_c(1S)X}/\mathcal{B}_{b\to J/\psi X} = 0.48 \pm 0.03_{stat} \pm 0.03_{syst} \pm 0.05_{norm}$$

and

$$\mathcal{B}_{b\to\eta_c(1S)X} = (5.51 \pm 0.32_{stat} \pm 0.29_{syst} \pm 0.77_{norm}) \times 10^{-3}.$$

using more precise *separation technique*.

Using also the LHCb measurement of the η_c prompt production at the $\sqrt{s}$ =7 TeV and $\sqrt{s}$ =8 TeV [13], the prompt η_c production cross-section is shown as a function of the centre-of-mass energy on Fig. 5.41. Using the J/ψ production cross-section ratio from Ref. [94], the ratio of η_c production at $\sqrt{s}$ =13 TeV and $\sqrt{s}$ =8 TeV is shown on Fig 5.42. The corresponding J/ψ production ratio in the same kinematic regime from Ref. [94] is shown for comparison. Note, that the uncertainty on the η_c ratio is strongly dominated by the statistical uncertainties of both measurements at 8 and 13 TeV and hence the ratio is less precise than the absolute cross-section measurement.

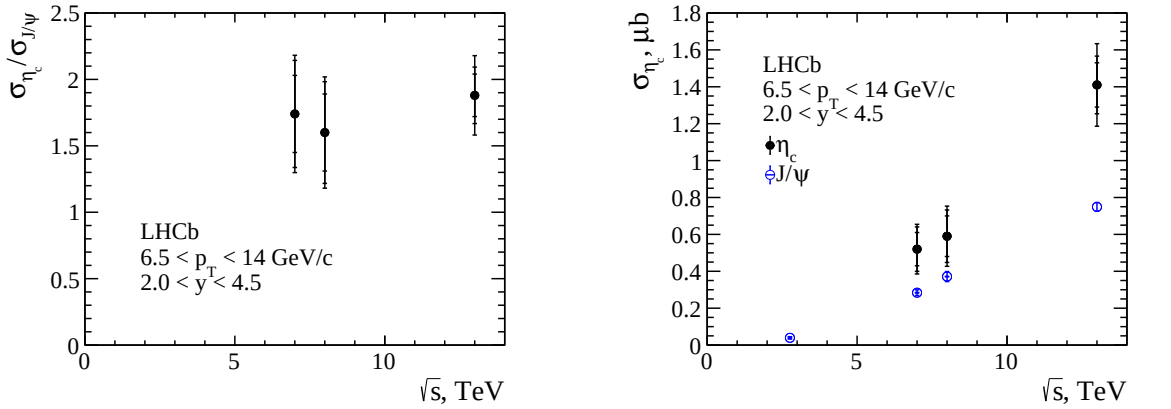

(a) Relative η_c prompt production cross section.

(b) Absolute η_c (black points) and J/ψ (blue points) prompt production cross section.

Figure 5.41: The η_c production as a function of centre-of-mass energy.

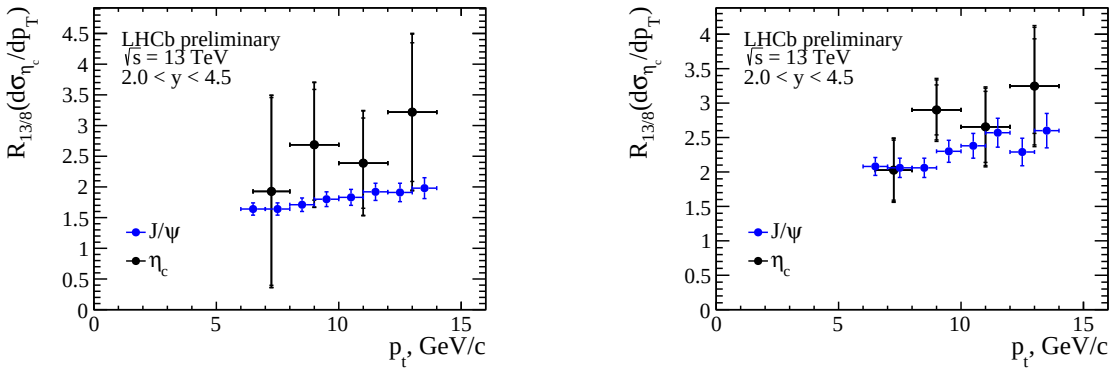

(a) Prompt production.

(b) Production in inclusive b-decays.

Figure 5.42: Ratios of the η_c (black points) and J/ψ (blue points) differential production cross-sections at $\sqrt{s}$ =13 and 8 TeV. The uncertainties shown are statistical, systematic and due to J/ψ production cross-section ratio.

Chapter 6

Study of charmonium states production using decays to $\phi\phi$

The charmonium decays to $\phi\phi$ is promising to access non-1^- states. It requires a reconstruction of four kaon tracks, which leads to smaller reconstruction efficiency compared to charmonium decays to $p\overline{p}$ with only two tracks in the final state. Nevertheless, it is not a priori clear, which channel is more advantageous to measure charmonium production. In proton-proton collisions, the number of produced $\phi\phi$ pairs is smaller than the number of $p\overline{p}$ pairs since four s quarks have to be created to produce $\phi\phi$ combination. In addition, the narrow ϕ resonance is situated near the K^+K^- threshold, and hence the background level under the ϕ signal is limited. Besides, the branching fractions of decays of excited charmonium states to $p\overline{p}$ are typically smaller than the ones for $\phi\phi$ decays.

This chapter summarises studies of charmonium states $\eta_c(1S)$, χ_{c0}, χ_{c1}, χ_{c2} and $\eta_c(2S)$ production in b-hadron inclusive decays using charmonia decays to $\phi\phi$ with the LHCb experiment. Within this analysis, the χ_{c0} and $\eta_c(2S)$ unambiguous signals are reconstructed, which is already essential to test theoretical predictions. Due to a much smaller number of $\phi\phi$ combinations produced at PV, the trigger aiming at the reconstruction of prompt $\phi\phi$ pairs would require much smaller trigger bandwidth compared to the trigger selecting $p\overline{p}$ combinations. Therefore, this analysis can also be considered as a first step to measuring prompt production of charmonium states, which are not accessible using other decay channels (e.g. $\eta_c(2S)$ and χ_{c0}).

This chapter is organised in the following way. After the analysis setup described in Section 6.1, the data and simulation samples are discussed in Section 6.2. The selection criteria and signal efficiencies are shown in Section 6.3. The results on the charmonium production in b-hadron decays are presented in Section 7.1. Section 6.6 stands for a search for production of charmonium-like states. Finally, the summary is given in Section 6.7.

6.1 Analysis setup

The main target of present analysis is to measure production of χ_c and $\eta_c(2S)$ states in inclusive b-hadron decays. Since strong decays of $J^{PC} = 1^{--}$ (J/ψ, $\psi(2S)$) states to two ϕ are forbidden, the decay mode $\eta_c(1S) \to \phi\phi$ is used as normalisation. The branching fraction of inclusive b decays to η_c meson was measured at LHCb [13] to be $\mathcal{B}(b \to \eta_c(1S)X) = (4.88 \pm 0.64 \pm 0.29 \pm 0.67_{\mathcal{B}}) \times 10^{-3}$, where the third uncertainty is due to uncertainties on the J/ψ inclusive branching fraction from b-hadron decays and branching fractions of the decays of J/ψ and $\eta_c(1S)$ to the $p\overline{p}$ final state.

A relative production of charmonium states A and B in the inclusive b-hadron decays is calculated from the ratio of observed event yields, efficiency ratio and ratio of branching fractions of A and B decays to $\phi\phi$,

$$\frac{\mathcal{B}(b \to AX) \times \mathcal{B}(A \to \phi\phi)}{\mathcal{B}(b \to BX) \times \mathcal{B}(B \to \phi\phi)} = \frac{N_A}{N_B} \times \frac{\varepsilon_B}{\varepsilon_A} \,, \tag{6.1}$$

where $N_A(N_B)$ are the observed yields of A(B) state; $\varepsilon_{A,B}$ are the corresponding total efficiencies to reconstruct, trigger and select $A \to \phi\phi$ and $B \to \phi\phi$ decays. For the states with similar kinematics - a good example is the ratio of the production of χ_c states - efficincies are similar, with their ratio close to unity.

6.2 Data sample, trigger and simulation

The present analysis uses the pp collision data recorded by the LHCb experiment at $\sqrt{s} = 7\,\text{TeV}$ in 2011 and at $\sqrt{s} = 8\,\text{TeV}$ in 2012. The analysis is based on an integrated luminosity $\int \mathcal{L}dt \approx 1.0\ \text{fb}^{-1}$ accumulated in 2011 and an integrated luminosity of $\int \mathcal{L}dt \approx 2.0\ \text{fb}^{-1}$ accumulated in 2012. For data processing, the reconstruction version 14 (Reco14), is used.

The same trigger lines as for the $B_s^0 \to \phi\phi$ study in Ref. [243] were used. The L0 Hadron decision `L0HadronDecision_TOS` or `L0Global_TIS` are applied at L0 trigger level. At the level of the HLT1, `HLT1TrackAllL0Decision_TOS` was used. At the level of the HLT2, `HLT2Topo(2,3,4)BodyBBDTDecision_TOS` or `HLT2IncPhiDecision_TOS` lines were used. The dedicated stripping lines (`StrippingCcbar2PhiPhiDetachedLine`, version 20r1 (Stripping20r1) are used.

The simulated events for this analysis are obtained using the `Pythia` (version 6 and 8) event generator and the `GEANT4` package. The following MC samples are used to study the η_c, χ_c and $\eta_c(2S)$ mass resolutions and efficiencies: In the simulation charmonium

Sample	Event type	Sample size
$\eta_c(1S) \to \phi\phi$	18104060	2.0 M
$\chi_{c0} \to \phi\phi$	18104030	1.1 M
$\chi_{c1} \to \phi\phi$	18104040	1.1 M
$\chi_{c2} \to \phi\phi$	18104050	1.1 M
$\eta_c(2S) \to \phi\phi$	18104080	1.1 M

Table 6.1: Simulation samples.

states are required to be produced in the decays of long-lived b-hadrons. Charmonia decays as well proceed via phase space decay model. At the generator level, all daughter particles are required to fly into LHCb acceptance. Reconstructed signal candidates and their daughter particles are required to match the generated ones.

6.3 Event selection

Selection aims at distinguishing pure ϕ candidates from the background by using charged kaon identification, narrow ϕ signal and at a later stage employing 2D fit procedure to select true $\phi\phi$ combinations (Section 6.4). In order to select b-hadrons, flying on average about 1 cm in the LHCb detector before their decay, and suppress combinatorial background associated to the PV, measurements of impact parameter of daughter kaons and a distance between b-production and b-decay vertices are used.

The ϕ candidates are reconstructed from oppositely charged particles identified as kaons by the LHCb detector, $ProbNNk > 0.1$. Both kaon track candidates are required to have a good quality of track reconstruction, $\chi^2/\text{ndf} < 3$. In order to suppress combinatorial background, the kaon tracks are required to have transverse momenta larger than 0.5 GeV. Since decays of b-hadrons are searched for, kaon tracks consistent with originating from PV are eliminated from the analysis by requiring large χ^2 value of the correcponding IP with respect to any PV, $\chi^2_{\text{IP}} > 4$.

The K^+K^- pairs forming ϕ candidates are required to have a good quality common vertex, $\chi^2/\text{ndf} < 25$. The K^+K^- invariant mass is required to be within ± 12 MeV from the known ϕ mass [77].

Two ϕ candidates are required to form good quality common vertex, $\chi^2/\text{ndf} < 9$. Finally, in order to further suppress combinatorial background associated with the tracks coming from PV, the common $\phi\phi$ vertex is required to be well-separated from the corresponding collision vertex with a flight distance significance of $\chi^2 > 100$.

	Variable	Denotion	Requirement
Kaons	Track quality	χ^2/ndf	< 3
	Impact parameter to primary vertex	χ^2_{IP}	> 4
	Transverse momentum	p_{T}, GeV	> 0.5
	Identification	ProbNNk	> 0.1
ϕ	Vertex quality	χ^2	< 25
	Invariant mass	$\lvert M_{K^+K^-} - M_\phi \rvert$, MeV	< 12
$\phi\phi$	Vertex quality	χ^2/ndf	< 9
	Distance between the decay vertex and the primary vertex	χ^2	> 100

Table 6.2: Selection criteria for charmonia decays to $\phi\phi$.

Table 9.2 summarizes selection criteria for charmonia and B^0_s meson decays to $\phi\phi$. Almost all selection had to be fixed already at the trigger/stripping level to limit the corresponding bandwidth. Exceptions are kaon identification and distance between primary and secondary vertices. The method applied to extract the signal does not seem to require strong kaon identification, since narrow ϕ peaks are selected. The charmonium yields are checked for stability against variantions in the PID requirement with no significant difference observed.

In order to obtain ratios of the branching fractions, efficiency ratios are determined using simulation samples to be

$$\begin{aligned}
\frac{\varepsilon(\chi_{c0} \to \phi\phi)}{\varepsilon(\eta_c(1S) \to \phi\phi)} &= 0.98 \pm 0.02 \ , \\
\frac{\varepsilon(\chi_{c1} \to \phi\phi)}{\varepsilon(\eta_c(1S) \to \phi\phi)} &= 1.04 \pm 0.02 \ , \\
\frac{\varepsilon(\chi_{c2} \to \phi\phi)}{\varepsilon(\eta_c(1S) \to \phi\phi)} &= 1.16 \pm 0.03 \ , \\
\frac{\varepsilon(\eta_c(2S) \to \phi\phi)}{\varepsilon(\eta_c(1S) \to \phi\phi)} &= 1.40 \pm 0.04 \ ,
\end{aligned}$$

where the uncertainties reflect the MC sample sizes.

Potential difference in the MC description of basic event properties and kinematics distributions could influence the efficiency ratios. A data-based cross-check for the distributions in p_{T}, pseudo-rapidity, event multiplicity, and polarization have been performed. Figures 6.1, 6.2, 6.3, and 6.4 show ratios of the χ_c states production in b-hadron decays to that of the $\eta_c(1S)$, in three bins of p_{T}, pseudo-rapidity, event multiplicity, and polarization, respectively. The potential impact on the efficiencies are compared to the corresponding statistical uncertainties in Table 6.3. No significant dependence within

	$\eta_c(1S)$	χ_{c0}	χ_{c1}	χ_{c2}
Statistical uncertainty	5%	15%	18%	18%
$\cos\theta_\phi$	+1%	−4%	−8%	+6%
Event multiplicity	−2%	−8%	< 1%	−7%
Pseudo-rapidity	−1%	−8%	−4%	−2%

Table 6.3: Effect on the efficiencies from potential differences in pseudo-rapidity, event multiplicity, and polarization, for considered charmonium states.

statistical uncertainties is observed in any bin of each variable considered. The efficiencies have nevertheless been corrected to the central values of the observed difference in p_{T} distribution. Given similar quantum numbers of the η_c states and a small-size sample of the reconstructed $\eta_c(2S)$ candidates, the ratio of the corresponding efficiencies from the simulation is used.

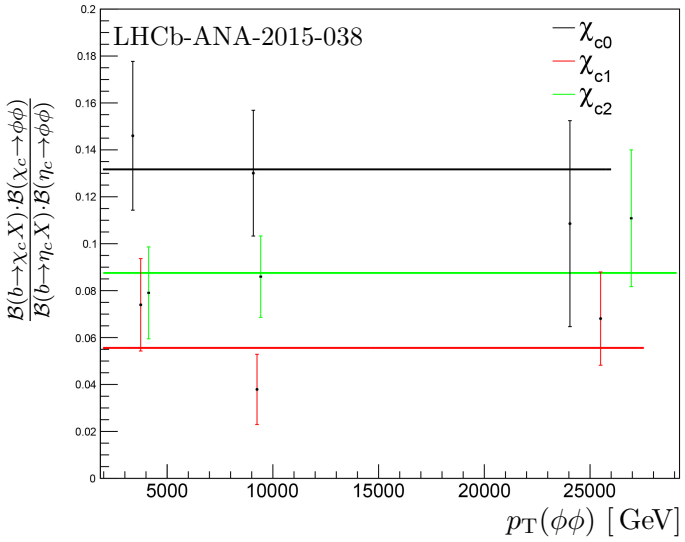

Figure 6.1: Ratio of the χ_c states production in b-hadron decays to that of $\eta_c(1S)$ in three bins of the p_{T}. Only statistical uncertainties are shown. Horizontal line corresponds to the fit result.

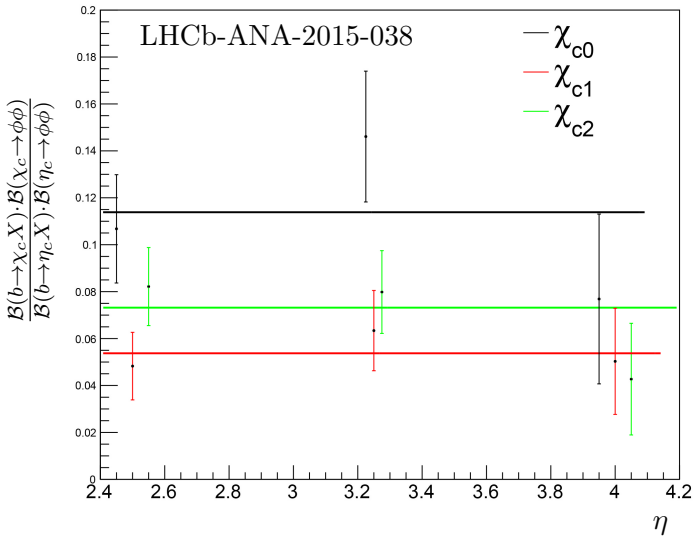

Figure 6.2: Ratio of the χ_c states production in b-hadron decays to that of $\eta_c(1S)$ in three bins of pseudo-rapidity. Only statistical uncertainties are shown. Horizontal line corresponds to the fit result.

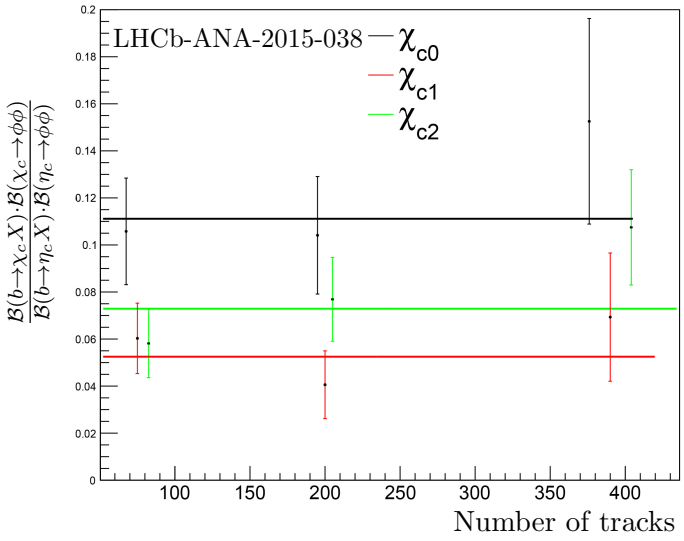

Figure 6.3: Ratio of the χ_c states production in b-hadron decays to that of $\eta_c(1S)$ in three bins of the event multiplicity. Only statistical uncertainties are shown. Horizontal line corresponds to the fit result.

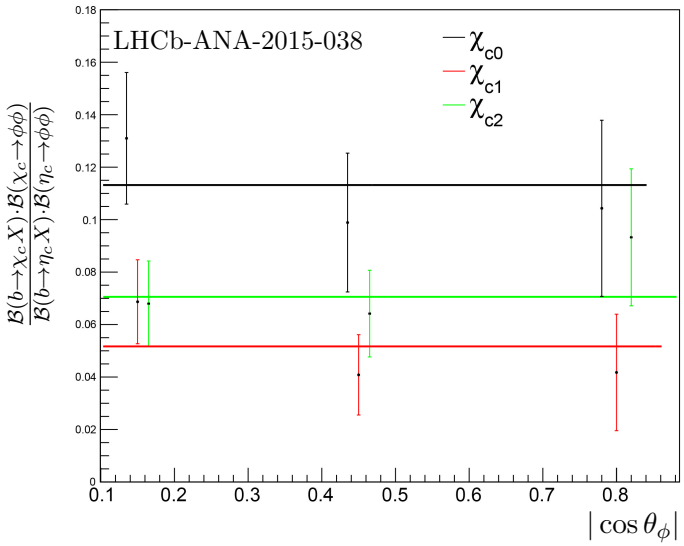

Figure 6.4: Ratio of the χ_c states production in b-hadron decays to that of $\eta_c(1S)$ in three bins of the absolute value of the $\cos\theta_\phi$, where θ_ϕ is the flight angle of the ϕ meson in the charmonium rest frame with respect to the charmonium boost direction. Only statistical uncertainties are shown. Horizontal line corresponds to the fit result.

6.4 Extraction of $\phi\phi$ signal yield

In order to extract a pure $\phi\phi$ component, the two-dimensional unbinned maximum likelihood fit corresponding to the two K^+K^- combinations, in the bins of the $K^+K^-K^+K^-$ invariant mass, was performed. Each of the two K^+K^- combinations is randomly assigned as the first or the second ϕ candidates. The two-dimensional fit accounts for the $\phi\phi$, ϕK^+K^- and $K^+K^-K^+K^-$ components, taking into account also the threshold factor. In the 2D fit of the K^+K^- invariant masses, ϕ signal is described by the convolution of the Breit-Wigner function to describe natural width of the ϕ resonance, and double Gaussian function to describe the effect of detector resolution. The ratio of the two Gaussian widths σ_1/σ_2 of 0.41 ± 0.01 and the fraction of narrow Gaussian $N_1/(N_1+N_2)$ of 0.87 ± 0.01 are taken from simulation. Combinatorial background is described by the first order polynomial. A threshold factor $\sqrt{x} = \sqrt{m_{KK} - 2m_K}$ to describe phase space difference is introduced in both signal and combinatorial background shapes. The complete description function is written as

$$\begin{aligned} F(x_1, x_2) = & N_{\phi\phi} \times S_1 \times S_2 + \\ & N_{\phi KK} \times (S_1 \times k_2 \times \sqrt{x_2} + S_2 \times k_1 \times \sqrt{x_1}) + \\ & N_{KKKK} \times (k_3 \times \sqrt{x_1} \times \sqrt{x_2}) \ , \end{aligned}$$

where signal functions S_1 and S_2 correspond to the PDF of the two ϕ candidates, and k_i are normalization coefficients. The fit shape accounts for $\phi\phi$, ϕK^+K^- and $K^+K^-K^+K^-$ contributions and takes into account the available phase space. The two-dimensional fit function as well as the projections on the two axes, for the complete event sample are shown on Figure 6.5, respectively.

The $\phi\phi$ mass spectrum is obtained from the $\phi\phi$ signal yield determined from the 2D-fit in each bin of invariant mass. The obtained sample contains true two-ϕ combinations, that are either random combinations or originate from the decay of common mother particles.

No clear contribution from the $f_0(980)$ resonance is seen in the K^+K^- invariant mass distribution. However a potential effect due to $f_0(980)$ is estimated in the following as a potential source of systematic uncertainty.

In the following production ratios are extracted from signal event yields obtained from the fit to the pure $\phi\phi$ invariant mass spectra. The invariant mass spectrum of pure $\phi\phi$ combinations is used to study charmonia production in inclusive b-hadron decays, study η_c and χ_c masses and the natural width of the $\eta_c(1S)$, and measure $\mathcal{B}(B_s^0 \to \phi\phi)$.

In Section 6.5.1, the 2D fit is performed in bins of the $K^+K^-K^+K^-$ invariant mass

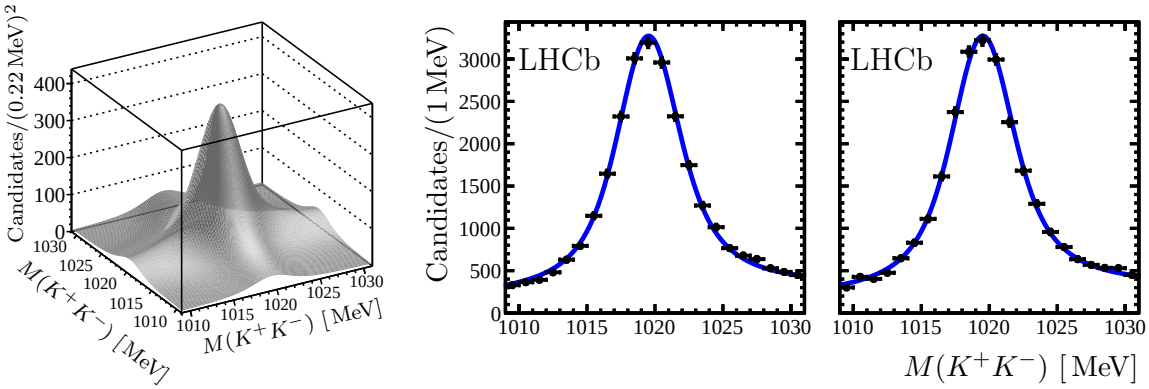

Figure 6.5: Result of the 2D fit to the $2(K^+K^-)$ invariant mass distribution along with the projections to the K^+K^- invariant mass axes in the $\eta_c(1S)$ signal region.

using the technique discussed in this section to construct the invariant mass distribution of the di-ϕ candidates, which is subsequently fit to extract charmonia yields.

6.5 Production of χ_c and $\eta_c(2S)$ in inclusive b-decays

6.5.1 Fit to the invariant mass of $\phi\phi$

Using the technique discussed in Section 6.4 the invariant mass spectrum of the pure $\phi\phi$ pairs is constructed and is fit to extract the yields of charmonia decaying to $\phi\phi$.

The invariant mass distribution of the $\phi\phi$ candidates is fit to the sum of the signal shapes for the η_c family, $\eta_c(1S)$ and $\eta_c(2S)$, and χ_c family, χ_{c0}, χ_{c1} and χ_{c2}, and the background shape. Each of the above charmonium states is described by the convolution of the relativistic Breit-Wigner function (RBW) to account for the natural width of the resonances,

$$
\begin{aligned}
RBW =& \frac{x \cdot \Gamma_f}{(M^2 - x^2)^2 + M^2 \cdot \Gamma_f^2} \ , \\
& \Gamma_f = \Gamma \times \left(\frac{K(x)}{K(M)} \right)^{2J+1} \times \left(\frac{F(rK(x))}{F(rK(M))} \right) \times \frac{M}{x} \ , \\
& K(y) = \frac{\sqrt{(y^2 - 2m_\phi^2)^2 - 4m_\phi^4}}{2y} \ , \\
& F(y) = \begin{cases} 1, & J = 0 \\ \frac{1}{1+y^2}, & J = 1 \\ \frac{1}{9+3y^2+y^4}, & J = 2 \ , \end{cases}
\end{aligned}
$$

and a double Gaussian function (DG) to account for detector resolution. In the above expression x and y are the decay products centre-of-mass energies, M and Γ are the resonance mass and natural width, respectively, J is the total angular momentum and r is the radial parameter of the decaying meson [244]. Natural width of the η_c (1S) state is left a free parameter in the fit, while natural widths of the χ_{c0}, χ_{c1}, χ_{c2} and η_c (2S) are fixed to their world average values [77].

The values of the ratio of two Gaussian widths and the fraction of the narrow Gaussian are fixed to the values determined from simulation - $\sigma_2/\sigma_1 = 2.16$ and $f_1 = 0.81$, respectively. Resolution effect is scaled according to the energy release in agreement with the MC based expectations (Fig. 6.6). In total, one free parameter in the $\phi\phi$ invariant mass fit accounts for the detector resolution effect. Resolution obtained in the simulation is compared to that from data in Table 6.4. The resolution values in the table are obtained from using a single free fit parameter both with the data and the simulation samples. The simulation values are obtained from the simultaneous fit to the simulated signal samples. The data values are obtained from the nominal fit to the combined data sample.

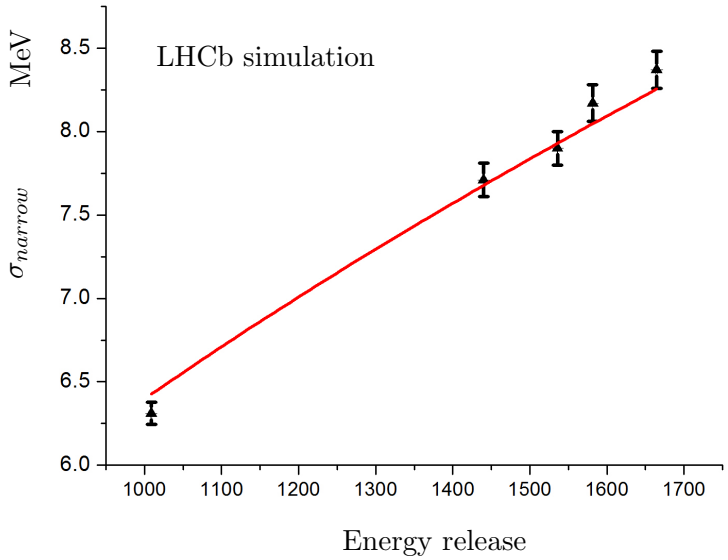

Figure 6.6: Resolution obtained on the simulated samples depending on the energy release. The η_c and χ_c states are shown on the plot. Fit using the function $k \cdot \sqrt{x - 4m_K}$.

Resonance	Simulation	Data
η_c (1S)	6.3 ± 0.1	7.4 ± 0.6
χ_{c0} (1P)	7.7 ± 0.1	8.8 ± 0.8
χ_{c1} (1P)	7.9 ± 0.1	9.1 ± 0.8
χ_{c2} (1P)	8.2 ± 0.1	9.2 ± 0.8
η_c (2S)	8.4 ± 0.1	9.5 ± 0.8

Table 6.4: Resolution (narrow Gaussian σ) as obtained from simulation and data samples.

Therefore in both cases the correlation is present. Resolution dependence on energy release is consistent for simulation and data samples wint a trend for a simulation to underestimate the resolution, as for other LHCb analyses.

The charmonium-like $X(3872)$ and $X(3915)$ (or $X(3915)$) states are taken into account in the fit, in order to evaluate systematic uncertainty of the main fit results, as well as to obtain upper limits on the probabilities $\mathcal{B}(b \to X(3872)X) \times \mathcal{B}(X(3872) \to \phi\phi)$ and $\mathcal{B}(b \to X(3915)X) \times \mathcal{B}(X(3915) \to \phi\phi)$. The upper limits of charonium-like states production is given in Section 6.6.

Natural width of the $\eta_c(2S)$ meson is fixed to the central value of $\Gamma_{\eta_c(2S)} = 11.3^{+3.2}_{-2.9}$ MeV from Ref. [77]. Possible variations are taken into account by providing the results as a function of the $\eta_c(2S)$ natural width.

The combinatorial background, i.e. a contribution from random $\phi\phi$ combinations, is described by the product of a first-order polynomial, exponential function and a factor to account for the available phase space:

$$BGR = \sqrt{z} \cdot \exp(Az) \cdot (1 + Bz) \ ,$$

where $z = M(K^+K^-K^+K^-) - 2M(\phi)$.

The complete description can then be denoted as

$$\begin{aligned} PDF = \ & RBW(M_{\eta_c(1S)}, \Gamma_{\eta_c(1S)}, J = 0, r = 1.5\,\mathrm{GeV}^{-1}) \otimes DG(M_{\eta_c(1S)}) + \\ + \ & RBW(M_{\chi_{c0}}, \Gamma_{\chi_{c0}} = const, J = 0, r = 1.5\,\mathrm{GeV}^{-1}) \otimes DG(M_{\chi_{c0}}) + \\ + \ & RBW(M_{\chi_{c1}}, \Gamma_{\chi_{c1}} = const, J = 1, r = 1.5\,\mathrm{GeV}^{-1}) \otimes DG(M_{\chi_{c1}}) + \\ + \ & RBW(M_{\chi_{c2}}, \Gamma_{\chi_{c2}} = const, J = 2, r = 1.5\,\mathrm{GeV}^{-1}) \otimes DG(M_{\chi_{c2}}) + \\ + \ & RBW(M_{\eta_c(2S)}, \Gamma_{\eta_c(2S)} = const, J = 0, r = 1.5\,\mathrm{GeV}^{-1}) \otimes DG(M_{\eta_c(2S)}) + \\ + \ & BGR \ . \end{aligned}$$

Free parameters in the fit are yields and masses of the resonances, the $\eta_c(1S)$ natural width, one resolution parameter k, A and B background description parameters.

A binned χ^2 fit is performed on the $\phi\phi$ invariant mass distribution taking into account the fact that the error bars reflect the 2D fit results, so the error on the yield is the one obtained from 2D fit but not Poisson error. Figure 6.7 shows the fit to the spectrum of the invariant mass of $\phi\phi$ combinations, for combined data sample. As explained before, each bin of the invariant mass distribution shown on Fig. 6.7 is a result of the 2D fit as described in Section 6.4. Signals from η_c (1S), χ_{c0}, χ_{c1}, χ_{c2} and η_c (2S) decays into $\phi\phi$ are clearly visible. For illustration, Fig. 6.8 shows invariant mass spectra for charmonia decays to $\phi\phi$ before performing 2D fit procedure. The background level on Fig.6.7 is almost twice smaller to that on Fig.6.8. The later is due to statistical unfolding of $\phi\phi$. However, the statistical errors on Fig.6.7 obtained from 2D fit are larger than poisson errors.

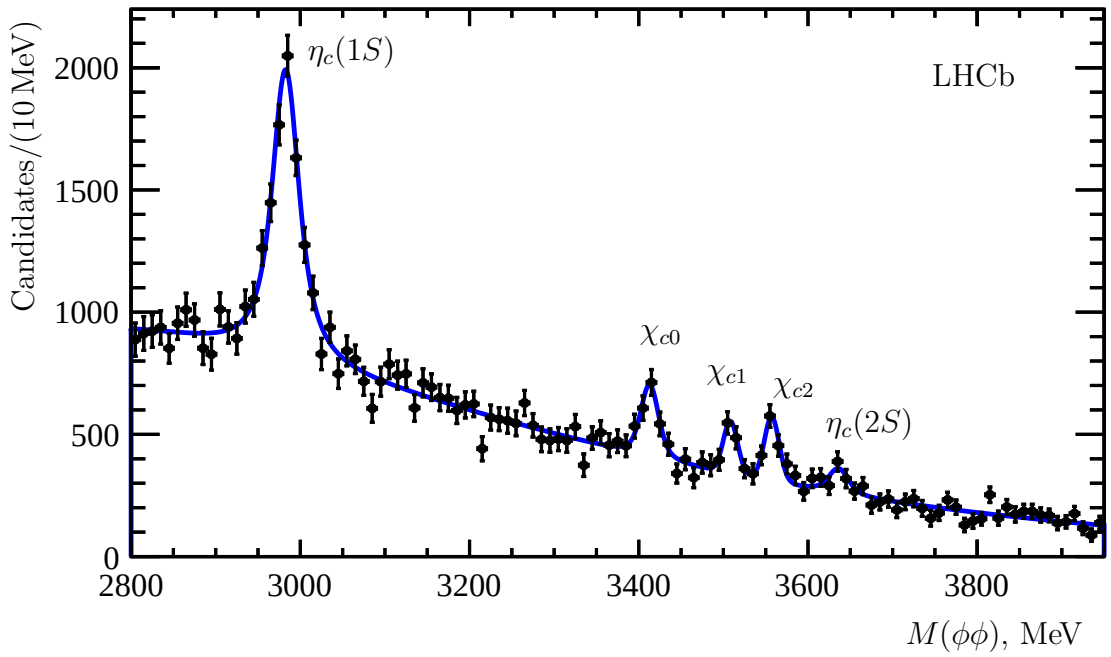

Figure 6.7: Distribution of the invariant mass of $\phi\phi$ combinations. The number of candidates in each bin is obtained from the corresponding 2D fit. The peaks corresponding to the $c\bar{c}$ resonances are marked on the plot.

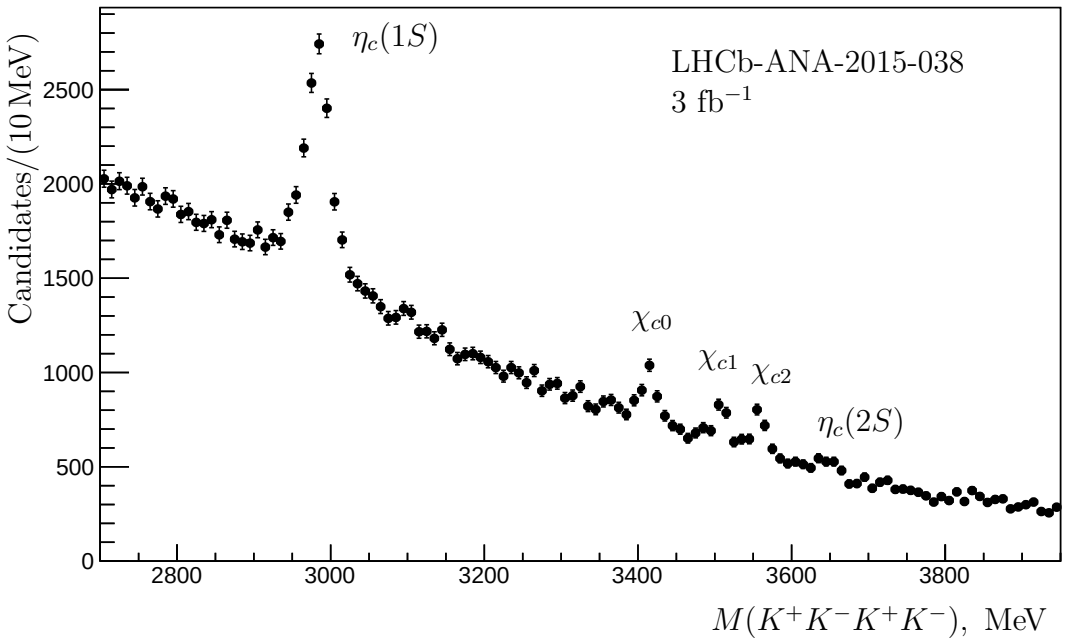

Figure 6.8: Distribution of the $\phi\phi$ invariant mass for combined data sample. No 2D fit is performed.

Figure 6.9 shows invariant mass spectra for the ϕK^+K^- and $K^+K^-K^+K^-$ combinations plotted using the results of the 2D fit. No significant resonance contributions are observed in the ϕK^+K^- and $K^+K^-K^+K^-$ invariant mass distributions.

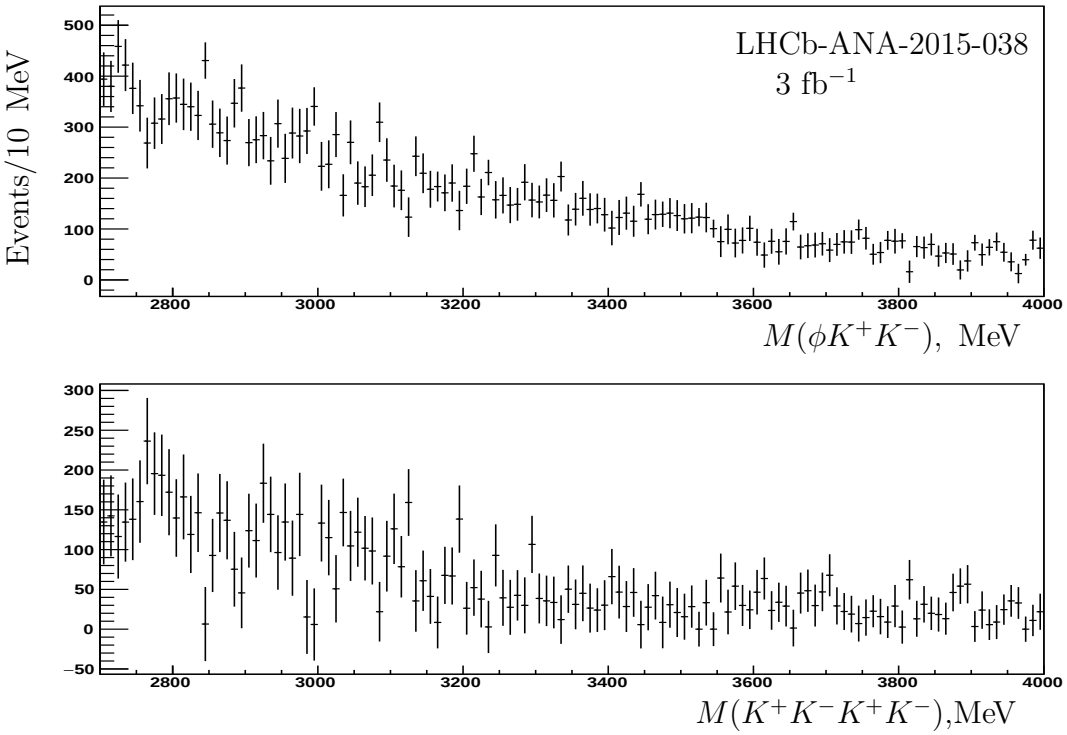

Figure 6.9: Distribution of the ϕK^+K^- (top) and $K^+K^-K^+K^-$ (bottom) invariant mass for combined data sample, accumulated at $\sqrt{s} = 7\,\text{TeV}$ and $\sqrt{s} = 8\,\text{TeV}$. Data points are the results of the 2D fit.

Table 6.5 compares the event yields at a centre-of-mass energy of $\sqrt{s} = 7$ TeV and $\sqrt{s} = 8$ TeV for the considered charmonum states. Scaling the $\eta_c(2S)$ yield from the

	$\eta_c(1S)$	χ_{c0}	χ_{c1}	χ_{c2}	$\eta_c(2S)$
$\sqrt{s} = 7\,\text{TeV}$	2008 ± 215	289 ± 74	141 ± 47	168 ± 52	20 ± 53
$\sqrt{s} = 8\,\text{TeV}$	4440 ± 350	619 ± 107	314 ± 72	431 ± 85	336 ± 86
All data	6476 ± 418	933 ± 128	460 ± 89	611 ± 97	365 ± 100

Table 6.5: Event yields at a centre-of-mass energy of $\sqrt{s} = 7$ TeV and $\sqrt{s} = 8$ TeV and for the combined data sample, for the considered charmonia states.

$\sqrt{s} = 7\,\text{TeV}$ data sample using the central values of the χ_{c2} yields from the $\sqrt{s} = 7\,\text{TeV}$ and $\sqrt{s} = 8\,\text{TeV}$ data samples (not taking into account their uncertainties), a difference between the $\eta_c(2S)$ yields for the $\sqrt{s} = 7\,\text{TeV}$ and $\sqrt{s} = 8\,\text{TeV}$ data samples as estimated

from statistical uncertainties only is about 2σ. Numbers of other signal candidates are consistent between the data samples collected at a centre-of-mass energy of $\sqrt{s} = 7\,\text{TeV}$ and $\sqrt{s} = 8\,\text{TeV}$, and with the combined data sample.

The ratios of resonance yields from the fit are summarized in Table 6.6 for the ratios inside the family, and in Table 6.7 for the ratios with respect to the decays to $b \to \eta_c(1S)X$.

Significance of the $\eta_c(2S)$ to $\eta_c(1S)$ event yield ratio is illustrated on Fig. 6.10. The

Resonance	Event yield ratio
$N_{\chi_{c1}}/N_{\chi_{c0}}$	$0.494 \pm 0.107 \pm 0.012$
$N_{\chi_{c2}}/N_{\chi_{c0}}$	$0.656 \pm 0.121 \pm 0.015$
$N_{\eta_c(2S)}/N_{\eta_c(1S)}$	$0.056 \pm 0.016 \pm 0.005$

Table 6.6: Charmonium event yield ratios inside families from the fit to $\phi\phi$ invariant mass spectrum.

Resonance	Event yield ratio
$N_{\chi_{c0}}/N_{\eta_c(1S)}$	$0.144 \pm 0.022 \pm 0.011$
$N_{\chi_{c1}}/N_{\eta_c(1S)}$	$0.071 \pm 0.015 \pm 0.006$
$N_{\chi_{c2}}/N_{\eta_c(1S)}$	$0.094 \pm 0.016 \pm 0.006$

Table 6.7: Charmonium event yield ratios with respect to decays to $\eta_c(1S)$ from the fit to $\phi\phi$ invariant mass spectrum.

statistical significance, not including systematic, for the $N_{\eta_c(2S)}$ signal is estimated from the χ^2-profile to be 3.7 standard deviations.

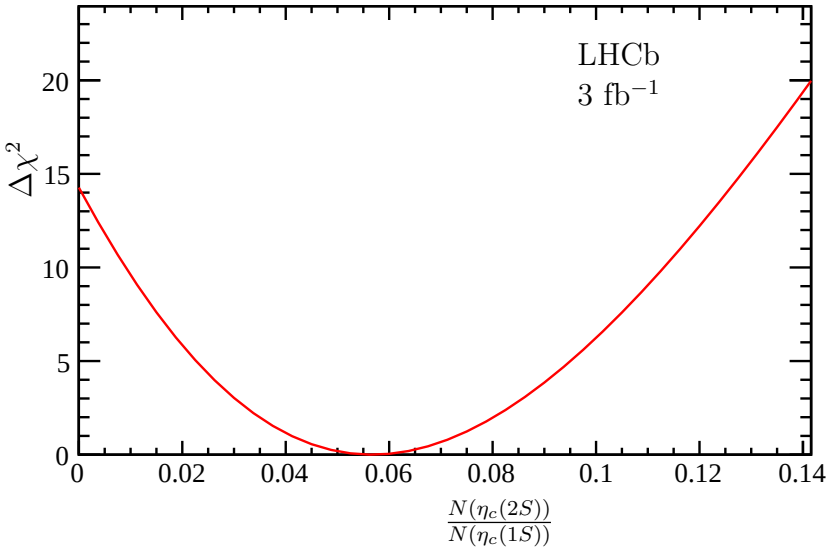

Figure 6.10: Difference of χ^2 of the fit as a function of the ratio of the $\eta_c(2S)$ and $\eta_c(1S)$ event yields.

6.5.2 Systematic uncertainties

Systematic uncertainties are obtained by including potential contribution from other resonances, varying detector resolution, varying fit range, implementing alternative background parametrization, accounting for potential contribution from the $f_0(980)$ state to the 2D fit, and fixing masses of the χ_c states to the known values [77]. In order to evaluate systematic uncertainty related to potential contribution from other resonances, contributions from $X(3872)$, $X(3915)$ and $\chi_{c2}(3930)$ are included in the fit. Systematic uncertainties related to detector resolution are conservatively estimated by using the $\eta_c(1S)$ resolution as obtained from the simulation. Systematic uncertainties associated to the impact of the detector resolution description on the signal shapes are estimated by comparing the nominal fit results to those obtained using a single Gaussian instead of double Gaussian shape. The uncertainty associated to the description using the Breit-Wigner shape is estimated by varying radial parameter r between $0.3\,\mathrm{GeV}^{-1}$ and $5\,\mathrm{GeV}^{-1}$. In order to estimate uncertainty related to the natural width of $\eta_c(2S)$ the $\Gamma_{\eta_c(2S)}$ value is varied within the PDG [77] uncertainties. The systematic associated to the fit range is estimated by restricting the fit to the χ_c and $\eta_c(2S)$ region ($3.15\,\mathrm{GeV}/c - 3.95\,\mathrm{GeV}/c$) is used to estimate the corresponding systematic uncertainty. Alternative background parametrization using a parabola function is used for the corresponding systematic uncertainty estimate. Systematic uncertainty associated to the background parametrization in the 2D fit is estimated by adding slope parameters for the ϕK^+K^- and $K^+K^-K^+K^-$ description.

Effect of potential contribution from the $f_0(980)$ state to the 2D fit is estimated by including the $f_0(980)$ contribution following the example from Ref. [245]. In order to evaluate potential contribution from the $f_0(980)$ state to the 2D fit, the signal regions for each considered resonance is fit including the term describing the $f_0(980)$ contribution, and varying the $f_0(980)$ parameters. Using the $f_0(980)$ description with the Breit-Wigner function and varying parameters according to the uncertainties from Ref. [77], the obtained results are shown in Table 6.8. Using the $f_0(980)$ description with the Flatte function [246] and varying parameters following the example from Ref. [245], the obtained results are shown in Table 6.9. Maximum differences (ΔN-max) over the two $f_0(980)$ parametrizations are conservatively attributed as an estimate of the corresponding source of systematic uncertainty for each charmonium state.

Uncertainty associated to the description of the ϕ signal peak resolution is estimated by fixing the resolution in the 2D fit at the value suggested by simulation. Uncertainty on the description of the χ_c signal peaks is estimated by fixing the χ_c masses at their nominal values. Uncertainty related to momentum scale calibration is negligible and is not

	$\eta_c(1S)$	χ_{c0}	χ_{c1}	χ_{c2}	$\eta_c(2S)$
$M = 990\,\text{MeV}$, $\Gamma = 70\,\text{MeV}$	< 1	1	2	< 1	3
$M = 990\,\text{MeV}$, $\Gamma = 40\,\text{MeV}$	< 1	3	3	< 1	6
$M = 990\,\text{MeV}$, $\Gamma = 100\,\text{MeV}$	1	< 1	1	< 1	< 1
$M = 970\,\text{MeV}$, $\Gamma = 70\,\text{MeV}$	< 1	1	< 1	< 1	3
$M = 1010\,\text{MeV}$, $\Gamma = 70\,\text{MeV}$	< 1	6	< 1	1	< 1
ΔN-max	1	6	3	1	6

Table 6.8: Estimated difference $\Delta N_{\phi\phi}$ in the region of the $\eta_c(1S)$ $(2920 - 3050\,\text{MeV})$, χ_{c0} $(3370 - 3460\,\text{MeV})$, χ_{c1} $(3460 - 3530\,\text{MeV})$, χ_{c2} $(3530 - 3600\,\text{MeV})$ and $\eta_c(2S)$ $(3600 - 3660\,\text{MeV})$ resonances originated from accounting for the contribution from the $f_0(980)$ state in the 2D fit. Parameters of the $f_0(980)$ state are varied according to the uncertainties from the Ref. [77].

	$\eta_c(1S)$	χ_{c0}	χ_{c1}	χ_{c2}	$\eta_c(2S)$
$M = 990\,\text{MeV}$, $g_2/g_1 = 4.12$	$+1$	-1	< 1	< 1	-2
$M = 990\,\text{MeV}$, $g_2/g_1 = 3.80$	-1	< 1	< 1	< 1	-2
$M = 990\,\text{MeV}$, $g_2/g_1 = 4.44$	-2	< 1	< 1	< 1	-3
$M = 970\,\text{MeV}$, $g_2/g_1 = 4.12$	$+2$	-1	< 1	< 1	-2
$M = 1100\,\text{MeV}$, $g_2/g_1 = 4.12$	-2	$+1$	< 1	< 1	-1
ΔN-max	2	1	< 1	< 1	3

Table 6.9: Estimated difference $\Delta N_{\phi\phi}$ in the region of the $\eta_c(1S)$ $(2920 - 3050\,\text{MeV})$, χ_{c0} $(3370 - 3460\,\text{MeV})$, χ_{c1} $(3460 - 3530\,\text{MeV})$, χ_{c2} $(3530 - 3600\,\text{MeV})$ and $\eta_c(2S)$ $(3600 - 3660\,\text{MeV})$ resonances originated from accounting for the contribution from the $f_0(980)$ state in the 2D fit with different Flatte parametrisations of the $f_0(980)$ resonance.

accounted in the evaluation of the systematic uncertainty on the yield ratios. Combined systematic uncertainty is obtained as a quadratic sum of the individual systematic contributions. Background description as well as potential contribution from other resonances dominate combined systematic uncertainties. In the yield ratios systematic uncertainty is smaller or comparable to the statistical one.

The details of systematic uncertainty estimates for the ratios of charmonia yields are shown in Tables 6.10 and 6.11.

Stability of the obtained results are checked by shifting the $\phi\phi$ invariant mass distribution by half a bin. Table 6.12 compares the results for yield ratios to those obtained with the shift by half a bin of the invariant mass distribution.

Another cross-check has been performed by using *sPlot* technique instead of the 2D fit procedure. No significant deviations from nominal result is observed. However, the *sPlot* technique is not strict enough for unfolding true $\phi\phi$ contributions in wide range of $M(\phi\phi)$ due to the correlation of background parameters and $M(\phi\phi)$.

	$N_{\chi_{c1}}/N_{\chi_{c0}}$	$N_{\chi_{c2}}/N_{\chi_{c0}}$	$N_{\eta_c(2S)}/N_{\eta_c(1S)}$
Including $X(3872)$, $X(3915)$, $\chi_{c2}(3930)$	0.006	0.008	0.003
Fix $\eta_c(1S)$ resolution to MC value	0.001	0.001	< 0.001
Resolution described with a single Gaussian	< 0.001	< 0.001	-0.002
Varying r parameter between 0.5 and $3\,\mathrm{GeV}^{-1}$	< 0.001	< 0.001	< 0.001
Varying $\Gamma_{\eta_c(2S)}$	< 0.001	0.001	-0.003
Fit χ_c and $\eta_c(2S)$ region only	0.001	-0.004	-
Alternative bgrd parametrization	0.002	0.011	< 0.001
Accounting for $f_0(980)$ in 2D fit	0.005	0.005	0.001
Fix χ_c masses at nominal values	-0.010	-0.002	< 0.001
Fix resolution in 2D fit at MC value	< 0.001	-0.001	< 0.001
Add slope parameter for the ϕK^+K^- component in 2D fit	< 0.001	0.001	< 0.001
Add slope parameter for the $K^+K^-K^+K^-$ component in 2D fit	< 0.001	< 0.001	< 0.001
Combined systematic uncertainty	0.012	0.015	0.005

Table 6.10: Systematic uncertainty of the obtained charmonium event yield ratios within families.

	$N_{\chi_{c0}}/N_{\eta_c(1S)}$	$N_{\chi_{c1}}/N_{\eta_c(1S)}$	$N_{\chi_{c2}}/N_{\eta_c(1S)}$
Including $X(3872)$, $X(3915)$, $\chi_{c2}(3930)$	0.004	0.003	0.003
Fix $\eta_c(1S)$ resolution to MC value	< 0.001	< 0.001	< 0.001
Resolution described with a single Gaussian	< 0.001	< 0.001	< 0.001
Varying r parameter between $0.5\,\mathrm{GeV}^{-1}$ and $3\,\mathrm{GeV}^{-1}$	< 0.001	< 0.001	< 0.001
Varying $\Gamma_{\eta_c(2S)}$	< 0.001	< 0.001	< 0.001
Alternative bgrd parametrization	-0.010	-0.005	-0.005
Accounting for $f_0(980)$ in 2D fit	0.001	< 0.001	< 0.001
Fix χ_c masses at nominal values	-0.002	-0.002	-0.001
Fix resolution in 2D fit at MC value	< 0.001	< 0.001	< 0.001
Add slope parameter for ϕK^+K^- component in 2D fit	-0.002	< 0.001	0.001
Add slope parameter for $K^+K^-K^+K^-$ component in 2D fit	< 0.001	< 0.001	< 0.001
Combined systematic uncertainty	0.011	0.006	0.006

Table 6.11: Systematic uncertainty of the obtained charmonium event yield ratios with respect to the decays with $\eta_c(1S)$.

	Measured value	Shift with respect to the measured value
$N_{\chi_{c0}}/N_{\eta_c(1S)}$	$0.144 \pm 0.022 \pm 0.011$	0.006
$N_{\chi_{c1}}/N_{\eta_c(1S)}$	$0.071 \pm 0.015 \pm 0.006$	0.004
$N_{\chi_{c2}}/N_{\eta_c(1S)}$	$0.094 \pm 0.016 \pm 0.007$	0.007
$N_{\eta_c(2S)}/N_{\eta_c(1S)}$	$0.056 \pm 0.016 \pm 0.005$	0.003
$N_{\chi_{c1}}/N_{\chi_{c0}}$	$0.494 \pm 0.107 \pm 0.012$	0.005
$N_{\chi_{c2}}/N_{\chi_{c0}}$	$0.656 \pm 0.121 \pm 0.014$	0.022

Table 6.12: Cross-check for charmonia yield ratios against a shift by half a bin of the invariant mass distribution.

6.5.3 Results and discussion

Branching fractions of inclusive charmonia production in b-decays

The double ratios of the inclusive branching fractions constitute the main results of the section since the branching fractions of charmonium states to $\phi\phi$ are not well measured. Hence, in the double ratios the related systematic uncertainties partially cancel. In addition to that, the PDG average and PDG fit values of the $\eta_c \to \phi\phi$ significantly differ, which is adressed in Section 9.1.3.

In order to exctract simple ratios or absolute branching fractions further input is needed. In the following the $\eta_c(1S)$ production rate in b-hadron decays and branching fractions of the charmonia decays to $\phi\phi$ are used. The $\eta_c(1S)$ inclusive production in b-decays was measured by LHCb using decays to $p\overline{p}$, $\mathcal{B}(b \to \eta_c(1S)X) = (4.88 \pm 0.97) \times 10^{-3}$ [13]. Branching fractions of the charmonia decays to $\phi\phi$ from Ref. [77] are used. However, the measured χ_c production shows a disagreement when measured using $\eta_c(1S)$ production for normalization and when measured without a normalization. In addition, Ref. [77] indicates a tension for the $\mathcal{B}(\eta_c(1S) \to \phi\phi)$ value when comparing a direct determination and a fit including all available measurements. Therefore, an average of the results from Belle [247] and BaBar [248] using B^+ decays to $\phi\phi K^+$, $\mathcal{B}(\eta_c(1S) \to \phi\phi) = (3.21 \pm 0.72) \times 10^{-3}$, is used below. The uncertainty of this average dominates a majority of the further results in this section, and improvement of the $\mathcal{B}(\eta_c(1S) \to \phi\phi)$ knowledge is critical to reduce the uncertainties of the related results. The values $\mathcal{B}(\chi_{c0} \to \phi\phi) = (7.7 \pm 0.7) \times 10^{-4}$, $\mathcal{B}(\chi_{c1} \to \phi\phi) = (4.2 \pm 0.5) \times 10^{-4}$, and $\mathcal{B}(\chi_{c2} \to \phi\phi) = (1.12 \pm 0.10) \times 10^{-3}$, are used for the χ_c decays.

Accounting for small differences in the trigger, reconstruction and selection efficiency for decays of the χ_c states into $\phi\phi$, relative yields of the χ_c states in b-hadron inclusive decays are derived as (Eq. 6.1)

$$\frac{\mathcal{B}(b \to \chi_{c1}X) \times \mathcal{B}(\chi_{c1} \to \phi\phi)}{\mathcal{B}(b \to \chi_{c0}X) \times \mathcal{B}(\chi_{c0} \to \phi\phi)} = 0.50 \pm 0.11 \pm 0.01 \ ,$$
$$\frac{\mathcal{B}(b \to \chi_{c2}X) \times \mathcal{B}(\chi_{c2} \to \phi\phi)}{\mathcal{B}(b \to \chi_{c0}X) \times \mathcal{B}(\chi_{c0} \to \phi\phi)} = 0.56 \pm 0.10 \pm 0.01 \ .$$

Dominant contribution to the systematic uncertainty comes from accounting for possible other resonances and using known χ_c mass values [77]. The systematic uncertainty is smaller than the statistical one, so that precision will improve with more data accumulated by LHCb.

Using branching fractions of the χ_c decays to $\phi\phi$ from Ref. [77], relative branching

fractions of b-hadron decays to χ_c states can be derived as

$$\frac{\mathcal{B}(b \to \chi_{c1} X)}{\mathcal{B}(b \to \chi_{c0} X)} = 0.92 \pm 0.20 \pm 0.02 \pm 0.14 \ ,$$
$$\frac{\mathcal{B}(b \to \chi_{c2} X)}{\mathcal{B}(b \to \chi_{c0} X)} = 0.38 \pm 0.07 \pm 0.01 \pm 0.05 \ ,$$

where the first uncertainty is statistical, the second one is systematic and the third one is due to the branching fractions $\mathcal{B}(\chi_c \to \phi\phi)$.

This is the first (χ_{c0} and χ_{c2}) or most precise (χ_{c1}) determination of the χ_c relative yields in b-hadron decays. These results are compared to the PDG average values [77] for the B^0/B^+ branching fractions into χ_{c1} and χ_{c2} mesons measured by CLEO [72, 74], Belle [75] and BaBar [71] experiments. In order to make the qualitative comparison, one need to add assumptions about the fraction of charmonium originating from decays of different b-hadrons. The average value for the branching fraction $\mathcal{B}(B \to \chi_{c2} X) = (1.4 \pm 0.4) \times 10^{-3}$ [77] has limited precision and is different from zero by a three standard deviations. This is a consequence of a descrepancy between the results of the Belle [75] and BaBar [71] experiments on one side and the CLEO result [74] on the other side, which calls for another measurement. The obtained result for relative χ_{c1} and χ_{c2} production in b-hadron decays reproduces the same ratio from B^0/B^+ production [77].

To derive absolute values of the χ_c yields from b-hadron decays, the result of the η_c inclusive yield measured using decay to $p\overline{p}$ [13] is used. Taking into account the difference in trigger, reconstruction and selection efficiencies for η_c and χ_c mesons, $\varepsilon_{\chi_c}/\varepsilon_{\eta_c}$, the yield ratios relative to the η_c yield are constructed as

$$\frac{\mathcal{B}(b \to \chi_{c0} X) \times \mathcal{B}(\chi_{c0} \to \phi\phi)}{\mathcal{B}(b \to \eta_c X) \times \mathcal{B}(\eta_c \to \phi\phi)} = 0.147 \pm 0.023 \pm 0.011 \ ,$$
$$\frac{\mathcal{B}(b \to \chi_{c1} X) \times \mathcal{B}(\chi_{c1} \to \phi\phi)}{\mathcal{B}(b \to \eta_c X) \times \mathcal{B}(\eta_c \to \phi\phi)} = 0.073 \pm 0.016 \pm 0.006 \ ,$$
$$\frac{\mathcal{B}(b \to \chi_{c2} X) \times \mathcal{B}(\chi_{c2} \to \phi\phi)}{\mathcal{B}(b \to \eta_c X) \times \mathcal{B}(\eta_c \to \phi\phi)} = 0.081 \pm 0.013 \pm 0.005 \ .$$

Relative branching fractions of b-hadron decays to χ_c states can be derived as

$$\frac{\mathcal{B}(b \to \chi_{c0} X)}{\mathcal{B}(b \to \eta_c X)} = 0.615 \pm 0.095 \pm 0.047 \pm 0.149 \ ,$$
$$\frac{\mathcal{B}(b \to \chi_{c1} X)}{\mathcal{B}(b \to \eta_c X)} = 0.562 \pm 0.119 \pm 0.047 \pm 0.131 \ ,$$
$$\frac{\mathcal{B}(b \to \chi_{c2} X)}{\mathcal{B}(b \to \eta_c X)} = 0.234 \pm 0.038 \pm 0.015 \pm 0.057 \ ,$$

where last uncertainties are due to branching fractions $\mathcal{B}(\eta_c, \chi_c \to \phi\phi)$ and are larger than the systematic ones.

With the branching fraction of η_c production in b-hadron decays $\mathcal{B}(b \to \eta_c X) = (4.88 \pm 0.97) \times 10^{-3}$ [13], the absolute branching fractions of χ_c production in b-hadron decays are obtained as

$$\mathcal{B}(b \to \chi_{c0} X) = (3.02 \pm 0.47 \pm 0.23 \pm 0.94) \times 10^{-3} \ ,$$
$$\mathcal{B}(b \to \chi_{c1} X) = (2.76 \pm 0.59 \pm 0.23 \pm 0.89) \times 10^{-3} \ ,$$
$$\mathcal{B}(b \to \chi_{c2} X) = (1.15 \pm 0.20 \pm 0.07 \pm 0.36) \times 10^{-3} \ ,$$

where the third uncertainty is due to the uncertainties on the branching fractions of the b-hadron decays to η_c meson $\mathcal{B}(b \to \eta_c X)$ and $\eta_c(1S)$ and χ_c decays to $\phi\phi$.

The branching fraction of b-hadron decays into χ_{c0} is measured for the first time, and is larger than the values predicted in Ref. [82].

The result for b-decays into χ_{c1} is the most precise measurement for the mixture of B^0, B^+, B_s^0 and b-baryons. The central value of the result for b-decays into χ_{c1} is lower than the value measured by DELPHI [67] and L3 [68] experiments at LEP, $0.0113^{+0.0058}_{-0.0050} \pm 0.0004$ and $0.019 \pm 0.007 \pm 0.001$, respectively. However, taking into account the LEP results limited precision, the LHCb result is consistent with them. It must also be noticed that the mixture of b-hadrons is slightly different for LEP and LHC, thus the $\mathcal{B}(b \to (c\bar{c})X)$ measured in each case is not expected to be exactly the same. However the difference in the b-hadron cocktail between LEP and LHC is small compare to the precisions of present measurement. The value obtained is also lower than than the branching fraction of b-decays into χ_{c1} measured by CLEO [72], Belle [76] and BaBar [71], which however only refers to a Bz and B^+ mixture, $0.00435 \pm 0.00029 \pm 0.00040$, $0.00363 \pm 0.00022 \pm 0.00034$, and $0.00333 \pm 0.00005 \pm 0.00024$, respectively. Finally, the LHCb result for b-decays into χ_{c1} is consistent with the prediction in Ref. [82].

The branching fraction of b-hadron decays into χ_{c2} is measured for the first time

with the B^0, B^+, B_s^0 and b-baryons mixture. The result is consistent with the average, corresponding to the B^0, B^+ mixture, from Ref. [77], given large PDG uncertainty. The obtained value has higher precision than the results from CLEO [74] and BaBar [71], less precise than recently updated Belle measurement $(0.98 \pm 0.06 \pm 0.10) \times 10^{-3}$ [76] is close to the CLEO result of $(0.67 \pm 0.34 \pm 0.03) \times 10^{-3}$ and is different by more than 2σ and BaBar, $(2.10 \pm 0.45 \pm 0.31) \times 10^{-3}$. The comparison of the obtained results with theory prediction [82] is given in Section 7.

It should be mentioned, that the measured branching fractions of b-hadron decays to charmonia comprise also decays via intermediate higher-mass charmonium resonances, contrary to the theory calculations, which consider only direct b-hadron transitions to the considered charmonium state.

Another goal is to quantify the observed signal of 365 ± 100 $\eta_c(2S)$ meson candidates in b-hadron inclusive decays. Taking into account the difference in trigger, reconstruction and selection efficiencies for $\eta_c(1S)$ and $\eta_c(2S)$ mesons, the yield ratio relative to the $\eta_c(1S)$ yield was constructed as

$$\frac{\mathcal{B}(b \to \eta_c(2S)X) \times \mathcal{B}(\eta_c(2S) \to \phi\phi)}{\mathcal{B}(b \to \eta_c(1S)X) \times \mathcal{B}(\eta_c(1S) \to \phi\phi)} = 0.040 \pm 0.011 \pm 0.004 \ ,$$

where systematic uncertainty is dominated by possible contributions possible contributions of other resonances and variation of the $\eta_c(2S)$ natural width. The dependence of this ratio on the $\eta_c(2S)$ natural width is shown in Fig. 6.11.

Since the decay of η_c (2S) meson to $\phi\phi$ had not been previously observed, only the product of the branching fraction of b-hadron decays to η_c (2S) and the branching fraction of the $\eta_c(2S) \to \phi\phi$ decay mode is determined as

$$\mathcal{B}(b \to \eta_c(2S)X) \times \mathcal{B}(\eta_c(2S) \to \phi\phi) = (6.34 \pm 1.81 \pm 0.57 \pm 1.89) \times 10^{-7} \ ,$$

where systematic uncertainty is dominated by the uncertainty of the η_c production in b-decays. This is the first indication of the $\eta_c(2S)$ production in b-decays, as well as the decay of $\eta_c(2S)$ meson to the $\phi\phi$ pair.

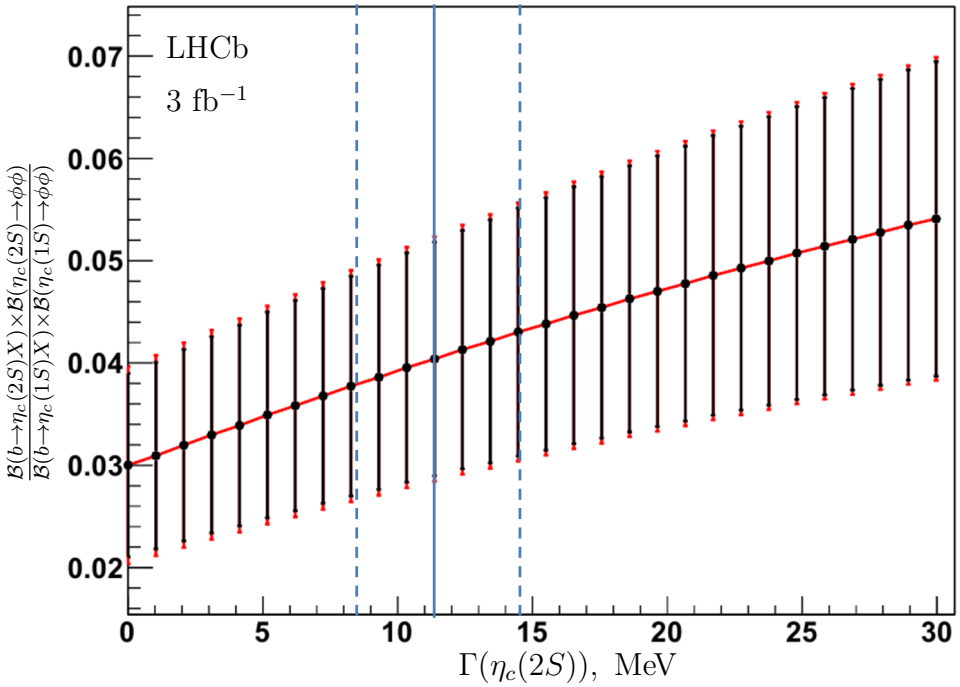

Figure 6.11: Obtained ratio of the $\eta_c(1S)$ and $\eta_c(2S)$ inclusive yields $\frac{\mathcal{B}(b\to\eta_c(2S)X)\times\mathcal{B}(\eta_c(2S)\to\phi\phi)}{\mathcal{B}(b\to\eta_c(1S)X)\times\mathcal{B}(\eta_c(1S)\to\phi\phi)}$ depending on the $\eta_c(2S)$ natural width. Statistical and total uncertainties for each point are shown separately. The $\eta_c(2S)$ natural width from Ref. [77] is shown as a vertical solid line, while dashed lines correspond to the Ref. [77] uncertainty.

The p_{T}-differential χ_c and $\eta_c(1S)$ production in b-decays

The shapes of the differential production cross-sections as a function of transverse momentum are studied in the LHCb acceptance ($2 < \eta < 5$) and for $3 < p_{\mathrm{T}} < 17\,\mathrm{GeV}$ and $2 < p_{\mathrm{T}} < 19\,\mathrm{GeV}$ for the $\eta_c(1S)$ and χ_c states, respectively. Figure 6.12 shows the differential cross-section of the $\eta_c(1S)$ production at $\sqrt{s} = 7\,\mathrm{TeV}$ and $8\,\mathrm{TeV}$. Only statistical and uncorrelated systematic uncertainties are taken into account. The distributions are fit to the exponential function. Dependence of the $\eta_c(1S)$ production on p_{T} is found to be similar in the studied kinematical regime for the two centre-of-mass energies (Table 6.13). As a cross-check the corresponding χ^2/ndf values are obtained using only statistical

Data sample	Exponential slope	χ^2/ndf
$\sqrt{s} = 7\,\mathrm{TeV}$	0.41 ± 0.02	0.41
$\sqrt{s} = 8\,\mathrm{TeV}$	0.39 ± 0.02	1.12

Table 6.13: Results of the fit to the $\eta_c(1S)$ differential cross-section data for the $\sqrt{s} = 7\,\mathrm{TeV}$ and $8\,\mathrm{TeV}$ data samples.

uncertainties, which also shows a good fit quality.

Figure 6.13 shows differential production cross-sections of the χ_c states for $\sqrt{s} = 7\,\text{TeV}$ and 8 TeV data samples. Only statistical and uncorrelated systematic uncertainties are taken into account. The fits of the numbers of χ_c states in p_T bins are performed simultaneously with the integral fit. The result of the fit is given in Table 6.14.

Table 6.14: Results of the fit to the χ_c differential cross-section data for the $\sqrt{s} = 7\,\text{TeV}$ and 8 TeV data samples.

Data sample	Slope			χ^2/ndf		
	χ_{c0}	χ_{c1}	χ_{c2}	χ_{c0}	χ_{c1}	χ_{c2}
$\sqrt{s} = 7\,\text{TeV}$	0.32 ± 0.04	0.31 ± 0.06	0.30 ± 0.05	0.61	0.69	0.17
$\sqrt{s} = 8\,\text{TeV}$	0.37 ± 0.04	0.41 ± 0.06	0.33 ± 0.04	0.03	0.42	0.27

Below, each differential production cross-section is normalized to the production cross-section integrated over the studied p_T region. Figure 6.14 shows the normalized differential cross-sections of $\eta_c(1S)$, χ_{c0}, χ_{c1} and χ_{c2} production at $\sqrt{s} = 7$ and 8 TeV.

An exponential function proportional to $\exp(-\alpha\, p_\text{T})$ is fitted to the distributions. The results for the slope parameters α are given in Table 6.15. Production dependence on p_T is found to be similar in the studied kinematical regime within uncertainties, for the two centre-of-mass energies (Table 6.15). For χ_{c1} and χ_{c2} production in b-hadron decays these results extend the ATLAS experiment studies [134] in p_T and rapidity. As a cross-check the corresponding χ^2/ndf values are obtained using only statistical uncertainties to check the effect of the systematic uncertainty, which remains negligible.

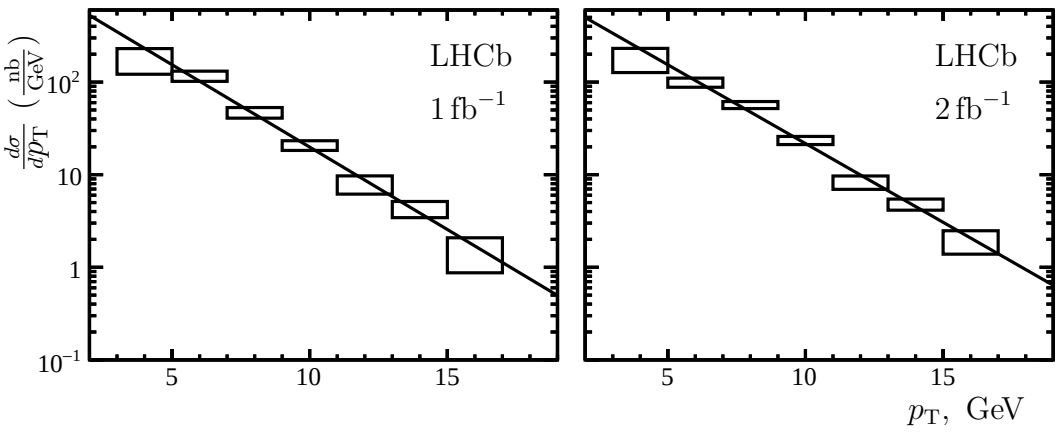

Figure 6.12: Differential production cross-section of the $\eta_c(1S)$ state for the $\sqrt{s} = 7\,\text{TeV}$ (left) and $\sqrt{s} = 8\,\text{TeV}$ (right) data samples. Fits (integral) to an exponential function are overlaid.

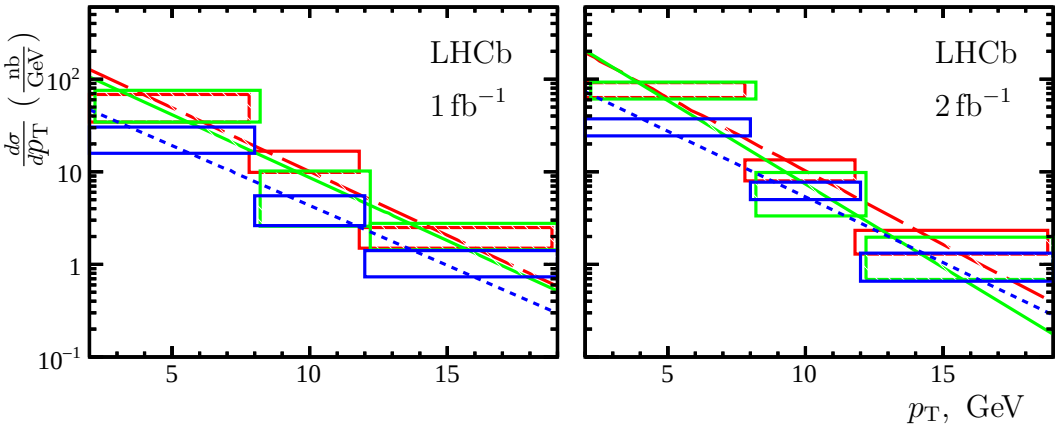

Figure 6.13: Differential production cross-section of the χ_{c0} (red), χ_{c1} (green) and χ_{c2} (blue) states for the $\sqrt{s} = 7\,\text{TeV}$ (left) and $\sqrt{s} = 8\,\text{TeV}$ (right) data samples. Fits (integral) to an exponential function are overlaid.

Table 6.15: Exponential slope parameter in units of GeV^{-1} from a fit to the p_T spectra of $\eta_c(1S)$, χ_{c0}, χ_{c1} and χ_{c2} mesons.

	$\eta_c(1S)$	χ_{c0}	χ_{c1}	χ_{c2}
$\sqrt{s} = 7\,\text{TeV}$	0.41 ± 0.02	0.32 ± 0.04	0.31 ± 0.06	0.30 ± 0.05
$\sqrt{s} = 8\,\text{TeV}$	0.39 ± 0.02	0.37 ± 0.04	0.41 ± 0.06	0.33 ± 0.04

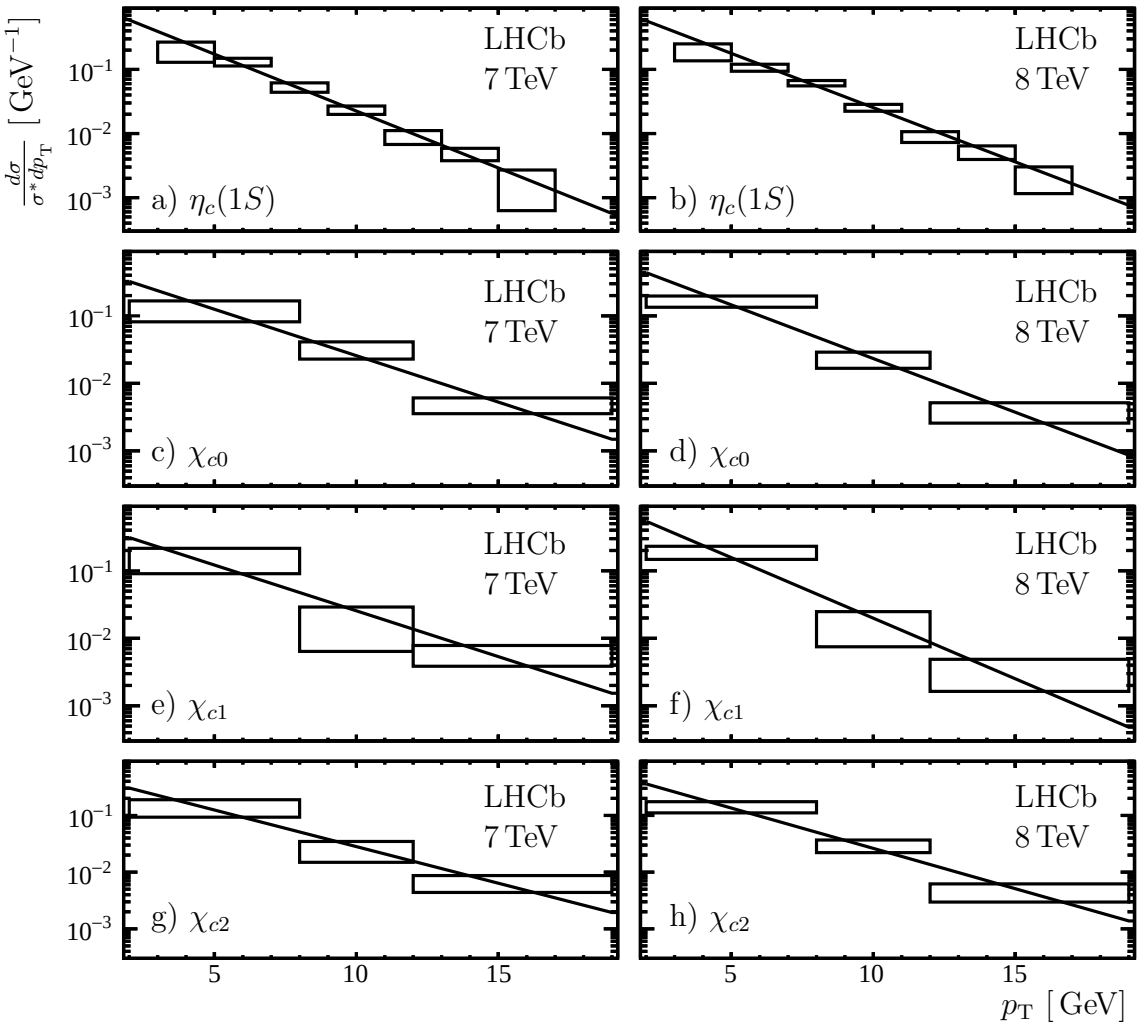

Figure 6.14: Differential cross-sections normalized to the production cross-section integrated over the studied region, σ^*, of the (top to bottom) $\eta_c(1S)$, χ_{c0}, χ_{c1} and χ_{c2} states for the (left) $\sqrt{s} = 7\,\text{TeV}$ and the (right) $\sqrt{s} = 8\,\text{TeV}$ data samples. The horizontal and vertical size of the boxes reflect the size of the p_T bins and the statistical and uncorrelated systematic uncertainties of the differential production cross-sections added in quadrature. Fits by an exponential function are overlaid.

6.6 Search for production of the $X(3872)$, $X(3915)$, and $\chi_{c2}(3930)$ states

Observation of the $X(3915)$ and $\chi_{c2}(3930)$ states in b-decays, or the $X(3872)$ decaying to the $\phi\phi$ pair, would provide interesting information on the properties of these states. For example, none of $X(3872)$ decays to light hadrons has been observed. Hence, the observation of the $X(3872) \to \phi\phi$ would lead to the estimation of fraction of the charmonium component in $X(3872)$ if one considers that $X(3872)$ is a mixed state of charmonium and hadronic molecule. Similar considerations apply for $X(3915)$ and $\chi_{c2}(3930)$ (named $X(3927)$ at the time of this analysis release).

Figure 6.7 shows no indication of signal from the $X(3872)$, $X(3915)$, and $\chi_{c2}(3930)$ states. From that upper limits are obtained, relative to the observed states with similar quantum numbers.

Figures 6.15, 6.16, and 6.17 show the Δ_{χ^2} and PDF distributions for the $\frac{N(X(3872))}{N(\chi_{c1})}$, $\frac{N(X(3915))}{N(\chi_{c0})}$, and $\frac{N(\chi_{c2}(3930))}{N(\chi_{c2})}$, respectively. The obtained PDF distributions take into accound possible systematic effects. For that, the fit likelihood has been convolved with a gaussian, representing total systematic uncertainty. The Bayessian upper limits at 90 % and 95 % confidence level (CL) are then extracted for the first time.

Vertical lines correspond to the 90% and 95% CL upper limits.

Using the efficiency ratios $\frac{\varepsilon(X(3872))}{\varepsilon(\chi_{c1})} = 1.11$, $\frac{\varepsilon(X(3915))}{\varepsilon(\chi_{c0})} = 1.16$, and $\frac{\varepsilon(\chi_{c2}(3930))}{\varepsilon(\chi_{c2})} = 1.12$, the following upper limits on the ratios of inclusive branching fractions are obtained:

$$\frac{\mathcal{B}(b \to X(3872)X) \times \mathcal{B}(X(3872) \to \phi\phi)}{\mathcal{B}(b \to \chi_{c1}X) \times \mathcal{B}(\chi_{c1} \to \phi\phi)} < 0.39(0.34), \tag{6.2}$$

$$\frac{\mathcal{B}(b \to X(3915)X) \times \mathcal{B}(X(3915) \to \phi\phi)}{\mathcal{B}(b \to \chi_{c0}X) \times \mathcal{B}(\chi_{c0} \to \phi\phi)} < 0.14(0.12), \tag{6.3}$$

$$\frac{\mathcal{B}(b \to \chi_{c2}(3930)X) \times \mathcal{B}(\chi_{c2}(3930) \to \phi\phi)}{\mathcal{B}(b \to \chi_{c2}X) \times \mathcal{B}(\chi_{c2} \to \phi\phi)} < 0.20(0.16) \tag{6.4}$$

at the 95% (90%) CL.

Using the branching fractions for the χ_{c0}, χ_{c1}, and χ_{c2} decays to the $\phi\phi$ final state [77], observed signals of these states on Fig. 6.7, the $\eta_c(1S)$ state production from Ref. [13] and efficiency ratios from the simulation, the upper limits at 95% (90%) CL on production of

the $X(3872)$, $X(3915)$, and $\chi_{c2}(3930)$ states are obtained as:

$$\mathcal{B}(b \to X(3872)X) \times \mathcal{B}(X(3872) \to \phi\phi) < 4.5(3.9) \times 10^{-7}, \tag{6.5}$$

$$\mathcal{B}(b \to X(3915)X) \times \mathcal{B}(X(3915) \to \phi\phi) < 3.1(2.7) \times 10^{-7}, \tag{6.6}$$

$$\mathcal{B}(b \to \chi_{c2}(3930)X) \times \mathcal{B}(\chi_{c2}(3930) \to \phi\phi) < 2.8(2.3) \times 10^{-7}. \tag{6.7}$$

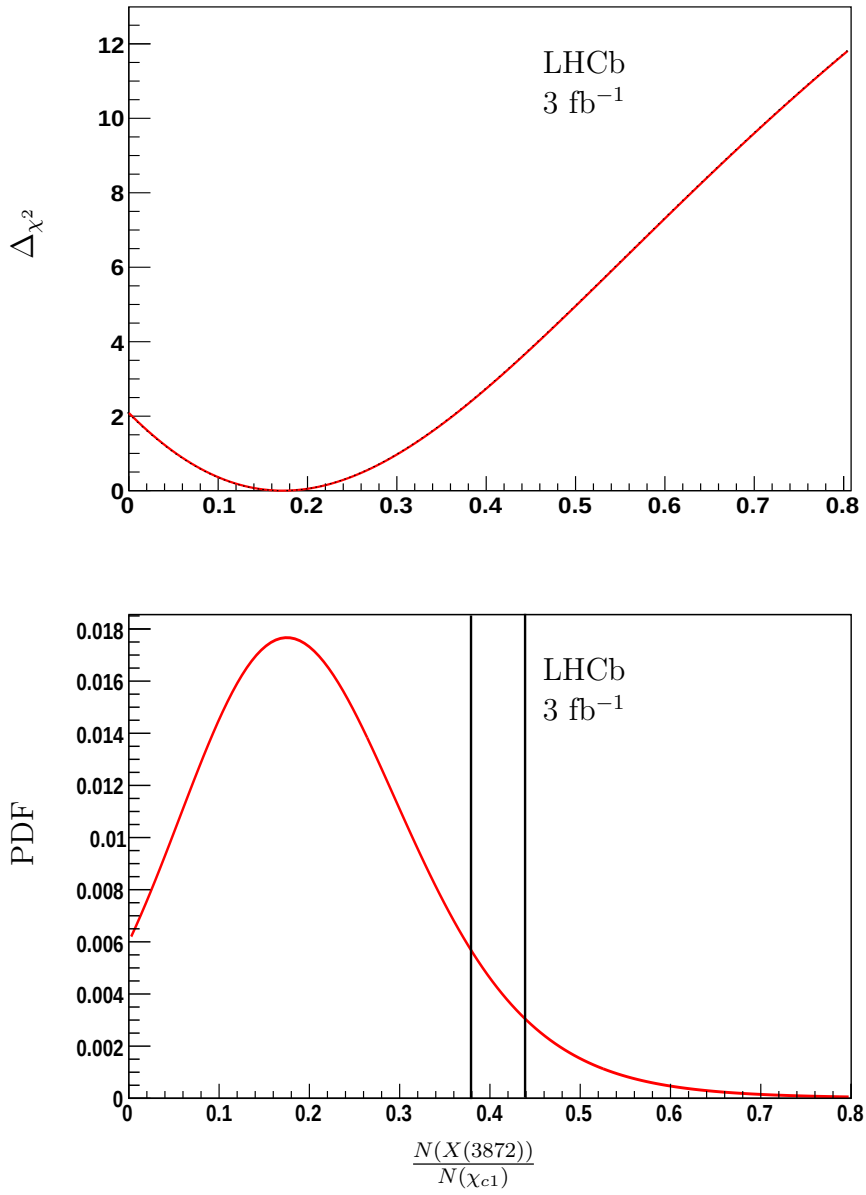

Figure 6.15: The Δ_{χ^2} and PDF distributions for the $\frac{N(X(3872))}{N(\chi_{c1})}$ ratio. Vertical lines correspond to 90 % CL and 95 % CL upper limits.

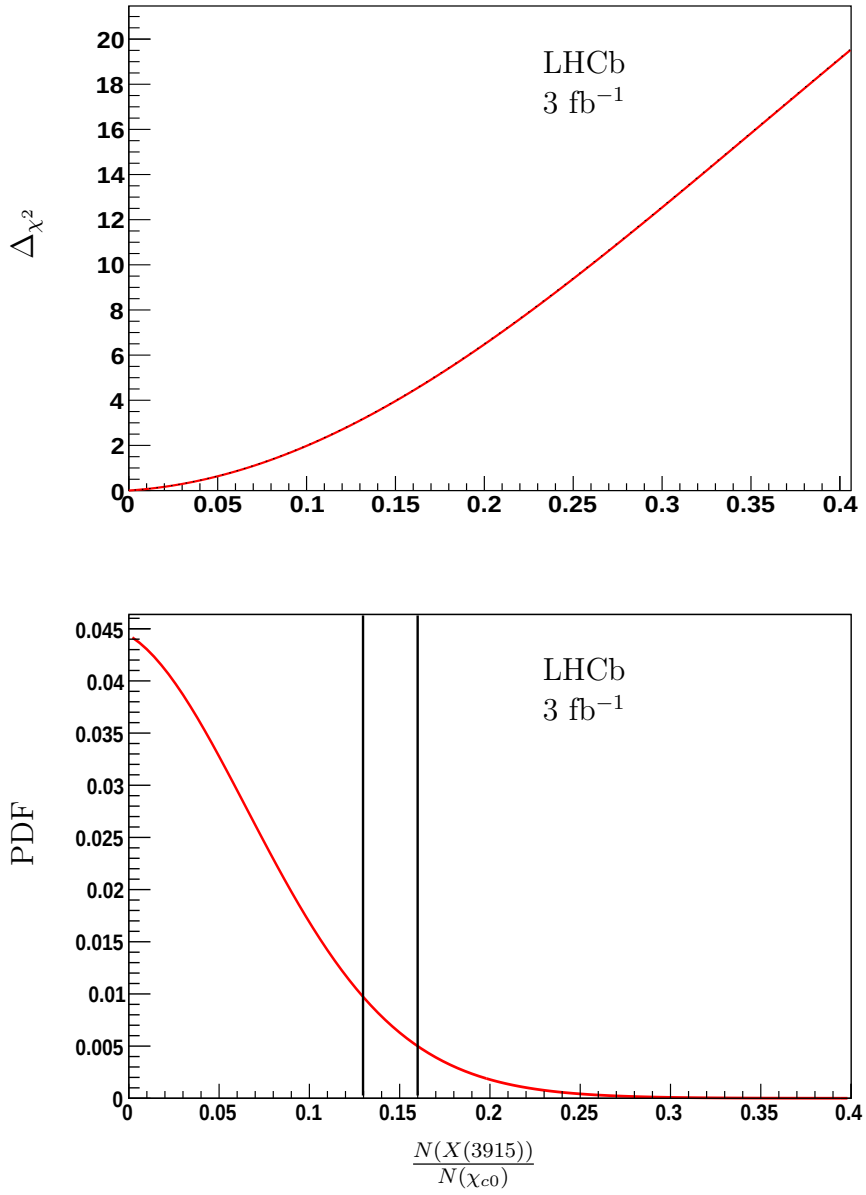

Figure 6.16: The Δ_{χ^2} and PDF distributions for the $\frac{N(X(3915))}{N(\chi_{c0})}$ ratio. Vertical lines correspond to 90 % CL and 95 % CL upper limit.

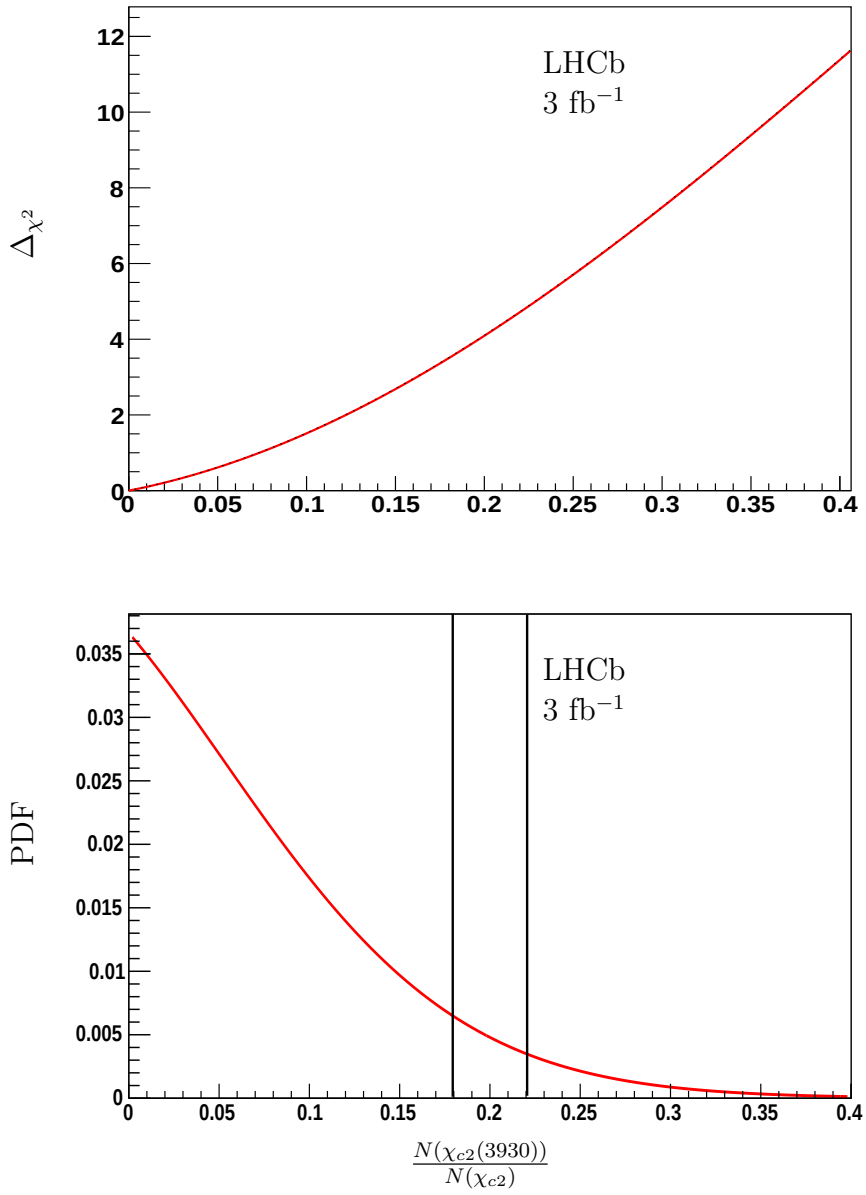

Figure 6.17: The Δ_{χ^2} and PDF distributions for the $\frac{N(\chi_{c2}(3930))}{N(\chi_{c2})}$ ratio. Vertical lines correspond to 90 % CL and 95 % CL upper limit.

6.7 Summary and discussion

In summary, charmonia production in b-hadron inclusive decays is studied with the integrated luminosity of 3 fb^{-1}, using charmonia decays to $\phi\phi$ pairs. These studies are performed using pure $\phi\phi$ yields from determined using a 2D-fit technique.

Inclusive production of the χ_c states in b-hadron decays are measured to be

$$\begin{aligned}
\mathcal{B}(b \to \chi_{c0} X) &= (3.02 \pm 0.47 \pm 0.23 \pm 0.94) \times 10^{-3} \ , \\
\mathcal{B}(b \to \chi_{c1} X) &= (2.76 \pm 0.59 \pm 0.23 \pm 0.89) \times 10^{-3} \ , \\
\mathcal{B}(b \to \chi_{c2} X) &= (1.15 \pm 0.20 \pm 0.07 \pm 0.36) \times 10^{-3} \ .
\end{aligned}$$

These results will be used in the phenomenological analysis described in Chapter 7.

Figure 6.18 shows a summary of the branching fraction measurements for inclusive decays of light B-mesons, $\mathcal{B}(B \to \chi_c X)$, and of mixtures of all b hadrons, $\mathcal{B}(b \to \chi_c X)$. Note that the mixture of b-hadrons is different for LEP and LHC. Also indicated are the PDG averages and averages including the results from this paper. Note, that the recent update from Belle experiment [76] was released after this analysis and did not enter the plot on Fig. 6.18. The Belle measurements are the most precise among all measurements at B-factories and are shown below.

$$\begin{aligned}
\mathcal{B}(B \to \chi_{c1} X)^{Belle} &= (3.33 \pm 0.05 \pm 0.24) \times 10^{-3}, \\
\mathcal{B}(B \to \chi_{c2} X)^{Belle} &= (9.8 \pm 0.6 \pm 1.0) \times 10^{-4}.
\end{aligned}$$

The LHCb result for b-hadron decays to χ_{c0} is the only available result and is not shown in the figure. Note, that no indirect contribution to the production rate is subtracted. However, limited contribution from $\psi(2S)$ decays to the χ_c states is present. Relations between the χ_c branching fractions are not consistent with those predicted in Ref. [82]. The branching fraction $\mathcal{B}(b \to \chi_{c0} X)$ is measured for the first time. The result for b-decays into χ_{c1} is the most precise measurement for the admixture of B^0, B^+, B_s^0 and b-baryons. Central value of the result for b-decays into χ_{c1} is lower than the value measured by DELPHI [67] and L3 [68] experiments at LEP, however, taking into account the LEP results limited precision, the LHCb result is consistent with them. The obtained value is lower than the branching fraction of b-decays into χ_{c1} measured by CLEO [72], Belle [75] and BaBar [71] using the admixture of B^0 and B^+. The branching fraction of b-hadron decays into χ_{c2} is measured for the first time with the B^0, B^+, B_s^0 and b-baryons admixture. The result is consistent with the average, corresponding to the B^0, B^+ admixture, from

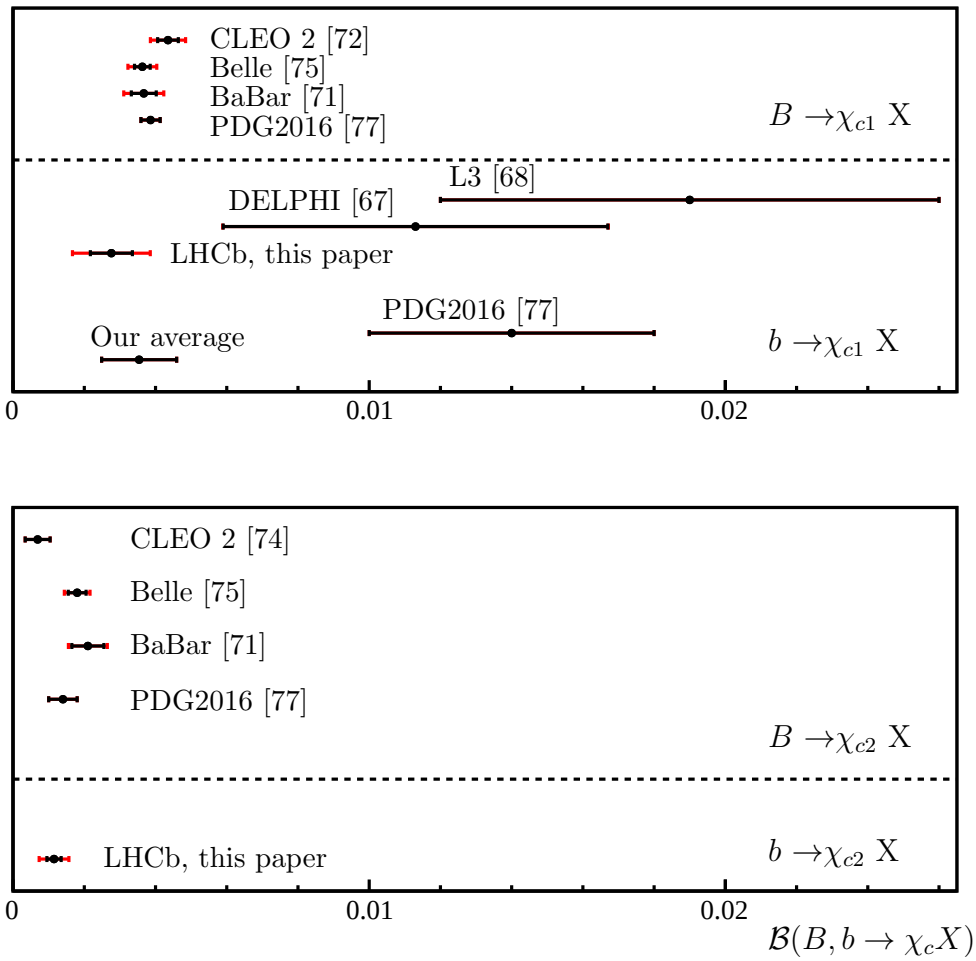

Figure 6.18: Summary of the branching fraction measurements for inclusive decays of light B mesons, $\mathcal{B}(B \to \chi_c X)$, and of all b hadrons, $\mathcal{B}(b \to \chi_c X)$, shown in each plot above and below the dashed line, respectively. The branching fractions for the decays to χ_{c1} and χ_{c2} are shown in the top and bottom plots, respectively. The world averages noted "PDG2016" do not include the LHCb results.

Ref. [77], given large PDG uncertainty. The obtained value has higher precision than the results from CLEO [74], Belle [75] and BaBar [71], is close to the CLEO result of $(0.67 \pm 0.34 \pm 0.03) \times 10^{-3}$ and is different by more than 2σ from the results of Belle, $(1.80^{+0.23}_{-0.28} \pm 0.26) \times 10^{-3}$, and BaBar, $(2.10 \pm 0.45 \pm 0.31) \times 10^{-3}$.

Transverse momentum p_{T} dependence of charmonia production in b-decays is studied for the $\eta_c(1S)$ and χ_c states in the LHCb acceptance and for $p_{\mathrm{T}} > 4\,\mathrm{GeV}/c$. Precision of about 15% for $\eta_c(1S)$ and between 20% and 30% for the χ_c states is achieved. The NLO calculations of the p_{T} dependence of the η_c and χ_c production in b-decays are important to translate the obtained results to the conclusions on the production mechanisms.

Production of the $\eta_c(2S)$ state in b-decays was determined to be

$$\mathcal{B}(b \to \eta_c(2S)X) \times \mathcal{B}(\eta_c(2S) \to \phi\phi) = (6.34 \pm 1.81 \pm 0.57 \pm 1.89) \times 10^{-7} \ .$$

This is the first indication of the $\eta_c(2S)$ production in b-decays, as well as the decay of $\eta_c(2S)$ meson to the $\phi\phi$ pair.

These are the first χ_c and $\eta_c(2S)$ inclusive production measurements, using charmonia decays to hadronic final state, in the high-multiplicity environment of a hadron machine.

In addition upper limits at 95% (90%) CL on the production of the $X(3872)$, $X(3915)$, and $\chi_{c2}(3930)$, states in b-decays are obtained as:

$$\begin{aligned}
\mathcal{B}(b \to X(3872)X) \times \mathcal{B}(X(3872) \to \phi\phi) &< 4.5(3.9) \times 10^{-7}, \\
\mathcal{B}(b \to X(3915)X) \times \mathcal{B}(X(3915) \to \phi\phi) &< 3.1(2.7) \times 10^{-7}, \\
\mathcal{B}(b \to \chi_{c2}(3930)X) \times \mathcal{B}(\chi_{c2}(3930) \to \phi\phi) &< 2.8(2.3) \times 10^{-7}.
\end{aligned}$$

One can qualitatively estimate an upper limit on the branching fraction of the $X(3872)$ decay to $\phi\phi$. Since the $X(3872)$ has likely $\chi_{c1}(2P)$ charmonium component, the radial suppresion of b-hadron decays should work similarly for different charmonium states. In other words:

$$\frac{\mathcal{B}(b \to X(3872)X)}{\mathcal{B}(b \to \chi_{c1}X)} \sim \frac{\mathcal{B}(b \to \psi(2S)X)}{\mathcal{B}(b \to J/\psi\, X)}. \tag{6.8}$$

The right part of this equation can be extracted from Ref. [73] to be

$$\frac{\mathcal{B}(b \to \psi(2S)X)}{\mathcal{B}(b \to J/\psi\, X)} = 0.25 \pm 0.03. \tag{6.9}$$

Then using Eqs.6.8 6.9 and 6.4 and the branching fraction of the $\chi_{c1} \to \phi\phi$ decay, one can estimate at a qualitative level that

$$\frac{\mathcal{B}(X(3872) \to \phi\phi)}{\mathcal{B}(\chi_{c1} \to \phi\phi)} < 1.6, \tag{6.10}$$

$$\mathcal{B}(X(3872) \to \phi\phi) < 7.5 \times 10^{-4}. \tag{6.11}$$

Chapter 7

Phenomenological analysis of charmonium production

The first measurement of the $\eta_c(1S)$ prompt production and production in b-hadron inclusive decays performed at LHCb [249] triggered an intention to simultaneously use all available experimental information on S-wave charmonium production to constrain involved LDMEs.

The χ_{c1} and χ_{c2} inclusive production in b-hadron decays were measured at B-factories and LEP. The results discussed in Chapter 5.6 provide the first measurement of branching fraction of χ_{c0} inclusive production in b-hadron decays. The relative χ_{c1}-to-χ_{c0}, χ_{c2}-to-χ_{c0} and χ_{c2}-to-χ_{c1} production rates have also been reported. These measurements provide a powerful test of theoretical predictions. While correlated experimental and theoretical uncertainties cancel in ratios, the implication of absolute branching fractions provides a more extensive number of independent measurements, i.e. larger number of constraints.

In this chapter the LHCb results on the absolute branching fractions $\mathcal{B}(b \to \eta_c(1S)X)$ and $\mathcal{B}(b \to \chi_{cJ}X)$ and their ratios are compared to predictions from Ref. [82] using a fit technique to quantify the agreement. For J/ψ and η_c mesons, a simultaneous study of prompt and b-decays production is performed thanks to the theory prediction provided by H.-S. Shao [250]. For the analysis presented in this chapter, I would like to acknowledge fruitful discussions with E. Kou, J.-P. Lansberg and H.-S. Shao.

This chapter is organised as follows. Experimental input of charmonium production in b-hadron decays is presented in Section 7.1. The NRQCD prediction for inclusive charmonium production in b-hadron decays used for further fits to theory is described in Section 7.2. A comparison of S-wave charmonium hadroproduction and production in b-hadron decays to theory together with simultaneous fit to both observables is shown in Section 7.3. In Section 7.4 theory predictions are compared to the measurements of P-wave charmonium production in b-hadron decays presented in Chapter 5.6. Finally the results are summarised in Section 7.5.

7.1 Experimental input, feed-down subtraction

While the J/ψ state production in b-hadron inclusive decays is well measured, $\mathcal{B} = (1.094 \pm 0.032)\%$, the only measurement of the $\eta_c(1S)$ production in b-hadron inclusive decays has been performed by the LHCb experiment [249]. LHCb measured the relative $\eta_c(1S)$ to J/ψ production in b-hadron inclusive decays [249] to be

$$\frac{\mathcal{B}(b \to \eta_c(1S)X)}{\mathcal{B}(b \to J/\psi X)} = 0.424 \pm 0.055 \pm 0.021 \pm 0.045_{\mathcal{B}}, \tag{7.1}$$

where the first uncertainty is statistical, the second is systematic, the third uncertainty is due to those on the branching fractions $\mathcal{B}(\eta_c(1S) \to p\overline{p})$ and $\mathcal{B}(J/\psi \to p\overline{p})$ [77]. Measurements of the χ_{c1} and χ_{c2} inclusive production in b-hadron decays from the e^+e^- experiments, where only light b-hadrons - B^+ and B^0 mesons - are produced, were performed at CLEO [251, 252], Belle [76, 253] and BaBar [254]. The world average values for branching fractions of light B-meson inclusive decays to the charmonium states of interest [77] are given in Table 7.1.

Table 7.1: Branching fractions of B-meson inclusive decays to charmonium states [77].

	η_c (1S)	J/ψ	χ_{c0}	χ_{c1}	χ_{c2}
$\mathcal{B}(B \to c\bar{c}X),\ \times 10^{-3}$	< 9	10.94 ± 0.32	-	3.55 ± 0.27	1.00 ± 0.17

The inclusive production of the χ_{c1} and χ_{c2} states in b-decays involving all b-hadrons (B^+, B^0, B_s^0, B_c^+ and b-baryons) has been studied at L3 [255] and DELPHI [256] experiments. Recently, LHCb reported the most precise χ_{c1} and χ_{c2} and the first χ_{c0} production measurements in b-hadron inclusive decays [257] as well as the corresponding χ_{c1}-to-χ_{c0} and χ_{c2}-to-χ_{c0} production ratios. LHCb measured the branching fractions of b-hadron inclusive decays into χ_c states to be

$$\mathcal{B}(b \to \chi_{c0}X) = (3.02 \pm 0.47 \pm 0.23 \pm 0.94_{\mathcal{B}}) \times 10^{-3}, \tag{7.2}$$

$$\mathcal{B}(b \to \chi_{c1}X) = (2.76 \pm 0.59 \pm 0.23 \pm 0.89_{\mathcal{B}}) \times 10^{-3}, \tag{7.3}$$

$$\mathcal{B}(b \to \chi_{c2}X) = (1.15 \pm 0.20 \pm 0.07 \pm 0.36_{\mathcal{B}}) \times 10^{-3}, \tag{7.4}$$

where the third uncertainty is due to the uncertainties on the branching fractions of the b-hadron inclusive decays to the $\eta_c(1S)$ meson, $\mathcal{B}(b \to \eta_c(1S)X)$ [249], and of the $\eta_c(1S)$ and χ_c decays to a pair of ϕ mesons [77]. The relative branching fractions are determined

to be

$$\frac{\mathcal{B}(b \to \chi_{c1}X)}{\mathcal{B}(b \to \chi_{c0}X)} = 0.92 \pm 0.20 \pm 0.02 \pm 0.14_{\mathcal{B}}, \tag{7.5}$$

$$\frac{\mathcal{B}(b \to \chi_{c2}X)}{\mathcal{B}(b \to \chi_{c0}X)} = 0.38 \pm 0.07 \pm 0.01 \pm 0.05_{\mathcal{B}}, \tag{7.6}$$

where the third uncertainty is due to the uncertainties on the branching fractions $\mathcal{B}(\chi_c \to \phi\phi)$ [77]. The results for the χ_{c1} and χ_{c2} production in b-hadron inclusive decays are close to those in B^0 and B^+ inclusive decays [77].

The mixture of b-hadrons in the LHCb measurements consists of about 76% of light B-mesons, 10% of B_s^0 and 14% of Λ_b^0 [258,259], while other contributions are considered to be negligible. The branching fraction $\mathcal{B}(\Lambda_b^0 \to (c\overline{c})X)$ is assumed to be small compared to $\mathcal{B}(B \to (c\overline{c})X)$, while $\mathcal{B}(B_s^0 \to (c\overline{c})X)$ is assumed to be of the same value as $\mathcal{B}(B \to (c\overline{c})X)$. Hence, no significant difference in the ratio of branching fractions of inclusive decays to χ_c states is expected between all b-hadron and light B-meson systems.

The dominant feed-down contributions to J/ψ production originate from the $\psi(2S) \to J/\psi X$, $\chi_{c1} \to J/\psi\gamma$ and $\chi_{c2} \to J/\psi\gamma$ transitions. The feed-down contributions to the $\eta_c(1S)$ yield originate from the h_c and χ_c decays. The feed-down to the $\eta_c(1S)$ sample is expected to be small and is not taken into account, so that it is assumed that $\mathcal{B}(b \to \eta_c(1S)X) = \mathcal{B}(b \to \eta_c(1S)^{direct}X)$. The feed-down subtracted $\eta_c(1S)$ to J/ψ relative production in b-inclusive decays is obtained in the following way

$$\begin{aligned}\frac{\mathcal{B}(b \to \eta_c(1S)^{direct}X)}{\mathcal{B}(b \to J/\psi^{direct}X)} = \frac{\mathcal{B}(b \to \eta_c(1S)X)}{\mathcal{B}(b \to J/\psi X)} \times \\ \times\Big[1 - \frac{\mathcal{B}(b \to \chi_{c1}X)}{\mathcal{B}(b \to \eta_c(1S)X)}\frac{\mathcal{B}(b \to \eta_c(1S)X)}{\mathcal{B}(b \to J/\psi X)}\mathcal{B}(\chi_{c1} \to J/\psi\gamma) \\ - \frac{\mathcal{B}(b \to \chi_{c2}X)}{\mathcal{B}(b \to \eta_c(1S)X)}\frac{\mathcal{B}(b \to \eta_c(1S)X)}{\mathcal{B}(b \to J/\psi X)}\mathcal{B}(\chi_{c2} \to J/\psi\gamma) \\ - \frac{\mathcal{B}(b \to \psi(2S)X)}{\mathcal{B}(b \to J/\psi X)}\mathcal{B}(\psi(2S) \to J/\psi X)\Big]^{-1}.\end{aligned} \tag{7.7}$$

Using the measurements (7.1), (7.2), (7.3) and (7.4) and the values of $\mathcal{B}(b \to \psi(2S)X)$, $\mathcal{B}(\psi(2S) \to J/\psi X)$ and $\mathcal{B}(\chi_c \to J/\psi\gamma)$ from Ref. [77], the branching fraction of the direct $\eta_c(1S)$ production in b-hadron decays relative to that of the J/ψ meson, is calculated to be

$$\frac{\mathcal{B}(b \to \eta_c(1S)^{direct}X)}{\mathcal{B}(b \to J/\psi^{direct}X)} = 0.691 \pm 0.090 \pm 0.024 \pm 0.103, \tag{7.8}$$

where the third uncertainty is due to that on the branching fractions involved in the calculation.

The dominant feed-down contribution to the χ_c yield is from the $\psi(2S) \to \chi_c\gamma$ transition and is measured to be around 10% for each of the χ_{c0}, χ_{c1} and χ_{c2} states [77]. The feed-down contributions to the χ_c production is subtracted in the following way

$$\begin{aligned}
\mathcal{B}(b \to {\chi_{c0}}^{direct} X) &= \mathcal{B}(b \to \chi_{c0} X) - \mathcal{B}(b \to \psi(2S) X) \cdot \mathcal{B}(\psi(2S) \to \chi_{c0}\gamma), \\
\mathcal{B}(b \to {\chi_{c1}}^{direct} X) &= \mathcal{B}(b \to \chi_{c1} X) - \mathcal{B}(b \to \psi(2S) X) \cdot \mathcal{B}(\psi(2S) \to \chi_{c1}\gamma), \\
\mathcal{B}(b \to {\chi_{c2}}^{direct} X) &= \mathcal{B}(b \to \chi_{c2} X) - \mathcal{B}(b \to \psi(2S) X) \cdot \mathcal{B}(\psi(2S) \to \chi_{c2}\gamma),
\end{aligned}$$

$$\begin{aligned}
\frac{\mathcal{B}(b \to {\chi_{c1}}^{direct} X)}{\mathcal{B}(b \to {\chi_{c0}}^{direct} X)} &= \frac{\mathcal{B}(b \to \chi_{c1} X)}{\mathcal{B}(b \to \chi_{c0} X)} \times \frac{1 - \frac{\mathcal{B}(b \to \psi(2S) X) \cdot \mathcal{B}(\psi(2S) \to \chi_{c1}\gamma)}{\mathcal{B}(b \to \chi_{c1} X)}}{1 - \frac{\mathcal{B}(b \to \psi(2S) X) \cdot \mathcal{B}(\psi(2S) \to \chi_{c0}\gamma)}{\mathcal{B}(b \to \chi_{c1} X)}}, \\
\frac{\mathcal{B}(b \to {\chi_{c2}}^{direct} X)}{\mathcal{B}(b \to {\chi_{c0}}^{direct} X)} &= \frac{\mathcal{B}(b \to \chi_{c1} X)}{\mathcal{B}(b \to \chi_{c0} X)} \times \frac{1 - \frac{\mathcal{B}(b \to \psi(2S) X) \cdot \mathcal{B}(\psi(2S) \to \chi_{c2}\gamma)}{\mathcal{B}(b \to \chi_{c1} X)}}{1 - \frac{\mathcal{B}(b \to \psi(2S) X) \cdot \mathcal{B}(\psi(2S) \to \chi_{c0}\gamma)}{\mathcal{B}(b \to \chi_{c1} X)}}.
\end{aligned}$$

Using measurements (7.2), (7.3), (7.4), (7.5) and (7.6) and the values of $\mathcal{B}(b \to \psi(2S)X)$ and $BR(\psi(2S) \to \chi_c\gamma)$ from Ref. [77], the direct χ_c production rates in b-hadron decays are calculated to be

$$\mathcal{B}(b \to {\chi_{c0}}^{direct} X) = (2.74 \pm 0.47 \pm 0.23 \pm 0.94_{\mathcal{B}}) \times 10^{-3}, \tag{7.9}$$

$$\mathcal{B}(b \to {\chi_{c1}}^{direct} X) = (2.49 \pm 0.59 \pm 0.23 \pm 0.89_{\mathcal{B}}) \times 10^{-3}, \tag{7.10}$$

$$\mathcal{B}(b \to {\chi_{c2}}^{direct} X) = (0.89 \pm 0.20 \pm 0.07 \pm 0.36_{\mathcal{B}}) \times 10^{-3}, \tag{7.11}$$

where the third uncertainty is due to the uncertainties on the branching fractions of the b-hadron decays to the $\eta_c(1S)$ meson, $\mathcal{B}(b \to \eta_c(1S)X)$ [249], $\eta_c(1S)$ and χ_c decays to $\phi\phi$, $\mathcal{B}(\eta_c \to \phi\phi)$ and $\mathcal{B}(\chi_{cJ} \to \phi\phi)$ [77] and due to the feed-down contribution uncertainties.

The relative direct χ_c production rates in b-hadron decays are calculated to be

$$\frac{\mathcal{B}(b \to {\chi_{c1}}^{direct} X)}{\mathcal{B}(b \to {\chi_{c0}}^{direct} X)} = 0.91 \pm 0.20 \pm 0.02 \pm 0.15_{\mathcal{B}}, \tag{7.12}$$

$$\frac{\mathcal{B}(b \to {\chi_{c2}}^{direct} X)}{\mathcal{B}(b \to {\chi_{c0}}^{direct} X)} = 0.34 \pm 0.06 \pm 0.01 \pm 0.05_{\mathcal{B}}, \tag{7.13}$$

where the third uncertainty is due to those on the branching fractions $\mathcal{B}(\chi_{cJ} \to \phi\phi)$ [77] and due to the uncertaities of the branching fractions of the decays contributing to the feed-down. Correlations between the uncertainties of the values of $\mathcal{B}(b \to \chi_{c0}X)$, $\mathcal{B}(b \to \chi_{c1}X)$

and $\mathcal{B}(b \to \chi_{c2}X)$ are not taken into account in the feed-down contribution uncertainty estimation, because the correlation effect is small compared to other uncertainties.

Finally, the relative branching fractions of the $b \to \chi_c X$ inclusive decays to the measured relative branching fractions of exclusive B-meson decays to the χ_c states are compared. A selection of the measured exclusive branching fractions from Ref. [77] is listed in Table 7.2. All these branching fractions show suppression of the decays to the χ_{c2} state compared to the decays to the χ_{c1} and χ_{c0} states. The branching fractions of the exclusive b-hadron decays to the χ_{c0} state are smaller than the branching fractions of decays to the χ_{c1} state. The values of the branching fractions $\mathcal{B}(B \to \chi_c K)$ are similar to those of $\mathcal{B}(B \to \chi_c K^*)$.

Table 7.2: Branching fractions of exclusive B-meson decays to χ_c states [77].

	χ_{c0}	χ_{c1}	χ_{c2}
$\mathcal{B}(B^+ \to \chi_c K^+)$	$(1.50 \pm 0.15) \times 10^{-4}$	$(4.79 \pm 0.23) \times 10^{-4}$	$(1.1 \pm 0.4) \times 10^{-5}$
$\mathcal{B}(B^0 \to \chi_c K^0)$	$(1.47 \pm 0.27) \times 10^{-4}$	$(3.93 \pm 0.27) \times 10^{-4}$	$< 1.5 \times 10^{-5}$
$\mathcal{B}(B^+ \to \chi_c K^{*+})$	$< 2.1 \times 10^{-4}$	$(3.0 \pm 0.6) \times 10^{-4}$	$< 1.52 \times 10^{-4}$
$\mathcal{B}(B^0 \to \chi_c K^{*0})$	$(1.7 \pm 0.4) \times 10^{-4}$	$(2.39 \pm 0.19) \times 10^{-4}$	$(4.9 \pm 1.2) \times 10^{-5}$
$\mathcal{B}(B^+ \to \chi_c \pi^+)$	$< 1 \times 10^{-7}$	$(2.2 \pm 0.5) \times 10^{-5}$	$< 1 \times 10^{-7}$
$\mathcal{B}(B^0 \to \chi_c \pi^0)$	–	$(1.12 \pm 0.28) \times 10^{-5}$	–
$\mathcal{B}(B^0 \to \chi_c K^- \pi^+)$	–	$(3.8 \pm 0.4) \times 10^{-4}$	–
$\mathcal{B}(B_s^0 \to \chi_c \phi)$	–	$(2.03 \pm 0.29) \times 10^{-4}$	–

7.2 Predictions for charmonium yields in B-meson decays

A theoretical description of the inclusive b-hadron decays to S-wave and in particular to P-wave charmonium states is challenging. Despite the fact that many problems have been recognised, no clear solutions have been identified yet. More theoretical efforts are certainly called for.

Authors of Ref. [82] consider two mechanisms - CS and CO - of charmonia production in B-meson decays. A negative NLO correction has been pointed out for the CS contribution, which makes it difficult to deliver a precise theoretical prediction.

For S-wave charmonium the four Fock states are expected to be dominating, namely $O_1^{J/\psi}(^3S_1)$, $O_8^{J/\psi}(^3S_1)$, $O_8^{J/\psi}(^1S_0)$ and $O_8^{J/\psi}(^3P_0)$ for J/ψ and $O_1^{\eta_c}(^1S_0)$, $O_8^{\eta_c}(^1S_0)$, $O_8^{\eta_c}(^3S_1)$ and $O_8^{\eta_c}(^1P_1)$ for $\eta_c(1S)$. According to the proposed formalism, the J/ψ and the $\eta_c(1S)$ production rates in inclusive b-decays are expressed as [1]:

$$\mathcal{B}(B \to J/\psi X) = 0.754 \cdot 10^{-3}\langle O_1^{J/\psi}(^3S_1)\rangle + 0.195\langle O_8^{J/\psi}(^3S_1)\rangle + 0.342\Big[\langle O_8^{J/\psi}(^1S_0)\rangle + \frac{3.10}{m_c^2}\langle O_8^{J/\psi}(^3P_0)\rangle\Big], \tag{7.14}$$

$$\mathcal{B}(B \to \eta_c(1S)X) = 2.500 \cdot 10^{-3}\langle O_1^{\eta_c}(^1S_0)\rangle + 0.342\langle O_8^{\eta_c}(^1S_0)\rangle + 0.195\Big[\langle O_8^{\eta_c}(^3S_1)\rangle - \frac{0.240}{m_c^2}\langle O_8^{\eta_c}(^1P_1)\rangle\Big], \tag{7.15}$$

where m_c is the mass of the c-quark. In Eq. 7.15 the coefficient of the colour singlet contribution suffers from large theoretical uncertainties. However, in this discussion we quote the so-called *improved* value, which is the NLO calculation with one term from NNLO level (see Ref. [82] for details).

Within the same formalism, the two Fock states, $O_1^{\chi_{cJ}}(^3P_J)$ and $O_8^{\chi_{cJ}}(^3S_1)$, are expected to be dominating in the description of the $B \to \chi_{cJ}X$ decays as discussed in Chapter 2. The branching fractions of the χ_c production in inclusive B-meson decays are then

[1] Since the present discussion is qualitative, I simply quote the central values ignoring the theoretical uncertainties related to the charm mass, renormalisation scale etc.

expressed as:

$$\mathcal{B}(B \to \chi_{c0} X) = \frac{-0.0148}{m_c^2}\langle O_1^{\chi_{c0}}(^3P_0)\rangle + 0.195\langle O_8^{\chi_{c0}}(^3S_1)\rangle, \tag{7.16}$$

$$\mathcal{B}(B \to \chi_{c1} X) = \frac{-0.00783}{m_c^2}\langle O_1^{\chi_{c1}}(^3P_1)\rangle + 0.195\langle O_8^{\chi_{c1}}(^3S_1)\rangle, \tag{7.17}$$

$$\mathcal{B}(B \to \chi_{c2} X) = \frac{-0.0120}{m_c^2}\langle O_1^{\chi_{c2}}(^3P_2)\rangle + 0.195\langle O_8^{\chi_{c2}}(^3S_1)\rangle. \tag{7.18}$$

Here again I quote only *improved* values for the singlet contribution.

The LDMEs are linked by the spin relations. For the J/ψ and $\eta_c(1S)$ meson production, this gives:

$$\begin{aligned}
\langle O_1^{\eta_c}(^1S_0)\rangle &= \frac{1}{3}\langle O_1^{J/\psi}(^3S_1)\rangle,\\
\langle O_8^{\eta_c}(^1S_0)\rangle &= \frac{1}{3}\langle O_8^{J/\psi}(^3S_1)\rangle,\\
\langle O_8^{\eta_c}(^3S_1)\rangle &= \langle O_8^{J/\psi}(^1S_0)\rangle,\\
\langle O_8^{\eta_c}(^1P_1)\rangle &= 3\langle O_8^{J/\psi}(^3P_0)\rangle.
\end{aligned}$$

Hence, both $\mathcal{B}(B \to \eta_c(1S)X)$ and $\mathcal{B}(B \to J/\psi X)$ can be expressed as a function of only four LDMEs:

$$\begin{aligned}
\mathcal{B}(B \to J/\psi X) = 7.54 \cdot 10^{-4}\langle O_1^{J/\psi}(^3S_1)\rangle + 0.195\langle O_8^{J/\psi}(^3S_1)\rangle + \\
0.342\Big[\langle O_8^{J/\psi}(^1S_0)\rangle + \frac{3.10}{m_c^2}\langle O_8^{J/\psi}(^3P_0)\rangle\Big],
\end{aligned} \tag{7.19}$$

$$\begin{aligned}
\mathcal{B}(B \to \eta_c(1S)X) = 8.33 \cdot 10^{-4}\langle O_1^{J/\psi}(^3S_1)\rangle + 0.114\langle O_8^{J/\psi}(^3S_1)\rangle + \\
0.195\Big[\langle O_8^{J/\psi}(^1S_0)\rangle - \frac{0.720}{m_c^2}\langle O_8^{J/\psi}(^3P_0)\rangle\Big].
\end{aligned} \tag{7.20}$$

The spin relations for the χ_c states production yield

$$\begin{aligned}
O_1 &\equiv \langle O_1^{\chi_{c0}}(^3P_0)\rangle/m_c^2,\\
O_8 &\equiv \langle O_8^{\chi_{c0}}(^3S_1)\rangle,\\
\langle O_1^{\chi_{cJ}}(^3P_J)\rangle/m_c^2 &= (2J+1)O_1,\\
\langle O_8^{\chi_{cJ}}(^3S_1)\rangle &= (2J+1)O_8.
\end{aligned}$$

Thus, three branching fractions, $\mathcal{B}(B \to \chi_{c0}X), \mathcal{B}(B \to \chi_{c1}X)$ and $\mathcal{B}(B \to \chi_{c2}X)$, are

expressed as a function of only two LDMEs:

$$\mathcal{B}(B \to \chi_{c0} X) = -0.0148\ O_1 + 0.195\ O_8, \tag{7.21}$$

$$\mathcal{B}(B \to \chi_{c1} X) = -0.0234\ O_1 + 0.585\ O_8, \tag{7.22}$$

$$\mathcal{B}(B \to \chi_{c2} X) = -0.0600\ O_1 + 0.975\ O_8. \tag{7.23}$$

Therefore, a measurement of the three $\mathcal{B}(B \to \chi_{cJ} X)$ values would in principle overconstrain the model and provide a crucial consistency check.

The problem of the description of the P-wave states production has already been pointed out in the same paper [82]. If the O_1 value is computed using the potential model [260],

$$O_1 = 4.8 \times 10^{-2}\,\mathrm{GeV}^3,$$

and the O_8 value is adjusted to reproduce the χ_{c2} meson production rate measured at the CLEO experiment [252],

$$O_8 = 4.5 - 6.5 \times 10^{-3}\,\mathrm{GeV}^3,$$

the χ_{c1} state production rate is predicted to be in the range

$$\mathcal{B}(b \to \chi_{c1} X) = (0.15 - 0.27)\%,$$

which is below the value measured by CLEO even after taking into account large uncertainties.

In addition, authors of Ref. [261] extracted O_8 from the simultaneous fit of the χ_c hadroproduction measurements at CMS [135], LHCb [136], ATLAS [134] and CDF [262] to be

$$O_8 = (11.12 \pm 0.68) \times 10^{-3}\,\mathrm{GeV}^3,$$

which exceeds the value tuned using $\mathcal{B}(B \to \chi_{c2} X)$ from Ref. [252].

The solution to the problem of P-wave production seems to be a combination of different contributions. So far it remains an unsolved puzzle in the description of charmonium production. In the next section, I perform the fit of LDMEs using the LHCb results (Eqs. 7.9-7.13) as an attempt to pin down the origin of the problem, while in the remaining part of this section, I qualitatively discuss this puzzle exploiting Eqs. 7.16-7.18.

First of all, at the LO of the singlet model, only the χ_{c1} state can be produced since the production of the χ_{c0} and χ_{c2} states is allowed only via non-factorisable contribution within the $V-A$ theory. As in the case of the J/ψ meson production, the NLO corrections to the singlet contribution are negative, which induces a large theoretical uncertainty. Nevertheless, we can see from Eq. 7.17 that the NLO singlet contribution partially cancels the LO singlet contribution of the χ_{c1} meson, which makes its branching ratio much too small.

There are enough evidences that the colour octet contributions are necessary to explain the observed charmonium production in B decays (see e.g. [84]). The octet contributions to the $B \to \chi_{cJ} X$ decays are the same for $J = 0, 1, 2$ as shown in Eqs. 7.16-7.18. Thus, together with the spin relations, the octet contributions follow a simple ratio $\chi_{c0} : \chi_{c1} : \chi_{c2} = 1 : 3 : 5$ (see Eqs. 7.21-7.23). For the χ_{c0} and χ_{c2} states, as the singlet contributions also have similar coefficients, they follow approximately the same ratio, $\chi_{c0} : \chi_{c2} \sim 1 : 5$. Therefore, the total branching fractions would also follow such a ratio, while the LHCb results in Eq. 7.6 suggest rather opposite, $\mathcal{B}(b \to \chi_{c0} X) > \mathcal{B}(b \to \chi_{c2} X)$. This is a new discrepancy between experimental results and NLO calculations.

Interestingly, for the exclusive decays $B \to \chi_{cJ} K^{(*)}$, we find a similar enhancement (suppression) of χ_{c0} (χ_{c2}) (c.f. Table 1). Possible solution has been pointed out in Ref. [263]. We may resort to exclusive channels for finding the solution to the inclusive puzzle. However, from a comparison to the inclusive branching ratios, many more channels than $B \to \chi_{cJ} K^{(*)}$ are needed to fill the inclusive branching ratio, which may dilute the ratio seen in these observed channels. In any case, the explanation of the difference between the branching fractions of the $B \to \chi_{c0} K^{(*)}$ and $B \to \chi_{c2} K^{(*)}$ channels is rather complicated and it might occur that the solution to the inclusive channel puzzle comes from several contributions.

7.3 Comparison of η_c and J/ψ production to theory

7.3.1 Production in b-hadron decays

The values of LDMEs for the J/ψ and $\eta_c(1S)$ production extracted from the fits of prompt J/ψ and $\psi(2S)$ production and polarization measurements [80, 95, 102, 104, 105, 113, 264] to theoretical predictions [114, 117, 120, 265] are summarised in Table 7.3. The values of the relative $\eta_c(1S)$ production in b-hadron inclusive decays derived from these predictions (Eqs. 7.19 and 7.20) and the values from Table 7.3 are shown in Table 7.4. Theoretical

Table 7.3: Values of LDMEs calculated in Refs. [114, 117, 120, 265] from the J/ψ prompt production measurements used to predict $\eta_c(1S)$ production in b-hadron inclusive decays.

	M. Butenschoen, B. A. Kniehl [265]	K.-T. Chao et al. [128]	B. Gong et al. [117]	G. T. Bodwin et al. [120]
$\langle O_1^{J/\psi}(^3S_1)\rangle$	1.32	1.16	1.16	-
$\langle O_8^{J/\psi}(^3S_1)\rangle$	0.0017 ± 0.0005	0.0030 ± 0.0012	-0.0046 ± 0.0013	0.011 ± 0.010
$\langle O_8^{J/\psi}(^1S_0)\rangle$	0.0304 ± 0.0035	0.0890 ± 0.0098	0.097 ± 0.009	0.099 ± 0.022
$\langle O_8^{J/\psi}(^3P_0)\rangle/m_c^2$	-0.0040 ± 0.0007	0.0056 ± 0.0021	-0.0095 ± 0.0025	0.0049 ± 0.0044

Table 7.4: Predictions of $\mathcal{B}(B \to \eta_c(1S)X)$ using LDMEs from Refs. [114, 117, 120, 265] and the LHCb measurement [249].

	LHCb [249]	M. Butenschoen, B. A. Kniehl [265]	K.-T. Chao et al. [128]	B. Gong et al. [117]	G. T. Bodwin et al. [120]
$\mathcal{B}(B \to \eta_c(1S)X)$	0.69 ± 0.14	1.04 ± 1.34	0.47 ± 0.07	0.90 ± 0.67	0.48 ± 0.07

predictions for $\mathcal{B}(b \to \eta_c(1S)X)$ are in general agreement with the measurement. The values of LDMEs from Refs. [128] and [120] provide more precise prediction for the $\eta_c(1S)$ production in b-hadron decays because $\langle O_8^{J/\psi}(^3P_0)\rangle$ is positive.

Using expressions (7.19) and (7.20) for $\mathcal{B}(B \to J/\psi\, X)$ and $\mathcal{B}(B \to \eta_c(1S)X)$ and the measurement (7.8), a fit is performed to determine the allowed regions for LDMEs.

The reliable value $\langle O_1^{J/\psi}(^3S_1)\rangle = 1.16\,\text{GeV}^3$, originally coming from Buschmuller-Tye potential model [21], is fixed in the fits. The values for other LDMEs are fixed one after another to perform a fit on the plane of two remaining LDMEs as shown in Table 7.5.

The LDMEs from the following calculations are displayed on all following plots for comparison:

- NRQCD fit to J/ψ production with a constraint from η_c production [128],
- Simulnateous fit to hadroproduction and photoproduction [116],
- Simultaneous k_{T}-factorization fit to J/ψ and η_c prompt production [129].

Using expressions (7.19) and (7.20) for $\mathcal{B}(B \to J/\psi X)$ and $\mathcal{B}(B \to \eta_c(1S)X)$, the measurements (7.8) and $\mathcal{B}(B \to J/\psi^{\,direct} X)$ [77] are fitted simultaneously to theory in terms of LDME parameters.

Figure 7.1 shows the $\Delta\chi^2$ of the fit on the $(\langle O_8^{J/\psi}(^3S_1)\rangle); \langle O_8^{J/\psi}(^1S_0)\rangle)$, $(\langle O_8^{J/\psi}(^3S_1)\rangle); \langle O_8^{J/\psi}(^3P_0)\rangle/m_c^2$ and $\langle O_8^{J/\psi}(^3P_0)\rangle/m_c^2; \langle O_8^{J/\psi}(^1S_0)\rangle)$ planes. The values of LDMEs from [128] are overlaid. Total experimental uncertainties are taken into account in the fit as well as theoretical uncertainties on the short-distance coefficient for the CS part. The correlations between the measurements are small and are therefore neglected.

Values of LDMEs, determined by the fit, for various fit options are listed in Table 7.5. The $\langle O_1^{J/\psi}(^3S_1)\rangle$ matrix element is fixed to the value from Ref. [128], the values of $\langle O_8^{J/\psi}(^3S_1)\rangle$, $\langle O_8^{J/\psi}(^1S_0)\rangle$ or $\langle O_8^{J/\psi}(^3P_0)\rangle/m_c^2$ are fixed (A,C,E) or Gaussian constrained (B,D,F) to the values from Ref. [128]. The results show that the fit chooses different optimal

Table 7.5: Results of simultaneous fits of the LDMEs to the $\mathcal{B}(b \to \eta_c(1S)^{direct}X)/\mathcal{B}(b \to J/\psi^{\,direct}X)$ from Eq. (7.8) and $\mathcal{B}(B \to J/\psi^{\,direct}X)$ [77].

	A	B	C	D	E	F
$\langle O_1^{J/\psi}(^3S_1)\rangle$, GeV^3	1.16 (fixed)	1.16 (fixed)	1.16 (fixed)	1.16 (fixed)	1.16 (fixed)	1.16 (fixed)
$\langle O_8^{J/\psi}(^3S_1)\rangle$, GeV^3	0.0030 (fixed)	0.0030 (constrained)	-0.115 ± 0.008	-0.115 ± 0.019	1.65 ± 0.38	1.65 ± 0.66
$\langle O_8^{J/\psi}(^1S_0)\rangle$, GeV^3	0.020 ± 0.005	0.020 ± 0.005	0.089 (fixed)	0.089 (constrained)	-0.94 ± 0.22	-0.94 ± 0.38
$\langle O_8^{J/\psi}(^3P_0)\rangle/m_c^2$, GeV^3	-0.0006 ± 0.0015	-0.0006 ± 0.0015	-0.0011 ± 0.0014	-0.0011 ± 0.0014	0.0056 (fixed)	0.0056 (constrained)

values for $\langle O_8^{J/\psi}(^3S_1)\rangle$ and $\langle O_8^{J/\psi}(^1S_0)\rangle$ depending on the fit assumptions, which are also different from the values in Ref. [128]. The fit also chooses a value for $\langle O_8^{J/\psi}(^3P_0)\rangle/m_c^2$ that is similar for all fit assumptions, which is however different different from the value from Ref. [128].

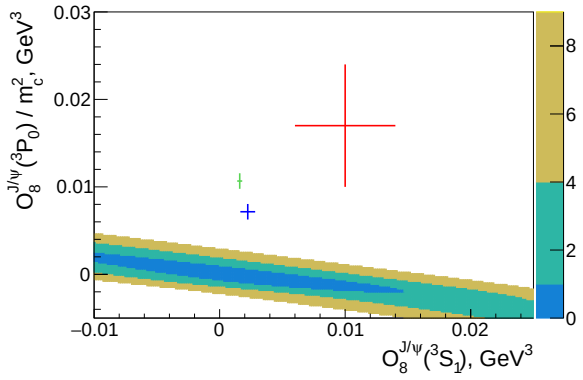

(a)

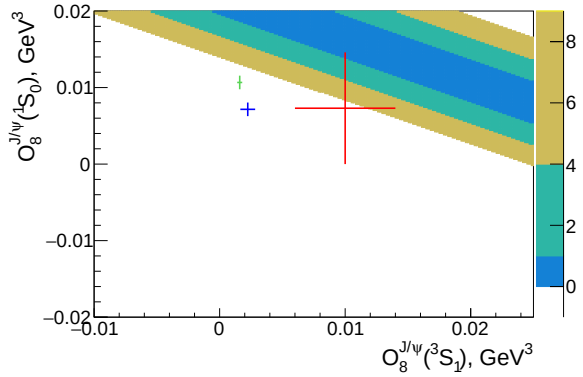

(b)

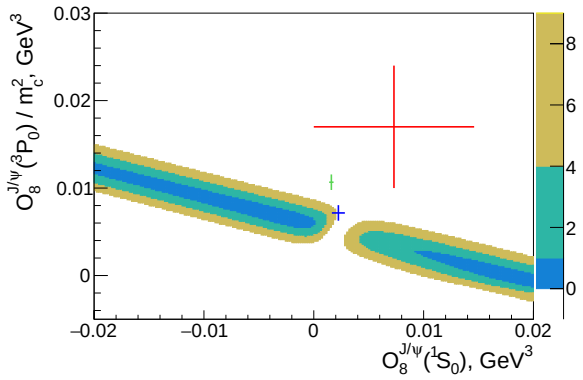

(c)

Figure 7.1: The $\Delta\chi^2\rangle$ fit distribution using the measurements of $\frac{\mathcal{B}(b\to\eta_c(1S)^{direct}X)}{\mathcal{B}(b\to J/\psi^{direct}X)}$ from Eq. (7.8) and $\mathcal{B}(B\to J/\psi^{direct}X)$ [77]. For all listed plots $\langle O_1^{J/\psi}(^3S_1)\rangle = 1.16\,\text{GeV}^3$ is used. Only area with $\Delta\chi^2 < 9$ is shown with colour code. Red points correspond to the values from Ref. [128], green points - from Ref. [129], blue points - from Ref. [116].

7.3.2 Hadroproduction

A theoretical description of the η_c hadroproduction using the LHCb measurement as one of the inputs is given in Ref. [128]. The authors perform a fit to the J/ψ prompt production measurement performed at CDF. The fit reasonably describes the measured cross-sections. The following linear combinations are defined:

$$\begin{aligned} M_0 &= \langle O_8^{J/\psi}(^1S_0)\rangle + r_0 \cdot \langle O_8^{J/\psi}(^3P_0)/m_c^2\rangle, \\ M_1 &= \langle O_8^{J/\psi}(^3S_1)\rangle + r_1 \cdot \langle O_8^{J/\psi}(^3P_0)/m_c^2\rangle, \end{aligned} \tag{7.24}$$

where $r_0 = -3.9$ and $r_1 = -0.56$. The CO combinations M_0 and M_1 are defined in order to separate different p_{T} behaviour. Namely, the CO contribution related to M_0 behaves as $\sim {p_{\mathrm{T}}}^{-6}$ and the contribution related to M_1 behaves as $\sim {p_{\mathrm{T}}}^{-4}$, so that these contributions can be distinguished from the fit to p_{T}-differential cross-section. The obtained from the fit values of M_0 and M_1 are:

$$\begin{aligned} M_0 &= (7.4 \pm 1.9) \times 10^{-2}\,\mathrm{GeV}^3, \\ M_1 &= (0.05 \pm 0.02) \times 10^{-2}\,\mathrm{GeV}^3. \end{aligned} \tag{7.25}$$

Note that the value of M_1 is very small and is consistent with zero. In addition, uses the LHCb measurement of η_c prompt production to further constrain CO LDMEs. By neglecting the dominant CS contribution a fit to η_c production has been performed by letting CO contributions to saturate the measured cross-section. This way the following upper limit on $O_8^{J/\psi}(^1S_0)$ CO LDME was obtained.

$$\langle O_8^{J/\psi}(^1S_0)\rangle < 1.46 \times 10^{-2}\,\mathrm{GeV}^3 \tag{7.26}$$

By having the constraint from Eqs. 7.25 and 7.26 and the fit to η_c production cross-section, one can describe the η_c and J/ψ hadroproduction simultaneously.

Figure 7.2 shows the fit $\Delta\chi^2$ on the $(\langle O_8^{J/\psi}(^3S_1)\rangle; \langle O_8^{J/\psi}(^1S_0)\rangle)$, $(\langle O_8^{J/\psi}(^3S_1)\rangle; \langle O_8^{J/\psi}(^3P_0)\rangle/m_c^2$ and $\langle O_8^{J/\psi}(^3P_0)\rangle/m_c^2; \langle O_8^{J/\psi}(^1S_0)\rangle)$ planes. The values of LDMEs from Ref. [128] are overlaid. Total experimental uncertainties are taken into account in the fit as well as theoretical uncertainties on the short-distance coefficient for the CS part. The dominant source of theory uncertainty is coming from the renormalisation and factorisation scales and amounts to about 35%. The experimental uncertainty is dominated by statistical one and amounts to about 30 to 70%. The fit central values points are in agreement with the results from Ref. [128] but with significantly reduced uncertainties. The agreement is explained by the fact that

the measurement of the J/ψ production is much more precise and dominates the fit. The measurement of the η_c production is not well described by the fit which causes a significant reduction in the LDMEs allowed regions.

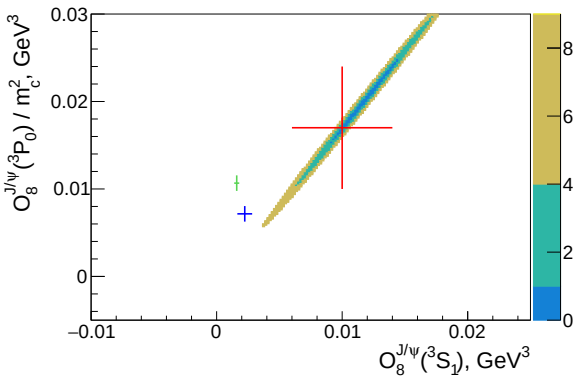

(a)

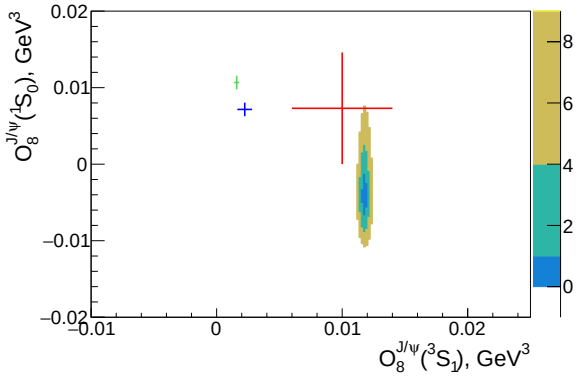

(b)

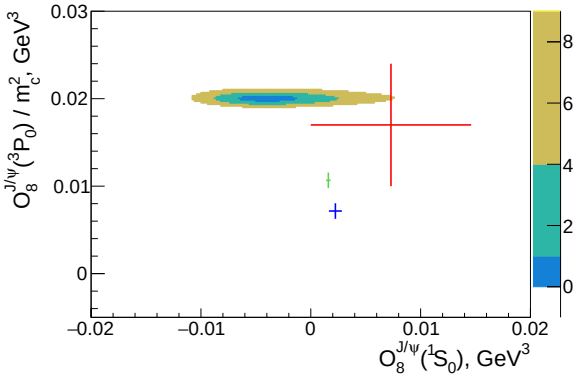

(c)

Figure 7.2: The $\Delta\chi^2$ fit distribution using the η_c hadroproduction measurements and constraints from Eq.(7.25). For all listed plots $\langle O_1^{J/\psi}(^3S_1)\rangle = 1.16\,\mathrm{GeV}^3$ is used. Only area with $\Delta\chi^2 < 9$ is shown with colour code. Red points correspond to the values from Ref. [128], green points - from Ref. [129], blue points - from Ref. [116].

7.3.3 Simultaneous study of hadroproduction and production in b-hadron decays

Similarly, one can perform a fit to η_c and J/ψ hadroproduction and production in b-hadron decays simultaneously by using the same technique as in previous sections.

Figure 7.3 shows the fit $\Delta\chi^2$ on the $(\langle O_8^{J/\psi}(^3S_1)\rangle); \langle O_8^{J/\psi}(^1S_0)\rangle)$, $(\langle O_8^{J/\psi}(^3S_1)\rangle); \langle O_8^{J/\psi}(^3P_0)\rangle/m_c^2$ and $\langle O_8^{J/\psi}(^3P_0)\rangle/m_c^2; \langle O_8^{J/\psi}(^1S_0)\rangle)$ planes. The values of LDMEs from [128] are overlaid. Total experimental uncertainties are taken into account in the fit as well as theoretical uncertainties on the short-distance coefficient for the CS part.

The goodness of fit is reasonable, $\chi^2/\text{ndf} = 9.7/8$. The result shows that the parameter space, which can describe all measurements is reduced. This is most remarkable for $\langle O_8^{J/\psi}(^3S_1)\rangle;\langle O_8^{J/\psi}(^1S_0)\rangle$ plane. The optimal points differ from the ones obtained from the fit to prompt production only. This indicates a possible difference in LDMEs for the two production processes, contrary to basic NRQCD assumptions.

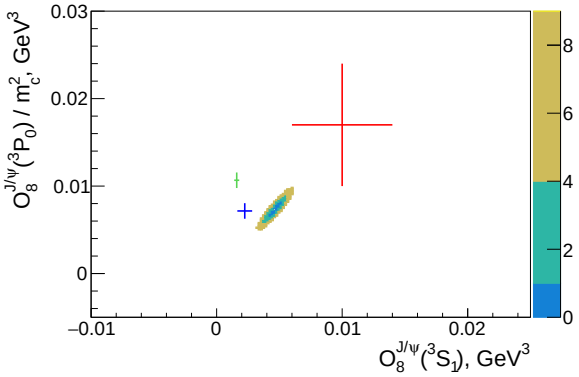

(a)

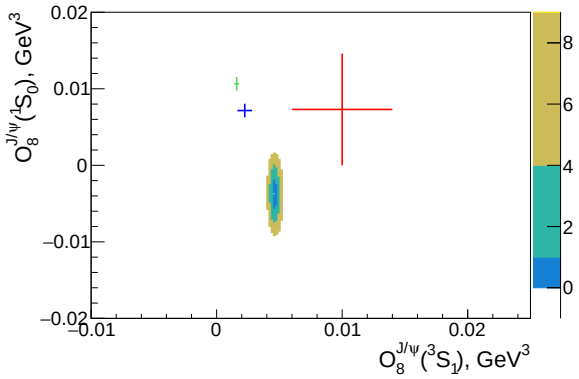

(b)

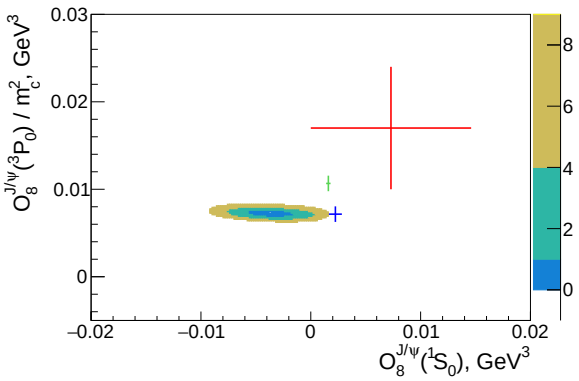

(c)

Figure 7.3: The $\Delta\chi^2$ fit distribution using the η_c hadroproduction measurements, constraints from Eqs.(7.25, 7.26) and measurements on η_c and J/ψ production in b-hadron inclusive decays. For all listed plots $\langle O_1^{J/\psi}(^3S_1)\rangle = 1.16\,\text{GeV}^3$ is used. Only area with $\Delta\chi^2 < 9$ is shown with colour code. Red points correspond to the values from Ref. [128], green points - from Ref. [129], blue points - from Ref. [116].

7.4 Comparison of the χ_c production in b-hadron decays to theory

Using expressions (7.21), (7.22) and (7.23) for $\mathcal{B}(B \to \chi_{cJ}X)$, the measurements of $\mathcal{B}(b \to \chi_c X)$ were fitted in terms of colour singlet and colour octet matrix elements. Figure 7.4 shows the $\langle\chi^2\rangle$ of the fit as a function of the CS (O_1) and the CO (O_8) matrix elements. The fit was performed separately for the $\mathcal{B}(b \to \chi_{c0}{}^{direct}X)$, $\mathcal{B}(b \to \chi_{c1}{}^{direct}X)$ and $\mathcal{B}(b \to \chi_{c2}{}^{direct}X)$ measurements and using all three measurements simultaneously. The total experimental uncertainties are taken into account in the fit, while the correlations between the measurements are not taken into account. The fit allows to strongly restrict the allowed range for LDMEs. The most probable values of LDMEs are determined from simultaneous fit to be

$$O_1^{opt} = 0.0755\,\mathrm{GeV}^3,$$
$$O_8^{opt} = 0.00575\,\mathrm{GeV}^3.$$

As another representation of the results obtained with simultaneous fit of all $\mathcal{B}(b \to \chi_{cJ}{}^{direct}X)$ measurements, Figure 7.5 shows one, two and three standard deviations contours in the (O_1;O_8) plane taking into account non-physical regions, where at least one of the $\mathcal{B}(b \to \chi_{cJ}X)$ becomes negative. In order to extract the contours, the $\langle\chi^2\rangle$ fit distribution from Fig. 7.4(d) is used to generate toy frequency distribution $PDF(O_1, O_8)$ in the (O_1;O_8) plane.

The $\langle\chi^2\rangle$ fit for the O_1 and O_8 matrix elements using the measurements of $\mathcal{B}(b \to \chi_{c1}{}^{direct}X)/\mathcal{B}(b \to \chi_{c0}{}^{direct}X)$ and $\mathcal{B}(b \to \chi_{c2}{}^{direct}X)/\mathcal{B}(b \to \chi_{c0}{}^{direct}X)$ is shown on Fig. 7.6. The fit is performed separately for $\frac{\mathcal{B}(b\to\chi_{c1}{}^{direct}X)}{\mathcal{B}(b\to\chi_{c0}{}^{direct}X)}$ and $\frac{\mathcal{B}(b\to\chi_{c2}{}^{direct}X)}{\mathcal{B}(b\to\chi_{c0}{}^{direct}X)}$ and using both measurements simultaneously. Total experimental uncertainties are taken into account in the fit, while the correlations between the measurements are not taken into account. Note, that in this case correlations are negligible and can be ignored.

While the fit using absolute branching fractions $\mathcal{B}(b \to \chi_{cJ}{}^{direct}X)$ can accommodate a limited range of O_1 and O_8 due to large experimental uncertainties, the fit to the ratio of branching fractions $\mathcal{B}(b \to \chi_{c1}{}^{direct}X)/\mathcal{B}(b \to \chi_{c0}{}^{direct}X)$ significantly reduces the allowed O_1 and O_8 range. The χ_{c2} ratio of branching fractions $\mathcal{B}(b \to \chi_{c2}{}^{direct}X)/\mathcal{B}(b \to \chi_{c0}{}^{direct}X)$ is then not consistent with the assumed theoretical framework.

Note that the fits to theory (Fig. 7.6) prefer negative values of O_1. This confirms the problem of unphysical negative short-distance coefficient relative to the CS LDME discussed by the authors of Ref. [82].

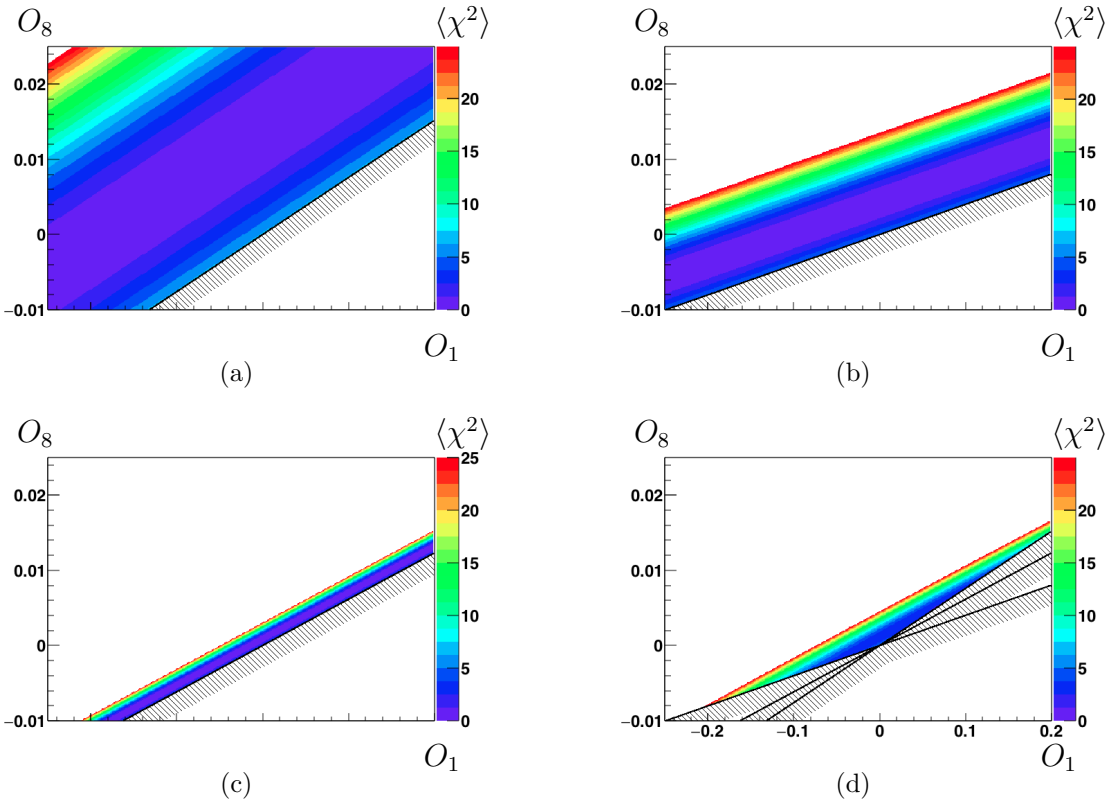

Figure 7.4: The $\langle\chi^2\rangle$ fit distribution for the O_1 and O_8 matrix elements using the measurement of the

- (a) $\mathcal{B}(b \to \chi_{c0}{}^{direct} X)$ from Eq. 7.9,
- (b) $\mathcal{B}(b \to \chi_{c1}{}^{direct} X)$ from Eq. 7.10,
- (c) $\mathcal{B}(b \to \chi_{c2}{}^{direct} X)$ from Eq. 7.11,
- (d) simultaneously all branching fractions $\mathcal{B}(b \to \chi_{cJ}^{direct} X)$.

Black lines indicate boundaries, where branching fractions become negative. Only area with $\langle\chi^2\rangle < 25$ is shown with colour code.

The values of CS matrix elements are extracted from Eqs. (7.16), (7.17), (7.18) and $O_8 = (11.22 \pm 0.68)^{-3}\,\text{GeV}^3$ [261] allow to extract the values of the CS matrix elements from the $\mathcal{B}(b \to \chi_{cJ}^{direct} X)$ measurements without using spin symmetry relations to be:

$$\langle O_1^{\chi_{c0}}({}^3S_1)\rangle = -0.04 \pm 0.07\,\text{GeV}^3,$$
$$\langle O_1^{\chi_{c1}}({}^3S_1)\rangle = 0.51 \pm 0.14\,\text{GeV}^3,$$
$$\langle O_1^{\chi_{c2}}({}^3S_1)\rangle = 0.83 \pm 0.04\,\text{GeV}^3.$$

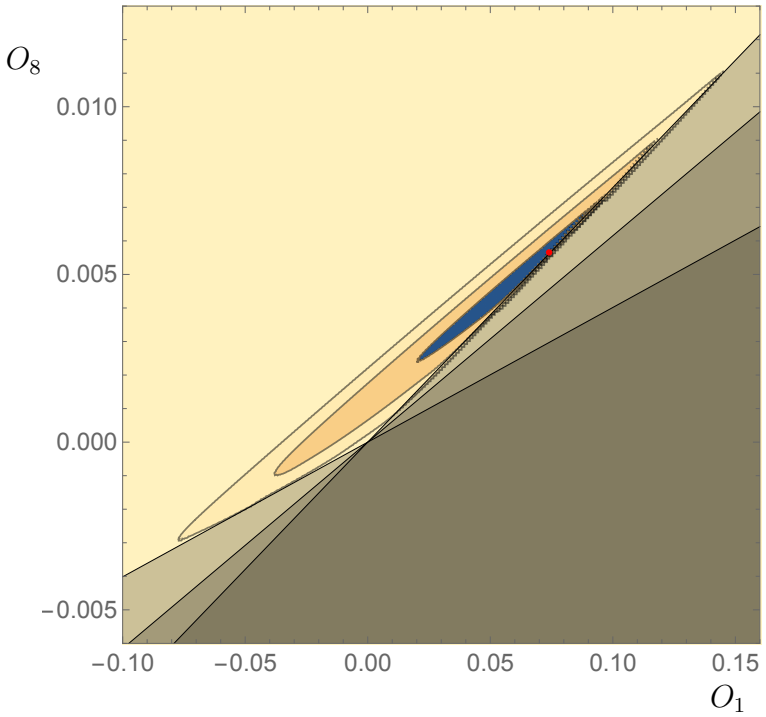

Figure 7.5: The contour plot for O_1 and O_8 describing one, two and three sigma statistical contours taking into account unphysical area where at least one of the $\mathcal{B}(b \to \chi_{cJ}^{direct} X)$ becomes negative. The unphysical area is filled in grey. The most probable values (O_1^{opt}, O_8^{opt}) are shown in red.

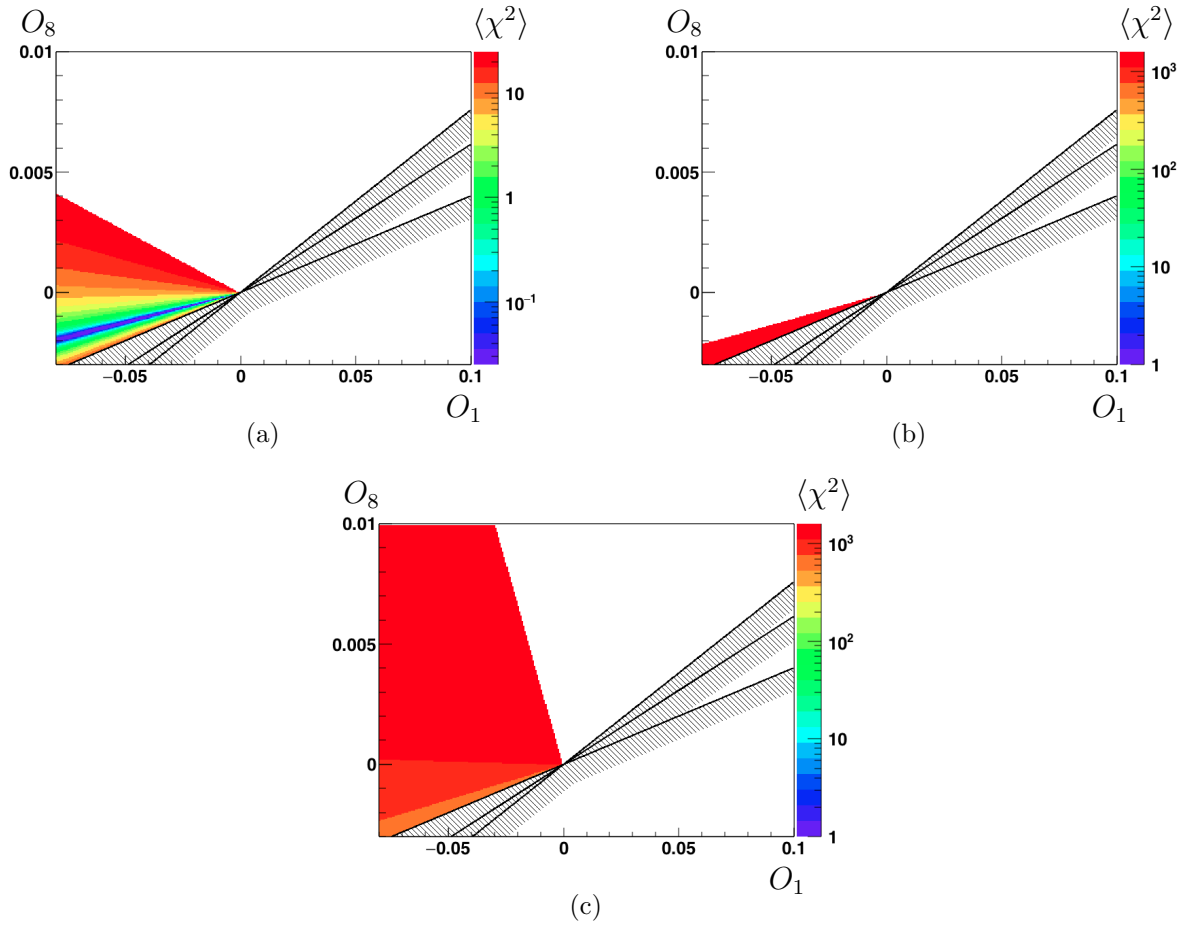

Figure 7.6: The $\langle\chi^2\rangle$ fit distribution using the measurement of the relative branching fractions

- (a) $\mathcal{B}(b \to \chi_{c1}{}^{direct}X)/\mathcal{B}(b \to \chi_{c0}{}^{direct}X)$ from Eq. 7.12,
- (b) $\mathcal{B}(b \to \chi_{c2}{}^{direct}X)/\mathcal{B}(b \to \chi_{c0}{}^{direct}X)$ from Eq. 7.13,
- (c) both $\mathcal{B}(b \to \chi_{c1}{}^{direct}X)/\mathcal{B}(b \to \chi_{c0}{}^{direct}X)$ and $\mathcal{B}(b \to \chi_{c2}{}^{direct}X)/\mathcal{B}(b \to \chi_{c0}{}^{direct}X)$

for the O_1 and O_8 matrix elements. Black lines indicate boundaries, where branching fractions become negative Only area with (a) $\langle\chi^2\rangle < 25$ and (b),(c) $\langle\chi^2\rangle < 1600$ is shown with colour code.

7.5 Summary and discussion

This chapter proposes a technique of constraining theory using simultaneously results on charmonium hadroproduction and charmonium production in b-hadron inclusive decays, under the assumption of factorization, universality of LDMEs and heavy-quark spin symmetry, where different charmonium states are involved. Alternatively, when the hadroproduction and production in b-hadron inclusive decays will be measured for the charmonium states with linked LDMEs, the above assumptions can be tested in a qualitative way.

The relative $\eta_c(1S)$ to J/ψ production measurement is found to be in agreement with the theory prediction when using LDMEs values from the fits [114, 117, 120, 265] of prompt $\eta_c(1S)$ production measurement. However, matrix elements extracted from the simultaneous fit of the J/ψ and $\eta_c(1S)$ production in inclusive b-decays slightly differ from the matrix elements, extracted using measurements of the prompt J/ψ production. At the same time, a simultaneous fit is able to describe both S-wave charmonium prompt production and production in b-hadron inclusive decays.

The $\mathcal{B}(b \to \chi_{cJ}{}^{direct} X)$ measurements are fitted according to theoretical formalism with two free parameters representing CS and CO LDMEs linked between the decays to the χ_{c0}, χ_{c1} and χ_{c2} charmonia. It is shown that the measurement of the ratio of the branching fractions $\mathcal{B}(b \to \chi_{c1}{}^{direct} X)/\mathcal{B}(b \to \chi_{c0}{}^{direct} X)$ can be accommodated by theory model and can constrain LDMEs, while the measurement of the ratio of the branching fractions $\mathcal{B}(b \to \chi_{c2}{}^{direct} X)/\mathcal{B}(b \to \chi_{c0}{}^{direct} X)$ is not consistent with the theory prediction. Hence, calculations of the χ_{cJ} production in inclusive b-hadron decays need to be revisited.

The predictions describe b-decays to the S-wave charmonia within reduced parameter space, while the description of b-decays to P-wave charmonia is not entirely consistent with the LHCb measurement. Particularly, the χ_{c2} production in inclusive b-decays is not described by theory; the χ_{c0} production cannot be accomodated by theory using prediction for CS matrix element. The problems in describing the χ_{cJ} production in inclusive b decays were expected by authors of Ref. [82] in the CS part. It was noted that negative short-distance coefficient before the CS LDME is not physical. This would justify why the fit prefers negative values for the CS LDME.

Examining the exclusive branching fractions $\mathcal{B}(B \to \chi_{cJ} K)$, authors of Ref. [263] pointed out a potentially important contribution of spectator scattering to the CO production. Measurement of the h_c production is important to test P-wave charmonia production in b-hadron decays, since it is expected to be problematic similarly to χ_{c2}.

Chapter 8

Measurement of charmonium resonance parameters

This chapter summarises the measurements of charmonium resonance parameters performed using LHCb data samples of charmonia produced in b-hadron inclusive decays. The $p\overline{p}$ and $\phi\phi$ decays of charmonium are used similarly to production measurements described in Sections 5 and 5.6. The obtained measurements of the η_c mass and potentially natural width can compete with the world average values. It proves that much larger production rate of the η_c meson at LHCb already provides better accessibility to the η_c properties compared to that at charm and B-factories. However, this is not yet the case for other charmonium states.

After introducing the charmonium spectroscopy in Section 8.1, the measurement of the η_c mass using the decay $\eta_c \to p\overline{p}$ is described in Section 8.2. The measurement of the η_c mass and natural width using the decay $\eta_c \to \phi\phi$ is described in Section 8.3.

8.1 Charmonium resonance parameters

The charmonium states below the $D\overline{D}$ threshold are well identified as bound states of $c\bar{c}$. Their masses and natural widths are summarized in Table 8.4. The reported average values take into account also the results from Chapter 5.6. The most precise mass and width

	Mass, MeV	Natural width, MeV
$\eta_c(1S)$	2983.9 ± 0.5	32.0 ± 0.8
J/ψ	3096.900 ± 0.006	0.0929 ± 0.0028
χ_{c0}	3414.71 ± 0.30	10.8 ± 0.6
χ_{c1}	3510.67 ± 0.05	0.84 ± 0.04
h_c	3525.38 ± 0.11	0.7 ± 0.4
χ_{c2}	3556.17 ± 0.07	1.97 ± 0.09
$\eta_c(2S)$	3637.6 ± 1.2	$11.3^{+3.2}_{-2.9}$
$\psi(2S)$	3686.097 ± 0.025	0.294 ± 0.008

Table 8.1: Charmonia masses (in MeV) and natural widths (in MeV) [73].

measurements of J/ψ and $\psi(2S)$ have been performed by KEDR collaboration [266]. The world average values for the J/ψ and $\psi(2S)$ natural width are dominated by measurements of CLEO [267], E835 [268] and BES [269].

The world average values of the η_c mass and width are dominated by LHCb [190] and BES III [270] measurements. The LHCb measurement takes into account a possible interference between the $B^+ \to (\eta_c \to p\overline{p})K^+$ and the non-resonant $B^+ \to p\overline{p}K^+$ decays. The BES III measurement required a complex description of the η_c lineshape since the η_c sample from radiative decays $\psi(2S) \to \eta_c\gamma$ was used. The tension of 2σ between the two measurements of the η_c mass calls for other measurements of the η_c resonance parameters.

The world average values of the χ_c resonance parameters are dominated by the BES III [271], E835 [272, 273], E760 [274] measurements and the measurement of LHCb [196] using recently discovered $\chi_{c1,2} \to J/\psi\,\mu^+\mu^-$ decays. Similarly, the h_c mass and width world average values are dominated by the results from BES III [275] and CLEO [276].

The charmonium state below the $D\overline{D}$ threshold with the least studied resonance parameters is the $\eta_c(2S)$. The $\eta_c(2S)$ mass is known to a precision of 1.2 MeV and is dominated by the LHCb [190] and BaBar [277] measurements, while the most precise measurements of the $\eta_c(2S)$ natural width have been performed by BaBar [277] and BES II [278]. This reflects a limited sample of $\eta_c(2S)$ mesons at BES experiment.

Theoretically, a spectrum of charmonium states is predicted by potential models and lattice calculations. A comparison of the observed spectrum with the theoretical prediction by Godfrey-Isgur model [279, 280] is shown on Fig. 8.1. As demostrated by Fig. 8.1, the

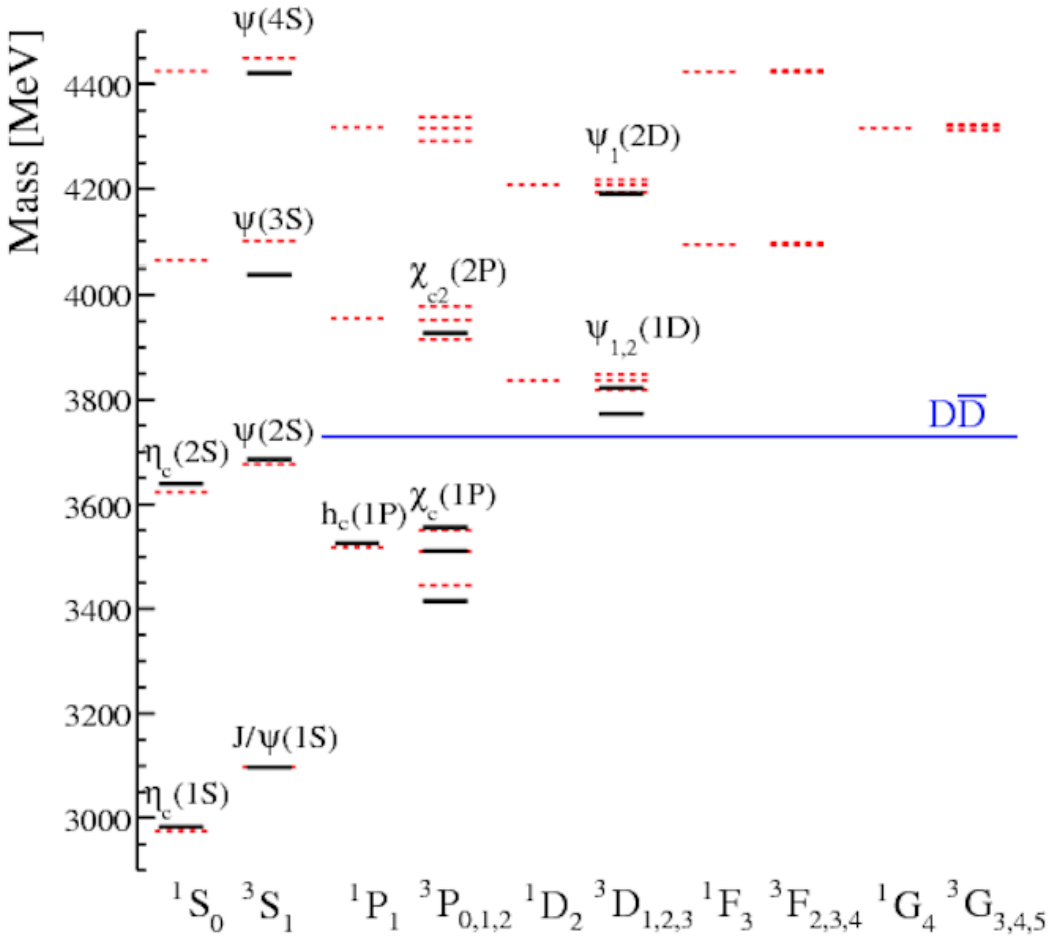

Figure 8.1: The comparison of charmonium spectrum to the Godfrey-Isgur model calculation [280]. Figure is taken from Ref. [281].

potential model provides a good spectrum description.

While a qualitative picture of charmonium spectrum is well described by the potential model, a hyperfine splittings is another subject to be addressed by theory. Rigorous predictions of P-wave charmonium masses maybe studied using information directly from lattice QCD or by using potentials obtained from lattice and then embedded in EFTs.

For example, the splitting between the η_c and J/ψ masses, reflects the effect of relativistic spin-dependent forces. As was already stated before, the hyperfine splitting of S-wave quarkonium can be computed perturbatively and is a subject for precision tests. The first precise lattice calculations of the S-wave quarkonium mass splitting based on NRQCD with spin-dependent terms have been performed in Ref. [282] followed by Ref. [283]. In the latter article, authors expect further large relativistic corrections. As shown in Ref. [284], the predicted J/ψ-η_c mass difference is underestimated compared

to measurements. A similar situation takes place for the mass splitting between the χ_{cJ} states. Recent results performed at the next-to-next-to-next-to-leading logarithmic (N^3LL) accuracy show a better agreement (see e.g. Ref. [285]). The predictions are done using pNRQCD as discussed in Ref. [286]. The η_c mass and width can be also determined precisely using $J/\psi \to \eta_c\gamma$ transition description [287], namely description of the signal lineshape. Note that the theoretical precision is worse than the experimental one. However, it has to be proven that measurements are converging to the same average and no systematic effects can cause a significant change in the world average values.

The spectroscopy of resonant charmonium states above the $D\overline{D}$ threshold is more complicated due to their large natural width. There are still charmonium resonances to be discovered. The last to date discovery of charmonium state has been performed by LHCb [288], where the state $X(3842)$ state has been observed. It is interpreted as the 1^3D_3 charmonium state. This observation was performed using $D\overline{D}$ spectroscopy, while decays to light hadrons do not significantly contribute to the study of charmonia above the $D\overline{D}$ threshold.

Apart from charmonium states above the $D\overline{D}$ threshold, the so-called charmonium-like exotics candidates appear in the spectrum. These states do not fit the charmonium model and hence hypotheses on their tetraquark, molecular, hybrid and adjoint charmonium are most natural to assume. Another feature of the states in this region is that they are expected to be mixed states. For example, the current understanding of the $X(3872)$ state is that it is rather a mixture of charmonium and DD^* molecular state [289]. The key properties of $X(3872)$ is that it is much narrower than any charmonium state expected at this mass and hence cannot be described by pure charmonium model; and that it decays to $\psi(2S)\gamma$ with relatively large branching fraction and hence cannot be accommodated by pure molecular model. In addition to that, the prompt production study of $X(3872)$ showed that it behaves consistently with a prediction for $\chi_{c1}(2P)$ state. All mentioned above led to the mixed interpretation of $X(3872)$ and it has been renamed as the $\chi_{c1}(3872)$ in the latest PDG release [290]. However, the available experimental inputs and theory do not allow to establish the nature of this state. Therefore, the renaming points to ithe quantum numbers of the state without suggesting charmonium interpretation. However, a discovery of any hadronic decay of $X(3872)$ would immediately add information about its possible charmonium component. Other exotics candidates such as $X(3915)$, $X(3832)$ and many others have been identified. The problem of these states is such that they have to be distinguished from the so-called cusp effects appearing close to the opening threshold due to a virtual hadrons loop [291, 292]. The spectrum of charmonium-like states is shown on Fig. 8.2.

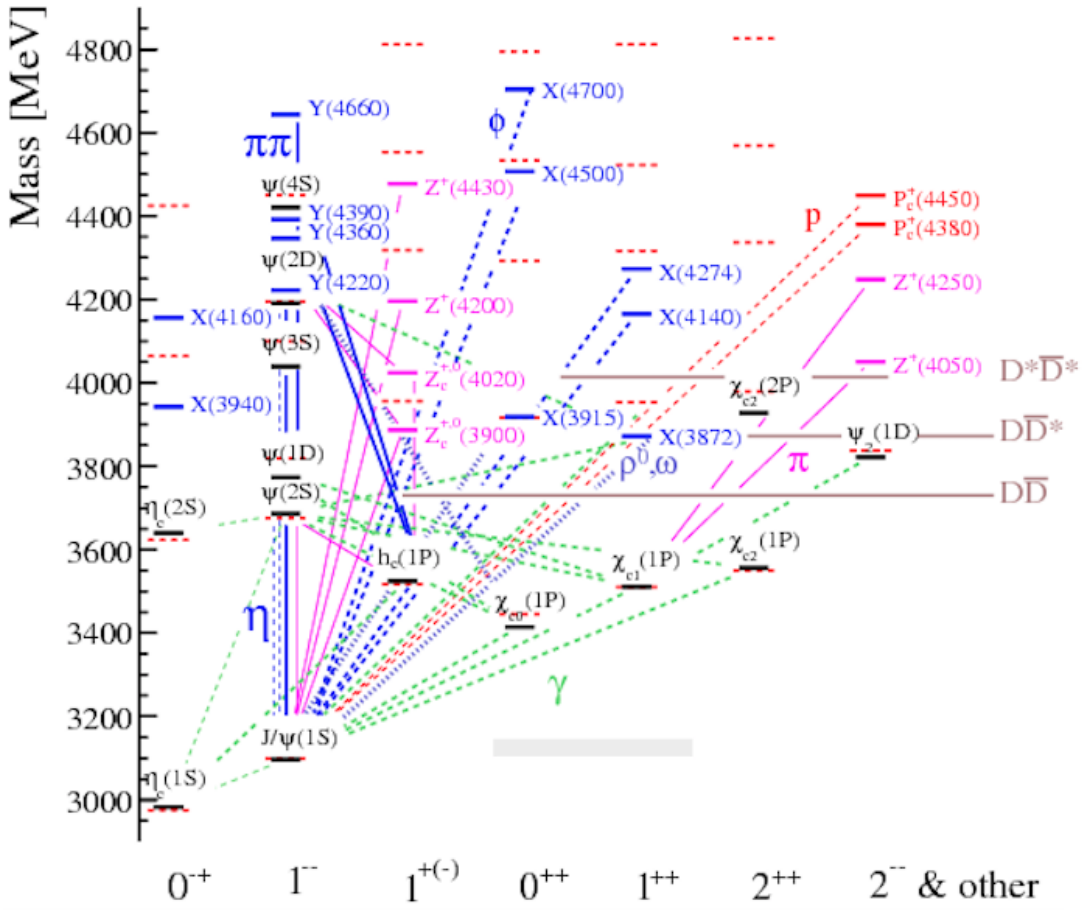

Figure 8.2: The spectrum of charmonium-like states. Figure is taken from Ref. [281].

Systematic studies of exotics states are performed at B-factories and LHCb experiment. This is, however, not the topic of this work.

8.2 Measurement of the J/ψ and η_c mass difference using decays to $p\bar{p}$

The prompt η_c production measurement requires extreme selection applied at the trigger level to compete with the challenging background conditions, at the same time avoiding biases to retain robust efficiency estimates. Charmonia produced in b-decays are reconstructed over controlled background level and are more suitable to measure J/ψ-η_c mass difference. A looser selection adjusted for the mass difference determination is chosen contrary to the production measurement, where same selection for prompt charmonium and charmonium from b-hadron decays is used in order to avoid potential biases in the efficiency estimates.

Below, the η_c mass relative to the well-reconstructed and well-known J/ψ mass, $\Delta M_{J/\psi,\eta_c} = M_{J/\psi} - M_{\eta_c}$ is measured.

8.2.1 Selection and optimisation

In the data sample the basic level `L0 Hadron decision` (L0HadronDecision_TOS) trigger is applied. The trigger lines `TOS` of HLT1, `Hlt1(Two)TrackMVADecision_TOS`, and HLT2, `Hlt2Topo(2,3,4)BodyDecision_TOS` are used for mass measurement for the combined 2015 and 2016 data sample.

The set of selection criteria used in the preselection (`StrippingCcbar2PpbarDetachedLineDecision`) is summarised in Table 8.2. In comparison to preselection used for the η_c production measurement in Chapter 5, less tight requirements on proton and charmonium candidates p_{T} is used as well as less tight requirement of proton identification.

Further optimisation of cut-based selection is performed on four basic variables: minimal p_{T} of charmonium, minimal p_{T} of both proton and antiproton, minimal χ^2 of track impact parameter with respect to the closest primary vertex, minimal χ^2 of flight distance of charmonium. Optimisation finds the best requirements to achieve the largest possible value of Figure-of-Merit (FoM) $N_{sig}/\sqrt{N_{sig}+N_{bkg}}$, where N_{sig} is the number of signal η_c events estimated from MC simulation and scaled to the yield in data, N_{bkg} is the number of background events from data sidebands ($2850\,\mathrm{MeV} < M_{p\bar{p}} < 2920\,\mathrm{MeV}$). The projections of the optimisation map as a function of applied requirements are shown on Fig.8.3.

Optimisation results suggest the optimal requirements to be $p_{\mathrm{T}}(p\bar{p}) > 5.5\,\mathrm{GeV}$ and $\chi^2(FD) > 81$, which are then applied in the offline analysis. Using prompt production

	Variable	Selection criteria
Trigger		L0_Hadron_TOS Hlt1(Two)TrackMVADecision_TOS Hlt2Topo(2,3,4)BodyDecision_TOS
Proton candidates	p_{T}, GeV Track χ^2/NDF Impact parameter χ^2 $\Delta \log \mathcal{L}^{p-\pi}$ $\Delta \log \mathcal{L}^{p-K}$	$> 1.0\,\mathrm{GeV}/c$ < 5.0 > 9 > 15 > 10
Charmonium candidates	p_{T}, GeV Vertex χ^2 Flight distance χ^2 Rapidity y	$-$ < 9 > 25 $2 < y < 4.5$
Multiplicity	SPD multiplicity	< 600

Table 8.2: Preselection criteria for the η_c and J/ψ mass difference measurement.

cross-sections of the η_c and J/ψ from Section 5.6 and efficiencies from MC simulation, the contamination by prompt J/ψ and η_c in the data sample is estimated to be below 10^{-3}. This number is quoted for illustration purposes.

8.2.2 Fit to the invariant mass

The mass difference $\Delta M_{J/\psi\,,\eta_c}$ is measured from extended maximum likelihood fit to the $M_{p\bar{p}}$ distribution. The signal and background components are modelled in the same way as discussed in Section 5.4.1. The p_{T} dependence of the σ_w, f_n and $\sigma_{\eta_c}/\sigma_{J/\psi}$ are extracted from fits to MC simulation samples of the J/ψ from b-decays and η_c from b-decays in the same way as discussed in Section 5.5.2, while σ_n is a free fit parameter.

The master distribution allowing the determination of the η_c mass is shown on Fig. 8.4. In general, fit yields a good description of the experimental points. The fit yields the J/ψ and η_c mass difference to be $\Delta M_{J/\psi\,,\eta_c} = 112.99 \pm 0.67\,\mathrm{MeV}$.

This result is in agreement with the world average value $\Delta M_{J/\psi}$, ${\eta_c}^{PDG} = (113.5 \pm 0.5)\,\mathrm{MeV}$ [188].

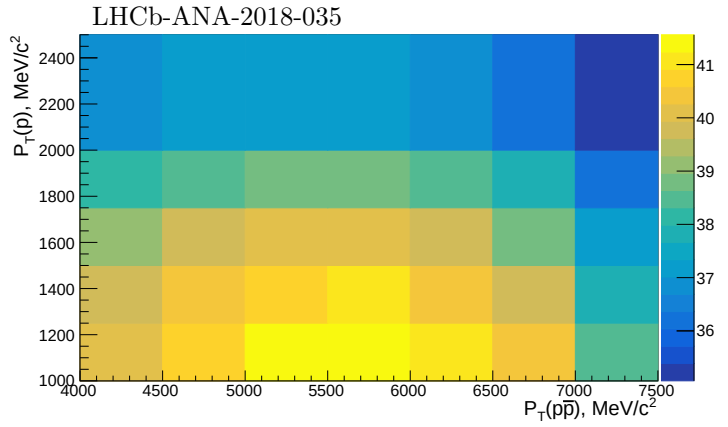

(a)

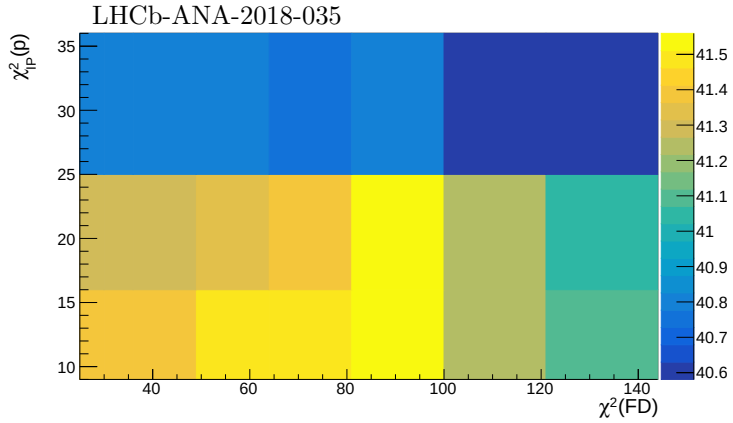

(b)

Figure 8.3: Optimisation map as a function of applied requirements on proton transverse momentum p_{T} (p) and charmonium transverse momentum p_{T} ($p\bar{p}$) (a), χ^2 of flight distance of charmonium candidates $\chi^2(FD)$ and χ^2 of track impact parameter (b) with respect to the best primary vertex $\chi^2_{IP}(p)$. The $FoM = N_{sig}/\sqrt{N_{sig} + N_{bkg}}$ is shown with the color code. The plots are 2D projections of the 4D optimisation.

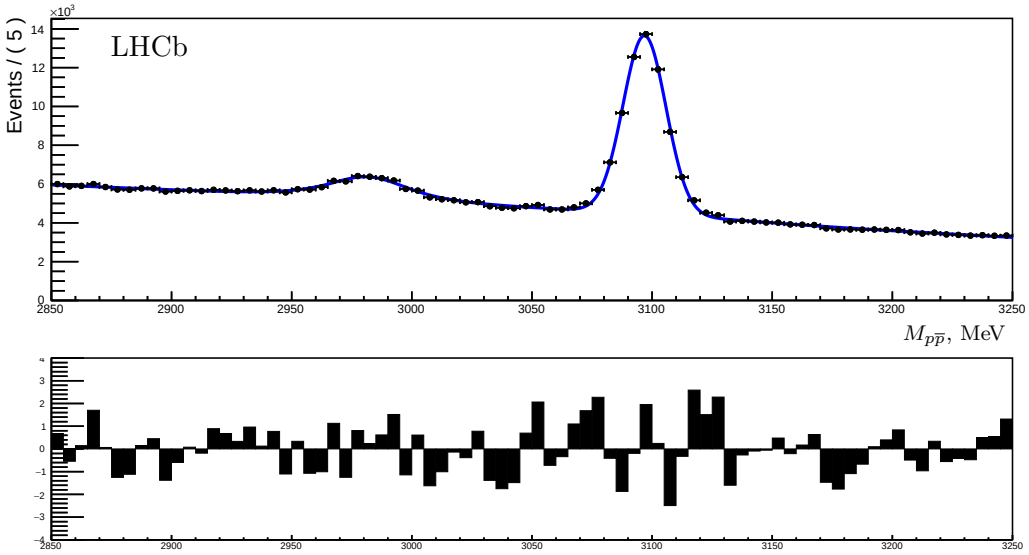

Figure 8.4: The distribution of $M_{p\bar{p}}$. The solid blues line represent the fit result. The corresponding pull distribution is shown below each plot.

8.2.3 Systematic uncertainties

The following list of systematic uncertainties is identical for both η_c production measurement analysis and the $\Delta M_{J/\psi,\eta_c}$ mass difference measurement:

- Signal description in simultaneous fit to the invariant mass distribution:
  - Knowledge of the η_c natural width Γ_{η_c};
  - Invariant mass resolution mismodeling;
  - p_{T}-dependence of the η_c and J/ψ resolution ratio $\sigma_{\eta_c}/\sigma_{J/\psi}$;
- Background description in simultaneous fit to the invariant mass distribution:
  - Combinatorial background description;
  - Description of the feed-down from the $J/\psi \to p\bar{p}\pi^0$ decay.

The estimation of each of these uncertainties is done in the same way as for the η_c production analysis as discussed in Section 5.4.3. The systematic uncertainty related to momentum scale calibration is estimated by comparing fit result with and without momentum scale calibration applied.

The total systematic uncertainty is calculated as a quadratic sum of individual systematic uncertainties. Table 8.3 summarises the systematic uncertainty estimates. The dominant source of systematic uncertainty is related to the resolution model and its p_{T} dependence. The total systematic uncertainty is smaller than the statistical one. Hence enlarging data sample by adding more data will improve the precision of this measurement.

As a cross-check, the fit of the invariant mass is performed simultaneously in 7 bins of charmonium transverse momentum to take into account the dependence of resolution on charmonium p_{T}. The bin edges of charmonium p_{T} are [5.5, 6.5, 8.0, 10.0, 12.0, 14.0, 18.0, 30.0] expressed in GeV. Distributions of invariant mass in each p_{T}-bin is shown on Fig. 8.5. In general, fit yields a good description of all $M_{p\bar{p}}$ distributions in each p_{T}-bin. The fit gives the value of the J/ψ and η_c mass difference to be $\Delta M_{J/\psi,\eta_c} = (113.22 \pm 0.67)\,\mathrm{MeV}$, which is consistent with the nominal result.

Since inclusive b-decays comprise many exclusive decays of different long-lived b-hadrons, no significant interference between non-resonant $b \to p\bar{p}X$ S-wave decays and $b \to \eta_c X$ is expected. In the conservative estimate, the shape of the η_c peak is described together with the background by the following expression:

$$f_{[b\to(\eta_c\to p\bar{p})X]+[b\to p\bar{p}X]+interf.} = |A_{RelBW(\eta_c)} + e^{i\cdot\phi} A_{non.res.}|^2, \tag{8.1}$$

where $A_{RelBW(\eta_c)}$ is the Relativistic Breit-Wigner amplitude for η_c, $A_{non.res.}$ in the non-resonant amplitude of the $b \to p\bar{p}X$ decays, ϕ is the phase difference between the η_c and the non-resonant amplitudes. The non-resonant amplitude is described by the empirical expression:

$$A_{non.res.} = A + B \cdot e^{i \cdot \phi_B} \cdot M_{p\bar{p}} + C \cdot e^{i \cdot \phi_C} \cdot M^2_{p\bar{p}}, \tag{8.2}$$

where A, B, C, ϕ_B and ϕ_C are real free fit parameters.

The result of this fit is is shown on Fig. 8.6. The data are well described by the fit, and the mass difference is $\Delta M_{J/\psi}$, $\eta_c = 113.87 \pm 0.64\,\text{MeV}$, consistent with the baseline fit.

	$M_{J/\psi} - M_{\eta_c}$, MeV
Mean value	112.99
Stat. uncertainty	0.67
Mass resolution model	0.08
Variation of $\sigma_{\eta_c}/\sigma_{J/\psi}$	0.01
Variation of $\Gamma(\eta_c)$	0.04
Comb. bkg. description	0.03
Contribution from $J/\psi \to p\bar{p}\pi^0$	< 0.01
Momentum scale	0.05
Total systematic uncertainty	0.11
Total uncertainty	0.68

Table 8.3: Systematic uncertainties (in MeV) for the measurement of the J/ψ and η_c mass difference.

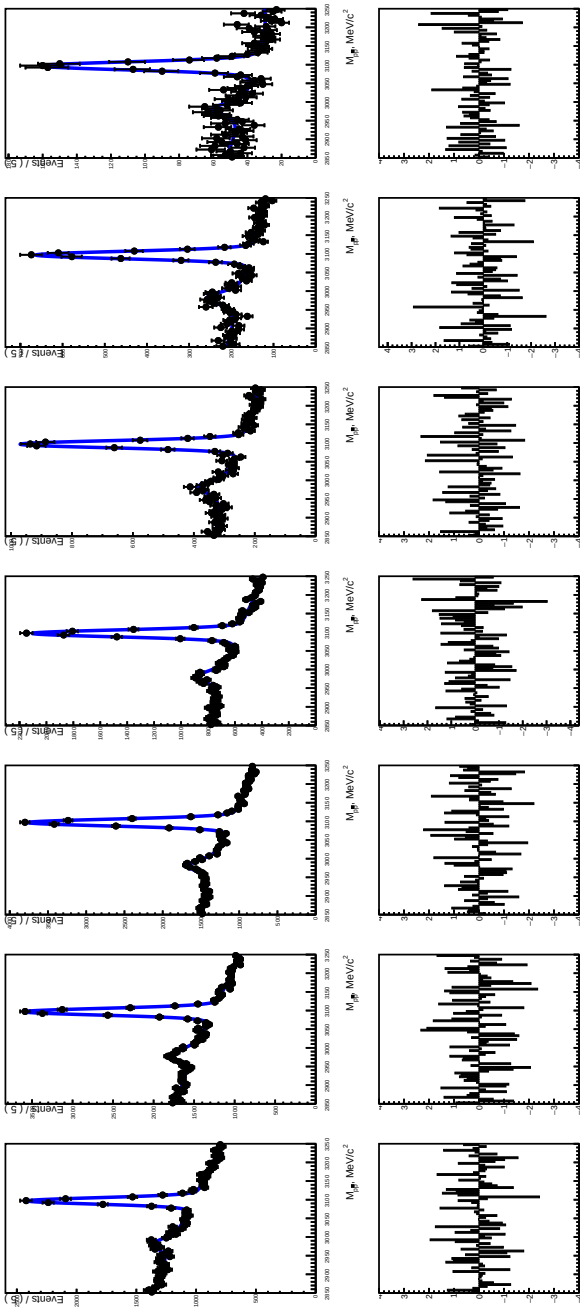

Figure 8.5: Distributions of $M_{p\bar{p}}$ in p_{T} bins. The solid blues line represent the simultaneous fit result. The corresponding pull distribution is shown below each plot.

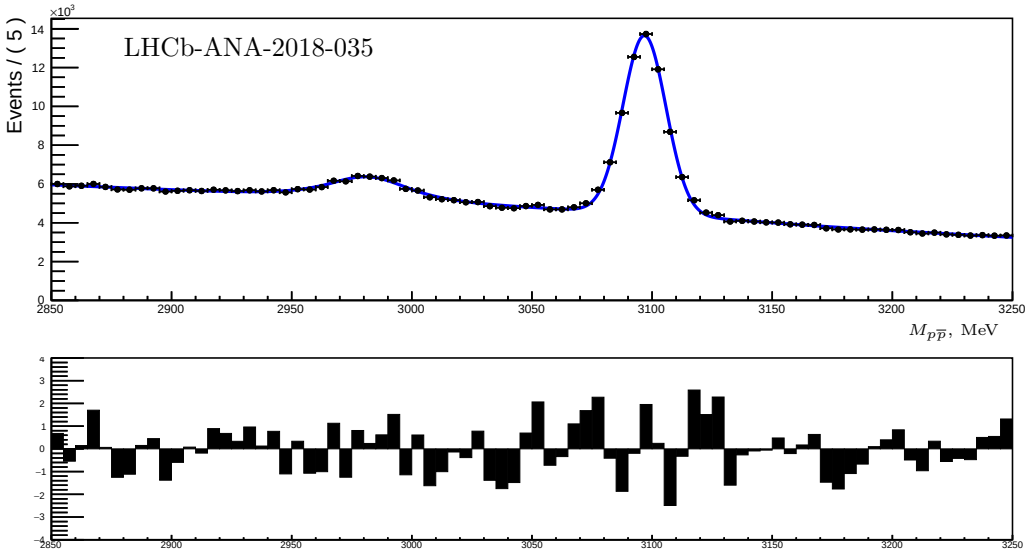

Figure 8.6: The distribution of $M_{p\bar{p}}$. The solid blues lines represent the fit result, which includes the possible interference contribution. The corresponding pull distributions are shown below each plot.

8.3 Charmonium spectroscopy study using decays to $\phi\phi$

Masses of the η_c and χ_c states and natural width of the η_c state are studied below. Mass differences within the η_c and χ_c families are specifically extracted. The measurements in this section are done using the same data sample as in Chapter 5.6. Moreover, the same baseline fit is used.

In a preview to this section the PDG averages and the values obtained in the presented study are summarized in Table 8.4. The last column represents results obtained using charmonium decays to $\phi\phi$.

	PDG	$p\overline{p}$ (Section 8.2)	Measured value
$M_{\eta_c(1S)}$	2983.7 ± 0.7	$2983.91 \pm 0.77 \pm 0.11$	$2982.81 \pm 0.99 \pm 0.45$
$M_{\chi_{c0}}$	3414.75 ± 0.31		$3412.99 \pm 1.91 \pm 0.62$
$M_{\chi_{c1}}$	3510.66 ± 0.07		$3508.38 \pm 1.91 \pm 0.66$
$M_{\chi_{c2}}$	3556.20 ± 0.09		$3557.29 \pm 1.71 \pm 0.66$
$M_{\eta_c(2S)}$	3639.4 ± 1.3		$3636.35 \pm 4.06 \pm 0.69$
$\Gamma_{\eta_c(1S)}$	32.0 ± 0.9		$31.35 \pm 3.51 \pm 2.01$
$\Gamma_{\eta_c(2S)}$	$11.3^{+3.2}_{-2.9}$		–

Table 8.4: Charmonia masses (in MeV) and natural widths (in MeV).

Systematic uncertainties from the fit to the $\phi\phi$ invariant mass spectrum including additional resonances, variation of detector resolution, variation of the fit range, variation of the background parametrization, uncertainties on the χ_c mass values, and momentum scale calibration uncertainty are taken into account. In order to evaluate systematic uncertainty related to a potential contribution from other resonances, contributions from $X(3872)$, $\chi_{c0}(2P)$, and $\chi_{c2}(2P)$ are included in the fit. Systematic uncertainties related to detector resolution are conservatively estimated by using the $\eta_c(1S)$ resolution as obtained from the simulation. Fit range including only the χ_c and $\eta_c(2S)$ region ($3.15\,\mathrm{GeV}/c^2 - 3.95\,\mathrm{GeV}/c^2$) and another one ($2.80\,\mathrm{GeV}/c^2 - 3.70\,\mathrm{GeV}/c^2$) excluding $\eta_c(2S)$ region, are used to estimate the corresponding systematic uncertainties. Alternative background parametrization using a parabola function is used for the systematic uncertainty estimate. Uncertainties related to the momentum scale calibration are estimated by varying the calibration parameter α by 3×10^{-4} [293]. Effect of a potential contribution from the $f_0(980)$ state to the 2D fit is estimated by including the $f_0(980)$ contribution with the PDG parameters. Varying the $f_0(980)$ mass and natural width within the uncertainties from Ref. [77] is taken into account. The *sPlot* technique also gives mass values that are consistent with those in

Tab. 8.4 within uncertainties. Resulting systematic uncertainty is obtained as a quadratic sum of the individual contributions. Details of the systematic uncertainty estimate are summarized in Table 8.5.

	$M_{\eta_c(1S)}$	$M_{\chi_{c0}}$	$M_{\chi_{c1}}$	$M_{\chi_{c2}}$	$M_{\eta_c(2S)}$	$\Gamma_{\eta_c(1S)}$
With $X(3872)$, $\chi_{c0}(2P)$, $\chi_{c2}(2P)$	-0.01	-0.02	< 0.01	0.08	-0.01	-0.55
$\eta_c(1S)$ resolution at MC value	-0.02	-0.02	< 0.01	0.03	-0.02	0.64
Resolution described by a single Gaussian	< 0.01	< 0.01	< 0.01	< 0.01	0.13	0.01
Variation of the r parameter in RBW						
between 0.5 GeV/c^{-1} and 3 GeV/c^{-1}	< 0.01	< 0.01	< 0.01	< 0.01	< 0.01	< 0.01
Variation of $\Gamma_{\eta_c(2S)}$	< 0.01	< 0.01	< 0.01	< 0.01	0.19	0.01
Fit region (3.15,3.95) GeV/c^2	–	0.01	-0.02	-0.08	-0.06	–
Fit region (2.80,3.70) GeV/c^2	-0.02	-0.01	-0.01	< 0.01	0.02	-0.19
Background parametrization	-0.04	0.05	0.04	-0.06	0.20	1.57
χ_c at PDG values	< 0.01	–	–	–	0.02	0.14
MC resolution in 2D fit	< 0.01	0.01	-0.04	0.01	0.01	0.02
Add slope parameter						
for ϕK^+K^- component in 2D fit	-0.11	0.04	-0.02	-0.01	0.02	0.89
Add slope parameter						
for $K^+K^-K^+K^-$ component in 2D fit	< 0.01	0.03	-0.02	< 0.01	-0.01	< 0.01
Momentum scale calibration	0.43	0.62	0.66	0.66	0.69	–
Combined systematic uncertainty	0.45	0.62	0.66	0.66	0.69	2.01

Table 8.5: Systematic uncertainties (deviation from the baseline value) in the measurement of charmonia masses (in MeV) and natural widths (in MeV).

Uncertainty related to the momentum scale calibration dominates mass determination for all η_c and χ_c states. The uncertainty on $\Gamma(\eta_c(1S))$ measurement is dominated by the background description.

Measured charmonia masses agree with the PDG average values. The obtained precision of the $\eta_c(1S)$ mass is similar to the precision of the PDG value, while other masses are determined with precisions below the PDG ones. The obtained $\eta_c(1S)$ mass is in agreement with the LHCb measurement using decays to the $p\overline{p}$ final states [13]. The value of the $\eta_c(1S)$ natural width is consistent to the PDG average [77].

As a cross-check, a stability of the results is checked by using *sPlot* instead of the 2D fit technique. Note that the amount of the pure $\phi\phi$ yield extracted using the *sPlot* technique might be affected due to possible correlation of the background shape and the $\phi\phi$ invariant mass. Table 8.6 compares the results for yield ratios obtained in section 6.5.1 to those obtained with the *sPlot* technique. The weighting coefficients were obtained from

	Measured value	Shift with respect to the measured value
$N_{\chi_{c0}}/N_{\eta_c(1S)}$	$0.144 \pm 0.022 \pm 0.011$	-0.006
$N_{\chi_{c1}}/N_{\eta_c(1S)}$	$0.071 \pm 0.015 \pm 0.006$	-0.002
$N_{\chi_{c2}}/N_{\eta_c(1S)}$	$0.094 \pm 0.016 \pm 0.007$	-0.002
$N_{\eta_c(2S)}/N_{\eta_c(1S)}$	$0.056 \pm 0.016 \pm 0.005$	-0.007
$N_{\chi_{c1}}/N_{\chi_{c0}}$	$0.494 \pm 0.107 \pm 0.012$	-0.006
$N_{\chi_{c2}}/N_{\chi_{c0}}$	$0.656 \pm 0.121 \pm 0.014$	-0.013

Table 8.6: Cross-check for charmonia yield ratios using the *sPlot* technique.

the ϕ_1 vs. ϕ_2 fit. Then they were used for unbinned maximum log likelihood fit of the $M(2\phi)$. Table 8.7 compares the results for charmonia mass and $\Gamma_{\eta_c(1S)}$ values obtained in section 8.3 to those obtained with the *sPlot* technique. Table 8.8 compares the results for charmonia mass difference values obtained in section 8.3 to those obtained with the *sPlot* technique. The results are found to be stable within the statistical uncertainties.

Charmonia mass differences within families $M_{\chi_{c1}} - M_{\chi_{c0}}$, $M_{\chi_{c2}} - M_{\chi_{c0}}$, and $M_{\eta_c(2S)} - M_{\eta_c(1S)}$ are obtained in order to cancel part of the systematic uncertainty, and provide inputs for direct comparison with theory. Table 8.9 summarizes the results for charmonia mass differences. Systematic uncertainties from the fit to the $\phi\phi$ invariant mass spectrum including additional resonances, variation of detector resolution, variation of the fit range, variation of the background parametrization (parabola), momentum scale calibration uncertainty, and potential contribution from the $f_0(980)$ state with a mass and natural width varied within uncertainties of Ref. [77] to the 2D fit technique are taken into

	Measured value, MeV (MeV)	Shift with respect to the measured value, MeV
$M_{\eta_c(1S)}$	$2982.81 \pm 0.99 \pm 0.45$	0.37
$M_{\chi_{c0}}$	$3412.99 \pm 1.91 \pm 0.62$	0.32
$M_{\chi_{c1}}$	$3508.38 \pm 1.91 \pm 0.66$	0.82
$M_{\chi_{c2}}$	$3557.29 \pm 1.71 \pm 0.66$	0.33
$M_{\eta_c(2S)}$	$3636.35 \pm 4.06 \pm 0.69$	-1.33
$\Gamma_{\eta_c(1S)}$	$31.35 \pm 3.51 \pm 2.00$	-0.20

Table 8.7: Cross-check for charmonia mass and $\Gamma_{\eta_c(1S)}$ values using the *sPlot* technique.

	Measured value, MeV	Shift with respect to the measured value, MeV
$M_{\chi_{c1}} - M_{\chi_{c0}}$	$95.38 \pm 2.71 \pm 0.11$	0.50
$M_{\chi_{c2}} - M_{\chi_{c0}}$	$144.28 \pm 2.59 \pm 0.17$	0.01
$M_{\eta_c(2S)} - M_{\eta_c(1S)}$	$653.54 \pm 4.22 \pm 0.42$	-1.71

Table 8.8: Cross-check for charmonia mass difference values using the *sPlot* technique.

account. Resulting systematic uncertainty is obtained as a quadratic sum of the individual contributions. Details of the systematic uncertainty estimate are summarized in Table 8.10. Uncertainty related to the momentum scale calibration dominates the $M_{\chi_{c1}} - M_{\chi_{c0}}$ and $M_{\eta_c(2S)} - M_{\eta_c(1S)}$ mass difference measurements. Systematic uncertainty of the $M_{\chi_{c2}} - M_{\chi_{c0}}$ measurement is dominated by the MC resolution.

The results are consistent to the central values obtained above withing statistical uncertainties. Measured charmonia mass differences agree with the PDG average values but are less precise than the world averages.

Stability of the obtained results on the mass difference has been also cross-checked by shifting the $\phi\phi$ invariant mass distribution by half a bin and and by using *sPlot* technique instead of the 2D fit.

	PDG	Measured value
$M_{\chi_{c1}} - M_{\chi_{c0}}$	95.91 ± 0.83	$95.38 \pm 2.71 \pm 0.11$
$M_{\chi_{c2}} - M_{\chi_{c0}}$	141.45 ± 0.32	$144.28 \pm 2.59 \pm 0.17$
$M_{\eta_c(2S)} - M_{\eta_c(1S)}$	655.70 ± 1.48	$653.54 \pm 4.22 \pm 0.42$

Table 8.9: Charmonia mass differences (in MeV).

	$M_{\chi_{c1}} - M_{\chi_{c0}}$	$M_{\chi_{c2}} - M_{\chi_{c0}}$	$M_{\eta_c(2S)} - M_{\eta_c(1S)}$
With $X(3872)$, $\chi_{c0}(2P)$, $\chi_{c2}(2P)$	0.03	0.11	-0.01
Masses of χ_c states at nominal values	–	–	0.02
$\eta_c(1S)$ resolution at MC value	0.01	0.05	-0.04
Resolution described by a single Gaussian	< 0.01	< 0.01	< 0.01
Variation of r parameter between $0.5\,\mathrm{GeV}/c^{-1}$ and $3\,\mathrm{GeV}/c^{-1}$	< 0.01	< 0.01	< 0.01
Variation of $\Gamma_{\eta_c(2S)}$	0.01	0.01	0.19
Fit region (3.15,3.95) GeV/c^2	-0.01	-0.06	–
Fit region (2.80,3.70) GeV/c^2	0.02	0.03	0.02
Background parametrization	< 0.01	-0.08	0.24
MC resolution in the 2D fit	-0.05	< 0.01	-0.01
Add slope parameter for the ϕK^+K^- component in 2D fit	-0.06	-0.04	0.12
Add slope parameter for the $K^+K^-K^+K^-$ component in 2D fit	-0.05	-0.03	-0.01
Momentum scale calibration	0.04	0.04	0.26
Combined systematic uncertainty	0.11	0.17	0.42

Table 8.10: Systematic uncertainties (deviation from the baseline value) in the measurement of charmonia mass differences (in MeV).

8.4 Summary and discussion

Using a sample of $b \to (c\bar{c} \to p\bar{p})X$ candidates, the J/ψ and η_c mass difference is measured. The obtained result, $\Delta M_{J/\psi,\,\eta_c} = M_{J/\psi} - M_{\eta_c} = (112.99 \pm 0.67_{stat} \pm 0.11_{syst})$ MeV, is consistent with the world average value and is the most precise single η_c mass measurement to date. The comparison of the obtained result with recent BES III result [270], the latest B-factory measurement [294], the LHCb result using decays to $p\bar{p}$ within Run I data [13], the LHCb measurement using $b \to \phi\phi X$ [257] and the LHCb measurement using exclusive $B^+ \to p\bar{p}K^+$ decays [240] is shown on Fig. 8.7. The second most precise to date measurement of η_c mass has been performed by BES III [270], where a sample of η_c produced in $\psi(2S) \to \eta_c\gamma$ was used. The BES III measurement is more complicated requiring a description of the corresponding tails of the η_c signal model taking place due to radiative transitions in the production process. The LHCb measurement from Ref. [240] takes into account interference between $B^+ \to (\eta_c \to p\bar{p})K^+$ and $B^+ \to p\bar{p}K^+$ non-resonant decays. The new LHCb result obtained here represents not only the single most precise determination of the mass splitting between the J/ψ and the η_c, but it is also free from the systematic effects which can influence other measurements of similar precision.

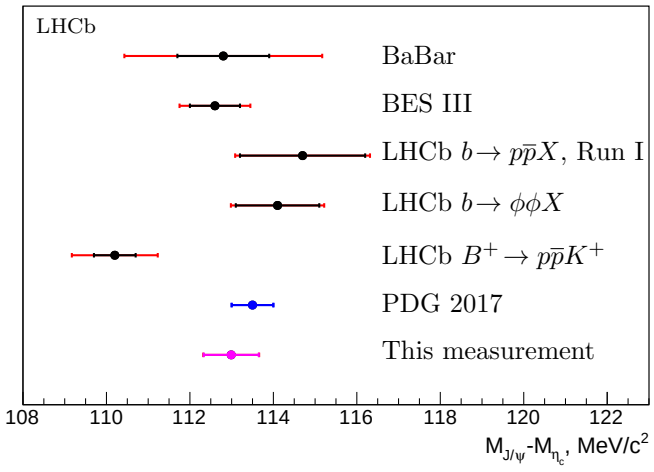

Figure 8.7: Mass difference $M_{J/\psi} - M_{\eta_c}$ measurement compared to the measurements from BaBar [294], BES III [270] and LHCb [13, 240, 257]; black error bars represent statistical uncertainties, red error bars represent total uncertainties. The blue point with error bars shows the world average, the magenta point with error bars represents this measurement.

Masses and natural widths of the η_c and χ_c states are determined to be

$$
\begin{aligned}
M_{\eta_c(1S)} &= 2982.81 \pm 0.99 \pm 0.45\,\text{MeV}\ , \\
M_{\chi_{c0}} &= 3412.99 \pm 1.91 \pm 0.62\,\text{MeV}\ , \\
M_{\chi_{c1}} &= 3508.38 \pm 1.91 \pm 0.66\,\text{MeV}\ , \\
M_{\chi_{c2}} &= 3557.29 \pm 1.71 \pm 0.66\,\text{MeV}\ , \\
M_{\eta_c(2S)} &= 3636.35 \pm 4.06 \pm 0.69\,\text{MeV}\ , \\
\Gamma_{\eta_c(1S)} &= 31.35 \pm 3.51 \pm 2.00\,\text{MeV}\ .
\end{aligned}
$$

using a sample of $b \to (c\bar{c} \to \phi\phi)X$ decays. Measured charmonia masses agree with the PDG average values. The obtained precision of the $\eta_c(1S)$ mass is similar to the precision of the PDG value, while other masses are determined with precisions below the PDG ones.

Fig. 8.8 shows the $\Gamma_{\eta_c(1S)}$, $M_{\eta_c(1S)}$ contour plot, obtained from the analysis of b-hadron decays into η_c meson, where the η_c candidates are reconstructed via the $\eta_c(1S) \to \phi\phi$ decay, for the combined data sample. Measurements of the η_c mass and natural width using η_c

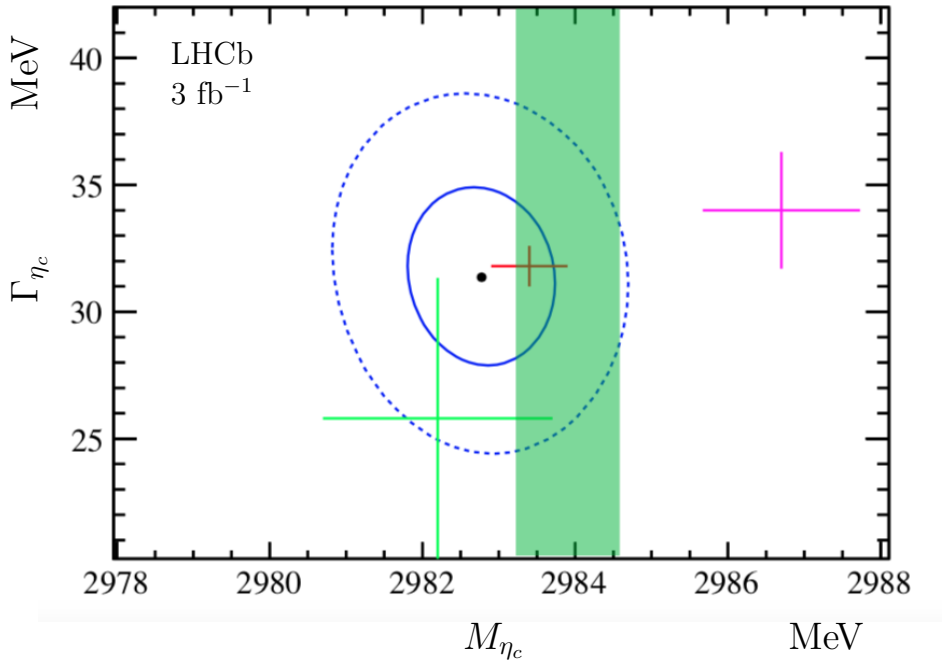

Figure 8.8: The η_c mass measurements from Section 8.2 (green band) and contour plot of Γ_{η_c} and M_{η_c} using $\eta_c \to \phi\phi$ (blue contour) decay for the combined data sample. The two curves indicate 68.3 C.L. (one-sigma) and 95.5 C.L. (two-sigma) contours. Only statistical uncertainties are shown. The red, green, and magenta points with error bars indicate the PDG average [77], the result from Ref. [13], and the result from Ref. [240], respectively.

meson decays to $\phi\phi$ are consistent with the studies using decays to $p\overline{p}$ [13] superimposed on the plot as a green point with error bars, and with the PDG average [77] superimposed on the plot as a red point with error bars. The measured η_c mass is below the result in Ref. [240]. The obtained precision of the $\eta_c(1S)$ mass is similar to the precision of the PDG value, while the η_c natural width measurement has a precision below that of the PDG average value.

Mass differences within charmonia families are measured to be

$$\begin{aligned} M_{\chi_{c1}} - M_{\chi_{c0}} &= 95.38 \pm 2.71 \pm 0.11\,\text{MeV} \ , \\ M_{\chi_{c2}} - M_{\chi_{c0}} &= 144.28 \pm 2.59 \pm 0.17\,\text{MeV} \ , \\ M_{\eta_c(2S)} - M_{\eta_c(1S)} &= 653.54 \pm 4.22 \pm 0.42\,\text{MeV} \ . \end{aligned}$$

Measured charmonia mass differences agree with the PDG average values and have precisions below the PDG ones.

For all measurements listed in this chapter statistical uncertainty is larger that the systematic one. Therefore, measurements will benefit from larger data samples.

Chapter 9

Study of B_s^0 decays to ϕ mesons

In addition to charmonium production measurements, signatures of multiple ϕ mesons can be used to study decays of the B_s^0 meson. Large centre-of-mass energy together with the powerful charged hadron ID and selective trigger make the LHCb experiment the ideal place for the measurements of B_s^0 decays.

Section 9.1 describes the analysis of relatively well-known $B_s^0 \to \phi\phi$ decay and measurement of its branching fraction, which is, however, a cross-check to another more precise LHCb measurement [295]. The analysis described in Section 9.1 compares the yields of observed $\eta_c \to \phi\phi$ and $B_s^0 \to \phi\phi$ and has another normalisation channel to that of nominal LHCb measurement, which leads to different sources of systematic uncertainties between the two measurements. In addition to that, using the measured $\mathcal{B}(B_s^0 \to \phi\phi)$, the $\mathcal{B}(\eta_c \to \phi\phi)$ is extracted aiming to solve a consistency problem in the corresponding world average value.

Section 9.2 describes a first evidence of the $B_s^0 \to \phi\phi\phi$ decay, studies of its decay model and search for intermediate resonances. Finally, the results obtained are summarised in Section 9.3.

9.1 The $B_s^0 \to \phi\phi$ decay

The $B_s^0 \to \phi\phi$ is forbidden at the tree level in the SM and proceeds via a gluonic penguin diagram $b \to s\bar{s}s$ shown on Fig. 9.1. This rare decay is an excellent probe of potential New Physics (NP) contributions and can be used to search for new heavy particles, which enter the penquin loop [296–298].

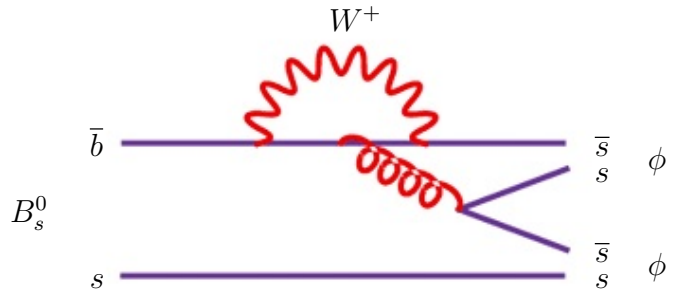

Figure 9.1: Quark diagram describing $B_s^0 \to \phi\phi$ decay.

Measurements of the polarization amplitudes and triple product asymmetries in the $B_s^0 \to \phi\phi$ decay mode were pointed out to provide important probes of the non-factorizable penguin-annihilation effects [299], final state interactions [300], and NP contributions to the penguin loops [301, 302]. Recently, the LHCb experiment performed a measurement of the time-dependent *CP*-violating asymmetry in $B_s^0 \to \phi\phi$ decays [303], and probed the *CP*-violating phase ϕ_s for the first time. The branching fraction $\mathcal{B}(B_s^0 \to \phi\phi)$ is calculated using pertubative QCD approach (Ref. [304] and references therein) and QCD factorization (Ref. [297, 298] and references therein). However, experimental knowledge of the branching fraction for this mode remains limited, with measurements from CDF [305, 306] and upper limit set by the SLD experiment [307]. In the recent CDF result [306], $\mathcal{B}(B_s^0 \to \phi\phi) = (17.7 \pm 2.4^{+5.7}_{-3.2}) \times 10^{-6}$, the systematic uncertainty is dominated by the precision of the branching fraction for the normalization channel $B_s^0 \to J/\psi\,\phi$. This measurement was limited by large systematic uncertainties and calls for the $\mathcal{B}(B_s^0 \to \phi\phi)$ determination using alternative approach. Later, LHCb provided a new measurement using the $B \to \phi K^{*0}(892)$ decay as a normalization $\mathcal{B}(B_s^0 \to \phi\phi) = (18.4 \pm 0.5 \pm 0.7 \pm 1.1_{f_s/f_d} \pm 1.2_{norm}) \times 10^{-6}$, where the third uncertainty is due to b quark fragmentation ratio f_s/f_d and the last uncertainty is related to normalization and relevant branching fraction [295].

Reconstructing the B_s^0 meson via its decay to $\phi\phi$, and comparing the η_c and B_s^0 event yields, I suggested a new alternative approach to access $\mathcal{B}(B_s^0 \to \phi\phi)$ described below.

9.1.1 Signal extraction and systematic uncertainties

The $B_s^0 \to \phi\phi$ decay mode is studied below to extract the $\mathcal{B}(B_s^0 \to \phi\phi)/\mathcal{B}(\eta_c \to \phi\phi)$ ratio and as a normalization mode for the $\mathcal{B}(B_s^0 \to \phi\phi\phi)$ measurement.

The $B_s^0 \to \phi\phi$ candidates are reconstructed using selection criteria similar to those applied for charmonia reconstruction via decays to $\phi\phi$ in the production analysis, as discussed in section 6.5.1. Charged kaon separation against pions, $ProbNNk > 0.1$, and kaon transverse momentum $p_{\rm T} > 0.5\,{\rm GeV}$ are required. Kaons from each ϕ candidate are required to form a good quality vertex, $\chi^2 < 25$. Two ϕ candidates are required to also form a good quality common vertex, $\chi^2/{\rm ndf} < 9$, well distinguished from the corresponding primary vertex with a significant distance between the two vertices, $\chi^2 > 100$. A dedicated MC sample of $B_s^0 \to \phi\phi$ decays is used to study signal resolution and efficiency. The decay model uses amplitudes measured by CDF. The following efficiency ratio for $\eta_c \to \phi\phi$ and $B_s^0 \to \phi\phi$ decays was obtained.

$$\frac{\varepsilon(\eta_c(1S) \to \phi\phi)}{\varepsilon(B_s^0 \to \phi\phi)} = 0.31 \pm 0.01$$

The two-dimensional fit selects pure $\phi\phi$ combinations, suppressing a significant reflection from $B^0 \to \phi K^{*0}$. Separate analysis of the data samples, corresponding to $\sqrt{s} = 7\,{\rm TeV}$ and $\sqrt{s} = 8\,{\rm TeV}$, shown consistent results for signal and background models and event yields, so that the combined data sample is considered. A fit to the $\phi\phi$ invariant mass spectrum in the region of the B_s^0 mass is shown on Fig. 9.2.

A double Gaussian function is used to describe the B_s^0 signal shape, while an exponential function modelled combinatorial background. The ratio of the two Gaussian widths of 0.52 ± 0.01 and the fraction of narrow Gaussian of 0.81 ± 0.01 are taken from simulation. The fit yields $2701 \pm 114 \pm 84$ candidates in the B_s^0 signal peak, and the B_s^0 mass value $M_{B_s^0} = 5366.15 \pm 0.64\,{\rm MeV}$, in agreement with the PDG average of $5366.77 \pm 0.24\,{\rm MeV}$ [77].

In the measurement of the B_s^0 signal yield, systematic uncertainties from the variation of background shape (constant), resolution description and potential $f_0(980)$ contribution to the 2D fit technique are taken into account. Resulting systematic uncertainty is obtained as a quadratic sum of the individual contributions. Details of the systematic uncertainty estimate are summarized in Table 9.1. Uncertainty related to the resolution description in the 2D fit and the B_s^0 resolution description give the largest contribution the systematic uncertainty in the B_s^0 signal yield determination.

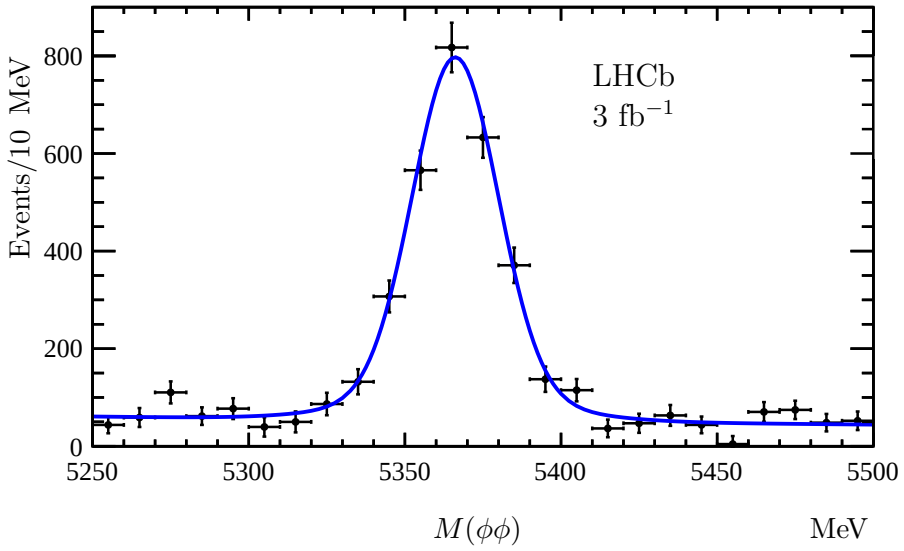

Figure 9.2: Invariant mass spectrum of the $\phi\phi$ combinations in the region of the B_s^0 mass for combined data sample. The number of candidates in each bin comes from the 2D fit, decribed in section 6.4.

	$N(B_s^0)$
Background shape variation, $\phi\phi$	-2
Resolution in 2D fit at MC value	-23
$f_0(980)$ in the 2D fit	2
Resolution for B_s^0 described by a single Gaussian	-81
Combined	84

Table 9.1: Systematic uncertainties (deviation from the baseline value) in the measurement of the B_s^0 signal yield (in number of candidates)

9.1.2 Extraction of $\mathcal{B}(B_s^0 \to \phi\phi)$

Relating $B_s^0 \to \phi\phi$ decay to the production of the $\eta_c(1S)$ state in b-hadron decays provides an alternative approach of the $\mathcal{B}(B_s^0 \to \phi\phi)$ determination.

In the measurement of the $B_s^0 \to \phi\phi$ branching fraction, the normalization to the $b \to \eta_c(1S)X$ is used, where the $\eta_c(1S)$ production in b-decays was measured in Ref. [13]. Thus having reconstructed the η_c and B_s^0 mesons in the $\eta_c \to \phi\phi$ and $B_s^0 \to \phi\phi$ decay modes, comparing the η_c and B_s^0 event yields, and accounting for the efficiency difference, the branching fraction $\mathcal{B}(B_s^0 \to \phi\phi)$ can be obtained. In the ratio of the B_s^0 production, where B_s^0 is reconstructed via the $B_s^0 \to \phi\phi$ decay, to the η_c production in b-hadron

inclusive decays, the B_s^0 fragmentation from the b-quark has to be taken into account,

$$\frac{\mathcal{B}(\bar{b} \to B_s^0) \times \mathcal{B}(B_s^0 \to \phi\phi)}{\mathcal{B}(b \to \eta_c X) \times \mathcal{B}(\eta_c \to \phi\phi)} = \frac{N_{B_s^0}}{N_{\eta_c}} \times \frac{\varepsilon_{\eta_c}}{\varepsilon_{B_s^0}} \ , \tag{9.1}$$

where N_{η_c} and $N_{B_s^0}$ are the event yields for η_c and B_s^0 signals, respectively, and the efficiency ratio estimated using MC. The ratio of B_s^0 production to the η_c inclusive production in b-hadron decays is thus obtained to be

$$\frac{\mathcal{B}(\bar{b} \to B_s^0) \times \mathcal{B}(B_s^0 \to \phi\phi)}{\mathcal{B}(b \to \eta_c X) \times \mathcal{B}(\eta_c \to \phi\phi)} = 0.128 \pm 0.010 \pm 0.007 \ . \tag{9.2}$$

Using the above value, together with the ratio $\mathcal{B}(b \to \eta_c X)/\mathcal{B}(b \to J/\psi\, X)$ obtained in the same p_{T} region, allows to extract the branching fraction $\mathcal{B}(B_s^0 \to \phi\phi)$ as

$$\mathcal{B}(B_s^0 \to \phi\phi) = \frac{N_{B_s^0}}{N_{\eta_c}} \times \frac{\varepsilon_{\eta_c}}{\varepsilon_{B_s^0}} \times \tag{9.3}$$

$$\times \frac{\mathcal{B}(b \to \eta_c X) \times \mathcal{B}(\eta_c \to p\overline{p})}{\mathcal{B}(b \to J/\psi\, X) \times \mathcal{B}(J/\psi \to p\overline{p})} \times \tag{9.4}$$

$$\times \frac{\mathcal{B}(\eta_c \to \phi\phi)}{\mathcal{B}(\eta_c \to p\overline{p})} \times \mathcal{B}(b \to J/\psi\, X) \times \mathcal{B}(J/\psi \to p\overline{p})/\mathcal{B}(\bar{b} \to B_s^0) \ . \tag{9.5}$$

In the above expression, the ratio on the second line has been measured in Ref. [13] to be $\frac{\mathcal{B}(b\to\eta_c X)\times\mathcal{B}(\eta_c\to p\overline{p})}{\mathcal{B}(b\to J/\psi\, X)\times\mathcal{B}(J/\psi\to p\overline{p})} = 0.302 \pm 0.039 \pm 0.015 = 0.302 \pm 0.042$ for $p_{\mathrm{T}}(\eta_c, J/\psi) > 6.5\,\mathrm{GeV}$, and can be used as an estimate for the present calculations; the ratio of the η_c branching fractions to the $\phi\phi$ and $p\overline{p}$ final states $\mathcal{B}(\eta_c \to \phi\phi)/\mathcal{B}(\eta_c \to p\overline{p}) = 1.17 \pm 0.18$ [77] and is dominated by the accuracy of BES measurements; the inclusive branching fraction of b-hadrons into J/ψ, $\mathcal{B}(b \to J/\psi\, X) = (1.16 \pm 0.10)\%$, where decays of the mixture of $B^{\pm}$, B^0, B_s^0 and b baryons are considered [77]; and the branching fraction of the J/ψ meson decay to the $p\overline{p}$ final state $\mathcal{B}(J/\psi \to p\overline{p}) = (2.120 \pm 0.029) \times 10^{-3}$ [77].

The fragmentation of the $\bar{b}$ quark to B_s^0 is driven by strong dynamics in the nonperturbative regime, and no reliable theoretical prediction can be made. Thus the f_s is also determined experimentally. The LHCb experiment determined $\frac{f_s}{f_d}$ via semileptonic [308] and hadronic [309] decays, and found it consistent with being independent on the rapidity and transverse momentum. The two measurements agree to each other, and yield the average of

$$\frac{f_s}{f_d} = 0.256 \pm 0.020 \ .$$

Though $\frac{f_s}{f_d}$ is not a priori a "universal" number, the LHCb result is similar to those obtained by the experiments at LEP and Tevatron. Assuming universality, the Ref. [77] proposes a value of $f_s = \mathcal{B}(\overline{b} \to B_s^0) = 0.107 \pm 0.014$.

From the above input, the branching fraction $\mathcal{B}(B_s^0 \to \phi\phi)$ is obtained to be

$$\mathcal{B}(B_s^0 \to \phi\phi) = (2.06 \pm 0.16 \pm 0.12 \pm 0.27_{f_s} \pm 0.47_{\mathcal{B}}) \times 10^{-5} \ ,$$

where the first uncertainty is statistical, the second is systematic, the third one is due to f_s and the last one is due to normalization and especially due to $\frac{\mathcal{B}(\eta_c \to \phi\phi)}{\mathcal{B}(\eta_c \to p\overline{p})}$, which limits precision of this measurement.

Alternatively, the f_s can be extracted from the LHCb results on b-hadron production [310] yielding $f_s = 0.096 \pm 0.005$. Using this value, the branching fraction $\mathcal{B}(B_s^0 \to \phi\phi)$ is obtained to be

$$\mathcal{B}(B_s^0 \to \phi\phi) = (2.18 \pm 0.17 \pm 0.11 \pm 0.14_{f_s} \pm 0.65_{\mathcal{B}}) \times 10^{-5} \ .$$

The above value of $\mathcal{B}(B_s^0 \to \phi\phi)$ is measured with a different technique with respect to the previous results [305–307]. The measurement is consistent with the previous CDF results and has a precision similar to that of the PDG value [77]. The measurement is consistent with the new LHCb result [295] using normalization to the $B \to \phi K^{*0}(892)$ decay mode, $\mathcal{B}(B_s^0 \to \phi\phi) = (1.84 \pm 0.05 \pm 0.07 \pm 0.11_{f_s/f_d} \pm 0.12_{norm}) \times 10^{-5}$. The result is also consistent with theoretical calculations [297, 298, 304].

Precision of the measured branching fraction $\mathcal{B}(B_s^0 \to \phi\phi)$ is fully dominated by the systematic uncertainty, which is in turn dominated by the uncertainty in the ratio of the η_c branching fractions $\frac{\mathcal{B}(\eta_c \to \phi\phi)}{\mathcal{B}(\eta_c \to p\overline{p})}$, and the knowledge of the f_s parameter. Averages [77] of the branching fractions $\mathcal{B}(\eta_c \to \phi\phi)$ and $\mathcal{B}(\eta_c \to p\overline{p})$ rely on the so far most precise measurements by DM2 [311] and BES [275, 312, 313] experiments. Precision of all above measurements is dominated by systematic uncertainties. None of the two experiments directly performed a measurement of the ratio of the two branching fractions, which would allow partial cancellation of systematic uncertainty, and would consequently reduce the systematic uncertainty of the branching fraction $\mathcal{B}(B_s^0 \to \phi\phi)$ measured in this section.

In summary, the branching ratio $\mathcal{B}(B_s^0 \to \phi\phi) = (2.18 \pm 0.17 \pm 0.11 \pm 0.14_{f_s} \pm 0.65_{\mathcal{B}}) \times 10^{-5}$ is calculated with a different technique with respect to the previous results [305–307]. The measurement is consistent with the previous CDF results and has a precision similar to that of the PDG value [77]. The result is consistent and is less precise than the new LHCb result [295]. The result is also consistent with theoretical calculations [297, 298, 304].

9.1.3 Extraction of the $\mathcal{B}(\eta_c \to \phi\phi)/\mathcal{B}(\eta_c \to p\overline{p})$

An opposite approach with respect to that discussed in Section 9.1 can be elaborated to resolve a tension between the PDG average and PDG fit values of $\mathcal{B}(\eta_c \to \phi\phi)$ [73]

$$\begin{aligned} \mathcal{B}(\eta_c \to \phi\phi)^{PDG\,fit} &= (1.79 \pm 0.20) \times 10^{-3} \\ \mathcal{B}(\eta_c \to \phi\phi)^{PDG\,average} &= (2.8 \pm 0.4) \times 10^{-3} \end{aligned} \tag{9.6}$$

Using Eq. 9.5 and external inputs, the ratio of the branching fractions for the $\eta_c(1S)$ decays to $\phi\phi$ and to $p\overline{p}$ is determined below. The measured B_s^0 and $\eta_c(1S)$ yields and efficiency ratio, the branching fraction $\mathcal{B}(B_s^0 \to \phi\phi) = (1.84 \pm 0.05 \pm 0.07 \pm 0.11_{f_s/f_d} \pm 0.12_{\rm norm}) \times 10^{-5}$ [314], the J/ψ production rate in b-hadron decays $\mathcal{B}(b \to J/\psi\, X) = (1.16 \pm 0.10)\%$ [77], the relative production rates of $\eta_c(1S)$ and J/ψ in b-hadron decays $\frac{\mathcal{B}(b\to\eta_c(1S)X)\times\mathcal{B}(\eta_c(1S)\to p\overline{p})}{\mathcal{B}(b\to J/\psi\, X)\times\mathcal{B}(J/\psi\to p\overline{p})} = 0.302 \pm 0.042$ [13], the branching fraction $\mathcal{B}(J/\psi \to p\overline{p}) = (2.120 \pm 0.029) \times 10^{-3}$ [77], the ratio of fragmentation fractions $f_s/f_d = 0.259 \pm 0.015$ [315], and the Λ_b^0 fragmentation fraction $f_{\Lambda_b^0}$ momentum dependence from Ref. [310] are used. The ratio of the branching fractions for the $\eta_c(1S)$ decays to $\phi\phi$ and to $p\overline{p}$ is determined as

$$\frac{\mathcal{B}(\eta_c(1S) \to \phi\phi)}{\mathcal{B}(\eta_c(1S) \to p\overline{p})} = 1.79 \pm 0.14 \pm 0.09 \pm 0.10_{f_s/f_d} \pm 0.03_{f_{\Lambda_b^0}} \pm 0.29_{\mathcal{B}},$$

where the third uncertainty is related to f_s/f_d, the fourth uncertainty is related to $f_{\Lambda_b^0}$, and the fifth uncertainty is related to uncertainties of the production rates and decay branching fractions involved. This value is larger than the value computed from the world average branching fractions given in Ref. [77], $\frac{\mathcal{B}(\eta_c(1S)\to\phi\phi)}{\mathcal{B}(\eta_c(1S)\to p\overline{p})} = 1.19 \pm 0.14$, and indicates a consistency problem.

9.2 The $B_s^0 \to \phi\phi\phi$ decay

The three-body $B_s^0 \to \phi\phi\phi$ decay can be described by a penguin quark diagram shown on Fig. 9.3. This diagram is similar to the diagram describing the $B_s^0 \to \phi\phi$ decay mode, (Fig. 9.1) and involves a creation of an additional $s\overline{s}$ pair. The transition thus leads to the final state with six strange quarks.

The $B_s^0 \to \eta_c\phi$ decay mode followed by the $\eta_c \to \phi\phi$ decay, is an example of the decay via intermediate resonance, yielding three-ϕ system. The $B_s^0 \to \eta_c\phi$ decay is described by an internal emission of W boson. This decay has been observed by LHCb recently and

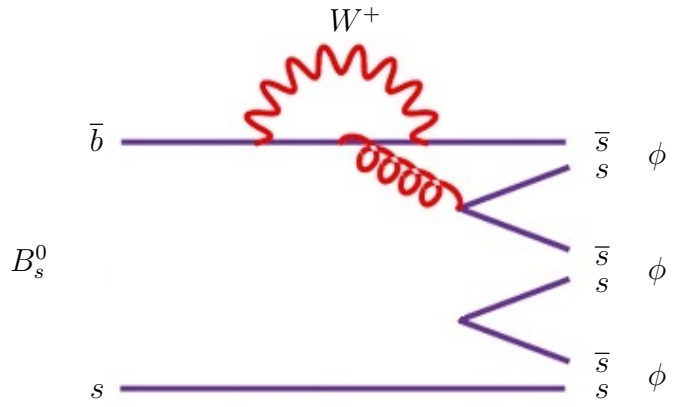

Figure 9.3: Quark diagram describing three-body $B_s^0 \to \phi\phi\phi$ decay.

the branching fraction was measured to be

$$\mathcal{B}(B_s^0 \to \eta_c\phi) = (5.01 \pm 0.53 \pm 0.27 \pm 0.63) \times 10^{-4}, \tag{9.7}$$

where the last uncertainty is due to the limited knowledge of the external branching fractions. The similar $B_s^0 \to J/\psi\,\phi$ decay occurs with a branching fraction of $\mathcal{B}(B_s^0 \to J/\psi\,\phi) = (1.08 \pm 0.08) \times 10^{-3}$ [73] and was used as a normalization. The four decay modes were used to reconstruct the η_c meson, namely decays to $p\overline{p}$, $K^+K^-K^+K^-$, $K^+K^-\pi^+\pi^-$ and $\pi^+\pi^-\pi^+\pi^-$ final states.

The difference between the branching fractions for the $B_s^0 \to \eta_c\phi$ and $B_s^0 \to J/\psi\,\phi$ decays can however be expected due to the fact, that the latter decay is a $P \to VV$ transition. For example, branching fractions of light B-meson decays to $J/\psi\,K^*$ exceed those of light B-meson decays to $\eta_c K^*$ by a factor 2, where only neutral B-decays are measured precisely enough to draw this conclusion at a quantitative level [73].

In addition, in order to make a comparison between the $B_s^0 \to \eta_c\phi$ and three-body contributions to the $B_s^0 \to \phi\phi\phi$ decay, the $\eta_c \to \phi\phi$ branching fraction should be taken into account. Once the $B_s^0 \to \phi\phi\phi$ decay is observed, studying its resonance structure can yield interesting information on the QCD contribution to weak b-decays.

9.2.1 Signal extraction and systematic uncertainties

Adding another reconstructed ϕ candidate to the $\phi\phi$ system, allows to search for the $B_s^0 \to \phi\phi\phi$ decay. The $B_s^0 \to \phi\phi$ decay is used as normalization.

Reconstruction of the $B_s^0 \to \phi\phi\phi$ decay mode employs selection criteria, that are similar to those used for the analysis of the $B_s^0 \to \phi\phi$ decay. Table 9.2 summarizes selection criteria for charmonia and B_s^0 meson decays to $\phi\phi$ and B_s^0 decays to $\phi\phi\phi$.

	Variable	Denotion	Requirement
Kaons	Track quality	χ^2/ndf	< 3
	Impact parameter to primary vertex	χ^2_{IP}	> 4
	Transverse momentum	p_{T}, GeV	> 0.5
	Identification	ProbNNk	> 0.1
ϕ	Vertex quality	χ^2	< 25
	Invariant mass	$\lvert M_{K^+K^-} - M_\phi \rvert$, MeV	< 12
$\phi\phi$	Vertex quality	χ^2/ndf	< 9
	Distance between the decay vertex and the primary vertex	χ^2	> 100
$\phi\phi\phi$	Vertex quality	χ^2/ndf	< 9
	Distance between the decay vertex and the primary vertex	χ^2	> 100

Table 9.2: Selection criteria for charmonia and B_s^0 meson decays to $\phi\phi$ and B_s^0 decays to $\phi\phi\phi$.

A dedicated MC sample of $B_s^0 \to \phi\phi\phi$ decays is used to describe detector resolution and signal efficiency. The efficiency ratio of $B_s^0 \to \phi\phi\phi$ and $B_s^0 \to \phi\phi$ decay modes is determined to be

$$\frac{\varepsilon(B_s^0 \to \phi\phi\phi)}{\varepsilon(B_s^0 \to \phi\phi)} = 0.26 \pm 0.01.$$

In the $B_s^0 \to \phi\phi\phi$ analysis, in order to extract pure $\phi\phi\phi$ combinations a maximum likelihood unbinned 3D fit is used, similar to the 2D fit used to extract pure $\phi\phi$ combinations,

$$\begin{aligned} F(x_1, x_2, x_3) = & N_{\phi\phi\phi} \times S_1 \times S_2 \times S_3 + \\ & N_{\phi\phi KK} \times (S_1 \times S_2 \times B_3 \ + \ S_1 \times B_2 \times S_3 \ + \ B_1 \times S_2 \times S_3) + \\ & N_{\phi KKKK} \times (S_1 \times B_2 \times B_3 \ + \ B_1 \times S_2 \times B_3 \ + \ B_1 \times B_2 \times S_3) + \\ & N_{KKKKKK} \times B_1 \times B_2 \times B_3 \ , \end{aligned}$$

where signal contributions S_1, S_2 and S_3 are described by the product of the convolution of the Breit-Wigner function and double Gaussian function and the square root to account

for the phase space difference, and background contributions B_1, B_2 and B_3 are decribed by the square root function. The ratio of the two Gaussian widths σ_1/σ_2 of 0.40 ± 0.01 and the fraction of narrow Gaussian $N_1/(N_1+N_2)$ of 0.87 ± 0.01 are taken from simulation. The fit shape accounts for $\phi\phi\phi$, $\phi\phi K^+K^-$, $\phi K^+K^-K^+K^-$ and $K^+K^-K^+K^-K^+K^-$ contributions and takes into account the available phase space. Projections of the 3D fit for the entire sample of candidates on each ϕ candidate are shown on Fig. 9.4. No

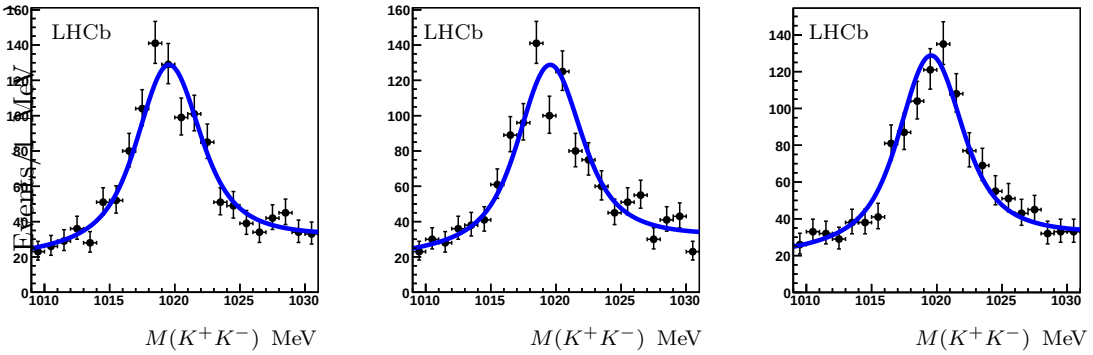

Figure 9.4: Projections of the entire sample of the $\phi\phi\phi$ candidates 3D fit on each ϕ candidate.

contribution from the $f_0(980)$ resonance is seen on the plots. However a potential effect due to $f_0(980)$ is estimated in the following as a potential source of systematic uncertainty.

Figure 9.5 shows invariant mass distribution for pure $\phi\phi\phi$ combinations. A fit to the

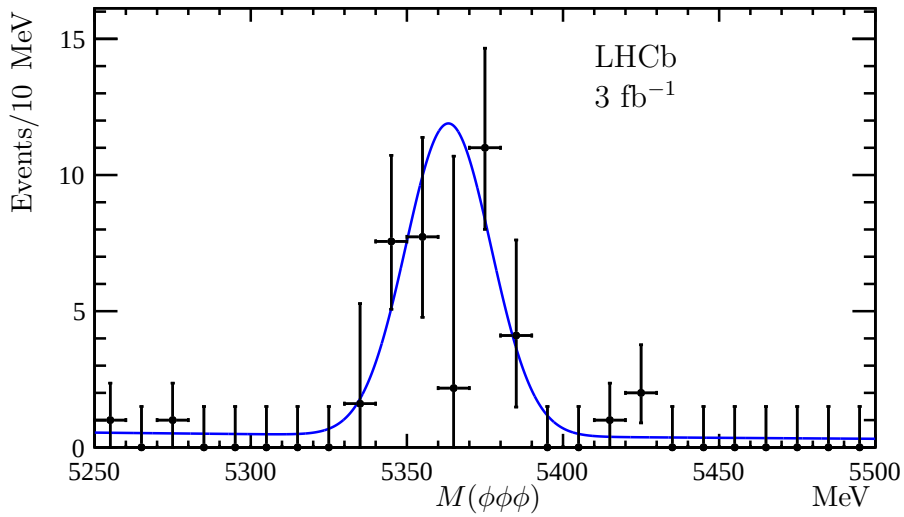

Figure 9.5: Distribution of the $\phi\phi\phi$ invariant mass for combined data sample accumulated at $\sqrt{s} = 7\,\text{TeV}$ and $\sqrt{s} = 8\,\text{TeV}$.

invariant mass spectrum, using a double Gaussian function to describe a clear B_s^0 signal corresponding to the transition $B_s^0 \to \phi\phi\phi$, and an exponential to describe combinatorial background, is performed. The ratio of the two Gaussian widths σ_1/σ_2 of 0.45 ± 0.02 and the fraction of narrow Gaussian $N_1/(N_1 + N_2)$ of 0.85 ± 0.03 are taken from simulation[1] The fit yields $41 \pm 10 \pm 5$ B_s^0 candidates over a low level background. Significance of the $B_s^0 \to \phi\phi\phi$ signal is estimated by judging the fit quality using the fit function comprising or not the signal shape. An estimate of about 4.7σ is obtained from Fig. 9.6. Here the mass and resolution of B_s^0 are fixed to the values calculated in the $B_s^0 \to \phi\phi$ analysis.

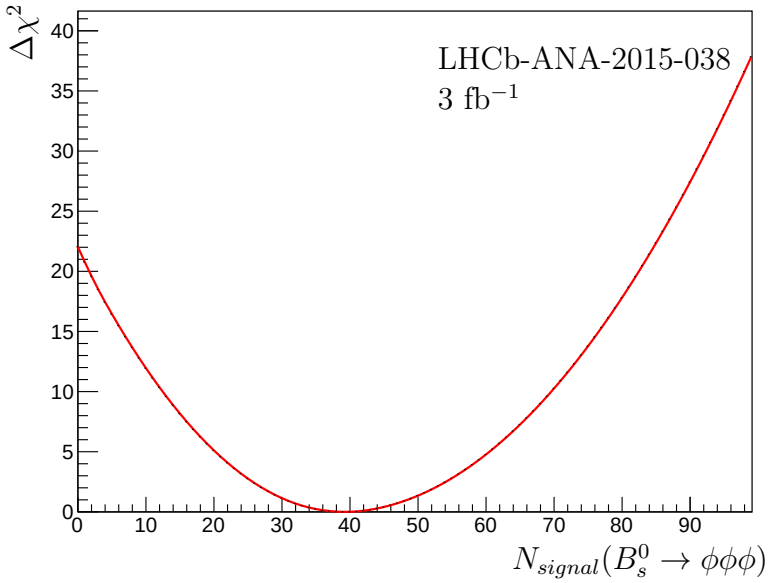

Figure 9.6: Fit quality of the $B_s^0 \to \phi\phi\phi$ signal $\Delta\chi^2$ depending on the number of signal candidates assumed by the fit.

Alternatively, the 3×10^7 toy simulation samples, were generated according to the fit to data with corresponding uncertainties, excluding the signal region. These samples were fit to the background shape only and to a sum of the background and signal shapes. A difference between the corresponding χ^2 values of the fit, χ^2_B and χ^2_{S+B}, is shown on Fig. 9.7. Arrow points to the $\chi^2_B - \chi^2_{S+B}$ value of 22.0 as obtained from the fit to the data sample. This corresponds to the significance above 4.9σ and p-value of 8.1×10^{-7} for the observed signal [316]. Details of the systematic uncertainty estimate are summarized in Table 9.3. Uncertainties related to the background description in the 3D fit and to the

[1]Resolutions are found to be $\sigma_1 = 9.8 \pm 0.2$ MeV (MC) and 13.2 ± 2.9 MeV (data). The ϕ resolution is fixed to the value from the fit in the whole mass range.. One parameter of the B_s^0 resolution is left free in the fit, ratio of the two Gaussians and the fraction of the narrow Gaussian are fixed to the MC values.

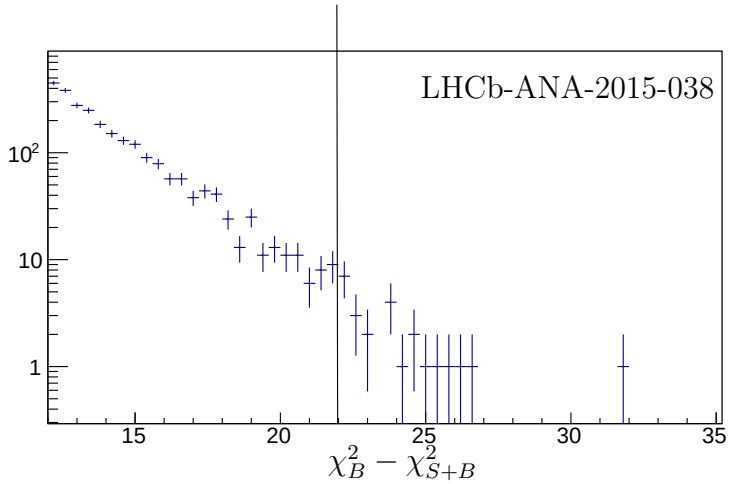

Figure 9.7: Difference between the χ^2 values of the fit with background shape only and signal and background shapes, χ^2_B and χ^2_{S+B}, for the 3×10^7 toy simulation samples generated according to the fit to data with corresponding uncertainties, excluding a signal region.

	$N(B_s^0)$
Background shape variation, $\phi\phi\phi$	< 1
Resolution at MC value in 3D fit	-1
Resolution of B_s^0 described by a single Gaussian	-2
$f_0(980)$ in the 3D fit	1
Decay model	4
Combined	5

Table 9.3: Systematic uncertainties (deviation from the baseline value) in the measurement of the B_s^0 signal yield (in number of candidates).

decay model of ϕ polarisation dominate the systematic uncertainty in the B_s^0 signal yield determination.

Effect of the MC description of the B_s^0 p_{T} spectrum

When calculating a ratio of the branching fractions for the $B_s^0 \to \phi\phi\phi$ and $B_s^0 \to \phi\phi$ decays, knowledge of the p_{T} spectrum of the B_s^0 mesons can modify the ratio of corresponding efficiencies. The p_{T} dependence of B_s^0 candidates reconstructed via the $B_s^0 \to \phi\phi$ decay in data and simulation is shown on Fig. 9.8. The difference between the two spectra was accounted as a correction to the efficiency ratio for the $B_s^0 \to \phi\phi\phi$ and $B_s^0 \to \phi\phi$ channels.

The estimated effect is found to be at the level of 8.8%. Corresponding correction is applied. The corresponding contribution to the systematic uncertainty is below 1% and is neglected.

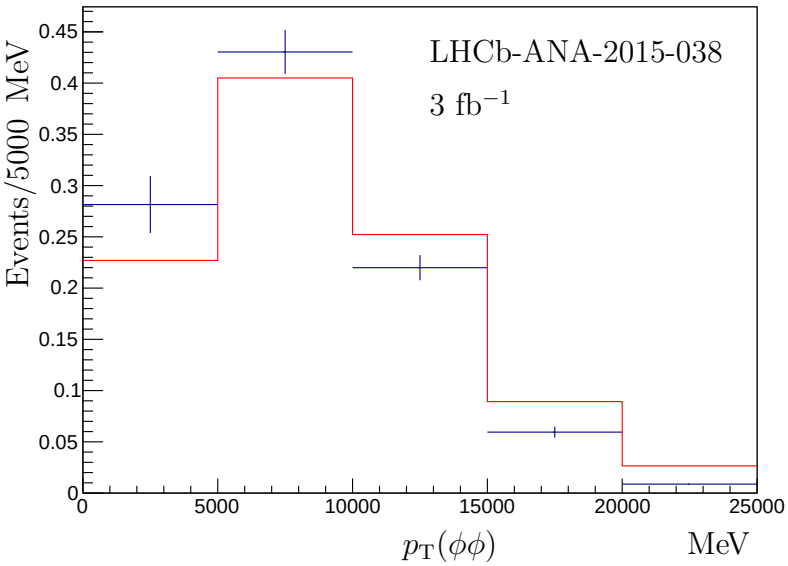

Figure 9.8: Reconstructed p_{T} dependence of B_s^0 candidates reconstructed via the $B_s^0 \to \phi\phi$ decay in data (blue points with error bars) and simulation (red histogram).

9.2.2 Measurement of the $\mathcal{B}(B_s^0 \to \phi\phi\phi)$

The $B_s^0 \to \phi\phi\phi$ branching fraction is measured relatively to the $B_s^0 \to \phi\phi$ channel,

$$\frac{\mathcal{B}(B_s^0 \to \phi\phi\phi)}{\mathcal{B}(B_s^0 \to \phi\phi)} = \frac{N_{B_s^0 \to \phi\phi\phi}}{N_{B_s^0 \to \phi\phi}} \times \frac{\varepsilon_{B_s^0 \to \phi\phi}}{\varepsilon_{B_s^0 \to \phi\phi\phi}} \times \frac{1}{\mathcal{B}(\phi \to K^+K^-)} \,. \tag{9.8}$$

Reconstructing the decays of B_s^0 meson to two ϕ mesons, $B_s^0 \to \phi\phi$, and three ϕ mesons, $B_s^0 \to \phi\phi\phi$, with similar selection criteria, allows a determination of the ratio of their branching fractions to be

$$\frac{\mathcal{B}(B_s^0 \to \phi\phi\phi)}{\mathcal{B}(B_s^0 \to \phi\phi)} = \frac{N_{B_s^0 \to \phi\phi\phi}}{N_{B_s^0 \to \phi\phi}} \times \frac{\varepsilon_{B_s^0 \to \phi\phi}}{\varepsilon_{B_s^0 \to \phi\phi\phi}} \times \frac{1}{\mathcal{B}(\phi \to K^+K^-)} \,.$$

In the above expression, the event yields are measured in the present analysis, and the efficiency ratio is estimated using MC simulation to be $\varepsilon_{B_s^0 \to \phi\phi\phi}/\varepsilon_{B_s^0 \to \phi\phi} = 0.26 \pm 0.01$, assuming that the $B_s^0 \to \phi\phi\phi$ transition proceeds as a three-body decay. The efficiency correction of $\alpha = 0.912 \pm 0.001$ related to the MC description of the B_s^0 p_{T} spectrum is additionally applied. The ratio of the branching fraction is thus obtained as

$$\frac{\mathcal{B}(B_s^0 \to \phi\phi\phi)}{\mathcal{B}(B_s^0 \to \phi\phi)} = 0.117 \pm 0.030 \pm 0.015 \,,$$

where the systematic uncertainty is dominated by the uncertainty due to the decay model. Using $\mathcal{B}(B_s^0 \to \phi\phi) = (1.84 \pm 0.05 \pm 0.07 \pm 0.12_{norm} \pm 0.11_{f_s/f_d}) \times 10^{-5}$ from Ref. [314], the branching fraction for the B_s^0 meson decay to three ϕ mesons is found to be

$$\mathcal{B}(B_s^0 \to \phi\phi\phi) = (2.15 \pm 0.54 \pm 0.28 \pm 0.21) \times 10^{-6},$$

where the last uncertainty is due to involved exteranl branching fractions knowledge.

9.2.3 Decay model of the $B_s^0 \to \phi\phi\phi$ decay

In order to search for contributions from possible intermediate resonances the invariant mass of $\phi\phi$ pairs is looked at. Fig. 9.9 shows the invariant mass distribution of $\phi\phi$ pairs from the $B_s^0 \to \phi\phi\phi$ candidates. The candidates with invariant mass between 5.325 GeV/c and 5.415 GeV/c are considered. With the limited sample of $B_s^0 \to \phi\phi\phi$ candidates the 3D fit technique to remove contributions from K^+K^- combinations that are not from ϕ decays cannot be used for this measurement. Instead, all ϕ mesons contributing in the mass range of the B_s^0 are used, with an estimated signal purity of 71%. A phase space distribution as

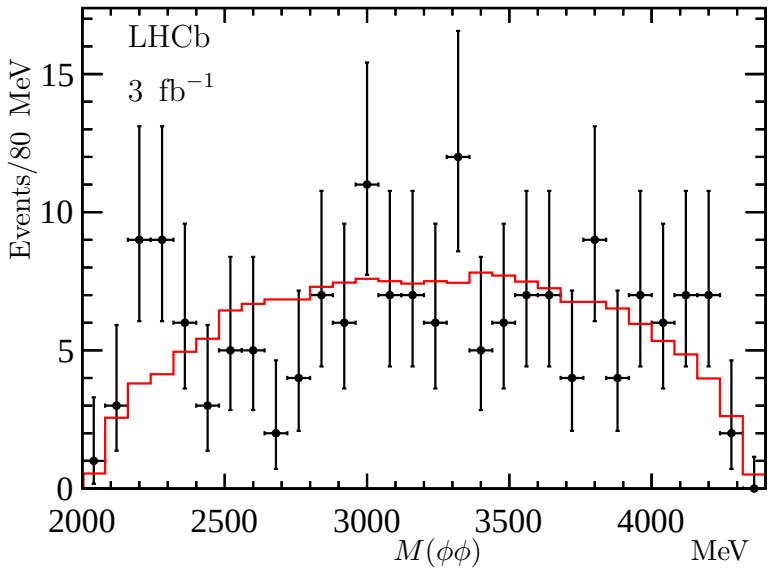

Figure 9.9: Invariant mass distribution of the $\phi\phi$ pair from the $B_s^0 \to \phi\phi\phi$ candidates for combined data sample accumulated at $\sqrt{s} = 7$ TeV and $\sqrt{s} = 8$ TeV. A phase space distribution as obtained from simulation (red histogram) is overlaid.

obtained from simulation is overlaid for comparison. Though the event sample is too small to conclude, no indication of a dominating resonance contribution is visible for the $\eta_c(1S)$, χ_{c0}, χ_{c1}, χ_{c2} or $\eta_c(2S)$ contribution. In addition, there is no indication of the $f_2(2300)$ or $f_2(2340)$ presence. A small increase in the number of candidates is observed around 2200 MeV close to the phase space threshold, which is however not compatible with any known resonant state. This increase cannot be attributed to a nearby $\phi(2170)$ state, since $\phi(2170)$ has the quantum numbers $J^{PC} = 1^{--}$ incompatible with the decay to $\phi\phi$.

As an attempt to improve the resolution, Fig. 9.10 shows the invariant mass distribution of $\phi\phi$ pairs from the $B_s^0 \to \phi\phi\phi$ candidates, using a constraint to the B_s^0 mass. No significant improvement is observed.

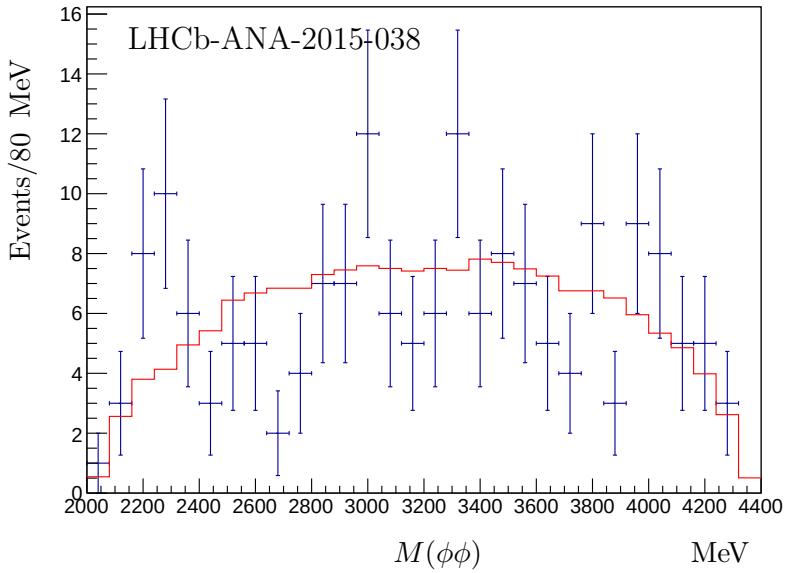

Figure 9.10: Invariant mass distribution of the $\phi\phi$ pair from the $B_s^0 \to \phi\phi\phi$ candidates for combined data sample accumulated at $\sqrt{s} = 7\,\text{TeV}$ and $\sqrt{s} = 8\,\text{TeV}$, using a constraint to the B_s^0 mass. A phase space distribution as obtained from simulation (red histogram) is overlaid.

As another cross-check, a symmetrized Dalitz plot is constructed following Ref. [317] for the B_s^0 signal region (Fig. 9.11, left) and sidebands ($4.925-5.325\,\text{GeV}$ and $5.415-5.815\,\text{GeV}$, Fig. 9.11, right), using the $X = \sqrt{3}(T_1 - T_2)/Q$ and $Y = 3T_3/Q - 1$ axes, where $T_{1,2,3}$ are kinetic energies of ϕ mesons in the rest frame of B_s^0 and Q is the energy released in the $B_s^0 \to \phi\phi\phi$ decay. The B_s^0 candidates are constrained to the known B_s^0 mass. No evidence for resonant contributions is observed with the available statistics.

The polarization of the ϕ mesons is studied by means of the angle θ between the direction of flight of a ϕ meson in the B_s^0 rest frame and the B_s^0 direction in the laboratory frame. Figure 9.12 compares the $\cos(\theta)$ distribution for the $B_s^0 \to \phi\phi\phi$ signal candidates in data with expectations from simulation using different assumptions for the polarization. The purely longitudinal polarization clearly does not describe the data. The difference between the expectations for no polarization and purely transverse polarization is used to estimate the corresponding systematic uncertainty in the $\mathcal{B}(B_s^0 \to \phi\phi\phi)$ measurement.

To quantify the fraction of transverse polarization, f_T, in the data, the probability density function (PDF) for f_T is shown in Fig. 9.13. The most probable value is $f_\text{T} = 0.86$. Assuming a uniform prior in the physically allowed range, a Bayesian lower limit of $f_\text{T} > 0.28$ at 95% CL is found.

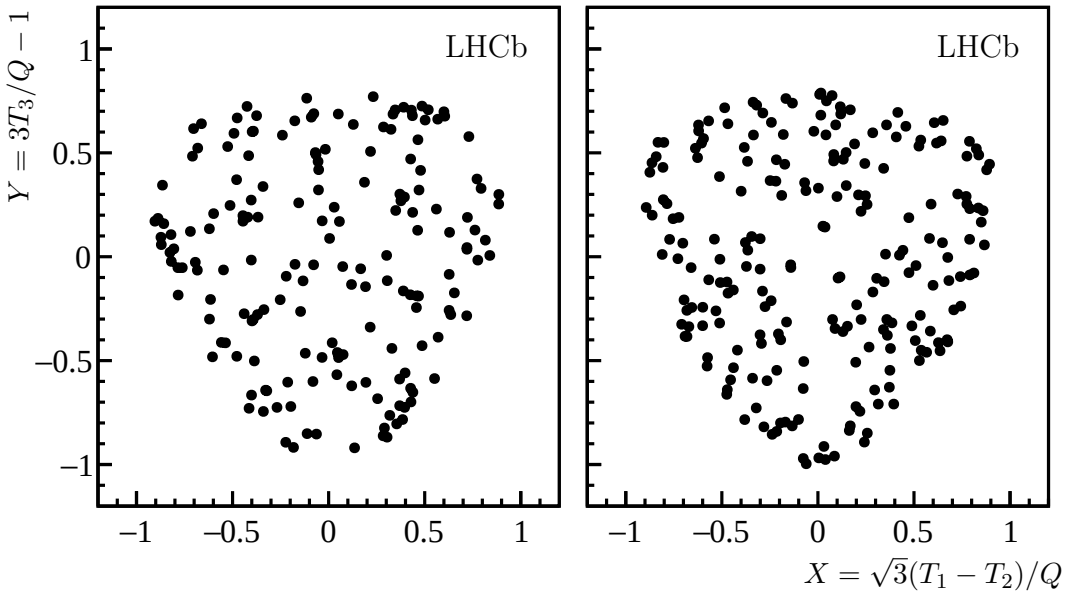

Figure 9.11: Symmetrized Dalitz plot [317] for (left) the B_s^0 signal and (right) the sideband regions. The B_s^0 candidates are constrained to the known B_s^0 mass.

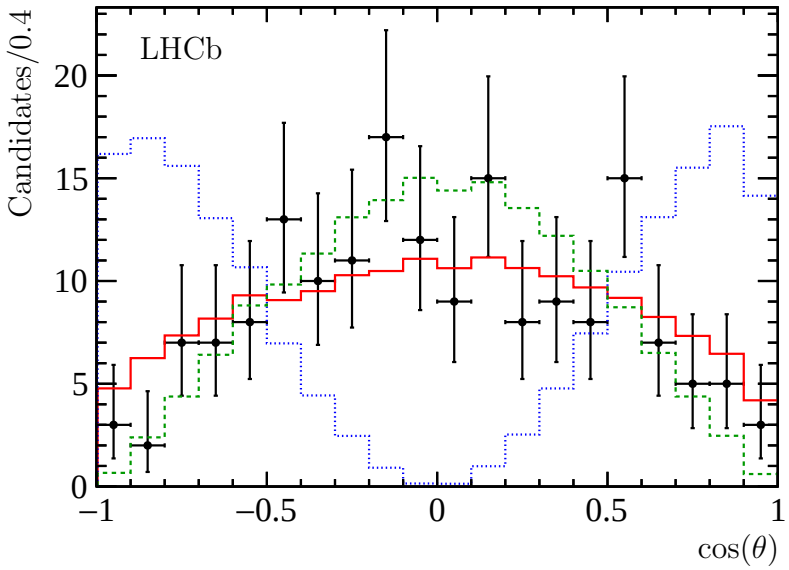

Figure 9.12: The ϕ meson angular distribution for the $B_s^0 \to \phi\phi\phi$ candidates (points with error bars) with the overlaid distribution from the simulation with no polarization (red solid histogram) and two extreme, transverse (green dashed histogram) and longitudinal (blue dotted histogram), polarizations.

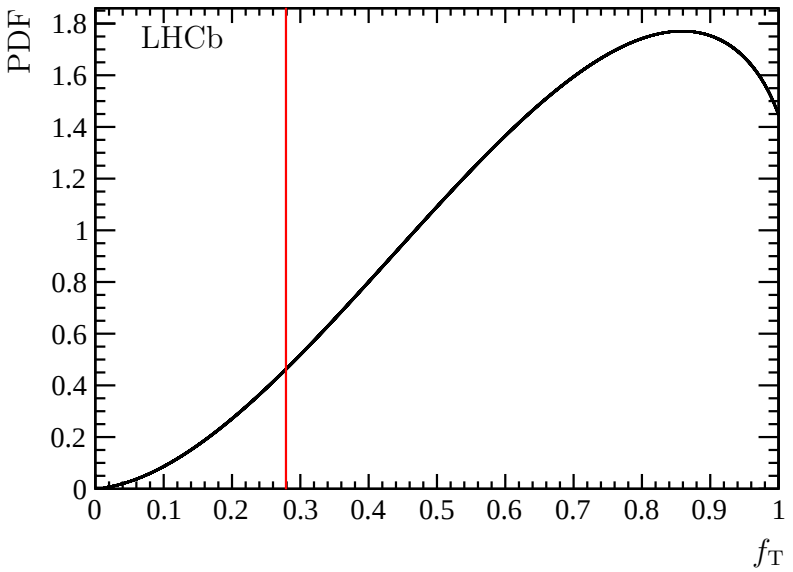

Figure 9.13: The PDF for the fraction of transverse ϕ meson polarization f_T for the $B_s^0 \to \phi\phi\phi$ candidates. The 95% Bayesian lower limit is shown by the red vertical line.

9.3 Summary and discussion

To validate the analysis technique, the $\mathcal{B}(B_s^0 \to \phi\phi)$ is first determined to be

$$\mathcal{B}(B_s^0 \to \phi\phi) = (2.18 \pm 0.17 \pm 0.11 \pm 0.14_{f_s} \pm 0.65_{\mathcal{B}}) \times 10^{-5}$$

and is measured with a different technique with respect to the previous results [305–307]. The result is consistent with the previous CDF and LHCb results and has a precision worse than that of the PDG value [73]. The result is also consistent with theoretical calculations [297, 298, 304]. The ratio of the branching fractions for the $\eta_c(1S)$ decays to $\phi\phi$ and to $p\overline{p}$ is determined as

$$\frac{\mathcal{B}(\eta_c(1S) \to \phi\phi)}{\mathcal{B}(\eta_c(1S) \to p\overline{p})} = 1.79 \pm 0.14 \pm 0.09 \pm 0.10_{f_s/f_d} \pm 0.03_{f_{\Lambda_b^0}} \pm 0.29_{\mathcal{B}},$$

which is larger than the world average value and indicates a problem in it.

The transition $B_s^0 \to \phi\phi\phi$ is observed for the first time with a significance about 4σ, and its branching fraction is measured to be

$$\mathcal{B}(B_s^0 \to \phi\phi\phi) = (2.15 \pm 0.54 \pm 0.28 \pm 0.21) \times 10^{-6}.$$

No clear resonant structure is observed in the $\phi\phi$ invariant mass distribution. Depending on how the $B_s^0 \to \phi\phi\phi$ transition proceeds, the above value becomes an upper limit on the penguin transition and pickup of the $s\overline{s}$ pair, with six strange quarks in the final state, and/or on the contribution of intermediate resonances such as the $B_s^0 \to \eta_c\phi$ mode. The result does not contradict to the LHCb measurement of the $\mathcal{B}(B_s^0 \to \eta_c\phi)$. Finally, transverse polarization of ϕ mesons from $B_s^0 \to \phi\phi\phi$ decays is favoured by LHCb data. The contribution from transversly polarised ϕ measons is found to be larger than $f_{\rm T} > 0.28$ at 95% CL.

Chapter 10

Summary and prospects

In summary, using an integrated luminosity of 2.0 fb^{-1} collected in 2015 and 2016, the prompt η_c production at $\sqrt{s} = 13$ TeV centre-of-mass energy is measured for the first time using the decay $\eta_c \to p\overline{p}$. The relative prompt production rates of the η_c and J/ψ states in the LHCb fiducial region ($2.0 < y < 4.5$, $6.5\,\text{GeV}/c < p_\text{T} < 14.0\,\text{GeV}/c$) are measured using *$t_z$-fit technique* and *separation technique* to distinguish prompt charmonium and charmonium produced in b-hadron decays. The measurement uncertainty is dominated by the statistical one, therefore it can be improved by using larger data sample. The obtained precision is better that the one of the measurement performed at $\sqrt{s}$ =7 and 8 TeV mainly due to larger production cross-section and hence reduced statistical uncertainty. Since the precision of the measurement is already better than the theoretical one, a new possible measurement of the η_c prompt production at $\sqrt{s}$ =13 TeV with a larger data sample will not further constrain the theory. However, the full Run II LHCb data sample can potentially allow a small extension of the p_T-range studied.

The additional high-p_T point of the differential production cross-section measurement can potentially separate more efficiently CS and CO contributions.

The branching fraction from b-hadron to η_c inclusive decays is measured. The precision of the measurement is limited by systematic uncertainty, which is dominated by that on $\mathcal{B}(\eta_c \to p\overline{p})$. Hence, further significant improvements on $\mathcal{B}(b \to \eta_c X)$ precision can come from measuring $\mathcal{B}(\eta_c \to p\overline{p})$ to a better precision at available or future charm factories. The results of this work confirm the first measurement of the branching fraction of inclusive b-decays to the η_c meson and provides the most precise measurement of $\mathcal{B}(b \to \eta_c X)$.

A phenomenological analysis shows that the measured value of $\mathcal{B}(b \to \eta_c X)/\mathcal{B}(b \to J/\psi\, X)/$ can be accomodated by available theoretical prediction [82]. A simultaneous fit to the η_c prompt production measurements using prediction from Ref. [128]; the J/ψ

prompt production cross-section measurement in limited p_{T}-range; the measurement of η_c production in b-decays [82]; and the measurement of η_c inclusive production in b-decays allows to reduce the parameter space of involved LDMEs, which provides a reasonable description of all observables. However, the latter is achieved by numerical cancelation of large CO contributions. This calls for new theoretical predictions and possibly new approaches. A good description of the η_c prompt production by k_{T}-factorization approach should be tested using other observables such as, for example, photoproduction and e^+e^- production cross-sections and J/ψ polarisation.

Production of other charmonium states in b-hadron inclusive decays is studied with an integrated luminosity of $3\,fb^{-1}$, using charmonia decays to $\phi\phi$ pairs. Inclusive production of all χ_c states in b-hadron inclusive decays are measured. The branching fraction $\mathcal{B}(b \to \chi_{c0}X)$ is measured for the first time. The result for b-decays into χ_{c1} is the most precise measurement for the mixture of B^0, B^+, B_s^0 and b-baryons. The branching fraction of b-hadron decays into χ_{c2} is measured for the first time with the B^0, B^+, B_s^0 and b-baryons mixture. The result is consistent with the world average of the B^0, B^+ mixture from Ref. [290]. The measurements can be further improved using a larger LHCb Run II data sample. The precision of the absolute inclusive branching fraction measurements is limited by the knowledge of the branching fractions of charmonium decays to $\phi\phi$. In this thesis it is demonstrated that the current world average value of the $\mathcal{B}(\eta_c \to \phi\phi)$ is rather not reliable and new measurements at charm factories are called for.

The shape of transverse momentum dependence of charmonia production in b-decays is studied for the $\eta_c(1S)$ and χ_c states in the LHCb acceptance and for $p_{\mathrm{T}} > 4\,\mathrm{GeV}/c$. A precision of about 15% for $\eta_c(1S)$ and between 20% and 30% for the χ_c states is achieved.
.

The first evidence of the $\eta_c(2S)$ production in inclusive b-decays and the first evindence of the $\eta_c(2S) \to \phi\phi$ are reported in this thesis. A measurement of $\mathcal{B}(b \to \eta_c(2S)X \times \mathcal{B}(\eta_c(2S) \to \phi\phi))$ has been performed. A larger data sample will improve the precision of the measurement. A future measurement of the $\mathcal{B}(\eta_c(2S) \to \phi\phi)$ is needed in order to extract $\mathcal{B}(b \to \eta_c(2S)X)$.

A limits on the productuct of inclusive branching fraction of b quark decays to $X(3872)$, $X(3915)$ and $\chi_{c2}(3930)$ and branching fractions of the corresponding decays to $\phi\phi$ are reported.

Using a sample of $b \to (c\bar{c} \to p\bar{p})X$ candidates, the J/ψ and η_c mass difference is measured. The obtained result, is consistent with the world average value and is the most precise single η_c mass measurement to date. This measurement is consistent to and is competing with the most precise individual measurements. Possibly, the entire LHCb

Run II data sample of $b \to (c\overline{c} \to p\overline{p})X$ candidates can provide results of η_c mass and natural width competing with the world average value. All obrained measurements of charmonium resonance parameters agree with the corresponding world averages.

A branching fraction of the $B_s^0 \to \phi\phi$ decay has been determined using $\eta_c \to \phi\phi$ as a reference. An evidence for the $B_s^0 \to \phi\phi\phi$ decay has been reported at the level of about four standard deviations together with a branching fraction measurement. The resonant structure of the decay including the $B_s^0 \to (\eta_c \to \phi\phi)\phi$ contribution is expected to be seen within the entire Run II data sample. This study is an important cross-check of the $\mathcal{B}(\eta_c \to \phi\phi)$ value.

Finally, I would like to outline the following wish list of experimental prospects at LHCb based on charmonium decays to hadrons. This list reflects my personal vision and preferences with no aim of being exhaustive. The main goal is to improve precision of charmonium production measurements, to access more charmonium states, and to search for further complementary measurements.

1. The natural extension of the work presented in this thesis is a measurement of **prompt** $\eta_c(2S)$ **production** using its decays to $p\overline{p}$ and $\phi\phi$. The corresponding trigger lines have been prepared in this work and included in the online trigger during the proton-proton collisions program of LHCb in 2018. The data sample corresponds to about $2.2\,\text{fb}^{-1}$ of integrated luminosity recorded at $\sqrt{s}$ =13 TeV.

   According to preliminary studies, the expected upper limit on the $\eta_c(2S)$ production using the $p\overline{p}$ decay channel is smaller than the CO contributions projected from $\psi(2S)$ production measurements. If the $\eta_c(2S)$ production is saturated by the CS contribution (as for the η_c prompt production) the amount of data would be however not sufficient to perform a measurement. Only an upper limit could be set. In this case, the upper limit would anyway test of the available predictions. Moreover, this upper limit should be used in the simultaneous description of $\psi(2S)$ prompt production cross-section and polarisation.

   Projections for the $\phi\phi$ final states are more difficult, since it is the first data sample of prompt $\phi\phi$ decays at LHCb and the backround properties are not studied yet. While the branching fraction of the $\eta_c(2S) \to p\overline{p}$ can be extracted using available experimental inputs, there is no experimental information on the $\mathcal{B}(\eta_c(2S) \to \phi\phi)$. That is why this branching fraction can be extracted from theory only. Potentially, signals from χ_c states can be seen in the prompt invariant mass spectrum as well. Especially, a measurement of χ_{c0} prompt production would be extremely important since it has not been measured yet.

The analysis of the $\eta_c(2S)$ production using both decay channels has been started. However, no judgements can be done before the corresponding simulation samples will be produced.

2. Probes of prompt charmonium production using **other hadronic decays with available Run II (and Run I) data**. Most of prompt charmonium studies require a dedicated trigger operating during the data taking. Final states including long-lived particles can be triggered using universal LHCb trigger lines requiring a presence of track(s) displaced from PV. However, a common problem of such decays is that the signal efficiency is reduced due to, particularly, the absence of downstream track reconstruction at the HLT1 trigger level. Nevertheless, I suggest the two following final states.

   - **The $K^0_S K\pi$ final state**. The advantage is that the typical branching fraction of charmonium decays to $K^0_S K\pi$ is at least an order of magnitude larger than the branching fractions of decays to $p\overline{p}$ and $\phi\phi$. On the other hand, a high level of combinatorial background is expected since most of the hadrons created at PV are pions. Besides, four tracks have to be reconstructed. The $K^0_S K\pi$ decay channel is promising for the η_c mass and width measurement, since a sample $c\bar{c} \to K^0_S K\pi$ of exclusive b-decays can potentially provide the cleanest η_c signal at LHCb. This work has been started at LHCb. The preselection for charmonium decays to $K^0_S K\pi$ has been written and the entire LHCb data set for this analysis will be available by the end of 2019.
   - **The $\Lambda\bar{\Lambda}$ final state**. This final state requires a reconstruction of two long-lived baryons and therefore the efficiency will be even smaller than for the decay to $K^0_S K\pi$ channel. Another disadvantage is that the branching fractions are much smaller than the ones of decays to $K^0_S K\pi$. Since the mass of the Λ baryon is close to the $p\pi$ threshold, this decay channel can be compared to $\phi\phi$. A larger production rate of $\Lambda\bar{\Lambda}$ combinations can be naively expected compared to that of $\phi\phi$. A random $\phi\phi$ combination at PV is more rarely produced because it requires a creation of four s-quarks in PV compared to only two s quarks for $\Lambda\bar{\Lambda}$. On the other hand, the selection can benefit from variables describing Λ lifetime or its vertex displacement from PV. Therefore charmonium decays to $\Lambda\bar{\Lambda}$ are rather less promising than to $K^0_S K\pi$. The preselection of charmonium decays to $\Lambda\bar{\Lambda}$ have been prepared and the entire LHCb data for the analysis set will be available by the end of 2019.

3. **The η_b production**. I would like to particularly stress this item. All other items in the list appeared to be within experimental possibilities and expectations, while the η_b production provides crucial observables for NRQCD and is an essential extension of this work. The measurement can provide an answer, whether the simultaneous description of S-wave bottomonium states production has the same complications as the ones observed for charmonium. It can also shed the light in the CO and CS interplay in bottomonium production.

   This task is challenging due to a poor knowledge of the η_b meson. No exclusive η_b decay branching fraction has been measured yet. The studies of η_b will also require a dedicated trigger line in future. Compared to charmonium case, the combinatorial background level in the bottomonium mass region is much reduced. Hence, a smaller bandwdith will be required to reconstruct η_b using the same decay channel. I would suggest to develop additional trigger lines for the η_b decays to two and four stable hadrons and to $K^0_S K\pi$. A trigger line for bottomonium decays to K^*K^* was active during the LHCb Run II, but because of four tracks reconstruction its efficiency is small.

4. **The h_c study** at LHCb. The h_c meson has not been seen at LHCb yet. The study of prompt h_c production is well motivated by theory since it provides a new obervable, which has never been measured at hadron machines. The same apply for production in b-hadron decays

   - The first promising channel to access $h_c \to K^0_S K\pi$ discussed above. The data is already available and the analysis has been started.
   - Alternatively, the h_c can be resonstructed using decays to $\eta_c\gamma$ and $\eta_c\mu^+\mu^-$ final states. This, however, requires a reconstruction of the η_c state. The trigger line aiming at prompt $\eta_c\mu^+\mu^-$ selection was operational during the data taking in 2018.
   - Following the observation of the h_c decay to $p\overline{p}\pi^+\pi^-$, this decay channel can be used to access h_c produced in b-hadron decays.

5. **Central exclusive production** (CEP) of η_c. This topic requires a relatively easy analysis, The observation of the η_c produced in CEP will be directly interpreted as the odderon discovery. Different decay channels can be considered, while the data is available only for the $p\overline{p}$ final state.

6. Similarly, studies of the η_c **production in ion-ion collisions** can be studied. In this

case, dedicated trigger lines are not needed since the LHCb stores all information from ion-ion collisions. On the other hand, relatively low luminosity limits the measurement.

7. **Other hadronic decays of charmonium** to study charmonium from b-decays. Among possible final states I would highlight $\Lambda\Lambda(1\bar{5}20)$ and $\Lambda(1520)\bar{\Lambda}$. The studies of these decays can yield their branching fraction measurements with the data already available.

8. Studies involving η_c reconstruction. This subject is not related to charmonium production but the experience on η_c production measurements can be transferred to other studies involving η_c meson in the final state.

   - Study of **semileptonic decays $B_c^+ \to \eta_c \mu\nu$ and possibly $B_c^+ \to \eta_c \tau\nu$**. This subject is interesting for future lepton universality measurement of the ratio $\mathcal{B}(B_c^+ \to \eta_c \tau\nu)/\mathcal{B}(B_c^+ \to \eta_c \mu\nu)$. The $\eta_c \to p\overline{p}$ and $\eta_c \to K^0_S K\pi$ decay channels can be used. Due to a small lifetime of B_c^+ meson, the universal b-hadron trigger lines are not optimal. Therefore, a dedicated trigger line should be developed in future. Nevertheless, the situation is not that much extreme as for prompt charmonium case, so that the studies have been started with already available data. The corresponding preselection has been prepared and the entire LHCb data set will be available by the end of 2019.
   - Another example of non-production measurements is **a search for hadron exotic candidates decaying to the η_c meson**. One of such studies has been already performed, finding evidence of $Z(4010) \to \eta_c \pi$. Similar studies can be performed for other decay channels involving η_c, to (in)validate charmonium-like states previously observed via decays to J/ψ and $\psi(2S)$.

Main thesis results

Main results obtained in the thesis are listed below.

1. LHCb operation
    - **Trigger development** for prompt charmonium decays to $p\overline{p}$ and $\phi\phi$ final states
    - **Preparation of data sets** (stripping) for charmonium produced in b-hadron decays using a list of charmonium decays to hadrons
2. Physics analysis
    - First measurement of **prompt η_c production at $\sqrt{s}$ =13 TeV**
    - First or most precise measurements of **production of η_c, χ_{c0}, χ_{c1}, χ_{c2} and $\eta_c(2S)$ in b-hadron inclusive decays**
    - Search for $X(3872)$, $X(3915)$, $\chi_{c2}(2P)$ production in b-hadron inclusive decays
    - Measurement of the **η_c resonance parameters**
    - Measurement of the branching fraction of the $\eta_c \to \phi\phi$ decay
    - Measurement of the branching fraction of the $B_s^0 \to \phi\phi$ decay
    - First evidence of the $\mathbf{B_s^0 \to \phi\phi\phi}$ decay
3. Phenomenological analysis
    - Proposal of a **new technique of simultaneous fit to long-distance matrix elements**
    - Simultaneous study of the η_c and J/ψ prompt production and production in b-hadron inclusive decays
    - Simultaneous study of χ_{cJ} states production in b-hadron inclusive decays

List of measurements

A list of the most important measurements performed in this thesis is summarized below.

η_c prompt production at $\sqrt{s}$ =13 TeV

Integral prompt production cross-section, relative and absolute measurements:

$$(\sigma_{\eta_c}/\sigma_{J/\psi})^{6.5\,\mathrm{GeV}/c<p_T<14.0\,\mathrm{GeV}/c,2.0<y<4.5}_{13\,\mathrm{TeV}} = 1.88 \pm 0.16_{stat} \pm 0.14_{syst} \pm 0.21_{norm},$$

$$(\sigma_{\eta_c})^{6.5\,\mathrm{GeV}/c<p_T<14.0\,\mathrm{GeV}/c,2.0<y<4.5}_{13\,\mathrm{TeV}} = (1.41 \pm 0.12_{stat} \pm 0.10_{syst} \pm 0.16_{norm})\,\mu\mathrm{b}.$$

p_{T}-differential prompt production cross-section, relative and absolute measurements:

p_{T}, GeV	$d\sigma^{prompt}_{\eta_c}/d\sigma^{prompt}_{J/\psi}$
6.5 - 8.0	1.68 ± 0.33 ± 0.06 ± 0.11 ± 0.21
8.0 - 10.0	2.01 ± 0.28 ± 0.09 ± 0.13 ± 0.25
10.0 - 12.0	2.27 ± 0.36 ± 0.13 ± 0.14 ± 0.28
12.0 - 14.0	3.30 ± 0.62 ± 0.22 ± 0.21 ± 0.41

Table 10.1: The relative p_{T}-differential η_c prompt production.

p_{T}, GeV	$d\sigma^{prompt}_{\eta_c}/dp_{\mathrm{T}}$, nb/ GeV
6.5 - 8.0	536.09 ± 105.04 ± 19.61 ± 34.19 ± 70.67
8.0 - 10.0	180.92 ± 24.81 ± 7.90 ± 11.35 ± 24.97
10.0 - 12.0	73.92 ± 11.57 ± 4.07 ± 4.60 ± 10.32
12.0 - 14.0	42.12 ± 7.95 ± 2.83 ± 2.62 ± 6.01

Table 10.2: The p_{T}-differential η_c prompt production.

η_c production in b-hadron inclusive decays

Absolute branching fraction:

$$\mathcal{B}_{b\to\eta_c(1S)X}/\mathcal{B}_{b\to J/\psi X} = 0.48 \pm 0.03_{stat} \pm 0.03_{syst} \pm 0.05_{norm},$$
$$\mathcal{B}_{b\to\eta_c(1S)X} = (5.51 \pm 0.32_{stat} \pm 0.29_{syst} \pm 0.77_{norm}) \times 10^{-3}.$$

p_{T}-differential production cross-section in b-hadron inclusive decays, relative and absolute measurements:

p_{T}, GeV	$d\sigma_{\eta_c}^{b-decays}/d\sigma_{J/\psi}^{b-decays}$
6.5 - 8.0	0.41 ± 0.06 ± 0.01 ± 0.02 ± 0.05
8.0 - 10.0	0.61 ± 0.05 ± 0.03 ± 0.03 ± 0.08
10.0 - 12.0	0.45 ± 0.06 ± 0.02 ± 0.02 ± 0.06
12.0 - 14.0	0.54 ± 0.07 ± 0.03 ± 0.02 ± 0.07

Table 10.3: The relative p_{T}-differential η_c production in inclusive b-decays.

p_{T}, GeV	$d\sigma_{\eta_c}^{b-decays}/dp_{\mathrm{T}}$, nb/ GeV
6.5 - 8.0	27.16± 4.23± 0.99± 1.34± 3.74
8.0 - 10.0	18.82± 1.52± 0.81± 0.91± 2.61
10.0 - 12.0	6.56± 0.84± 0.34± 0.32± 0.93
12.0 - 14.0	3.79± 0.51± 0.23± 0.18± 0.55

Table 10.4: The p_{T}-differential η_c production cross-section in inclusive b-decays

First or most precise measurements of χ_{cJ} production in b-hadron inclusive decays

Double ratio measurements:

$$\frac{\mathcal{B}(b \to \chi_{c0}X) \times \mathcal{B}(\chi_{c0} \to \phi\phi)}{\mathcal{B}(b \to \eta_c X) \times \mathcal{B}(\eta_c \to \phi\phi)} = 0.147 \pm 0.023 \pm 0.011 \ ,$$
$$\frac{\mathcal{B}(b \to \chi_{c1}X) \times \mathcal{B}(\chi_{c1} \to \phi\phi)}{\mathcal{B}(b \to \eta_c X) \times \mathcal{B}(\eta_c \to \phi\phi)} = 0.073 \pm 0.016 \pm 0.006 \ ,$$
$$\frac{\mathcal{B}(b \to \chi_{c2}X) \times \mathcal{B}(\chi_{c2} \to \phi\phi)}{\mathcal{B}(b \to \eta_c X) \times \mathcal{B}(\eta_c \to \phi\phi)} = 0.081 \pm 0.013 \pm 0.005 \ .$$

Single ratio measurements:

$$\frac{\mathcal{B}(b \to \chi_{c0}X)}{\mathcal{B}(b \to \eta_c X)} = 0.615 \pm 0.095 \pm 0.047 \pm 0.149 \ ,$$
$$\frac{\mathcal{B}(b \to \chi_{c1}X)}{\mathcal{B}(b \to \eta_c X)} = 0.562 \pm 0.119 \pm 0.047 \pm 0.131 \ ,$$
$$\frac{\mathcal{B}(b \to \chi_{c2}X)}{\mathcal{B}(b \to \eta_c X)} = 0.234 \pm 0.038 \pm 0.015 \pm 0.057 \ .$$

Absolute branching fractions:

$$\mathcal{B}(b \to \chi_{c0}X) = (3.02 \pm 0.47 \pm 0.23 \pm 0.94) \times 10^{-3} \ ,$$
$$\mathcal{B}(b \to \chi_{c1}X) = (2.76 \pm 0.59 \pm 0.23 \pm 0.89) \times 10^{-3} \ ,$$
$$\mathcal{B}(b \to \chi_{c2}X) = (1.15 \pm 0.20 \pm 0.07 \pm 0.36) \times 10^{-3} \ .$$

First measurement of $\eta_c(2S)$ production in b-hadron inclusive decays

Double ratio measurement:

$$\frac{\mathcal{B}(b \to \eta_c(2S)X) \times \mathcal{B}(\eta_c(2S) \to \phi\phi)}{\mathcal{B}(b \to \eta_c(1S)X) \times \mathcal{B}(\eta_c(1S) \to \phi\phi)} = 0.040 \pm 0.011 \pm 0.004.$$

Product of branching fractions:

$$\mathcal{B}(b \to \eta_c(2S)X) \times \mathcal{B}(\eta_c(2S) \to \phi\phi) = (6.34 \pm 1.81 \pm 0.57 \pm 1.89) \times 10^{-7}.$$

Search for $X(3872)$, $X(3915)$, $\chi_{c2}(2P)$ production in b-hadron inclusive decays
Upper limits on double ratios:

$$\frac{\mathcal{B}(b \to X(3872)X) \times \mathcal{B}(X(3872) \to \phi\phi)}{\mathcal{B}(b \to \chi_{c1}X) \times \mathcal{B}(\chi_{c1} \to \phi\phi)} < 0.39(0.34),$$
$$\frac{\mathcal{B}(b \to X(3915)X) \times \mathcal{B}(X(3915) \to \phi\phi)}{\mathcal{B}(b \to \chi_{c0}X) \times \mathcal{B}(\chi_{c0} \to \phi\phi)} < 0.14(0.12),$$
$$\frac{\mathcal{B}(b \to \chi_{c2}(3930)X) \times \mathcal{B}(\chi_{c2}(3930) \to \phi\phi)}{\mathcal{B}(b \to \chi_{c2}X) \times \mathcal{B}(\chi_{c2} \to \phi\phi)} < 0.20(0.16).$$

Upper limits on product of branching fractions:

$$\mathcal{B}(b \to X(3872)X) \times \mathcal{B}(X(3872) \to \phi\phi) < 4.5(3.9) \times 10^{-7},$$
$$\mathcal{B}(b \to X(3915)X) \times \mathcal{B}(X(3915) \to \phi\phi) < 3.1(2.7) \times 10^{-7},$$
$$\mathcal{B}(b \to \chi_{c2}(3930)X) \times \mathcal{B}(\chi_{c2}(3930) \to \phi\phi) < 2.8(2.3) \times 10^{-7}.$$

Measurement of charmonia masses and natural width

	using $c\overline{c} \to p\overline{p}$	using $c\overline{c} \to \phi\phi$
$M_{\eta_c(1S)}$	$2983.91 \pm 0.77 \pm 0.11$	$2982.81 \pm 0.99 \pm 0.45$
$M_{\chi_{c0}}$		$3412.99 \pm 1.91 \pm 0.62$
$M_{\chi_{c1}}$		$3508.38 \pm 1.91 \pm 0.66$
$M_{\chi_{c2}}$		$3557.29 \pm 1.71 \pm 0.66$
$M_{\eta_c(2S)}$		$3636.35 \pm 4.06 \pm 0.69$
$\Gamma_{\eta_c(1S)}$		$31.35 \pm 3.51 \pm 2.01$

Table 10.5: Charmonia masses (in MeV) and natural width (in MeV).

Measurement of the branching fraction $\mathcal{B}(\eta_c \to \phi\phi)$
Ratio of branching fractions:

$$\frac{\mathcal{B}(\eta_c(1S) \to \phi\phi)}{\mathcal{B}(\eta_c(1S) \to p\overline{p})} = 1.79 \pm 0.14 \pm 0.09 \pm 0.10_{f_s/f_d} \pm 0.03_{f_{\Lambda_b^0}} \pm 0.29_{\mathcal{B}}.$$

Measurements of branching fractions for B_s^0 decays to $\phi\phi$ and $\phi\phi\phi$
Branching fraction of $B_s^0 \to \phi\phi$ decay:

$$\mathcal{B}(B_s^0 \to \phi\phi) = (2.18 \pm 0.17 \pm 0.11 \pm 0.14_{f_s} \pm 0.65_{\mathcal{B}}) \times 10^{-5},$$

$B_s^0 \to \phi\phi\phi$, ratio of branching fractions:

$$\frac{\mathcal{B}(B_s^0 \to \phi\phi\phi)}{\mathcal{B}(B_s^0 \to \phi\phi)} = 0.117 \pm 0.030 \pm 0.015 \ ,$$

$B_s^0 \to \phi\phi\phi$, absolute branching fraction:

$$\mathcal{B}(B_s^0 \to \phi\phi\phi) = (2.15 \pm 0.54 \pm 0.28 \pm 0.21) \times 10^{-6}.$$

Acknowledgements

I want to thank my supervisor Sergey Barsuk, for all his help, support, guidings, useful advices and suggestions during the whole period of my work. Also, I found very important his help with my integration into the life of the LHCb collaboration. I appreciate that I had much freedom to do research and to push it forward.

I would also thank Jean-Philippe Lansberg, Hua-Sheng Shao and Emi Kou for beneficial discussions on the theory of charmonium production.

I would also like to express my great appreciation to my colleagues from LHCb group of LAL - Patrick, Jibo, Jacques, Marie-Héléne, Frédéric, Guy, Michael, Yanxi, Francesco, Laure, Vladik, Vitalii, Fabrice, Renato, Victor, Joao, Carla, Elizabeth and Davide. I was pleased to work with you, and I will be happy to continue collaborating with you at LHCb!

I would thank students I had a great pleasure to work with - Valeriia, Taras and Pavlo. I have no doubts that you will become great physicists!

I can't omit my thanks to my school teacher of physics, Yury Pasikhov, and my university teacher, Oleg Bezshyiko. Without your inspiration, I wouldn't start my research in physics.

I thank my friends Denys, Rita, Nefedka, Kolya, Iaroslava, Nastya, Andrii, Igor, Salama, Edoardo, Yacine and Alenka for the time we spent together and for all discussions we had.

Finally, I thank my incredible wife Olga and my family for their strong support.

Synthèse en français

Les études de production de charmonium fournissent les tests rigoureux de modèles théoriques basés sur chromodynamique quantique (QCD) non-relativiste. A ce jour les modèles sont confrontés principalement aux mesures expérimentales des etats $J^{PC} = 1^{--}$ de charmonium, comme les mésons J/ψ et $\psi(2S)$, qui désintègrent à une paire de muons. De plus, les états χ_{c1} et χ_{c2} sont reconstruits via leurs transitions radiatives en J/ψ, ce qui nécessite cependant une reconstruction de photons des basses énergies. La reconstruction des désintégrations vers les hadrons permet de réaliser les études de production pour tous les états connus du charmonium. En utilisant les états finaux $p\overline{p}$ et $\phi\phi$ j'ai étudié la production des états $\eta_c(1S)$, $\eta_c(2S)$ et χ_{cJ} de charmonium avec l'expérience LHCb.

En utilisant les données LHCb prises en 2015 et 2016 à l'énergie du centre de masse $\sqrt{s} = 13$ TeV, qui correspondent à une luminosité intégrée de 2.0 fb^{-1}, la section efficace de la production prompte du méson η_c est mesurée pour la première fois avec la désintégration $\eta_c \to p\overline{p}$. Les taux de production relatifs des mésons η_c et J/ψ dans la région fiduciale de LHCb ($2.0 < y < 4.5, 6.5\,\text{GeV}/c < p_{\text{T}} < 14.0\,\text{GeV}/c$) sont mesurés à l'aide de techniques t_z-*fit technique* et *separation technique* pour distinguer le charmonium produit dans le vertex de collision proton-proton et le charmonium produit dans les désintégrations des hadrons b. Étant dominée par la statistique, l'incertitude de mesure sera améliorée en utilisant un plus grand échantillon de données. La précision obtenue est meilleure que celle de la mesure effectuée à $\sqrt{s} = 7$ et 8 TeV principalement en raison d'une section efficace de production plus élevée. Puisque la précision de la mesure est déjà meilleure que la

prédiction théorique, une nouvelle mesure basée sur un plus grand échantillon de données ne contraindra plus la théorie. Toutefois, l'échantillon complet de données Run II LHCb potentiellement permettra une extension de la plage p_{T} étudiée. Les mesures de la section efficace de la production différentielle dans la région du p_{T} élargie permettront de séparer plus efficacement les contributions des éléments de matrice color-singlet et color-octet.

Je mesure le rapport d'embranchement de la désintégration inclusive des hadrons b vers l'état η_c. La précision de la mesure est limitée par l'incertitude systématique, dominée par celle de $\mathcal{B}(\eta_c \to p\overline{p})$. Par conséquent, les futures améliorations sur la précision de $\mathcal{B}(b \to \eta_c X)$ demandent la mesure plus précise de $\mathcal{B}(\eta_c \to p\overline{p})$, ce qui est attendu dans les usines du charme existantes ou futures. Un des résultat important de cette thèse porte sur la mesure la plus précise du rapport d'embranchement pour les désintégrations des hadrons b vers le méson η_c, $\mathcal{B}(b \to \eta_c X)$.

La production d'autres états du charmonium dans les désintégrations inclusives des hadrons b est étudiée avec une luminosité intégrée de 3 fb^{-1}, en utilisant les désintégrations de charmonia vers les paires de mésons ϕ, $\phi\phi$. L'analyse de la production de charmonium à l'aide de désintégrations de charmonium en $\phi\phi$ nécessite la soustraction de la contribution du fond de kaons non résonants. Pour cela, j'ai proposé une technique permettant de sélectionner des états finaux avec deux ou trois mésons ϕ libres du fond combinatoire de kaons.

Avec cette nouvelle technique, la production de tous les états χ_c dans les désintégrations inclusives des hadrons b est mesurée. Le rapport d'embranchement $\mathcal{B}(b \to \chi_{c0} X)$ est mesuré pour la première fois. Le résultat pour la production du méson χ_{c1} est la mesure la plus précise pour les échantillons des hadrons b avec le mélange de B^0, B^+, B_s^0 et baryons avec le quark b. Le rapport d'embranchement de la désintégration des hadrons b en χ_{c2} est mesurée pour la première fois pour les échantillons des hadrons b avec le mélange de B^0, B^+, B_s^0 et baryons avec le quark b. Le résultat est en accord avec la moyenne mondiale du rapport d'embranchement pour les échantillons de mésons B^0 et B^+ uniquement. Les

mesures peuvent être encore améliorées en utilisant toutes les données LHCb acquis en Run II. La précision des mesures des rapports d'embranchement inclusives est limitée par la connaissance des rapports d'embranchement de désintégrations du charmonium vers $\phi\phi$. Dans cette thèse, il est démontré que la valeur moyenne mondiale actuelle du $\mathcal{B}(\eta_c \to \phi\phi)$ n'est pas fiable et que des nouvelles mesures dans les usines du charme sont nécessaires. Je mesure le rapport d'embranchement de la désintégration $\eta_c(1S) \to \phi\phi$ pour résoudre une tension avec d'autres mesures existantes.

La dépendance de la production de charmonia issus des hadrons b en impulsion transverse p_{T} est étudiée pour les états $\eta_c(1S)$ et χ_c pour les désintégrations où les kaons finaux traversent le détecteur LHCb et pour $p_{\mathrm{T}} > 4\,\mathrm{GeV}/c$. Une précision d'environ 15% pour le méson $\eta_c(1S)$ et entre 20% et 30% pour les états χ_c sont atteints.

Les études de l'état $\eta_c(2S)$ dans la thèse ont fourni également des nouvelles mesures. LHCb a mesuré l'état $\eta_c(2S)$ dans les désintégrations des hadrons b pour la première fois. Et c'est aussi pour la première fois que LHCb a vu la désintégration $\eta_c(2S) \to \phi\phi$. Le rapport d'embranchement $\mathcal{B}(b \to \eta_c(2S)X \times \mathcal{B}(\eta_c(2S) \to \phi\phi))$ a été mesuré. Un plus grand échantillon de données améliorera la précision de la mesure. Une mesure de $\mathcal{B}(\eta_c(2S) \to \phi\phi)$ est nécessaire pour l'extraction de $\mathcal{B}(b \to \eta_c(2S)X)$.

En outre, une recherche de la production d'autres états de type charmonium dans les désintégrations avec b-hadrons est effectuée. Les états de charmonium avec des nombres quantiques similaires sont utilisés pour normalisation.

Les produits du rapport d'embranchement de la production inclusive des états $X(3872)$, $X(3915)$ et $\chi_{c2}(3930)$ dans les désintégrations des hadron b et le rapport d'embranchement des transitions de ces états vers $\phi\phi$ sont étudiés. Aucun signal est observé et la limite est obtenue pour la production de chaque état étudié.

Afin de comparer les résultats obtenus aux calculs théoriques, j'ai proposé d'utiliser un ajustement simultané les mesures de la production des états de charmonium et les éléments de matrice longue distance, les deux pour la production hadronique de charmonium et la

production dans les désintégrations inclusives des hadrons b. Cela permet de restreindre fortement l'espace de phase autorisé pour les éléments de la matrice décrivant la production de charmonium. Cela démontre également une limite d'application de la théorie et appelle à la poursuite du développement des modèles.

Une analyse phénoménologique montre que la valeur mesurée de $\mathcal{B}(b \to \eta_c X)/\mathcal{B}(b \to J/\psi X)$ peut être adaptée par les études théorique [82]. Une analyse simultanée de la hadroproduction de l'état η_c utilise la prédiction de Réf. [128] ; la mesure de la section efficace de hadroproduction de l'état J/ψ dans la plage p_{T} limitée ; la mesure de la production de η_c dans les désintégrations des hadrons b [82] ; et la mesure de la production inclusive de l'état η_c dans les désintégrations des hadrons b permettent de réduire l'espace de phase des LDME impliqués, ce qui fournit une description consistante de tous les observables. Toutefois, cette dernière est réalisée par l'annulation numérique de contributions importantes en CO. Cela motive des nouvelles prédictions théoriques et éventuellement de nouvelles approches. Une nouvelle description de la hadroproduction de l'état η_c par factorisation k_{T} doit être validée à l'aide d'autres observables, telles que, par exemple, les sections efficaces de la photoproduction et de la production de e^+e^-, et la polarisation de J/ψ.

En utilisant un échantillon de candidats $b \to (c\bar{c} \to p\bar{p})X$, la différence de masse entre les états J/ψ et η_c est mesurée. Le résultat obtenu est en accord avec la valeur moyenne mondiale. Cette mesure représente la détermination de la masse de l'état η_c la plus précise à ce jour. Cette mesure est aussi en accord avec des mesures individuelles les plus précises. Avec l'ensemble de données de Run II et la sélection de candidats $b \to (c\bar{c} \to p\bar{p})X$ LHCb améliorera la précision de mesure de la masse de l'état η_c et fournira la mesure de la largeur naturelle en concurrence avec la moyenne mondiale.

Enfin, les mésons B_s^0 sont reconstruits via les désintégrations en deux ou trois mésons ϕ. Cela permet d'effectuer une mesure indépendante de $\mathcal{B}(B_s^0 \to \phi\phi)$. En plus, l'évidence de la désintégration $B_s^0 \to \phi\phi\phi$ est obtenue pour la première fois. Une structure résonance

de la désintégration $B_s^0 \to \phi\phi\phi$ ainsi que la polarisation du méson ϕ sont également étudiés dans la thèse.

Le rapport d'embranchement de la désintégration $B_s^0 \to \phi\phi$ est déterminé en utilisant la mode $\eta_c \to \phi\phi$ comme une référence. L'évidence de la désintégration $B_s^0 \to \phi\phi\phi$ est obtenue au niveau d'environ quatre déviations standards avec la mesure d'un rapport d'embranchement. Les études détaillées de la structure résonance de la désintégration, y compris la contribution $B_s^0 \to (\eta_c \to \phi\phi)\phi$ deviendra possible avec l'ensemble de données de Run II.

La thèse porte principalement sur les études de la production des états de charmonium, η_c (1S), η_c (2S), χ_{c0}, χ_{c1}, χ_{c2}. Les études visent la vérification expérimentale des modèles basée sur la QCD non-relativiste. Production des états de charmonium dans le vertex de collision des faisceaux des proton sur LHC ainsi que la production des états de charmonium issus des hadron b sont étudiés. Les résultats présentés dans la thèse sont les premières mesures ou les mesures les plus précises à ce jour. En plus une nouvelle technique a été développée, qui permet de contraindre les valeurs des éléments de matrice longue distance de QCD non-relativiste. Les paramètres des états étudiés, la masse et la largeur naturelle, sont aussi déterminés. Finalement le rapport d'embranchement de la désintégration $B_s \to \phi\phi\phi$ est mesuré pour la première fois.

Bibliography

[1] N. Brambilla et al. Heavy quarkonium: progress, puzzles, and opportunities. *Eur. Phys. J.*, C71:1534, 2011. arXiv:1010.5827, doi:10.1140/epjc/s10052-010-1534-9.

[2] Murray Gell-Mann. A Schematic Model of Baryons and Mesons. *Phys. Lett.*, 8:214–215, 1964. doi:10.1016/S0031-9163(64)92001-3.

[3] Richard P. Feynman. Very high-energy collisions of hadrons. *Phys. Rev. Lett.*, 23:1415–1417, 1969. [,494(1969)]. doi:10.1103/PhysRevLett.23.1415.

[4] J. D. Bjorken and Emmanuel A. Paschos. Inelastic Electron Proton and gamma Proton Scattering, and the Structure of the Nucleon. *Phys. Rev.*, 185:1975–1982, 1969. doi:10.1103/PhysRev.185.1975.

[5] Elliott D. Bloom et al. High-Energy Inelastic *ep* Scattering at 6-Degrees and 10-Degrees. *Phys. Rev. Lett.*, 23:930–934, 1969. doi:10.1103/PhysRevLett.23.930.

[6] O. W. Greenberg. Spin and Unitary Spin Independence in a Paraquark Model of Baryons and Mesons. *Phys. Rev. Lett.*, 13:598–602, 1964. doi:10.1103/PhysRevLett.13.598.

[7] J. J. Aubert et al. Experimental Observation of a Heavy Particle *J*. *Phys. Rev. Lett.*, 33:1404–1406, 1974. doi:10.1103/PhysRevLett.33.1404.

[8] J. E. Augustin et al. Discovery of a Narrow Resonance in e^+e^- Annihilation. *Phys. Rev. Lett.*, 33:1406–1408, 1974. [Adv. Exp. Phys.5,141(1976)]. doi:10.1103/PhysRevLett.33.1406.

[9] J. D. Bjorken and S. L. Glashow. Elementary Particles and SU(4). *Phys. Lett.*, 11:255–257, 1964. doi:10.1016/0031-9163(64)90433-0.

[10] S. L. Glashow, J. Iliopoulos, and L. Maiani. Weak Interactions with Lepton-Hadron Symmetry. *Phys. Rev.*, D2:1285–1292, 1970. doi:10.1103/PhysRevD.2.1285.

[11] David J. E. Callaway and Aneesur Rahman. The Microcanonical Ensemble: A New Formulation of Lattice Gauge Theory. *Phys. Rev. Lett.*, 49:613, 1982. doi:10.1103/PhysRevLett.49.613.

[12] F. Abe et al. J/ψ and $\psi(2S)$ production in $p\bar{p}$ collisions at $\sqrt{s} = 1.8$ TeV. *Phys. Rev. Lett.*, 79:572–577, 1997. doi:10.1103/PhysRevLett.79.572.

[13] R. Aaij et al. Measurement of the $\eta_c(1S)$ production cross-section in proton-proton collisions via the decay $\eta_c(1S) \to p\bar{p}$. *Eur. Phys. J.*, C75:311, 2015. arXiv:1409.3612, doi:10.1140/epjc/s10052-015-3502-x.

[14] Markus Peter. The Static potential in QCD: A Full two loop calculation. *Nucl. Phys.*, B501:471–494, 1997. arXiv:hep-ph/9702245, doi:10.1016/S0550-3213(97)00373-8.

[15] York Schroder. The Static potential in QCD to two loops. *Phys. Lett.*, B447:321–326, 1999. arXiv:hep-ph/9812205, doi:10.1016/S0370-2693(99)00010-6.

[16] E. Eichten, K. Gottfried, T. Kinoshita, K. D. Lane, and Tung-Mow Yan. The Interplay of Confinement and Decay in the Spectrum of Charmonium. *Phys. Rev. Lett.*, 36:500, 1976. doi:10.1103/PhysRevLett.36.500.

[17] E. Eichten, K. Gottfried, T. Kinoshita, K. D. Lane, and Tung-Mow Yan. Charmonium: The Model. *Phys. Rev.*, D17:3090, 1978. [Erratum: Phys. Rev.D21,313(1980)]. doi:10.1103/PhysRevD.17.3090,10.1103/physrevd.21.313.2.

[18] E. Eichten, K. Gottfried, T. Kinoshita, K. D. Lane, and Tung-Mow Yan. Charmonium: Comparison with Experiment. *Phys. Rev.*, D21:203, 1980. doi:10.1103/PhysRevD.21.203.

[19] Estia J. Eichten, Kenneth Lane, and Chris Quigg. Charmonium levels near threshold and the narrow state $X(3872) \to \pi^+\pi^- J/\psi$. *Phys. Rev.*, D69:094019, 2004. arXiv:hep-ph/0401210, doi:10.1103/PhysRevD.69.094019.

[20] M. B. Voloshin. Charmonium. *Prog. Part. Nucl. Phys.*, 61:455–511, 2008. arXiv:0711.4556, doi:10.1016/j.ppnp.2008.02.001.

[21] W. Buchmuller and S. H. H. Tye. Quarkonia and Quantum Chromodynamics. *Phys. Rev.*, D24:132, 1981. doi:10.1103/PhysRevD.24.132.

[22] A. Barchielli, E. Montaldi, and G. M. Prosperi. On a Systematic Derivation of the Quark - Anti-quark Potential. *Nucl. Phys.*, B296:625, 1988. [Erratum: Nucl. Phys.B303,752(1988)]. doi:10.1016/0550-3213(88)90036-3.

[23] Lowell S. Brown and William I. Weisberger. Remarks on the Static Potential in Quantum Chromodynamics. *Phys. Rev.*, D20:3239, 1979. doi:10.1103/PhysRevD.20.3239.

[24] Adam P. Szczepaniak and Eric S. Swanson. On the Dirac structure of confinement. *Phys. Rev.*, D55:3987–3993, 1997. arXiv:hep-ph/9611310, doi:10.1103/PhysRevD.55.3987.

[25] Kenneth G. Wilson. Confinement of Quarks. *Phys. Rev.*, D10:2445–2459, 1974. [,319(1974)]. doi:10.1103/PhysRevD.10.2445.

[26] Dieter Gromes. Spin Dependent Potentials in QCD and the Correct Long Range Spin Orbit Term. *Z. Phys.*, C26:401, 1984. doi:10.1007/BF01452566.

[27] Gunnar S. Bali. QCD forces and heavy quark bound states. *Phys. Rept.*, 343:1–136, 2001. arXiv:hep-ph/0001312, doi:10.1016/S0370-1573(00)00079-X.

[28] W. Lucha, F. F. Schoberl, and D. Gromes. Bound states of quarks. *Phys. Rept.*, 200:127–240, 1991. doi:10.1016/0370-1573(91)90001-3.

[29] Nora Brambilla, Antonio Pineda, Joan Soto, and Antonio Vairo. The QCD potential at O(1/m). *Phys. Rev.*, D63:014023, 2001. arXiv:hep-ph/0002250, doi:10.1103/PhysRevD.63.014023.

[30] W. E. Caswell and G. P. Lepage. Effective Lagrangians for Bound State Problems in QED, QCD, and Other Field Theories. *Phys. Lett.*, 167B:437–442, 1986. doi:10.1016/0370-2693(86)91297-9.

[31] Geoffrey T. Bodwin, Eric Braaten, and G. Peter Lepage. Rigorous QCD analysis of inclusive annihilation and production of heavy quarkonium. *Phys. Rev.*, D51:1125–1171, 1995. [Erratum: Phys. Rev.D55,5853(1997)]. arXiv:hep-ph/9407339, doi:10.1103/PhysRevD.55.5853,10.1103/PhysRevD.51.1125.

[32] A. Pineda and J. Soto. Effective field theory for ultrasoft momenta in NRQCD and NRQED. *Nucl. Phys. Proc. Suppl.*, 64:428–432, 1998. [,428(1997)]. arXiv:hep-ph/9707481, doi:10.1016/S0920-5632(97)01102-X.

[33] Nora Brambilla, Antonio Pineda, Joan Soto, and Antonio Vairo. Potential NRQCD: An Effective theory for heavy quarkonium. *Nucl. Phys.*, B566:275, 2000. arXiv:hep-ph/9907240, doi:10.1016/S0550-3213(99)00693-8.

[34] Sean Fleming and Thomas Mehen. Hadronic Decays of the X(3872) to χ_{cJ} in Effective Field Theory. *Phys. Rev.*, D78:094019, 2008. arXiv:0807.2674, doi:10.1103/PhysRevD.78.094019.

[35] S. Fleming, M. Kusunoki, T. Mehen, and U. van Kolck. Pion interactions in the $X(3872)$. *Phys. Rev.*, D76:034006, 2007. arXiv:hep-ph/0703168, doi:10.1103/PhysRevD.76.034006.

[36] Eric Braaten and Meng Lu. Line shapes of the X(3872). *Phys. Rev.*, D76:094028, 2007. arXiv:0709.2697, doi:10.1103/PhysRevD.76.094028.

[37] John C. Collins, Davison E. Soper, and George F. Sterman. Factorization of Hard Processes in QCD. *Adv. Ser. Direct. High Energy Phys.*, 5:1–91, 1989. arXiv:hep-ph/0409313, doi:10.1142/9789814503266_0001.

[38] Raymond Brock et al. Handbook of perturbative QCD: Version 1.0. *Rev. Mod. Phys.*, 67:157–248, 1995. doi:10.1103/RevModPhys.67.157.

[39] L. V. Gribov, E. M. Levin, and M. G. Ryskin. Semihard Processes in QCD. *Phys. Rept.*, 100:1–150, 1983. doi:10.1016/0370-1573(83)90022-4.

[40] S. Catani, M. Ciafaloni, and F. Hautmann. High-energy factorization and small x heavy flavor production. *Nucl. Phys.*, B366:135–188, 1991. doi:10.1016/0550-3213(91)90055-3.

[41] L. N. Lipatov. Gauge invariant effective action for high-energy processes in QCD. *Nucl. Phys.*, B452:369–400, 1995. arXiv:hep-ph/9502308, doi:10.1016/0550-3213(95)00390-E.

[42] E. A. Kuraev, L. N. Lipatov, and Victor S. Fadin. Multi - Reggeon Processes in the Yang-Mills Theory. *Sov. Phys. JETP*, 44:443–450, 1976. [Zh. Eksp. Teor. Fiz.71,840(1976)].

[43] I. I. Balitsky and L. N. Lipatov. The Pomeranchuk Singularity in Quantum Chromodynamics. *Sov. J. Nucl. Phys.*, 28:822–829, 1978. [Yad. Fiz.28,1597(1978)].

[44] John C. Collins and Davison E. Soper. Parton Distribution and Decay Functions. *Nucl. Phys.*, B194:445–492, 1982. doi:10.1016/0550-3213(82)90021-9.

[45] S. Mert Aybat and Ted C. Rogers. TMD Parton Distribution and Fragmentation Functions with QCD Evolution. *Phys. Rev.*, D83:114042, 2011. arXiv:1101.5057, doi:10.1103/PhysRevD.83.114042.

[46] Xiang-dong Ji, Jian-Ping Ma, and Feng Yuan. Transverse-momentum-dependent gluon distributions and semi-inclusive processes at hadron colliders. *JHEP*, 07:020, 2005. arXiv:hep-ph/0503015, doi:10.1088/1126-6708/2005/07/020.

[47] Harald Fritzsch. Producing Heavy Quark Flavors in Hadronic Collisions: A Test of Quantum Chromodynamics. *Phys. Lett.*, 67B:217–221, 1977. doi:10.1016/0370-2693(77)90108-3.

[48] F. Halzen. CVC for Gluons and Hadroproduction of Quark Flavors. *Phys. Lett.*, 69B:105–108, 1977. doi:10.1016/0370-2693(77)90144-7.

[49] M. Gluck, J. F. Owens, and E. Reya. Gluon Contribution to Hadronic J/ψ Production. *Phys. Rev.*, D17:2324, 1978. doi:10.1103/PhysRevD.17.2324.

[50] Gerhard A. Schuler and Ramona Vogt. Systematics of quarkonium production. *Phys. Lett.*, B387:181–186, 1996. arXiv:hep-ph/9606410, doi:10.1016/0370-2693(96)00999-9.

[51] Michelangelo L. Mangano, Paolo Nason, and Giovanni Ridolfi. Fixed target hadroproduction of heavy quarks. *Nucl. Phys.*, B405:507–535, 1993. doi:10.1016/0550-3213(93)90557-6.

[52] J. F. Amundson, Oscar J. P. Eboli, E. M. Gregores, and F. Halzen. Quantitative tests of color evaporation: Charmonium production. *Phys. Lett.*, B390:323–328, 1997. arXiv:hep-ph/9605295, doi:10.1016/S0370-2693(96)01417-7.

[53] Geoffrey T. Bodwin, Eric Braaten, and Jungil Lee. Comparison of the color-evaporation model and the NRQCD factorization approach in charmonium production. *Phys. Rev.*, D72:014004, 2005. arXiv:hep-ph/0504014, doi:10.1103/PhysRevD.72.014004.

[54] Yan-Qing Ma and Ramona Vogt. Quarkonium Production in an Improved Color Evaporation Model. *Phys. Rev.*, D94(11):114029, 2016. arXiv:1609.06042, doi:10.1103/PhysRevD.94.114029.

[55] R. Vogt. Quarkonium Production and Polarization in an Improved Color Evaporation Model. *Nucl. Phys.*, A982:751–754, 2019. doi:10.1016/j.nuclphysa.2018.08.003.

[56] M. B. Einhorn and S. D. Ellis. Hadronic Production of the New Resonances: Probing Gluon Distributions. *Phys. Rev.*, D12:2007, 1975. doi:10.1103/PhysRevD.12.2007.

[57] S. D. Ellis, Martin B. Einhorn, and C. Quigg. Comment on Hadronic Production of Psions. *Phys. Rev. Lett.*, 36:1263, 1976. doi:10.1103/PhysRevLett.36.1263.

[58] C. E. Carlson and R. Suaya. Hadronic Production of psi/J Mesons. *Phys. Rev.*, D14:3115, 1976. doi:10.1103/PhysRevD.14.3115.

[59] Chao-Hsi Chang. Hadronic Production of J/ψ Associated With a Gluon. *Nucl. Phys.*, B172:425–434, 1980. doi:10.1016/0550-3213(80)90175-3.

[60] Kuang-Ta Chao and Yan-Qing Ma. Quarkonium production review. *PoS*, ConfinementX:003, 2012. doi:10.22323/1.171.0003.

[61] Sean Fleming, I. Z. Rothstein, and Adam K. Leibovich. Power counting and effective field theory for charmonium. *Phys. Rev.*, D64:036002, 2001. arXiv:hep-ph/0012062, doi:10.1103/PhysRevD.64.036002.

[62] A. Andronic et al. Heavy-flavour and quarkonium production in the LHC era: from proton–proton to heavy-ion collisions. *Eur. Phys. J.*, C76(3):107, 2016. arXiv:1506.03981, doi:10.1140/epjc/s10052-015-3819-5.

[63] N. Brambilla et al. QCD and Strongly Coupled Gauge Theories: Challenges and Perspectives. *Eur. Phys. J.*, C74(10):2981, 2014. arXiv:1404.3723, doi:10.1140/epjc/s10052-014-2981-5.

[64] Jean-Philippe Lansberg. New Observables in Inclusive Production of Quarkonia. 2019. arXiv:1903.09185.

[65] John C. Collins and Davison E. Soper. Angular Distribution of Dileptons in High-Energy Hadron Collisions. *Phys. Rev.*, D16:2219, 1977. doi:10.1103/PhysRevD.16.2219.

[66] M. Beneke, M. Kramer, and M. Vanttinen. Inelastic photoproduction of polarized J/ψ. *Phys. Rev.*, D57:4258–4274, 1998. arXiv:hep-ph/9709376, doi:10.1103/PhysRevD.57.4258.

[67] P. Abreu et al. J/ψ production in the hadronic decays of the Z. *Phys.Lett.*, B341:109–122, 1994. doi:10.1016/0370-2693(94)01385-3.

[68] O. Adriani et al. χ_c production in hadronic Z decays. *Phys.Lett.*, B317:467–473, 1993. doi:10.1016/0370-2693(93)91026-J.

[69] D. Buskulic et al. Measurements of mean lifetime and branching fractions of b-hadrons decaying to J/ψ. *Phys.Lett.*, B295:396–408, 1992. doi:10.1016/0370-2693(92)91581-S.

[70] M. S. Alam et al. A Study of the Decay $B \to \psi$ X. *Phys. Rev.*, D34:3279, 1986. doi:10.1103/PhysRevD.34.3279.

[71] Bernard Aubert et al. Study of inclusive production of charmonium mesons in B decay. *Phys.Rev.*, D67:032002, 2003. arXiv:hep-ex/0207097, doi:10.1103/PhysRevD.67.032002.

[72] S. Anderson et al. Measurements of inclusive $B \to \psi$ production. *Phys.Rev.Lett.*, 89:282001, 2002. arXiv:hep-ex/0207059, doi:10.1103/PhysRevLett.89.282001.

[73] M. Tanabashi et al. Review of Particle Physics. *Phys. Rev.*, D98(3):030001, 2018. doi:10.1103/PhysRevD.98.030001.

[74] S. Chen et al. Study of χ_{c1} and χ_{c2} meson production in B meson decays. *Phys.Rev.*, D63:031102, 2001. arXiv:hep-ex/0009044, doi:10.1103/PhysRevD.63.031102.

[75] K. Abe et al. Observation of χ_{c2} production in B meson decay. *Phys.Rev.Lett.*, 89:011803, 2002. arXiv:hep-ex/0202028, doi:10.1103/PhysRevLett.89.011803.

[76] V. Bhardwaj et al. Inclusive and exclusive measurements of B decays to χ_{c1} and χ_{c2} at Belle. *Phys. Rev.*, D93(5):052016, 2016. arXiv:1512.02672, doi:10.1103/PhysRevD.93.052016.

[77] C. Patrignani et al. Review of particle physics. *Chin. Phys.*, C40:100001, 2016. doi:10.1088/1674-1137/40/10/100001.

[78] R. Balest et al. Inclusive decays of B mesons to charmonium. *Phys.Rev.*, D52:2661–2672, 1995. doi:10.1103/PhysRevD.52.2661.

[79] R Aaij et al. Measurement of $\psi(2S)$ meson production in pp collisions at $\sqrt{s} = 7\ TeV$. *Eur. Phys. J.*, C72:2100, 2012. arXiv:1204.1258, doi:10.1140/epjc/s10052-012-2100-4.

[80] Serguei Chatrchyan et al. J/ψ and $\psi(2S)$ production in pp collisions at $\sqrt{s} = 7$ TeV. *JHEP*, 02:011, 2012. arXiv:1111.1557, doi:10.1007/JHEP02(2012)011.

[81] Pyungwon Ko, Jungil Lee, and H. S. Song. Inclusive S wave charmonium productions in B decays. *Phys. Rev.*, D53:1409–1415, 1996. arXiv:hep-ph/9510202, doi:10.1103/PhysRevD.53.1409.

[82] M. Beneke, F. Maltoni, and I. Z. Rothstein. QCD analysis of inclusive B decay into charmonium. *Phys. Rev.*, D59:054003, 1999. arXiv:hep-ph/9808360, doi:10.1103/PhysRevD.59.054003.

[83] J. P. Ma. Effects of the initial hadron in $B \to J/\psi + X$. *Phys. Lett.*, B488:55–62, 2000. arXiv:hep-ph/0006060, doi:10.1016/S0370-2693(00)00845-5.

[84] M. Beneke, G. A. Schuler, and S. Wolf. Quarkonium momentum distributions in photoproduction and B decay. *Phys. Rev.*, D62:034004, 2000. arXiv:hep-ph/0001062, doi:10.1103/PhysRevD.62.034004.

[85] Sean Fleming, Oscar F. Hernandez, Ivan Maksymyk, and Helene Nadeau. NRQCD matrix elements in polarization of J/ψ produced from b-decay. *Phys. Rev.*, D55:4098–4104, 1997. arXiv:hep-ph/9608413, doi:10.1103/PhysRevD.55.4098.

[86] P. Ko, J. Lee, and H. S. Song. Testing J/psi production mechanisms in $B \to J/\psi + X$. *J. Korean Phys. Soc.*, 34:301–305, 1999.

[87] Geoffrey T. Bodwin, Eric Braaten, Tzu Chiang Yuan, and G. Peter Lepage. P-wave charmonium production in B meson decays. *Phys. Rev.*, D46:R3703–R3707, 1992. arXiv:hep-ph/9208254, doi:10.1103/PhysRevD.46.R3703.

[88] Johann H. Kuhn, S. Nussinov, and R. Ruckl. Charmonium Production in B Decays. *Z. Phys.*, C5:117, 1980. doi:10.1007/BF01576192.

[89] Johann H. Kuhn and R. Ruckl. Clues on Color Suppression From $B \to J/\psi$ + X. *Phys. Lett.*, 135B:477–480, 1984. [Erratum: Phys. Lett.B258,499(1991)]. doi:10.1016/0370-2693(91)91125-F,10.1016/0370-2693(84)90319-8.

[90] F. Abe et al. Production of J/ψ mesons from χ_c meson decays in $p\bar{p}$ collisions at $\sqrt{s} = 1.8$ TeV. *Phys. Rev. Lett.*, 79:578–583, 1997. doi:10.1103/PhysRevLett.79.578.

[91] R. Aaij et al. Measurement of J/ψ production in pp collisions at $\sqrt{s} = 2.76\ TeV$. *JHEP*, 02:041, 2013. arXiv:1212.1045, doi:10.1007/JHEP02(2013)041.

[92] R. Aaij et al. Measurement of J/ψ production in pp collisions at $\sqrt{s} = 7$ TeV. *Eur. Phys. J.*, C71:1645, 2011. arXiv:1103.0423, doi:10.1140/epjc/s10052-011-1645-y.

[93] R. Aaij et al. Production of J/ψ and Υ mesons in pp collisions at $\sqrt{s} = 8\ TeV$. *JHEP*, 06:064, 2013. arXiv:1304.6977, doi:10.1007/JHEP06(2013)064.

[94] R. Aaij et al. Measurement of forward J/ψ production cross-sections in pp collisions at $\sqrt{s} = 13\ TeV$. *JHEP*, 10:172, 2015. arXiv:1509.00771, doi:10.1007/JHEP10(2015)172.

[95] Georges Aad et al. Measurement of the differential cross-sections of inclusive, prompt and non-prompt J/ψ production in proton-proton collisions at $\sqrt{s} = 7$ TeV. *Nucl. Phys.*, B850:387–444, 2011. arXiv:1104.3038, doi:10.1016/j.nuclphysb.2011.05.015.

[96] Georges Aad et al. Measurement of the differential cross-sections of prompt and non-prompt production of J/ψ and $\psi(2S)$ in pp collisions at $\sqrt{s} = 7$ and 8 TeV with the ATLAS detector. *Eur. Phys. J.*, C76(5):283, 2016. arXiv:1512.03657, doi:10.1140/epjc/s10052-016-4050-8.

[97] A. M. Sirunyan et al. Measurement of quarkonium production cross sections in pp collisions at $\sqrt{s} = 13$ TeV. *Phys. Lett.*, B780:251–272, 2018. arXiv:1710.11002, doi:10.1016/j.physletb.2018.02.033.

[98] B. Abelev et al. Inclusive J/ψ production in pp collisions at $\sqrt{s} = 2.76$ TeV. *Phys. Lett.*, B718:295–306, 2012. [Erratum: Phys. Lett.B748,472(2015)]. arXiv:1203.3641, doi:10.1016/j.physletb.2012.10.078,10.1016/j.physletb.2015.06.058.

[99] K. Aamodt et al. Rapidity and transverse momentum dependence of inclusive J/ψ production in pp collisions at $\sqrt{s} = 7$ TeV. *Phys. Lett.*, B704:442–455, 2011. [Erratum: Phys. Lett.B718,692(2012)]. arXiv:1105.0380, doi:10.1016/j.physletb.2011.09.054,10.1016/j.physletb.2012.10.060.

[100] R. Aaij et al. Measurement of J/ψ polarization in pp collisions at $\sqrt{s} = 7\ TeV$. *Eur. Phys. J.*, C73:2631, 2013. arXiv:1307.6379, doi:10.1140/epjc/s10052-013-2631-3.

[101] R. Aaij et al. Measurement of $\psi(2S)$ polarisation in pp collisions at $\sqrt{s} = 7\ TeV$. *Eur. Phys. J.*, C74:2872, 2014. arXiv:1403.1339, doi:10.1140/epjc/s10052-014-2872-9.

[102] Serguei Chatrchyan et al. Measurement of the prompt J/ψ and $\psi(2S)$ polarizations in pp collisions at $\sqrt{s} = 7$ Te . *Phys. Lett.*, B727:381–402, 2013. arXiv:1307.6070, doi:10.1016/j.physletb.2013.10.055.

[103] Betty Abelev et al. J/ψ polarization in pp collisions at $\sqrt{s} = 7$ TeV. *Phys. Rev. Lett.*, 108:082001, 2012. arXiv:1111.1630, doi:10.1103/PhysRevLett.108.082001.

[104] A. Abulencia et al. Polarization of J/ψ and ψ_{2S} mesons produced in $p\bar{p}$ collisions at $\sqrt{s} = 1.96$ TeV. *Phys. Rev. Lett.*, 99:132001, 2007. arXiv:0704.0638, doi:10.1103/PhysRevLett.99.132001.

[105] R. Aaij et al. Measurement of J/ψ production in pp collisions at $\sqrt{s}$ = 7 TeV. *Eur. Phys. J.*, C71:1645, 2011. arXiv:1103.0423, doi:10.1140/epjc/s10052-011-1645-y.

[106] Pierre Artoisenet. Quarkonium production at the Tevatron and the LHC. *PoS*, ICHEP2010:192, 2010. doi:10.22323/1.120.0192.

[107] Mathias Butenschoen and Bernd A. Kniehl. Reconciling J/ψ production at HERA, RHIC, Tevatron, and LHC with NRQCD factorization at next-to-leading order. *Phys. Rev. Lett.*, 106:022003, 2011. arXiv:1009.5662, doi:10.1103/PhysRevLett.106.022003.

[108] J. P. Lansberg. On the mechanisms of heavy-quarkonium hadroproduction. *Eur. Phys. J.*, C61:693–703, 2009. arXiv:0811.4005, doi:10.1140/epjc/s10052-008-0826-9.

[109] Yan-Qing Ma, Kai Wang, and Kuang-Ta Chao. $J/\psi\,(\psi')$ production at the Tevatron and LHC at $\mathcal{O}(\alpha_s^4 v^4)$ in nonrelativistic QCD. *Phys. Rev. Lett.*, 106:042002, 2011. arXiv:1009.3655, doi:10.1103/PhysRevLett.106.042002.

[110] Anthony D. Frawley, T. Ullrich, and R. Vogt. Heavy flavor in heavy-ion collisions at RHIC and RHIC II. *Phys. Rept.*, 462:125–175, 2008. arXiv:0806.1013, doi:10.1016/j.physrep.2008.04.002.

[111] S. P. Baranov, A. V. Lipatov, and N. P. Zotov. Prompt charmonia production and polarization at LHC in the NRQCD with k_T -factorization. Part I: $\psi(2S)$ meson. *Eur. Phys. J.*, C75(9):455, 2015. arXiv:1508.05480, doi:10.1140/epjc/s10052-015-3689-x.

[112] S. P. Baranov and A. V. Lipatov. Prompt charmonia production and polarization at LHC in the NRQCD with k_T-factorization. Part III: J/ψ meson. *Phys. Rev.*, D96(3):034019, 2017. arXiv:1611.10141, doi:10.1103/PhysRevD.96.034019.

[113] T. Affolder et al. Measurement of J/ψ and $\psi(2S)$ polarization in $p\bar{p}$ collisions at $\sqrt{s}$ = 1.8 TeV. *Phys. Rev. Lett.*, 85:2886–2891, 2000. arXiv:hep-ex/0004027, doi:10.1103/PhysRevLett.85.2886.

[114] Kuang-Ta Chao, Yan-Qing Ma, Hua-Sheng Shao, Kai Wang, and Yu-Jie Zhang. J/ψ Polarization at Hadron Colliders in Nonrelativistic QCD. *Phys.Rev.Lett.*, 108:242004, 2012. arXiv:1201.2675, doi:10.1103/PhysRevLett.108.242004.

[115] R Aaij et al. Measurement of J/ψ polarization in pp collisions at $\sqrt{s}$ = 7 TeV. *Eur. Phys. J.*, C73(11):2631, 2013. arXiv:1307.6379, doi:10.1140/epjc/s10052-013-2631-3.

[116] Mathias Butenschoen and Bernd A. Kniehl. World data of J/ψ production consolidate NRQCD factorization at NLO. *Phys. Rev.*, D84:051501, 2011. arXiv:1105.0820, doi:10.1103/PhysRevD.84.051501.

[117] Bin Gong, Lu-Ping Wan, Jian-Xiong Wang, and Hong-Fei Zhang. Polarization for Prompt J/ψ and $\psi(2S)$ Production at the Tevatron and LHC. *Phys. Rev. Lett.*, 110(4):042002, 2013. arXiv:1205.6682, doi:10.1103/PhysRevLett.110.042002.

[118] Roel Aaij et al. Measurement of $\psi(2S)$ polarisation in pp collisions at $\sqrt{s} = 7$ TeV. *Eur. Phys. J.*, C74(5):2872, 2014. arXiv:1403.1339, doi:10.1140/epjc/s10052-014-2872-9.

[119] H. S. Shao, H. Han, Y. Q. Ma, C. Meng, Y. J. Zhang, and K. T. Chao. Yields and polarizations of prompt J/ψ and $\psi(2S)$ production in hadronic collisions. *JHEP*, 05:103, 2015. arXiv:1411.3300, doi:10.1007/JHEP05(2015)103.

[120] Geoffrey T. Bodwin, Hee Sok Chung, U-Rae Kim, and Jungil Lee. Fragmentation contributions to J/ψ production at the Tevatron and the LHC. *Phys. Rev. Lett.*, 113(2):022001, 2014. arXiv:1403.3612, doi:10.1103/PhysRevLett.113.022001.

[121] Mathias Butenschoen, Zhi-Guo He, and Bernd A. Kniehl. η_c production at the LHC challenges nonrelativistic-QCD factorization. *Phys. Rev. Lett.*, 114(9):092004, 2015. arXiv:1411.5287, doi:10.1103/PhysRevLett.114.092004.

[122] Yu Feng, Jean-Philippe Lansberg, and Jian-Xiong Wang. Energy dependence of direct-quarkonium production in pp collisions from fixed-target to LHC energies: complete one-loop analysis. *Eur. Phys. J.*, C75(7):313, 2015. arXiv:1504.00317, doi:10.1140/epjc/s10052-015-3527-1.

[123] Zhan Sun and Hong-Fei Zhang. Reconciling charmonium production and polarization data in the midrapidity region at hadron colliders within the nonrelativistic QCD framework. *Chin. Phys.*, C42(4):043104, 2018. arXiv:1505.02675, doi:10.1088/1674-1137/42/4/043104.

[124] A. K. Likhoded, A. V. Luchinsky, and S. V. Poslavsky. Production of heavy quarkonia in hadronic experiments. *Phys. Atom. Nucl.*, 78(9):1056–1065, 2015. [Yad. Fiz.78,no.12,1119(2015)]. doi:10.1134/S1063778815090100.

[125] Xiangrui Gao, Yu Jia, LiuJi Li, and Xiaonu Xiong. Relativistic correction to gluon fragmentation function into pseudoscalar quarkonium. *Chin. Phys.*, C41(2):023103, 2017. arXiv:1606.07455, doi:10.1088/1674-1137/41/2/023103.

[126] Pietro Faccioli, Carlos Lourenço, Mariana Araújo, Valentin Knünz, Ilse Krätschmer, and João Seixas. Quarkonium production at the LHC: A data-driven analysis of remarkably simple experimental patterns. *Phys. Lett.*, B773:476–486, 2017. arXiv:1702.04208, doi:10.1016/j.physletb.2017.09.006.

[127] Mathias Butenschoen, Zhi-Guo He, and Bernd A. Kniehl. η_c Hadroproduction at Large Hadron Collider Challenges NRQCD Factorization. *EPJ Web Conf.*, 137:06009, 2017. doi:10.1051/epjconf/201713706009.

[128] Hao Han, Yan-Qing Ma, Ce Meng, Hua-Sheng Shao, and Kuang-Ta Chao. η_c production at LHC and indications on the understanding of J/ψ production. *Phys. Rev. Lett.*, 114(9):092005, 2015. arXiv:1411.7350, doi:10.1103/PhysRevLett.114.092005.

[129] S. P. Baranov and A. V. Lipatov. Prompt η_c meson production at the LHC in the NRQCD with k_T-factorization. 2019. arXiv:1904.00400.

[130] Vardan Khachatryan et al. Measurement of J/ψ and $\psi(2S)$ Prompt Double-Differential Cross Sections in pp Collisions at $\sqrt{s}$=7 TeV. *Phys. Rev. Lett.*, 114(19):191802, 2015. arXiv:1502.04155, doi:10.1103/PhysRevLett.114.191802.

[131] Roel Aaij et al. Measurement of the $\eta_c(1S)$ production cross-section in proton-proton collisions via the decay $\eta_c(1S) \to p\bar{p}$. *Eur. Phys. J.*, C75(7):311, 2015. arXiv:1409.3612, doi:10.1140/epjc/s10052-015-3502-x.

[132] Jean-Philippe Lansberg, Hua-Sheng Shao, and Hong-Fei Zhang. η_c' Hadroproduction at Next-to-Leading Order and= its Relevance to ψ' Production. *Phys. Lett.*, B786:342–346, 2018. arXiv:1711.00265, doi:10.1016/j.physletb.2018.10.009.

[133] Geoffrey T. Bodwin, Kuang-Ta Chao, Hee Sok Chung, U-Rae Kim, Jungil Lee, and Yan-Qing Ma. Fragmentation contributions to hadroproduction of prompt J/ψ, χ_{cJ}, and $\psi(2S)$ states. *Phys. Rev.*, D93(3):034041, 2016. arXiv:1509.07904, doi:10.1103/PhysRevD.93.034041.

[134] Georges Aad et al. Measurement of χ_{c1} and χ_{c2} production with $\sqrt{s} = 7$ TeV pp collisions at ATLAS. *JHEP*, 07:154, 2014. arXiv:1404.7035, doi:10.1007/JHEP07(2014)154.

[135] Serguei Chatrchyan et al. Measurement of the relative prompt production rate of χ_{c2} and χ_{c1} in pp collisions at $\sqrt{s} = 7$ TeV. *Eur. Phys. J.*, C72:2251, 2012. arXiv:1210.0875, doi:10.1140/epjc/s10052-012-2251-3.

[136] R. Aaij et al. Measurement of the relative rate of prompt χ_{c0}, χ_{c1} and χ_{c2} production at $\sqrt{s} = 7$TeV. *JHEP*, 10:115, 2013. arXiv:1307.4285, doi:10.1007/JHEP10(2013)115.

[137] Yan-Qing Ma, Kai Wang, and Kuang-Ta Chao. QCD radiative corrections to χ_{cJ} production at hadron colliders. *Phys. Rev.*, D83:111503, 2011. arXiv:1002.3987, doi:10.1103/PhysRevD.83.111503.

[138] S. P. Baranov. On the $\sigma(\chi_{c1})/\sigma(\chi_{c2})$ ratio in the k_T-factorization approach. *Phys. Rev.*, D83:034035, 2011. doi:10.1103/PhysRevD.83.034035.

[139] S. P. Baranov, A. V. Lipatov, and N. P. Zotov. Prompt charmonia production and polarization at LHC in the NRQCD with k_T-factorization. Part II: χ_c mesons. *Phys. Rev.*, D93(9):094012, 2016. arXiv:1510.02411, doi:10.1103/PhysRevD.93.094012.

[140] A.K. Likhoded, A.V. Luchinsky, and S.V. Poslavsky. Hadronic production of χ_c-mesons at LHC. 2013. arXiv:1305.2389.

[141] C. Adloff et al. Inelastic photoproduction of J/ψ mesons at HERA. *Eur. Phys. J.*, C25:25–39, 2002. arXiv:hep-ex/0205064, doi:10.1007/s10052-002-1009-8.

[142] F. D. Aaron et al. Inelastic Production of J/ψ Mesons in Photoproduction and Deep Inelastic Scattering at HERA. *Eur. Phys. J.*, C68:401–420, 2010. arXiv:1002.0234, doi:10.1140/epjc/s10052-010-1376-5.

[143] S. Chekanov et al. Measurements of inelastic J/ψ and ψ' photoproduction at HERA. *Eur. Phys. J.*, C27:173–188, 2003. arXiv:hep-ex/0211011, doi:10.1140/epjc/s2002-01130-2.

[144] S. Chekanov et al. Measurement of J/ψ helicity distributions in inelastic photoproduction at HERA. *JHEP*, 12:007, 2009. arXiv:0906.1424, doi:10.1088/1126-6708/2009/12/007.

[145] H. Abramowicz et al. Measurement of inelastic J/ψ and ψ' photoproduction at HERA. *JHEP*, 02:071, 2013. arXiv:1211.6946, doi:10.1007/JHEP02(2013)071.

[146] Michael Krämer. QCD corrections to inelastic J/ψ photoproduction. *Nucl. Phys.*, B459:3–50, 1996. arXiv:hep-ph/9508409, doi:10.1016/0550-3213(95)00568-4.

[147] Michael Krämer. Quarkonium production at high-energy colliders. *Prog. Part. Nucl. Phys.*, 47:141–201, 2001. arXiv:hep-ph/0106120, doi:10.1016/S0146-6410(01)00154-5.

[148] Mathias Butenschoen and Bernd A. Kniehl. Complete next-to-leading-order corrections to J/ψ photoproduction in nonrelativistic quantum chromodynamics. *Phys. Rev. Lett.*, 104:072001, 2010. arXiv:0909.2798, doi:10.1103/PhysRevLett.104.072001.

[149] P. Artoisenet, John M. Campbell, F. Maltoni, and F. Tramontano. J/ψ production at HERA. *Phys. Rev. Lett.*, 102:142001, 2009. arXiv:0901.4352, doi:10.1103/PhysRevLett.102.142001.

[150] Chao-Hsi Chang, Rong Li, and Jian-Xiong Wang. J/ψ polarization in photoproduction up-to the next-to-leading order of QCD. *Phys. Rev.*, D80:034020, 2009. arXiv:0901.4749, doi:10.1103/PhysRevD.80.034020.

[151] M. Butenschoen. J/ψ photoproduction at NLO in NRQCD. *Nucl. Phys. Proc. Suppl.*, 191:193–202, 2009. doi:10.1016/j.nuclphysbps.2009.03.126.

[152] Mathias Butenschoen and Bernd A. Kniehl. Direct J/ψ photoproduction at next-to-leading-order in nonrelativistic QCD. *PoS*, DIS2010:157, 2010. arXiv:1006.1776, doi:10.22323/1.106.0157.

[153] Mathias Butenschoen and Bernd A. Kniehl. J/ψ production in NRQCD: A global analysis of yield and polarization. *Nucl. Phys. Proc. Suppl.*, 222-224:151–161, 2012. arXiv:1201.3862, doi:10.1016/j.nuclphysbps.2012.03.016.

[154] S. P. Baranov. Highlights from the k_T factorization approach on the quarkonium production puzzles. *Phys. Rev.*, D66:114003, 2002. [,162(2002)]. doi:10.1103/PhysRevD.66.114003.

[155] B. A. Kniehl, D. V. Vasin, and V. A. Saleev. Charmonium production at high energy in the k_T -factorization approach. *Phys. Rev.*, D73:074022, 2006. arXiv:hep-ph/0602179, doi:10.1103/PhysRevD.73.074022.

[156] A. D. Martin, M. G. Ryskin, and G. Watt. NLO prescription for unintegrated parton distributions. *Eur. Phys. J.*, C66:163–172, 2010. arXiv:0909.5529, doi:10.1140/epjc/s10052-010-1242-5.

[157] A. Adare et al. Transverse momentum dependence of J/ψ polarization at midrapidity in $p + p$ collisions at $s^{1/2} = 200$ GeV. *Phys. Rev.*, D82:012001, 2010. arXiv:0912.2082, doi:10.1103/PhysRevD.82.012001.

[158] D. Acosta et al. Measurement of the J/ψ meson and $b-$hadron production cross sections in $p\bar{p}$ collisions at $\sqrt{s} = 1960$ GeV. *Phys. Rev.*, D71:032001, 2005. arXiv:hep-ex/0412071, doi:10.1103/PhysRevD.71.032001.

[159] Vardan Khachatryan et al. Prompt and non-prompt J/ψ production in pp collisions at $\sqrt{s} = 7$ TeV. *Eur. Phys. J.*, C71:1575, 2011. arXiv:1011.4193, doi:10.1140/epjc/s10052-011-1575-8.

[160] A first measurement of the differential cross section for the $J/\psi \to \mu\mu$ resonance and the non-prompt to prompt J/ψ cross-section ratio with pp collisions at $\sqrt{s}$=7 TeV in ATLAS. 2010.

[161] Betty Bezverkhny Abelev et al. Measurement of quarkonium production at forward rapidity in pp collisions at $\sqrt{s} = 7$ TeV. *Eur. Phys. J.*, C74(8):2974, 2014. arXiv:1403.3648, doi:10.1140/epjc/s10052-014-2974-4.

[162] Mathias Butenschoen and Bernd A. Kniehl. Probing nonrelativistic QCD factorization in polarized J/ψ photoproduction at next-to-leading order. *Phys. Rev. Lett.*, 107:232001, 2011. arXiv:1109.1476, doi:10.1103/PhysRevLett.107.232001.

[163] J. Abdallah et al. Study of inclusive J/ψ production in two photon collisions at LEP-2 with the DELPHI detector. *Phys. Lett.*, B565:76–86, 2003. arXiv:hep-ex/0307049, doi:10.1016/S0370-2693(03)00660-9.

[164] J. P. Ma, B. H. J. McKellar, and C. B. Paranavitane. J/ψ production at photon - photon colliders as a probe of the color octet mechanism. *Phys. Rev.*, D57:606–609, 1998. arXiv:hep-ph/9707480, doi:10.1103/PhysRevD.57.606.

[165] George Japaridze and Avto Tkabladze. Color octet contribution to J/ψ production at a photon linear collider. *Phys. Lett.*, B433:139–146, 1998. arXiv:hep-ph/9803447, doi:10.1016/S0370-2693(98)00697-2.

[166] R. M. Godbole, D. Indumathi, and M. Kramer. J/ψ production through resolved photon processes at e^+e^- colliders. *Phys. Rev.*, D65:074003, 2002. [,1594(2001)]. arXiv:hep-ph/0101333, doi:10.1103/PhysRevD.65.074003.

[167] M. Klasen, Bernd A. Kniehl, L. Mihaila, and M. Steinhauser. J/ψ plus dijet associated production in two photon collisions. *Nucl. Phys.*, B609:518–536, 2001. arXiv:hep-ph/0104044, doi:10.1016/S0550-3213(01)00318-2.

[168] M. Klasen, Bernd A. Kniehl, L. N. Mihaila, and M. Steinhauser. Evidence for color octet mechanism from CERN LEP-2 $\gamma\gamma \to J/\psi + X$ data. *Phys. Rev. Lett.*, 89:032001, 2002. arXiv:hep-ph/0112259, doi:10.1103/PhysRevLett.89.032001.

[169] Zi-Qiang Chen, Long-Bin Chen, and Cong-Feng Qiao. NLO QCD Corrections for $J/\psi + c + \bar{c}$ Production in Photon-Photon Collision. *Phys. Rev.*, D95(3):036001, 2017. arXiv:1608.06231, doi:10.1103/PhysRevD.95.036001.

[170] Bernard Aubert et al. Measurement of J/ψ production in continuum e^+e^- annihilations near $\sqrt{s} = 10.6$ GeV. *Phys. Rev. Lett.*, 87:162002, 2001. arXiv:hep-ex/0106044, doi:10.1103/PhysRevLett.87.162002.

[171] Kazuo Abe et al. Production of prompt charmonia in e^+e^- annihilation at $s^{1/2}$ is approximately 10.6 GeV. *Phys. Rev. Lett.*, 88:052001, 2002. arXiv:hep-ex/0110012, doi:10.1103/PhysRevLett.88.052001.

[172] Feng Yuan, Cong-Feng Qiao, and Kuang-Ta Chao. Prompt J/ψ production at e^+e^- colliders. *Phys. Rev.*, D56:321–328, 1997. arXiv:hep-ph/9703438, doi:10.1103/PhysRevD.56.321.

[173] Peter L. Cho and Adam K. Leibovich. Color singlet ψ_Q production at e^+e^- colliders. *Phys. Rev.*, D54:6690–6695, 1996. arXiv:hep-ph/9606229, doi:10.1103/PhysRevD.54.6690.

[174] Seungwon Baek, P. Ko, Jungil Lee, and H. S. Song. Polarized J/ψ production at CLEO. *J. Korean Phys. Soc.*, 33:97–101, 1998. [,225(1998)]. arXiv:hep-ph/9804455.

[175] Gerhard A. Schuler. Testing factorization of charmonium production. *Eur.Phys.J.*, C8:273–281, 1999. arXiv:hep-ph/9804349, doi:10.1007/s100529900948.

[176] V. V. Kiselev, A. K. Likhoded, and M. V. Shevlyagin. Double charmed baryon production at B-factory. *Phys. Lett.*, B332:411–414, 1994. arXiv:hep-ph/9408407, doi:10.1016/0370-2693(94)91273-4.

[177] Kui-Yong Liu, Zhi-Guo He, and Kuang-Ta Chao. Production of $J/\psi + c\bar{c}$ through two photons in e^+e^- annihilation. *Phys. Rev.*, D68:031501, 2003. arXiv:hep-ph/0305084, doi:10.1103/PhysRevD.68.031501.

[178] Kazuo Abe et al. Observation of double $c\bar{c}$ production in e^+e^- annihilation at $s^{1/2}$ approximately 10.6-GeV. *Phys. Rev. Lett.*, 89:142001, 2002. arXiv:hep-ex/0205104, doi:10.1103/PhysRevLett.89.142001.

[179] Kui-Yong Liu, Zhi-Guo He, and Kuang-Ta Chao. Inclusive charmonium production via double $c\bar{c}$ in e^+e^- annihilation. *Phys. Rev.*, D69:094027, 2004. arXiv:hep-ph/0301218, doi:10.1103/PhysRevD.69.094027.

[180] P. Pakhlov et al. Measurement of the $e^+e^- \to J/\psi c\bar{c}$ cross section at $s^{1/2}$ 10.6 GeV. *Phys. Rev.*, D79:071101, 2009. arXiv:0901.2775, doi:10.1103/PhysRevD.79.071101.

[181] Yu-Jie Zhang and Kuang-Ta Chao. Double charm production $e^+e^- \to J/\psi + c\bar{c}$ at B-factories with next-to-leading order QCD correction. *Phys. Rev. Lett.*, 98:092003, 2007. arXiv:hep-ph/0611086, doi:10.1103/PhysRevLett.98.092003.

[182] Yan-Qing Ma, Yu-Jie Zhang, and Kuang-Ta Chao. QCD correction to $e^+e^- \to J/\psi + gg$ at B Factories. *Phys. Rev. Lett.*, 102:162002, 2009. arXiv:0812.5106, doi:10.1103/PhysRevLett.102.162002.

[183] Bin Gong and Jian-Xiong Wang. Next-to-Leading-Order QCD Corrections to $e^+e^- \to J/\psi gg$ at the B-Factories. *Phys. Rev. Lett.*, 102:162003, 2009. arXiv:0901.0117, doi:10.1103/PhysRevLett.102.162003.

[184] Zhi-Guo He, Ying Fan, and Kuang-Ta Chao. Relativistic correction to $e^+e^- \to J/\psi + gg$ at B-factories and constraint on color-octet matrix elements. *Phys. Rev.*, D81:054036, 2010. arXiv:0910.3636, doi:10.1103/PhysRevD.81.054036.

[185] Yu Jia. Color-singlet relativistic correction to inclusive J/ψ production associated with light hadrons at B factories. *Phys. Rev.*, D82:034017, 2010. arXiv:0912.5498, doi:10.1103/PhysRevD.82.034017.

[186] Yu-Jie Zhang, Yan-Qing Ma, Kai Wang, and Kuang-Ta Chao. QCD radiative correction to color-octet J/ψ inclusive production at B Factories. *Phys. Rev.*, D81:034015, 2010. arXiv:0911.2166, doi:10.1103/PhysRevD.81.034015.

[187] Sergey Barsuk, Jibo He, Emi Kou, and Benoit Viaud. Investigating charmonium production at LHC with the $p\bar{p}$ final state. *Phys.Rev.*, D86:034011, 2012. arXiv:1202.2273, doi:10.1103/PhysRevD.86.034011.

[188] C. Patrignani et al. Review of particle physics. *Chin. Phys.*, C40:100001, 2016. and 2017 update. doi:10.1088/1674-1137/40/10/100001.

[189] Roel Aaij et al. Evidence for an $\eta_c(1S)\pi^-$ resonance in $B^0 \to \eta_c(1S)K^+\pi^-$ decays. *Submitted to: Eur. Phys. J.*, 2018. arXiv:1809.07416.

[190] Roel Aaij et al. Observation of $\eta_c(2S) \to p\bar{p}$ and search for $X(3872) \to p\bar{p}$ decays. *Phys. Lett.*, B769:305–313, 2017. arXiv:1607.06446, doi:10.1016/j.physletb.2017.03.046.

[191] Y. Kato et al. Measurements of the absolute branching fractions of $B^+ \to X_{c\bar{c}}K^+$ and $B^+ \to \bar{D}^{(*)0}\pi^+$ at Belle. *Phys. Rev.*, D97(1):012005, 2018. arXiv:1709.06108, doi:10.1103/PhysRevD.97.012005.

[192] R. Aaij et al. Study of charmonium production in b-hadron decays and first evidence for the decay $B_s^0 \to \phi\phi\phi$. *Eur. Phys. J.*, C77(9):609, 2017. arXiv:1706.07013, doi:10.1140/epjc/s10052-017-5151-8.

[193] M. Ablikim. Observation of χ_{cJ} decaying into the $p\bar{p}K^+K^-$ final state. *Phys. Rev.*, D83:112009, 2011. arXiv:1103.2661, doi:10.1103/PhysRevD.83.112009.

[194] Jacques Lefrancois. private communication, 2017.

[195] M. Ablikim et al. Search for $\eta_c(2S)/h_c \to p\bar{p}$ decays and measurements of the $\chi_{cJ} \to p\bar{p}$ branching fractions. *Phys. Rev.*, D88(11):112001, 2013. arXiv:1310.6099, doi:10.1103/PhysRevD.88.112001.

[196] Roel Aaij et al. χ_{c1} and χ_{c2} Resonance Parameters with the Decays $\chi_{c1,c2} \to J/\psi\,\mu^+\mu^-$. *Phys. Rev. Lett.*, 119(22):221801, 2017. arXiv:1709.04247, doi:10.1103/PhysRevLett.119.221801.

[197] Medina Ablikim et al. First observations of $h_c \to$ hadrons. *Phys. Rev.*, D99(7):072008, 2019. arXiv:1810.12023, doi:10.1103/PhysRevD.99.072008.

[198] Lyndon Evans and Philip Bryant. LHC Machine. *JINST*, 3:S08001, 2008. doi:10.1088/1748-0221/3/08/S08001.

[199] Christiane Lefèvre. The CERN accelerator complex. Complexe des accélérateurs du CERN. Dec 2008. URL: https://cds.cern.ch/record/1260465.

[200] G. Aad et al. The ATLAS Experiment at the CERN Large Hadron Collider. *JINST*, 3:S08003, 2008. doi:10.1088/1748-0221/3/08/S08003.

[201] S. Chatrchyan et al. The CMS Experiment at the CERN LHC. *JINST*, 3:S08004, 2008. doi:10.1088/1748-0221/3/08/S08004.

[202] K. Aamodt et al. The ALICE experiment at the CERN LHC. *JINST*, 3:S08002, 2008. doi:10.1088/1748-0221/3/08/S08002.

[203] O. Adriani et al. The LHCf detector at the CERN Large Hadron Collider. *JINST*, 3:S08006, 2008. doi:10.1088/1748-0221/3/08/S08006.

[204] G. Anelli et al. The TOTEM experiment at the CERN Large Hadron Collider. *JINST*, 3:S08007, 2008. doi:10.1088/1748-0221/3/08/S08007.

[205] James Pinfold et al. Technical Design Report of the MoEDAL Experiment. 2009.

[206] A. Augusto Alves, Jr. et al. The LHCb Detector at the LHC. *JINST*, 3:S08005, 2008. doi:10.1088/1748-0221/3/08/S08005.

[207] Roel Aaij et al. LHCb Detector Performance. *Int. J. Mod. Phys.*, A30(07):1530022, 2015. arXiv:1412.6352, doi:10.1142/S0217751X15300227.

[208] A. Abashian et al. The Belle Detector. *Nucl. Instrum. Meth.*, A479:117–232, 2002. doi:10.1016/S0168-9002(01)02013-7.

[209] Bernard Aubert et al. The BaBar detector. *Nucl. Instrum. Meth.*, A479:1–116, 2002. arXiv:hep-ex/0105044, doi:10.1016/S0168-9002(01)02012-5.

[210] M. Ablikim et al. Design and Construction of the BESIII Detector. *Nucl. Instrum. Meth.*, A614:345–399, 2010. arXiv:0911.4960, doi:10.1016/j.nima.2009.12.050.

[211] C. Patrignani et al. E835 at FNAL: Charmonium spectroscopy in anti-p p annihilations. *Nucl. Phys. Proc. Suppl.*, 142:98–103, 2005. doi:10.1016/j.nuclphysbps.2005.01.017.

[212] V. V. Anashin et al. The KEDR detector. *Phys. Part. Nucl.*, 44:657–702, 2013. doi:10.1134/S1063779613040035.

[213] Christian Elsässer. $\bar{b}b$ production angle plots. https://lhcb.web.cern.ch/lhcb/speakersbureau/html/bb_ProductionAngles.html, 2019.

[214] F. Follin and D. Jacquet. Implementation and experience with luminosity levelling with offset beam. In *Proceedings, ICFA Mini-Workshop on Beam-Beam Effects in Hadron Colliders (BB2013): CERN, Geneva, Switzerland, March 18-22 2013*, pages 183–187, 2014. [,183(2014)]. arXiv:1410.3667, doi:10.5170/CERN-2014-004.183.

[215] R. Aaij et al. Performance of the LHCb Vertex Locator. *JINST*, 9:P09007, 2014. arXiv:1405.7808, doi:10.1088/1748-0221/9/09/P09007.

[216] R. Arink et al. Performance of the LHCb Outer Tracker. *JINST*, 9:P01002, 2014. arXiv:1311.3893, doi:10.1088/1748-0221/9/01/P01002.

[217] M. Adinolfi et al. Performance of the LHCb RICH detector at the LHC. *Eur. Phys. J.*, C73:2431, 2013. arXiv:1211.6759, doi:10.1140/epjc/s10052-013-2431-9.

[218] A A Alves Jr. et al. Performance of the LHCb muon system. *JINST*, 8:P02022, 2013. arXiv:1211.1346, doi:10.1088/1748-0221/8/02/P02022.

[219] P. R. Barbosa-Marinho et al. LHCb VELO TDR: Vertex locator. Technical design report. *CERN-LHCC-2001-011*, 2001.

[220] Velo approved conference plots. `https://lbtwiki.cern.ch/bin/view/VELO/VELOConferencePlots`, 2019.

[221] R Aaij et al. Precision measurement of the B_s^0-$\bar{B}_s^0$ oscillation frequency with the decay $B_s^0 \to D_s^- \pi^+$. *New J. Phys.*, 15:053021, 2013. `arXiv:1304.4741`, `doi:10.1088/1367-2630/15/5/053021`.

[222] S. Amato et al. LHCb magnet: Technical design report. *CERN-LHCC-2000-007*, 2000.

[223] Silicon tracker approved conference plots. `https://lhcb.physik.uzh.ch/ST/public/material/`, 2019.

[224] P R Barbosa-Marinho et al. *LHCb inner tracker: Technical Design Report*. Technical Design Report LHCb. CERN, Geneva, 2002. revised version number 1 submitted on 2002-11-13 14:14:34. URL: `http://cds.cern.ch/record/582793`.

[225] R Arink et al. Performance of the LHCb Outer Tracker. *JINST*, 9(01):P01002, 2014. `arXiv:1311.3893`, `doi:10.1088/1748-0221/9/01/P01002`.

[226] S Amato et al. *LHCb calorimeters: Technical Design Report*. Technical Design Report LHCb. CERN, Geneva, 2000. URL: `http://cds.cern.ch/record/494264`.

[227] M. Adinolfi et al. Performance of the LHCb RICH detector at the LHC. *Eur. Phys. J.*, C73:2431, 2013. `arXiv:1211.6759`, `doi:10.1140/epjc/s10052-013-2431-9`.

[228] A. Papanestis and C. D'Ambrosio. Performance of the LHCb RICH detectors during the LHC Run II. *Nucl. Instrum. Meth.*, A876:221–224, 2017. `arXiv:1703.08152`, `doi:10.1016/j.nima.2017.03.009`.

[229] P. R. Barbosa-Marinho et al. LHCb muon system technical design report. *CERN-LHCC-2001-010*, 2001.

[230] R. Aaij et al. The LHCb trigger and its performance in 2011. *JINST*, 8:P04022, 2013. `arXiv:1211.3055`, `doi:10.1088/1748-0221/8/04/P04022`.

[231] V. V. Gligorov and Mike Williams. Efficient, reliable and fast high-level triggering using a bonsai boosted decision tree. *JINST*, 8:P02013, 2013. `arXiv:1210.6861`, `doi:10.1088/1748-0221/8/02/P02013`.

[232] Torbjörn Sjöstrand, Stephen Mrenna, and Peter" Skands. PYTHIA 6.4 physics and manual. *JHEP*, 05:026, 2006. `arXiv:hep-ph/0603175`, `doi:10.1088/1126-6708/2006/05/026`.

[233] Torbjörn Sjöstrand, Stephen Mrenna, and Peter" Skands. A brief introduction to PYTHIA 8.1. *Comput.Phys.Commun.*, 178:852–867, 2008. `arXiv:0710.3820`, `doi:10.1016/j.cpc.2008.01.036`.

[234] I. Belyaev et al. Handling of the generation of primary events in Gauss, the LHCb simulation framework. *J. Phys. Conf. Ser.*, 331:032047, 2011. doi:10.1088/1742-6596/331/3/032047.

[235] D. J. Lange. The EvtGen particle decay simulation package. *Nucl. Instrum. Meth.*, A462:152–155, 2001. doi:10.1016/S0168-9002(01)00089-4.

[236] Piotr Golonka and Zbigniew Was. PHOTOS Monte Carlo: A precision tool for QED corrections in Z and W decays. *Eur.Phys.J.*, C45:97–107, 2006. arXiv:hep-ph/0506026, doi:10.1140/epjc/s2005-02396-4.

[237] John Allison, K. Amako, J. Apostolakis, H. Araujo, P.A. Dubois, et al. Geant4 developments and applications. *IEEE Trans.Nucl.Sci.*, 53:270, 2006. doi:10.1109/TNS.2006.869826.

[238] S. Agostinelli et al. Geant4: A simulation toolkit. *Nucl. Instrum. Meth.*, A506:250, 2003. doi:10.1016/S0168-9002(03)01368-8.

[239] M Clemencic et al. The LHCb simulation application, Gauss: Design, evolution and experience. *J. Phys. Conf. Ser.*, 331:032023, 2011. doi:10.1088/1742-6596/331/3/032023.

[240] R. Aaij et al. Observation of $\eta_c(2S) \to p\overline{p}$ and search for $X(3872) \to p\overline{p}$ decays. *Phys. Lett.*, B769:305, 2017. arXiv:1607.06446, doi:10.1016/j.physletb.2017.03.046.

[241] Yu Feng, Jibo He, Jean-Philippe Lansberg, Hua-Sheng Shao, Andrii Usachov, and Hong-Fei Zhang. Phenomenological NLO analysis of η_c production at the LHC in the collider and fixed-target modes. *Nucl. Phys.*, B945:114662, 2019. arXiv:1901.09766, doi:10.1016/j.nuclphysb.2019.114662.

[242] Hong-Fei Zhang, Zhan Sun, Wen-Long Sang, and Rong Li. Impact of η_c hadroproduction data on charmonium production and polarization within NRQCD framework. *Phys. Rev. Lett.*, 114(9):092006, 2015. arXiv:1412.0508, doi:10.1103/PhysRevLett.114.092006.

[243] R. Aaij et al. Measurement of *CP* violation in $B_s^0 \to \phi\phi$ decays. *Phys. Rev.*, D90:052011, 2014. arXiv:1407.2222, doi:10.1103/PhysRevD.90.052011.

[244] F. Von Hippel and C. Quigg. Centrifugal-barrier effects in resonance partial decay widths, shapes, and production amplitudes. *Phys. Rev.*, D5:624–638, 1972. doi:10.1103/PhysRevD.5.624.

[245] R. Aaij et al. First observation of $B_s^0 \to J/\psi\, f_0(980)$ decays. *Phys. Lett.*, B698:115, 2011. arXiv:1102.0206, doi:10.1016/j.physletb.2011.03.006.

[246] Stanley M. Flatte. Coupled - Channel Analysis of the $\pi\eta$ and K anti-K Systems Near K anti-K Threshold. *Phys. Lett.*, B63:224, 1976. doi:10.1016/0370-2693(76)90654-7.

[247] H. C. Huang et al. Evidence for $B \to \phi\phi K$. *Phys. Rev. Lett.*, 91:241802, 2003. arXiv:hep-ex/0305068, doi:10.1103/PhysRevLett.91.241802.

[248] Bernard Aubert et al. Branching fraction measurements of $B \to \eta_c K$ decays. *Phys. Rev.*, D70:011101, 2004. arXiv:hep-ex/0403007, doi:10.1103/PhysRevD.70.011101.

[249] Roel Aaij et al. Measurement of the $\eta_c(1S)$ production cross-section in proton-proton collisions via the decay$\eta_c(1S) \to p\bar{p}$. *Eur. Phys. J.*, C75(7):311, 2015. arXiv:1409.3612, doi:10.1140/epjc/s10052-015-3502-x.

[250] H.-S. Shao. private communication.

[251] S. Anderson et al. Measurements of inclusive $B \to \psi$ production. *Phys. Rev. Lett.*, 89:282001, 2002. arXiv:hep-ex/0207059, doi:10.1103/PhysRevLett.89.282001.

[252] S. Chen et al. Study of χ_{c1} and χ_{c2} meson production in B meson decays. *Phys. Rev.*, D63:031102, 2001. arXiv:hep-ex/0009044, doi:10.1103/PhysRevD.63.031102.

[253] Kazuo Abe et al. Observation of χ_{c2} production in B meson decay. *Phys. Rev. Lett.*, 89:011803, 2002. arXiv:hep-ex/0202028, doi:10.1103/PhysRevLett.89.011803.

[254] Bernard Aubert et al. Study of inclusive production of charmonium mesons in B decay. *Phys. Rev.*, D67:032002, 2003. arXiv:hep-ex/0207097, doi:10.1103/PhysRevD.67.032002.

[255] O. Adriani et al. χ_c production in hadronic Z decays. *Phys. Lett.*, B317:467–473, 1993. doi:10.1016/0370-2693(93)91026-J.

[256] P. Abreu et al. J/ψ production in the hadronic decays of the Z. *Phys. Lett.*, B341:109–122, 1994. doi:10.1016/0370-2693(94)01385-3.

[257] R. Aaij et al. Study of charmonium production in b-hadron decays and first evidence for the decay $B_s^0 \to \phi\phi\phi$. *Eur. Phys. J.*, C77(9):609, 2017. arXiv:1706.07013, doi:10.1140/epjc/s10052-017-5151-8.

[258] R. Aaij et al. Measurement of b-hadron production fractions in 7 TeV pp collisions. *Phys. Rev.*, D85:032008, 2012. arXiv:1111.2357, doi:10.1103/PhysRevD.85.032008.

[259] R. Aaij et al. Study of the kinematic dependences of Λ_b^0 production in pp collisions and a measurement of the $\Lambda_b^0 \to \Lambda_c^+ \pi^-$ branching fraction. *JHEP*, 08:143, 2014. arXiv:1405.6842, doi:10.1007/JHEP08(2014)143.

[260] Estia J. Eichten and Chris Quigg. Quarkonium wave functions at the origin. *Phys. Rev.*, D52:1726–1728, 1995. arXiv:hep-ph/9503356, doi:10.1103/PhysRevD.52.1726.

[261] Vineet Kumar and Prashant Shukla. Charmonia production in $p + p$ collisions under NRQCD formalism. *J. Phys.*, G44(8):085003, 2017. arXiv:1606.08265, doi:10.1088/1361-6471/aa7818.

[262] A. Abulencia et al. Measurement of $\sigma_{\chi_{c2}}\mathcal{B}(\chi_{c2} \to J/\psi\gamma)/\sigma_{\chi_{c1}}\mathcal{B}(\chi_{c1} \to J/\psi\gamma)$ in $p\bar{p}$ Collisions at $\sqrt{s}$ 1.96 TeV. *Phys. Rev. Lett.*, 98:232001, 2007. arXiv:hep-ex/0703028, doi:10.1103/PhysRevLett.98.232001.

[263] M. Beneke and L. Vernazza. $B \to \chi_{cJ}K$ decays revisited. *Nucl. Phys.*, B811:155–181, 2009. arXiv:0810.3575, doi:10.1016/j.nuclphysb.2008.11.025.

[264] R Aaij et al. Measurement of $\psi(2S)$ meson production in pp collisions at $\sqrt{s}$=7 TeV. *Eur. Phys. J.*, C72:2100, 2012. arXiv:1204.1258, doi:10.1140/epjc/s10052-012-2100-4.

[265] Mathias Butenschoen and Bernd A. Kniehl. J/ψ polarization at Tevatron and LHC: Nonrelativistic-QCD factorization at the crossroads. *Phys.Rev.Lett.*, 108:172002, 2012. arXiv:1201.1872, doi:10.1103/PhysRevLett.108.172002.

[266] V. V. Anashin et al. Final analysis of KEDR data on J/ψ and $\psi(2S)$ masses. *Phys. Lett.*, B749:50–56, 2015. doi:10.1016/j.physletb.2015.07.057.

[267] G. S. Adams et al. Measurement of $\Gamma_{ee}(J/\psi)$, $\Gamma_{tot}(J/\psi)$, and $\Gamma_{ee}(\psi(2S))/Gamma_{ee}(J/\psi)$f. *Phys. Rev.*, D73:051103, 2006. arXiv:hep-ex/0512046, doi:10.1103/PhysRevD.73.051103.

[268] M. Andreotti et al. Precision Measurements of the Total and Partial Widths of the ψ_{2S} Charmonium Meson with A New Complementary-Scan Technique in $\bar{p}p$ Annihilations. *Phys. Lett.*, B654:74–79, 2007. arXiv:hep-ex/0703012, doi:10.1016/j.physletb.2007.08.044.

[269] J. Z. Bai et al. A Measurement of $\psi(2S)$ resonance parameters. *Phys. Lett.*, B550:24–32, 2002. arXiv:hep-ph/0209354, doi:10.1016/S0370-2693(02)02909-X.

[270] M. Ablikim et al. Measurements of the mass and width of the η_c using $\psi' \to \gamma\eta_c$. *Phys. Rev. Lett.*, 108:222002, 2012. arXiv:1111.0398, doi:10.1103/PhysRevLett.108.222002.

[271] M. Ablikim et al. Precise measurement of spin-averaged $\chi_{cJ}(1P)$ mass using photon conversions in $\psi(2S) \to \gamma\chi_{cJ}$. *Phys. Rev.*, D71:092002, 2005. arXiv:hep-ex/0502031, doi:10.1103/PhysRevD.71.092002.

[272] M. Andreotti et al. Interference study of the $\chi_{c0}(1^3P_0)$ in the reaction $p\bar{p} \to \pi^0\pi^0$. *Phys. Rev. Lett.*, 91:091801, 2003. arXiv:hep-ex/0308055, doi:10.1103/PhysRevLett.91.091801.

[273] M. Andreotti et al. Measurement of the resonance parameters of the $\chi_1(1^3P_1)$ and $\chi_2(1^3P_2)$ states of charmonium formed in $p\bar{p}$ annihilations. *Nucl. Phys.*, B717:34–47, 2005. arXiv:hep-ex/0503022, doi:10.1016/j.nuclphysb.2005.03.042.

[274] T. A. Armstrong et al. Study of the χ_1 and χ_2 charmonium states formed in anti-p p annihilations. *Nucl. Phys.*, B373:35–54, 1992. doi:10.1016/0550-3213(92)90448-K.

[275] M. Ablikim et al. Study of $\psi(3686) \to \pi^0 h_c, h_c \to \gamma\eta_c$ via η_c exclusive decays. *Phys. Rev.*, D86:092009, 2012. arXiv:1209.4963, doi:10.1103/PhysRevD.86.092009.

[276] S. Dobbs et al. Precision Measurement of the Mass of the $h_c(1P)$ State of Charmonium. *Phys. Rev. Lett.*, 101:182003, 2008. arXiv:0805.4599, doi:10.1103/PhysRevLett.101.182003.

[277] P. del Amo Sanchez et al. Observation of $\eta_c(1S)$ and $\eta_c(2S)$ decays to $K^+K^-\pi^+\pi^-\pi^0$ in two-photon interactions. *Phys.Rev.*, D84:012004, 2011. arXiv:1103.3971, doi:10.1103/PhysRevD.84.012004.

[278] M. Ablikim et al. Evidence for $\eta_c(2S)$ in $\psi(3686) \to \gamma K^0_S K^{\pm}\pi^{mp}\pi^+\pi^-$. *Phys. Rev.*, D87(5):052005, 2013. arXiv:1301.1476, doi:10.1103/PhysRevD.87.052005.

[279] S. Godfrey and Nathan Isgur. Mesons in a Relativized Quark Model with Chromodynamics. *Phys. Rev.*, D32:189–231, 1985. doi:10.1103/PhysRevD.32.189.

[280] T. Barnes, S. Godfrey, and E. S. Swanson. Higher charmonia. *Phys. Rev.*, D72:054026, 2005. arXiv:hep-ph/0505002, doi:10.1103/PhysRevD.72.054026.

[281] Stephen Lars Olsen, Tomasz Skwarnicki, and Daria Zieminska. Nonstandard heavy mesons and baryons: Experimental evidence. *Rev. Mod. Phys.*, 90(1):015003, 2018. arXiv:1708.04012, doi:10.1103/RevModPhys.90.015003.

[282] C. T. H. Davies, K. Hornbostel, G. P. Lepage, A. J. Lidsey, J. Shigemitsu, and J. H. Sloan. Precision charmonium spectroscopy from lattice QCD. *Phys. Rev.*, D52:6519–6529, 1995. arXiv:hep-lat/9506026, doi:10.1103/PhysRevD.52.6519.

[283] Howard D. Trottier. Quarkonium spin structure in lattice NRQCD. *Phys. Rev.*, D55:6844–6851, 1997. arXiv:hep-lat/9611026, doi:10.1103/PhysRevD.55.6844.

[284] M. Okamoto et al. Charmonium spectrum from quenched anisotropic lattice QCD. *Phys. Rev.*, D65:094508, 2002. arXiv:hep-lat/0112020, doi:10.1103/PhysRevD.65.094508.

[285] Clara Peset, Antonio Pineda, and Jorge Segovia. P-wave heavy quarkonium spectrum with next-to-next-to-next-to-leading logarithmic accuracy. *Phys. Rev.*, D98(9):094003, 2018. arXiv:1809.09124, doi:10.1103/PhysRevD.98.094003.

[286] Antonio Pineda. Review of Heavy Quarkonium at weak coupling. *Prog. Part. Nucl. Phys.*, 67:735–785, 2012. arXiv:1111.0165, doi:10.1016/j.ppnp.2012.01.038.

[287] Nora Brambilla, Pablo Roig, and Antonio Vairo. Precise determination of the η_c mass and width in the radiative $J/\psi \to \eta_c$ gamma decay. *AIP Conf. Proc.*, 1343:418–420, 2011. arXiv:1012.0773, doi:10.1063/1.3575048.

[288] Roel Aaij et al. Near-threshold $D\bar{D}$ spectroscopy and observation of a new charmonium state. 2019. arXiv:1903.12240.

[289] Mahiko Suzuki. The X(3872) boson: Molecule or charmonium. *Phys. Rev.*, D72:114013, 2005. arXiv:hep-ph/0508258, doi:10.1103/PhysRevD.72.114013.

[290] M. Tanabashi et al. Review of Particle Physics. *Phys. Rev.*, D98(3):030001, 2018. doi:10.1103/PhysRevD.98.030001.

[291] Samuel H. Blitz and Richard F. Lebed. Tetraquark Cusp Effects from Diquark Pair Production. *Phys. Rev.*, D91(9):094025, 2015. arXiv:1503.04802, doi:10.1103/PhysRevD.91.094025.

[292] E. S. Swanson. Cusps and Exotic Charmonia. *Int. J. Mod. Phys.*, E25(07):1642010, 2016. arXiv:1504.07952, doi:10.1142/S0218301316420106.

[293] R Aaij et al. Measurement of the Λ_b^0, Ξ_b^- and Ω_b^- baryon masses. *Phys.Rev.Lett.*, 110:182001, 2013. arXiv:1302.1072, doi:10.1103/PhysRevLett.110.182001.

[294] J. P. Lees et al. Dalitz plot analysis of $\eta_c \to K^+K^-\eta$ and $\eta_c \to K^+K^-\pi^0$ in two-photon interactions. *Phys. Rev.*, D89(11):112004, 2014. arXiv:1403.7051, doi:10.1103/PhysRevD.89.112004.

[295] Roel Aaij et al. Measurement of the $B_s^0 \to \phi\phi$ branching fraction and search for the decay $B^0 \to \phi\phi$. *JHEP*, 10:053, 2015. arXiv:1508.00788, doi:10.1007/JHEP10(2015)053.

[296] Matthaus Bartsch, Gerhard Buchalla, and Christina Kraus. $B \to V(L)V(L)$ decays at Next-to-Leading Order in QCD. 2008. arXiv:0810.0249.

[297] Martin Beneke, Johannes Rohrer, and Deshan Yang. Branching fractions, polarisation and asymmetries of $B \to VV$ decays. *Nucl.Phys.*, B774:64–101, 2007. arXiv:hep-ph/0612290, doi:10.1016/j.nuclphysb.2007.03.020.

[298] Hai-Yang Cheng and Chun-Khiang Chua. QCD factorization for charmless hadronic B_s^0 decays revisited. *Phys.Rev.*, D80:114026, 2009. arXiv:0910.5237, doi:10.1103/PhysRevD.80.114026.

[299] Alexander L. Kagan. Polarization in $B \to VV$ decays. *Phys.Lett.*, B601:151–163, 2004. arXiv:hep-ph/0405134, doi:10.1016/j.physletb.2004.09.030.

[300] Alakabha Datta, Andrei V. Gritsan, David London, Makiko Nagashima, and Alejandro Szynkman. Testing explanations of the $B \to \phi K^*$ polarization puzzle. *Phys.Rev.*, D76:034015, 2007. arXiv:0705.3915, doi:10.1103/PhysRevD.76.034015.

[301] Chuan-Hung Chen and Chao-Qiang Geng. Scalar interactions to the polarizations of $B \to \phi K^*$. *Phys.Rev.*, D71:115004, 2005. arXiv:hep-ph/0504145, doi:10.1103/PhysRevD.71.115004.

[302] Chao-Shang Huang, Pyungwon Ko, Xiao-Hong Wu, and Ya-Dong Yang. MSSM anatomy of the polarization puzzle in $B \to \phi K^*$ decays. *Phys.Rev.*, D73:034026, 2006. arXiv:hep-ph/0511129, doi:10.1103/PhysRevD.73.034026.

[303] R. Aaij et al. First measurement of the *CP*-violating phase in $B_s^0 \to \phi\phi$ decays. *Phys. Rev. Lett.*, 110:241802, 2013. arXiv:1303.7125, doi:10.1103/PhysRevLett.110.241802.

[304] Ahmed Ali, Gustav Kramer, Ying Li, Cai-Dian Lu, Yue-Long Shen, et al. Charmless non-leptonic B_s decays to PP, PV and VV final states in the pQCD approach. *Phys.Rev.*, D76:074018, 2007. arXiv:hep-ph/0703162, doi:10.1103/PhysRevD.76.074018.

[305] D. Acosta et al. First evidence for $B_s^0 \to \phi\phi$ decay and measurements of branching ratio and A_{CP} for $B^+ \to \phi K^+$. *Phys.Rev.Lett.*, 95:031801, 2005. arXiv:hep-ex/0502044, doi:10.1103/PhysRevLett.95.031801.

[306] T. Aaltonen et al. Measurement of polarization and search for CP-violation in $B_s^0 \to \phi\phi$ decays. *Phys. Rev. Lett.*, 107:261802, 2011. arXiv:1107.4999, doi:10.1103/PhysRevLett.107.261802.

[307] Kenji Abe et al. Search for charmless hadronic decays of B mesons with the SLD detector. *Phys.Rev.*, D62:071101, 2000. arXiv:hep-ex/9910050, doi:10.1103/PhysRevD.62.071101.

[308] R. Aaij et al. Measurement of b hadron production fractions in 7 TeV pp collisions. *Phys. Rev.*, D85:032008, 2012. arXiv:1111.2357, doi:10.1103/PhysRevD.85.032008.

[309] R. Aaij et al. Measurement of the fragmentation fraction ratio f_s/f_d and its dependence on B meson kinematics. *JHEP*, 04:001, 2013. arXiv:1301.5286, doi:10.1007/JHEP04(2013)001.

[310] R. Aaij et al. Study of the kinematic dependences of Λ_b^0 production in pp collisions and a measurement of the $\Lambda_b^0 \to \Lambda_c^+\pi^-$ branching fraction. *JHEP*, 08:143, 2014. arXiv:1405.6842, doi:10.1007/JHEP08(2014)143.

[311] D. Bisello et al. Study of the η_c decays. *Nucl.Phys.*, B350:1–24, 1991. doi:10.1016/0550-3213(91)90251-R.

[312] J.Z. Bai et al. Measurement of branching ratios for η_c hadronic decays. *Phys.Lett.*, B578:16–22, 2004. arXiv:hep-ex/0308073, doi:10.1016/j.physletb.2003.10.042.

[313] M. Ablikim et al. Experimental study of η_c decays into vector-vector final states. *Phys.Rev.*, D72:072005, 2005. arXiv:hep-ex/0507100, doi:10.1103/PhysRevD.72.072005.

[314] R. Aaij et al. Measurement of the $B_s^0 \to \phi\phi$ branching fraction and search for the decay $B^0 \to \phi\phi$. *JHEP*, 10:053, 2015. arXiv:1508.00788, doi:10.1007/JHEP10(2015)053.

[315] R Aaij et al. Measurement of the fragmentation fraction ratio f_s/f_d and its dependence on B meson kinematics. *JHEP*, 04:001, 2013. arXiv:1301.5286, doi:10.1007/JHEP04(2013)001.

[316] Glen Cowan, Kyle Cranmer, Eilam Gross, and Ofer Vitells. Asymptotic formulae for likelihood-based tests of new physics. *Eur.Phys.J.*, C71:1554, 2011. arXiv:1007.1727, doi:10.1140/epjc/s10052-011-1554-0,10.1140/epjc/s10052-013-2501-z.

[317] C. Adolph et al. Measurement of the $\eta \to 3\pi^0$ Dalitz plot distribution with the WASA detector at COSY. *Phys.Lett.*, B677:24–29, 2009. arXiv:0811.2763, doi:10.1016/j.physletb.2009.03.063.

université PARIS-SACLAY | ÉCOLE DOCTORALE PHENIICS

Titre : Études de production des états de charmonium avec leurs désintégrations vers des hadrons dans l'expérience LHCb

Mots clés : *Analyse de données, Production et désintégrations de charmonium, Désintégrations du méson Bs, Tests QCD, Spectroscopie*

Résumé : Les études des propriétés et du mécanisme de la production du charmonium ont débuté avec la découverte du méson J/ψ. Depuis plus de 40 ans, le mécanisme de production de charmonium n'est toujours pas clair. Les états de charmonium sont copieusement produits dans les collisionneurs hadroniques, ce qui permet d'étudier systématiquement leurs paramètres de résonance, leur production et leurs désintégrations. En dépit des taux de production élevés, de nombreux états de charmonium sont peu étudiés suite aux difficultés de leur reconstruction avec le bruit de fond important. L'expérience LHCb offre une opportunité unique d'étudier les états S et P de charmonium en utilisant leurs désintégrations vers des hadrons, et en particulier la production des états η_c et χ_c. Selon le formalisme de la QCD non relativiste (NRQCD), les éléments de matrice décrivant l'hadronisation des états S (ou P) du charmonium sont liés. Par conséquent, les mesures LHCb fournissent les nouveaux tests rigoureux de NRQCD. Dans le cadre de la thèse, la première mesure de la section efficace de production de l'état $\eta_c(1S)$ à $\sqrt{s} = 13\,TeV$ et la mesure la plus précise de la masse sont effectués, avec la désintégration de l'état $\eta_c(1S)$ vers $p\bar{p}$. De plus, la production des états χ_c et $\eta_c(2S)$ dans les désintégrations des hadrons b est étudiée en utilisant leurs désintégrations vers $\phi\phi$. Les résultats obtenus sont confrontés aux prédictions de modèles théoriques. L'analyse phénoménologique originale démontre que la description de la production de charmonium dans les collisions hadroniques et de la production dans les désintégrations inclusives des hadrons b dans la gamme entière des impulsions transverses demeure un défi.

Title : Study of charmonium production using decays to hadronic final states with the LHCb experiment

Key words : *Data analysis, Production and decays of charmonium, Decays of the Bs meson, QCD tests, Spectroscopy*

Abstract : Studies of charmonium properties and production mechanism started with the discovery of J/ψ meson. Since more than 40 years the charmonium production mechanism is still not entirely understood. Following the era of investigations at e^+e^- machines, nowadays, charmonium states are copiously produced at hadron colliders, that allows systematic studies of their resonance parameters, production observables and decays. Despite large production rates, many charmonium states are barely studied due to the complications of their reconstruction against a large background level. The LHCb experiment provides a unique opportunity to study S-wave and P-wave charmonium states using their decays to hadrons. This allows measuring production observables of η_c and χ_c charmonium states. According to the theoretical formalism of Non-Relativistic QCD (NRQCD), the production observables of the same wave charmonium states are linked. Hence, the LHCb measurements provide a series of stringent tests of NRQCD. In the framework of this thesis, the first measurement of the $\eta_c(1S)$ differential production cross-section at $\sqrt{s} = 13\,TeV$ and the most precise to date single mass measurement are performed, where the $\eta_c(1S)$ state is reconstructed via its decay to $p\bar{p}$. In addition, the production of the χ_c and $\eta_c(2S)$ states in b-hadron decays is studied using decays to $\phi\phi$. The obtained results are confronted with existing theory predictions. The original phenomenological analysis concludes that the description of charmonium prompt production and production in inclusive b-hadron decays in an entire range of transverse momentum remains a challenge.

Université Paris-Saclay
Espace Technologique / Immeuble Discovery
Route de l'Orme aux Merisiers RD 128 / 91190 Saint-Aubin, France